The Dynamics and Energetics of Radio-Loud Active Galaxies

Jeremy James Harwood

Centre for Astrophysics Research

University of Hertfordshire

Submitted to the University of Hertfordshire in partial fulfilment of the requirements of the degree of

Doctor of Philosophy (PhD)

April 2014

Abstract

In this thesis, I use the new generation of radio interferometer along with X-ray observations to investigate the dynamics and energetics of radio-loud active galaxies which are key to understanding AGN feedback and the evolution of galaxies as a whole.

I present new JVLA observations of powerful radio source and use innovative techniques to undertake a detailed analysis of JVLA observations of powerful radio galaxies. I compare two of the most widely used models of spectral ageing, the Kardashev-Pacholczyk and Jaffe-Perola models and also results of the more complex, but potentially more realistic, Tribble model. I find that the Tribble model provides both a good fit to observations as well as providing a physically realistic description of the source. I present the first high-resolution spectral maps of the sources and find that the best-fitting injection indices across all models take higher values than has previously been assumed. I present characteristic hot spot advance speeds and compare them to those derived from dynamical ages, confirming that the previously known discrepancy in speed remains present in older radio sources even when ages are determined at high spectral and spatial resolutions. I show that some previously common assumptions made in determining spectral ages with narrow-band radio telescopes may not always hold.

I present results from a study of the powerful radio galaxy 3C223 at low frequencies with LOFAR to determine its spectrum on spatially small scales and tightly constrain the injection index, which I find to be consistent with the high values found at GHz frequencies. Applying this new knowledge of the low energy electron population, I perform synchrotron / inverse-Compton model fitting and find that the total energy content of the radio galaxy lobes increases by a factor greater than 2 compared to previous studies. Using this result to provide revised estimates

of the internal pressure, I find the northern lobe to be in pressure balance with the external medium and the southern lobe to be overpressured.

I go on to present the first large sample investigation of the properties of jets in Fanaroff and Riley type I radio galaxies (FR-I) at X-ray energies based on data from the *Chandra* archive. I explore relations between the properties of the jets and the properties of host galaxies in which they reside. I find previously unknown correlations to exist, relating photon index, volume emissivity, jet volume and luminosity, and find that the previously held assumption of a relationship between luminosities at radio and X-ray wavelengths is linear in nature when bona fide FR-I radio galaxies are considered. In addition, I attempt to constrain properties which may play a key role in determination of the diffuse emission process. I test a simple model in which large-scale magnetic field variations are primarily responsible for determining jet properties; however, we find that this model is inconsistent with our best estimates of the relative magnetic field strengths in my sample.

Contents

List of Figures **vii**

List of Tables **xv**

1 Introduction **1**

1.1 Motivation: radio galaxies and their effect on galaxy evolution 1

1.2 An introduction to radio-loud active galaxies 3

1.2.1 General properties 4

1.2.2 The unified model of radio-loud AGN 6

1.3 The theory of radio-loud active galaxies 8

1.3.1 Non-thermal radiative processes 8

1.3.1.1 Synchrotron radiation 9

1.3.1.2 Inverse-Compton scattering 10

1.3.2 Spectral ageing 11

1.3.2.1 The standard models of spectral ageing 11

1.3.2.2 The Tribble model of spectral ageing 12

1.3.3 Particle content 14

1.3.3.1 Electron-proton jets 14

1.3.3.2 Electron-positron jets 15

1.3.3.3 Entrainment 16

1.3.4 Magnetic fields 17

1.4 The observational properties of radio galaxies 19

1.4.1 FR-I galaxies at radio wavelengths 19

1.4.2 FR-II galaxies at radio wavelengths 21

1.4.3 FR-I galaxies at X-ray energies 23

1.4.4 FR-II galaxies at X-ray energies . . . 25
1.5 The dynamics of radio galaxies . . . 28
1.5.1 The beam model of radio-loud active galaxies . . . 28
1.5.2 FR-I dynamics . . . 28
1.5.3 FR-II dynamics . . . 30
1.6 Galaxy evolution and the role of radio-loud AGN . . . 32
1.6.1 The environment of radio-loud AGN . . . 32
1.6.2 The impact of radio-loud AGN on their environment . . . 34
1.6.3 AGN feedback and its role in galaxy evolution . . . 35
1.6.3.1 Quasar mode . . . 35
1.6.3.2 Radio mode . . . 36
1.7 Outstanding questions and thesis aims . . . 36

2 Instrumentation and methods of analysis 41
2.1 X-ray observations . . . 41
2.1.1 *Chandra* . . . 41
2.1.2 Data reduction . . . 42
2.2 Radio observations . . . 44
2.2.1 Karl G. Jansky Very Large Array (JVLA) . . . 44
2.2.1.1 Typical JVLA continuum observations . . . 47
2.2.2 LOw-Frequency ARray (LOFAR) . . . 47
2.2.2.1 Typical LOFAR continuum observations . . . 49
2.2.3 Radio data reduction . . . 52
2.2.3.1 AIPS calibration . . . 53
2.2.3.2 CASA calibration . . . 54
2.2.3.3 LOFAR calibration . . . 55
2.2.3.4 Imaging . . . 56
2.2.3.5 Self and cross calibration . . . 58
2.3 The Broadband Radio Astronomy ToolS (BRATS) . . . 59
2.3.1 Overview . . . 59
2.3.2 Obtaining BRATS and installation . . . 60
2.3.3 Loading data and image requirements . . . 61
2.3.3.1 Image alignment . . . 62

2.3.4 Adaptive regions . . . 63
2.3.5 Model fitting and parameter determination . . . 64
2.3.5.1 Spectral index mapping . . . 64
2.3.5.2 Colour-colour plots . . . 65
2.3.5.3 Spectral age fitting . . . 65
2.3.5.4 Injection index determination . . . 70
2.3.6 Statistics . . . 70
2.3.7 Image combination . . . 71
2.3.8 Image reconstruction and difference maps . . . 71

3 Spectral ageing in the lobes of FR-II radio galaxies 73
3.1 Introduction . . . 73
3.2 Data reduction and spectral analysis . . . 76
3.2.1 Target selection and observations . . . 76
3.2.2 Data Reduction . . . 78
3.2.3 Spectral Analysis . . . 79
3.2.3.1 Region selection . . . 80
3.2.3.2 Model fitting and parameter determination . . . 82
3.3 Results . . . 86
3.3.1 Model Parameters . . . 86
3.3.2 Spectral age and model comparison . . . 86
3.3.3 Lobe speeds . . . 93
3.3.4 Source reconstruction . . . 96
3.4 Discussion . . . 99
3.4.1 Source morphology . . . 99
3.4.2 Injection index . . . 107
3.4.3 Spectral ages and lobe speeds . . . 110
3.4.4 Model comparison . . . 115
3.5 Conclusions . . . 115

4 Further investigations of spectral ageing at GHz frequencies 119
4.1 Introduction . . . 119
4.2 Data reduction and spectral analysis . . . 120
4.2.1 Target selection and observations . . . 120

4.2.2 Data Reduction . . . 121
4.2.3 Spectral analysis and region selection . . . 125
4.2.3.1 Model fitting and parameter determination . . . 126
4.3 Results . . . 126
4.3.1 Model Parameters . . . 126
4.3.2 Spectral age and model comparison . . . 129
4.3.3 Lobe Speeds . . . 133
4.4 Discussion . . . 139
4.4.1 Source orientation . . . 139
4.4.2 Jets . . . 139
4.4.3 Injection index . . . 140
4.4.4 Spectral ages and lobe speeds . . . 141
4.4.5 Model comparison . . . 144
4.5 Conclusions . . . 145

5 The energetics of radio galaxies at LOFAR wavelengths 147
5.1 Introduction . . . 147
5.2 Data reduction and spectral analysis . . . 148
5.2.1 Target selection and observations . . . 148
5.2.2 Data reduction . . . 149
5.2.3 Spectral analysis and region selection . . . 150
5.2.3.1 Model fitting and parameter determination . . . 152
5.3 Results . . . 157
5.3.1 Model Parameters . . . 157
5.3.2 Spectral age fitting . . . 159
5.3.3 Spectral index mapping . . . 160
5.3.4 Synchrotron / inverse-Compton fitting . . . 160
5.4 Discussion . . . 163
5.4.1 Spectral ages . . . 163
5.4.2 Injection index . . . 166
5.4.3 Synchrotron / inverse-Compton model fitting . . . 169
5.5 Conclusions . . . 170

6 What determines the properties of the X-ray jets in FR-I radio galaxies? 173
6.1 Introduction . . . 173
6.2 Target Galaxies and Analysis . . . 175
6.2.1 Jet and background region selection . . . 176
6.2.2 Collection of spectral and comparative data . . . 180
6.2.3 Treatment of special cases . . . 190
6.3 Results . . . 191
6.3.1 Statistical analysis . . . 191
6.3.2 Photon index relations . . . 191
6.3.3 Derived ratios . . . 194
6.3.4 Luminosity & emissivity relations . . . 194
6.4 Discussion . . . 199
6.4.1 Current models of particle acceleration . . . 199
6.4.2 Key emission process variables . . . 199
6.4.3 Testing of viable acceleration models . . . 201
6.5 Conclusions . . . 204

7 Conclusions and future work 205
7.1 New methods of analysis for broad bandwidth radio observations . . . 206
7.2 Parameters in models of spectral ageing . . . 206
7.3 Spectral ageing: reliability and its physical reality . . . 207
7.4 The spectral profile and energetics of powerful radio galaxy lobes at low frequencies . . . 207
7.5 Relationships and models of X-ray jets in FR-I radio galaxies . . . 208
7.6 Future work . . . 209

References 213

List of Figures

1.1 The typical FR-I and FR-II radio galaxies 3C31 (left, Laing & Bridle, 2002a) and 3C98 (right, Leahy et al., 1997) with characteristic features labelled. Note the faint one-sided jet located in the northern lobe of 3C98. 1 arcminute on the sky represents a physical distance of 20.4 kpc for 3C31 ($z = 0.0167$) and 36.7 kpc for 3C98 ($z = 0.0306$). 3

1.2 The quasar 3C273 with characteristic features labelled. 1 arcsecond on the sky represents a physical distance of 2.74 kpc ($z = 0.158$). 5

1.3 Graphical representation of the unified model of AGN (not to scale). Solid arrows indicate an observer's line of sight. Dotted lines indicate the key AGN features discussed in Section 1.2.2. 7

1.4 Example KP (top), JP (middle) and Tribble (bottom) models between 10 MHz and 10 THz for an arbitrary normalization with 0.6 injection index. Each plot shows model ages between 0 (red) and 10 (purple) megayears. 13

1.5 Plot of the total energy content (arbitrary units) of a radio source as a function of magnetic field strength as detailed in Section 1.3.4. The total energy content (solid red line) is given by the sum of the electron energy content U_E and the magnetic field energy U_B (dashed blue lines). Note that the minimum energy occurs close to the equipartition value ($B = 1$). 18

1.6 Plot by Owen & Ledlow (1994) of 1.4 GHz radio versus R-band luminosity for a sample of radio galaxies. Radio units are W Hz^{-}1. FR-I's and FR-II's are denoted by 1's and 2's respectively. 20

1.7 A collection of FR-I morphologies at radio wavelengths. Top left, M87 (Owen et al., 2000): Residing at only $\sim$ 20 Mpc, M87 is one of the brightest radio sources in the sky. Although being core dominated and displaying the plumes associated with an FR-I morphology, only a single jet is observed at radio wavelengths. Top right, 3C66B (Hardcastle et al., 1996): A classic FR-I radio galaxy with twin radio jets and plumes. Bottom left, 3C83.1B (O'Dea & Owen, 1986): A head-tail source with clear bending of the jets and plumes, most likely due to ram pressure as the galaxy moves through its environment. Bottom right, 3C75 (Hardcastle et al., 2004b): A peculiar FR-I source containing two radio cores. It displays two sets of twin jets and plumes. 1 arcsecond on the sky represents a physical distance of 0.088 kpc for M87 ($z = 0.00428$), 0.44 kpc for 3C66B ($z = 0.0215$), 0.51 kpc for 3C83.1B ($z = 0.0255$) and 0.47 kpc for 3C75 ($z = 0.0232$). 22

1.8 A collection of FR-II morphologies at radio wavelengths. Top, Cygnus A (Dreher et al., 1987): One of the brightest and well studied FR-IIs in the sky. Cygnus A is an archetypal FR-II galaxy displaying clear hot spots and lobes. Bottom left, 3C293 (Bridle et al., 1981): Example of a FR-II source with a highly asymmetric morphology. Bottom right, 3C33.1 (Leahy, Bridle and Strom, unpublished (http://www.jb.man.ac.uk/atlas/): An FR-II radio galaxy with an asymmetric morphology. A classical FR-II structure is seen to the north of the core, but only a weak hot spot and brightened emission along the jet length are observed in the southern lobe. 1 arcsecond on the sky represents a physical distance of 1.1 kpc for Cygnus A ($z = 0.0561$), 0.89 kpc for 3C293 ($z = 0.0450$) and 3.1 kpc for 3C33.1 ($z = 0.181$). 24

1.9 Plot of $\log(\nu\, S_\nu)$ versus $\log(\nu)$ for the FR-I radio galaxy Centaurus A. Data taken from the NASA extragalactic database (NED) and references therein. Note the large scatter at optical wavelengths is due to differing aperture sizes and optical core variability. 26

1.10 Plot by Croton et al. (2006) of luminosity functions in the K (left) and B (right) photometric bands. Overlaid are models including (solid line) and excluding (dashed line) radio mode feedback. When this feedback model is included, the predicted luminosity of massive ellipticals is in good agreement with observations. 37

2.1 Schematic view of the *Chandra* grazing mirror design. Image courtesy of NASA/CXC/D.Berry. 42

2.2 Schematic view of the *Chandra* X-ray observatory with instruments labelled. Image courtesy of NASA/CXC/NGST. 43

2.3 The Jansky Very Large Array (JVLA) in New Mexico, USA. Array shown in the compact D configuration. 46

2.4 Example of a typical JVLA observing plan as detailed in Section 2.2.1.1 of two target sources, 3C438 and 3C28. 48

2.5 Location of LOFAR stations throughout Europe. Image courtesy of ASTRON. . 50

2.6 Images of a LOFAR LBA (left) and HBA (right) station. Note the HBA antennas are located within the observed black casings. Images courtesy of ASTRON. . 51

2.7 Recommended directory structure for BRATS usage. Dotted lines represent the users preferred path, solid lines indicate directories located within the preceding level. Region files should ideally be contained within the working directory. Source directories should contain only the FITS files to be loaded. 61

2.8 Colour-colour plot of the radio relic CIZA J2242.8+5301 by Stroe et al. (2013). Black dots are the data points at various regions downstream of the source. Overlaid are various models of spectral ageing with varying injection indices. 'JP' and 'KP' refer to the models described in Section 1.3.2, 'CI' to the continuous injection model (Pacholczyk, 1970) in which a supply of freshly accelerate electrons are injected to the region of plasma, and 'KGJP' to the hybrid Komissarov-Gubanov model (Komissarov & Gubanov, 1994) in which freshly accelerated electrons are injected to the JP model for a finite time period. 66

2.9 Fitting of the JP model of spectral ageing to simulated observations. The simulated data consist of seven images between 153 MHz and 2.27 GHz determined from an ideal JP model with $\alpha_{inj} = 0.77$. Flux values are determined on a pixel by pixel (1 arcsec) basis between 0 and 40 Myrs, then convolved with a 15 arcsec beam. The resulting images were then analyzed with the BRATS '*fitjpmodel*' command to produce the above spectral ageing map, which recovers the input ages well. 69

3.1 Combined frequency radio maps of 3C436 (top), 3C300 (middle) and 3C234 (bottom) between 4 and 8 GHz scaled to 6.0 GHz. The off-source RMS of the combined maps is 27, 33 and 89 μJy beam^{-1} with peak fluxes of 68.5, 280 and 369 mJy beam^{-1} for 3C436, 3C300 and 3C234 respectively. 12 contours are spaced logarithmically between 5σ based on the on-source RMS noise and the peak flux. The restoring beam (red) is indicated in the bottom left corner of each image. 1 arcsecond on the sky represents a physical distance of 3.49 kpc for 3C436 ($z = 0.215$), 4.17 kpc for 3C300 ($z = 0.272$)and 3.11 kpc for 3C234 ($z = 0.185$). 77

3.2 χ^2 values for 3C436 (top) and 3C300 (bottom) for varying injection index values fitted with a natural cubic spline. The solid blue line represents the KP model, the red dashed line the JP model and the black dotted line the Tribble model. Data points are taken at intervals of 0.1 between 0.5 and 1.0 inclusive and intervals of 0.01 between 0.8 and 0.92 for 3C436 and between 0.8 and 0.87 for 3C300. As all data points lie on the fitted spline, they are not plotted for clarity. Note that minima occur at 0.86 for 3C436 and at 0.82 for 3C300 for all models. 84

3.3 Spectral ageing maps (left) and corresponding χ^2 maps (right) of 3C436 with 7.2 GHz flux contours. Three model fits are shown; KP model (top), JP model (middle) and Tribble model (bottom) with injection index 0.86. 88

3.4 Spectral ageing maps (left) and corresponding χ^2 maps (right) of 3C300 with 7.2 GHz flux contours. Three model fits are shown; KP model (top), JP model (middle) and Tribble model (bottom) with injection index 0.82. 89

3.5 Spectral age map of 3C300 (top) and reduced χ^2 map of 3C436 (bottom) for the JP model fitting with a 0.86 injection index. Locations of significant interest are marked as discussed in Section 3.3.2. 94

3.6 Errors for 3C436 (left) and 3C300 (right) for the KP (top), JP (middle) and Tribble (bottom) models of spectral ageing mapped as a function of position with 7.2 GHz flux contours overlaid. Positive error bars for the are shown for each model. Errors are determined using the methods described in Section 2.3.5.3. 95

3.7 Plots of flux against frequency for the high χ^2 regions of 3C436 (top) and 3C300 (middle) and the unexpected low ages region of 3C300 (bottom) as discussed in Section 3.3.2. Red lines indicate the best-fitting JP model with parameters as noted on each plot. 98

3.8 Plots of flux against frequency for two well fitted regions of 3C436 (top) and 3C300 (bottom) showing low (left) and high (right) spectral ages. Red lines indicate the best-fitting JP model with parameters as noted on each plot. 100

3.9 Maps of residual flux from the subtraction of the reconstructed model source from the observed source using the combined 6 GHz map described in Section 3.3.4. Model subtracted maps of 3C436 (top) and 3C300 (bottom) showing regions of model flux overestimation (left) and underestimation (right) are shown. Scale is in units of Jy beam^{-1}. Here the KP model has been used in reconstruction of the source using the best fitting spectral ages and normalizations. Maps are limited to the regions used in the model fitting of Sections 3.2.3.2 and 3.3.2. Overlaid are the 6 GHz contours of the combined frequency maps of Figure 3.1. 103

3.10 Maps of residual flux from the subtraction of the reconstructed model of 3C436 from 2 of the observed frequencies as described in Section 3.3.4. Model subtracted maps at 4.47 GHz (top) and 7.21 GHz (bottom) show regions of overestimation (left) and underestimation (right) of the model flux. Note that there are no underestimated regions at 4.47 GHz. Scale is in units of Jy beam^{-1}. Here the KP model has been used in reconstruction of the source using the best fitting spectral ages and normalizations. Maps are limited to the regions used in the model fitting of Sections 3.2.3.2 and 3.3.2. Overlaid are the 6 GHz contours of the combined frequency maps of Figure 3.1. 104

3.11 Maps of residual flux from the subtraction of the reconstructed model of 3C300 from 2 of the observed frequencies as described in Section 3.3.4. Model subtracted maps at 4.47 GHz (top) and 7.21 GHz (bottom) show regions of model flux overestimation (left) and underestimation (right). Scale is in units of Jy beam^{-1}. Here the KP model has been used in reconstruction of the source using the best fitting spectral ages and normalizations. Maps are limited to the regions used in the model fitting of Sections 3.2.3.2 and 3.3.2. Overlaid are the 6 GHz contours of the combined frequency maps of Figure 3.1. 105

3.12 High resolution total intensity maps of 3C436 (left) and 3C300 (right) by Hardcastle et al. (1997). The resolution of the maps are 0.75 and 0.50 arcseconds for 3C436 and 3C300 respectively. The flux scale has been adjusted to enhance the bright small scale features and jets described in Section 3.3.2. 106

3.13 Example of how spatially large regions can bias the true spectral age. Top: Combined frequency map of 3C300 at 5 GHz with a single, spatially large region overlaid. Bottom: A plot of the resulting JP model fit and statistics. 109

4.1 Combined A, B and C configuration radio map of 3C438 between 4 and 8 GHz. Imaged using multiscale CLEAN and CASA nterms = 2 to a central frequency of 6 GHz. The off-source RMS of the combined maps is 8μJy beam^{-1}. The restoring beam is indicated in the bottom left corner of the image. 123

4.2 χ^2 values for 3C438 including the jet region for varying injection index values using the JP model of spectral ageing. Data points are taken at intervals of 0.1 between 0.5 and 1.0 inclusive and intervals of 0.01 between 0.72 and 0.82 and fitted with a natural cubic spline. As all data points lie on the fitted spline, they are excluded for clarity. Note that a minimum occurs at 0.78. 127

4.3 χ^2 values for 3C438 with the jet region excluded for varying injection index values using the JP model of spectral ageing. Data points are taken at intervals of 0.1 between 0.5 and 1.0 inclusive and intervals of 0.01 between 0.75 and 0.85 and fitted with a natural cubic spline. As all data points lie on the fitted spline, they are excluded for clarity. Note that a minimum occurs at 0.80. 128

4.4 Spectral ageing maps (left) and corresponding χ^2 maps (right) of 3C438 with 7.9 GHz flux contours. Three model fits are shown; KP model (top), JP model (middle) and Tribble model (bottom) with injection index 0.78 134

4.5 Spectral age errors of 3C438 including (top) and excluding (bottom) the jet region, mapped as a function of position with 7.9 GHz flux contours overlaid. Positive errors for the JP model are shown. Errors are determined using the methods described in Section 2.3.5.3. 135

4.6 Two-point spectral index map created in BRATS of the southern lobe of 3C438 between 1.4 and 8 GHz. The data used is that presented by Treichel et al. (2001), reimaged at 0.42 arcsec resolution. 136

4.7 Plots of flux against frequency for six well fitted regions of 3C438 at low (top), moderate (middle) and high (right) spectral ages. Red lines indicate the best-fitting Tribble model with parameters as noted on each plot. 142

5.1 Radio maps of 3C223 at 140 MHz (top) and 51.6 MHz (bottom). Imaged using multiscale CLEAN in CASA. The off-source RMS noise is 0.78 mJy beam^{-1} for the 140 MHz map and 12.4 mJy beam^{-1} for the 51.6 MHz map. The restoring beam is indicated in the bottom left corner of the image. 153

5.2 χ^2 values for 3C223 for varying injection index values fitted with a natural cubic spline. The solid blue line represents the KP model and the red dashed line the JP model. Data points are taken at intervals of 0.1 between 0.5 and 1.0 inclusive and intervals of 0.01 between 0.65 and 0.75. As all data points lie on the fitted spline, they are excluded for clarity. Note that a minimum occurs at 0.71 for all models. 155

5.3 Spectral index map of 3C223 between 118 MHz and 1.48 GHz. Note the noise-like regions of flat spectrum in the northern lobe discussed in Section 5.3.3. . . 156

5.4 Spectral ageing maps (left) and corresponding χ^2 maps (right) of 3C223 with 1.4 GHz flux contours. Two model fits are shown; the KP model (top) and the JP model (bottom) with injection index 0.71 161

5.5 Spectral age errors of 3C223 mapped as a function of position with 1.4 GHz flux contours overlaid. Positive errors for the JP model are shown. Errors are determined using the methods described in Section 2.3.5.3. 162

5.6 Synchrotron / inverse-Compton model fitting for the northern (top) and southern (bottom) lobes of 3C223. The red stars show the radio and X-ray integrated flux measurements taken from Croston et al. (2004) and this thesis. The red 'bow tie' shows the model constraints imposed by the X-ray observations. The solid black line shows the model synchrotron spectrum normalized to the 51.6 MHz flux and subject to JP losses, the dotted blue line the model iC/CMB emission, and the green dot-dashed line the model SSC emission. The magnetic field strength has been adjusted to ensure that the X-ray flux measurement is reproduced by the inverse-Compton model. 164

5.7 Plots of flux against frequency for four well fitted regions of 3C223 at various spectral ages. Ages increase in a clockwise direction starting at the top left. Red lines indicate the best-fitting JP model with parameters as noted on each plot. . 165

5.8 χ^2 values for the radio relic CIZA J2242.8+5301 (the Sausage) for varying injection index values fitted with a natural cubic spline (Stroe et al., in prep). The solid red line represents the JP model of spectral ageing fitted to observations at 153, 323, 608, 1221, 1382, 1714 and 2272 MHz and a magnetic field strength of 0.6 nT. Data points are taken at intervals of 0.1 between 0.5 and 1.0 inclusive and intervals of 0.01 between 0.65 and 0.75. As all data points lie on the fitted spline, they are excluded for clarity. Note that a minimum occurs at 0.77. . . . 167

5.9 Spectral ageing map by Stroe et al. (in prep) of the radio relic CIZA J2242.8+5301 (the Sausage). The map shows the JP model fitted to observations at 153, 323, 608, 1221, 1382, 1714 and 2272 MHz using an injection index of 0.77 (Figure 5.8) and a magnetic field strength of 0.6 nT. 168

6.1 Examples of background region selection. Solid black regions denote the selected jet region; Solid green denotes are the boundary for inclusion in the background region; Red crossed areas denote regions excluded from consideration. Note: In the case of method 2 (bottom) black regions are included for the jet, but excluded for background measurements. The top image displays Cen A as an example of the method used for cases in which background emission varies irregularly as a function of position along the jet. The regions run alongside the jet to its furthest extent. Note the dust lane (see Section 6.2.3) which runs across the jet approximately $1/3$ of the way from the galactic centre and the exclusion of emission due to point sources which fall in the line of sight. The bottom image shows 3C 31 as a case in which background emission is symmetrical about the galactic centre. A large circular region encompasses the largest possible area for an improved uncertainty measurement. Note the exclusion of the jet and AGN regions. 181

6.2 Top left: The strong correlation between jet luminosity at radio and X-ray wavelengths. Top right: The correlations between 5 GHz core luminosity and X-ray jet luminosity discussed in Section 6.3.4. Bottom left: The relation between 8.46 GHz radio luminosity and photon index in *bona fide* FR-Is discussed in Section 6.3.2. Bottom right: Plot of flux ratio against radio luminosity discussed in Section 6.4.2. Blue points are those classed as *bona fide* FR-Is. Red points represent the BL Lacs and intermediate cases included in the full sample. . . . 202

List of Tables

2.1 Comparison of VLA and JVLA capabilities 45

3.1 List of target sources and galaxy properties 74
3.2 Observation Details 75
3.3 Summary of imaging parameters 79
3.4 Summary of maps by frequency 81
3.5 Summary of adaptive region parameters 82
3.6 Summary of SYNCH parameters 83
3.7 Model Fitting Results 85
3.8 3C436 Lobe Advance Speeds 91
3.9 3C300 Lobe Advance Speeds 92

4.1 List of target sources and galaxy properties 120
4.2 Observation Details 121
4.3 Summary of imaging parameters 122
4.4 Summary of maps by frequency 124
4.5 Summary of adaptive region parameters 126
4.6 Summary of SYNCH parameters 129
4.7 Model Fitting Results (Full Source) 130
4.8 Model Fitting Results (No Jet) 131
4.9 3C438 Lobe Advance Speeds (Full Source) 137
4.10 3C438 Lobe Advance Speeds (No Jet) 138

5.1 List of target sources and galaxy properties 148
5.2 Observation Details 149
5.3 Summary of HBA imaging parameters 150

5.4 Summary of LBA imaging parameters 151
5.5 Summary of maps by frequency 152
5.6 Summary of adaptive region parameters 154
5.7 Summary of synchrotron / inverse-Compton model parameters 157
5.8 Model Fitting Results (Spectral Ageing) 158
5.9 Model Fitting Results (Synchrotron / Inverse-Compton) 159
5.10 Summary of lobe pressures for 3C223 170

6.1 List of target galaxies, observation IDs and noted features 177
6.2 List of target galaxies, observation IDs and noted features (continued) 178
6.3 List of target galaxies, observation IDs and noted features (continued) 179
6.4 Tested host galaxy properties and their source 182
6.5 Observed jet properties 184
6.6 Observed jet properties (continued) 185
6.7 Jet volume and derived properties 186
6.8 Jet volume and derived properties (continued) 187
6.9 AGN core properties 189
6.10 Correlated test results (full sample) 192
6.11 Correlated test results (*bona fide* FR-Is only) 193
6.12 Uncorrelated test results (full sample) 197
6.13 Uncorrelated test results (*bona fide* FR-Is only) 198

Acknowledgements

I would like to thank all the people who have contributed to making this thesis possible, particularly my supervisor Martin Hardcastle for providing the scientific input, guidance and the freedom to pursue various avenues of research which have made for such an interesting PhD project and Judith Croston for her helpful comments and the research opportunities she has provided. I also wish to thank William Keel for providing the radio map of OL97 0313-192 used in Chapter 6, making a full a analysis of this unusual galaxy possible. I would also like to thank Andra Stroe for countless constructive discussions, making conferences that much more enjoyable and for all the moral support, especially at the late stages of writing this thesis. Last, but certainly not least, I would like to thank my wife and kids for all the help and support throughout my PhD, and for being so understanding over the last 3 years.

Declaration

I declare that the work in this thesis has been carried out in accordance with the regulations of the University of Hertfordshire. All work is my own except were otherwise stated. The synchrotron / inverse-Compton model fitting detailed in Chapter 5 was performed by my supervisor Judith Croston, using revised measurements provided by myself. Sections of this thesis are taken from material published in the Monthly Notices of the Royal Astronomical Society (Harwood & Hardcastle, 2012; Harwood et al., 2013). This thesis has not been previously submitted for any degree or diploma at this or any other university.

Jeremy Harwood

March 2014

1

Introduction

1.1 Motivation: radio galaxies and their effect on galaxy evolution

Since the late 90s, the standard lambda cold dark matter (ΛCDM) cosmological model has proved to be in excellent agreement with empirical evidence, including observations of the cosmic microwave background (CMB) (Spergel et al., 2007), total mass-density parameter (Peacock et al., 2001) and the Universe's current rate of accelerated expansion (Riess et al., 2000); however, models of galaxy evolution under this regime have fared less well, as first suggested by White & Rees (1978). Galaxies are thought to form through the hierarchical merging of dark matter halos into which gas condenses, but these models have historically produced an excess of cold gas, a deficit in hot gas, and an overpopulation of young stars when only gravitational heating and radiative cooling are accounted for (Balogh et al., 2001). This leads to a disparity in the luminosity and morphology of galaxies when compared to observation; the so-called "red and dead" paradox in which large elliptical galaxies, where cold gas for star formation should be most abundant, are observed to contain an old stellar population and low star formation rates. These simple models also imply that nearly all of the hot gas observed should have already cooled within the lifetime of the system (Cowie & Binney, 1977; Fabian & Nulsen, 1977), which is inconsistent with observations of X-ray emission in clusters of galaxies (Peterson et al., 2001; Tamura et al., 2001). It has therefore long been recognised (White & Frenk, 1991; Cole, 1991) that additional mechanisms must be included in the models if they are to account for what is observed.

The apparent over-cooling and the consequent overestimation of the population of young stars gives rise to two important questions; why is the gas in the system not cooling as predicted?

Why do the biggest elliptical galaxies have a lower star formation rate than smaller galaxies? Over the last decade it has become increasingly apparent (Croton et al., 2006; Bower et al., 2006) that radio-loud active galaxies could play an important role in answering these questions. Croton et al. (2006) suggest a feedback model in which cool molecular clouds that condense into star forming regions also feed the central supermassive black hole. This triggers the onset of active galactic nuclei (AGN) and their accompanying radio jets such as those observed in radio galaxies and quasars. These mechanically powerful jets drive cold gas from the galaxy and heat the cooling flows in a 'maintenance mode', suppressing the levels of possible star formation. In the most massive galaxies, this process can bring star formation almost to a halt, so explaining the 'red and dead' characteristics of big ellipticals. This model of AGN feedback has gained support not only because of its ability to account for observations in a self-regulating manner, but because it is also independent of star formation, on which many previous feedback models, such as those involving supernovae, relied (White & Rees, 1978; White & Frenk, 1991). However, the details of *how* AGN provide the required energetic input remain unclear.

The historic inability of radio interferometers to produce high sensitivity, high bandwidth observations with good *uv* coverage has at least partly been responsible for the many ambiguities which exist in our current understanding of radio-loud active galaxies. The new generation of radio telescopes currently becoming operational (Chapter 2) has changed this situation dramatically. The capabilities of instruments such as the Jansky Very Large Array (JVLA) and the LOw-Frequency ARray (LOFAR) mean that detailed spectral analysis can now be performed to unprecedented levels. These advances in radio astronomy, combined with complementary high resolution X-ray observations, mean we are now ideally placed to begin understanding the dynamics and energetics of these sources; a vital step if one is to understand their role in the context of galaxy evolution.

In this thesis I use next generation radio interferometers and X-ray energy observations to investigate the dynamics and energetics of nearby radio-loud active galaxies. Using innovative techniques I address four aims: to investigate the spectral profile of powerful radio galaxies at low and GHz frequencies, to constrain the model parameters of spectral ageing (an important factor in the determination of the age, hence power, of FR-II radio galaxies), to investigate new (potentially more realistic) models of spectral ageing, and to study what determines the particle acceleration properties of the jets in FR-I radio galaxies.

In this introductory chapter, I describe the theoretical understanding of the emission processes of these sources and of current and new models of spectral ageing which aim to describe

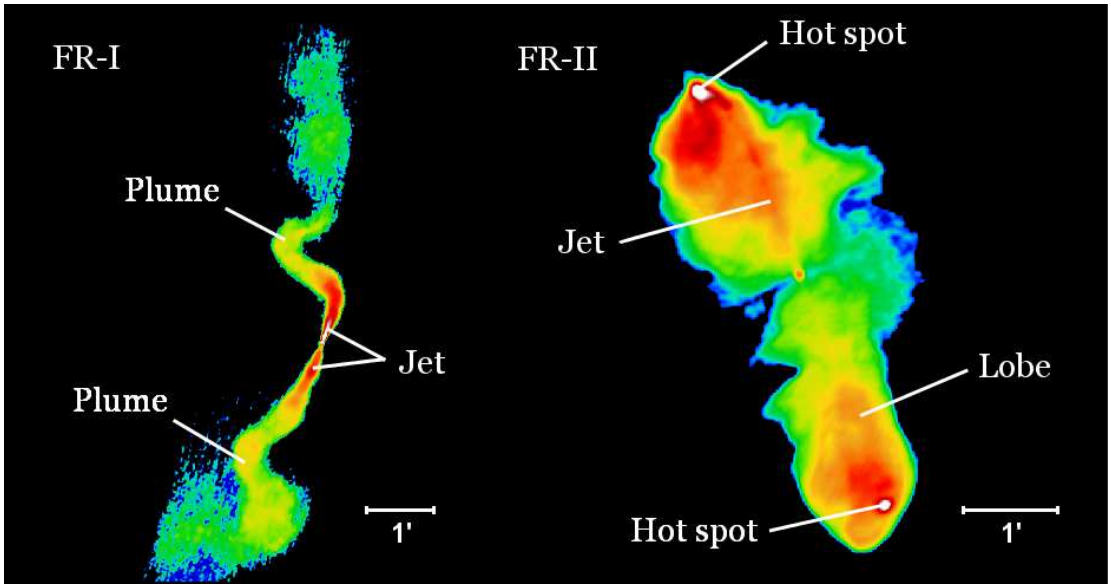

Figure 1.1: The typical FR-I and FR-II radio galaxies 3C31 (left, Laing & Bridle, 2002a) and 3C98 (right, Leahy et al., 1997) with characteristic features labelled. Note the faint one-sided jet located in the northern lobe of 3C98. 1 arcminute on the sky represents a physical distance of 20.4 kpc for 3C31 ($z = 0.0167$) and 36.7 kpc for 3C98 ($z = 0.0306$).

their spectral profile. I go on to detail the observational properties of radio galaxies and illustrate their importance in the role of galaxy evolution, particularly in the context of AGN feedback. I conclude this chapter by summarizing the outstanding questions on radio galaxies and the specific questions that this thesis aims to address.

Throughout this thesis, a concordance model in which $H_0 = 71$ km s^{-1} Mpc^{-1}, $\Omega_m = 0.27$ and $\Omega_\Lambda = 0.73$ is used.

1.2 An introduction to radio-loud active galaxies

The emission from the majority of galaxies is dominated by the billions of stars contained within them, but a small fraction of massive galaxies are observed to have emission at some wavelength greatly in excess of that which would be expected from stars, gas and dust alone. These active galaxies are observed to be some of the most energetic phenomena in the Universe and, as noted above, are thought to have a major impact on their environment and the evolution of galaxies as a whole. The additional energy release in active galaxies originates from a central region of the galaxy, known as the active galactic nucleus (AGN). These highly compact regions are

thought to be powered by matter accretion on to a supermassive black hole which is capable of producing emission across the majority of the electromagnetic spectrum. AGN can be divided into numerous categories based on, for example, their luminosity and optical emission lines, but it is those which display an excess of emission at radio wavelengths above that which would be expected from star formation alone which are the focus of this thesis.

Radio-loud active galaxies are a broad class of object which emit twin relativistic jets of high energy particles. These jets, and the associated structures described in the following sections, are observed to emit radiation across the entire electromagnetic spectrum through the non-thermal synchrotron and inverse-Compton processes (Section 1.3.1.1), but it is observations at radio and X-ray wavelengths which most often give key insights into the dynamics and energetics of these objects. Within this section, I briefly describe the various types of radio-loud active galaxies, their general properties, and how they have been combined into one unified model.

1.2.1 General properties

The term radio-loud active galaxy encompasses a range of 3 observationally distinct (although possibly intrinsically similar) types of object; radio galaxies, quasars, and blazars. Found primarily in massive ellipticals, radio galaxies are observed to have structure at radio wavelengths which can extend from parsec (Birkinshaw et al., 1981; Alexander, 1987; Konar et al., 2006; Machalski et al., 2009) to megaparsec (Mullin et al., 2006; Marscher & Jorstad, 2011) scales. Their distinct double structure was first noted by Jennison & Das Gupta (1953). This can broadly be divided into two sub-classes; Fanaroff & Riley (1974) type I (FR-I) and type II (FR-II). FR-Is are intrinsically low-powered and are characterized by their twin jet morphology and plumes (Figure 1.1). FR-IIs are high-powered and broadly consist of three large scale components; jets, lobes and hot spots. Blazars and quasars are classified as such due to their observed optical emission greatly exceeding that of the stellar component of the host galaxy. Radio-loud quasars are observed to be either be core or lobe dominated with either one-sided or highly non-symmetrical jets and strong optical and X-ray continuum emission (Figure 1.2). Blazars are the extreme counterpart to radio galaxies and quasars and describes the combination of two sub-classes; BL Lacs and optically violent variables (OVVs). BL Lacs are thought to be the intrinsically low-powered objects, whereas OVVs are the high-powered counterparts. Both blazar types are highly variable and observed to be point-like, with only a comparatively weak jet and extended emission although, as I discuss below, both of these features are thought to be intrinsically present.

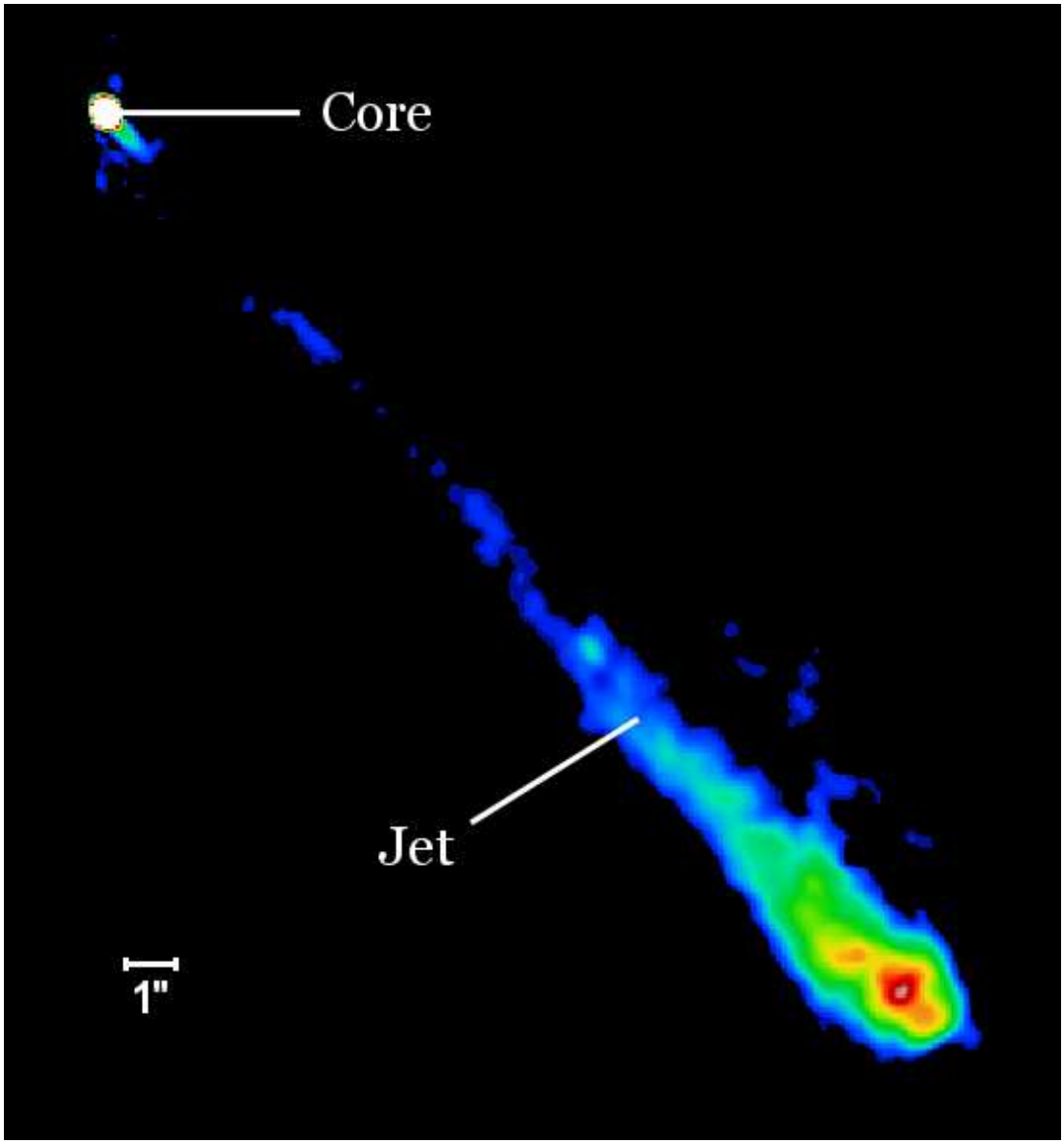

Figure 1.2: The quasar 3C273 with characteristic features labelled. 1 arcsecond on the sky represents a physical distance of 2.74 kpc ($z = 0.158$).

Although the observed properties of each galaxy type differ, it is generally agreed that the radio galaxies, quasars and blazars are intrinsically similar. In the following sections I describe this unified model of radio-loud AGN.

1.2.2 The unified model of radio-loud AGN

The classification of radio-loud AGN was originally defined based on the observational properties using low-resolution optical and radio observations. However, it has since been shown that it is likely that many radio-loud AGN are intrinsically the same objects with the jet oriented at varying angles to the observer (Barthel, 1989, 1994; Urry & Padovani, 1995).

From spectroscopic observations at optical wavelengths, it is clear that radio galaxies can be divided into three categories; the broad-line and narrow-line high-excitation radio galaxies (HERGs), and the low-excitation radio galaxies (LERGs) where both emission line types are absent. Blazars can display either broad-line or low-excitation properties, discussed further below, but quasars are always observed to have broad lines. Broad emission lines are thought to originate near the supermassive black hole (Figure 1.3) from high-velocity gas which causes a range of Doppler shifted emission to occur. In contrast, narrow-line features are emitted from slower, cooler, material further from the central AGN region. In the case of LERGs where no strong emission lines are observed, the optical and X-ray spectra are consistent with being jet emission. It has therefore been suggested that these are candidates for radiatively inefficient accretion (Hardcastle et al., 2006a).

In unified models, broad-line emission is intrinsically present in both broad- and narrow-line radio-loud active galaxies; however, the AGN is thought to be surrounded by a dusty torus. As this torus will absorb emission radiated from regions close to the central core when viewed from certain angles, it is possible to unify all AGN types purely through their orientation. When the jet is oriented close to the plane of the sky the central broad-line emitting region and the bright optical continuum emission from the accretion disk is obscured, but when observed with the jet close to the line of sight, the bright nucleus is seen with its broad-line features. This leads to two observationally different but intrinsically similar populations. Figure 1.3 shows that under this regime, as one rotates the orientation of the jet from being in the plane of the sky around towards the line of sight, there is a transition from narrow-line, through broad-line radio galaxies to radio-loud quasars. Due to the small line of sight to the jet, the additional brightness observed in quasars is easily explained by relativistic effects such as Doppler boosting.

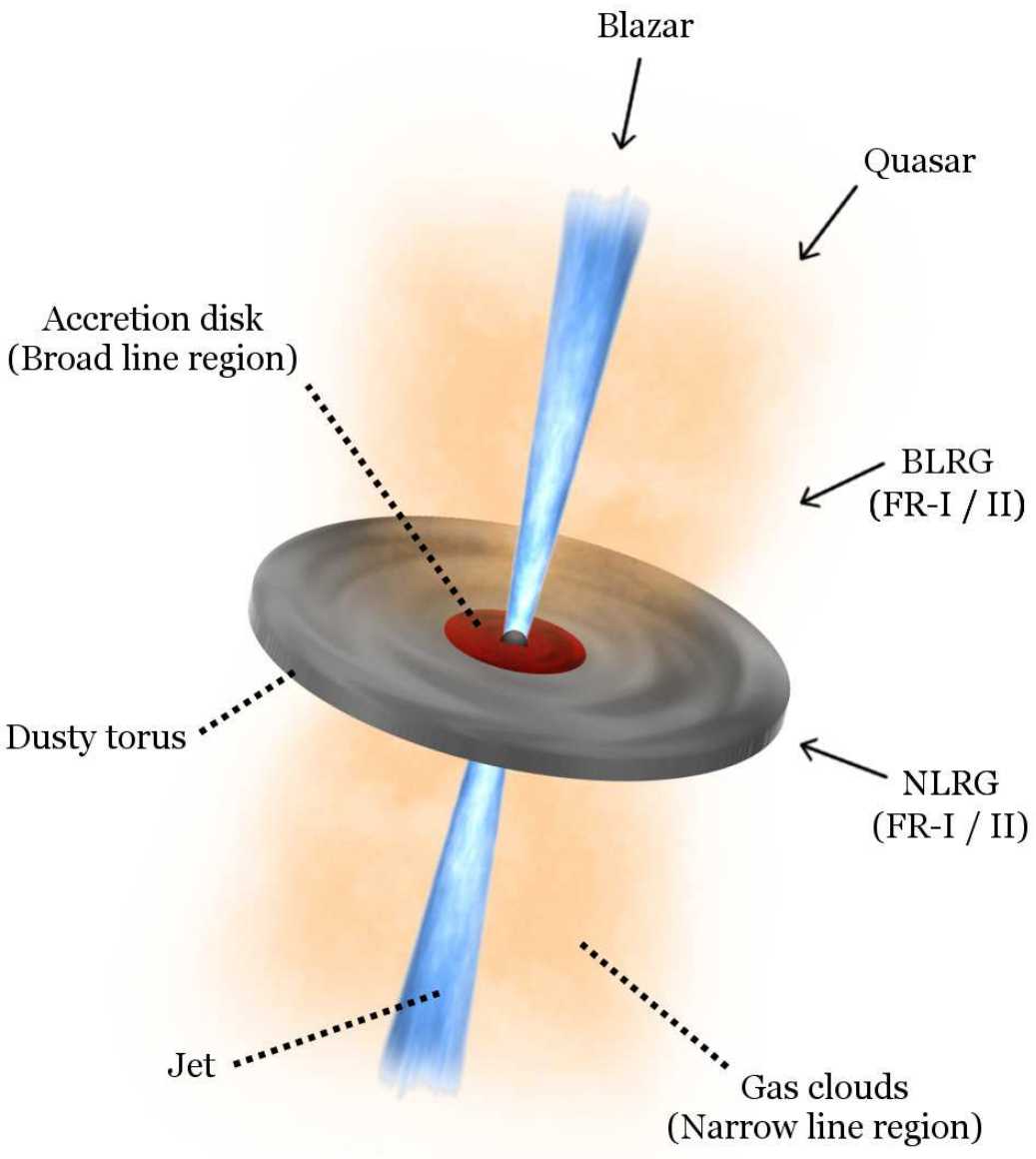

Figure 1.3: Graphical representation of the unified model of AGN (not to scale). Solid arrows indicate an observer's line of sight. Dotted lines indicate the key AGN features discussed in Section 1.2.2.

The jet of blazars which are viewed at very small angles to the line of sight have an additional problem to overcome if they are to fit into this unified model. Broad emission lines are only observed in some OVVs and even fewer BL Lacs. At these observing angles, there is no obscuring torus to absorb the broad-line emission; however, there are a number of plausible explanations for these observations. In some cases (e.g. Vermeulen et al., 1995), broad emission lines from BL Lacs are observed at the minima of variability. It is therefore likely that for at least some blazars, the emission from close to the accretion disk is dominated by the bright jet emission which is heavily influenced by relativistic effects (Urry & Padovani, 1995). Cases where emission lines are thought to be intrinsically missing are likely to be a result of LERGs aligned at narrow angles to the line of sight. Due to the small range of orientations required for a blazar to be observed, they make up only a very small proportion of the total radio loud AGN population but their observed high luminosity aids in the detection of these objects.

As quasars and blazars do not play any significant role in the results discussed within this thesis (although note the initial inclusions of BL Lacs in Chapter 6), I do not expand on these objects any further. Throughout this thesis I assume the unification model described here to be correct and no intrinsic differences to exist but, for conciseness, take the term radio galaxy to refer solely to the FR-I and FR-II populations in which the jet is oriented close to the plane of the sky.

1.3 The theory of radio-loud active galaxies

In this section, I review our current understanding of the theory behind radio-loud AGN. I describe the non-thermal radiative processes which are responsible for the observed emission at radio and non-thermal X-ray wavelengths, and the models of spectral ageing which attempt to describe the observed spectra in the lobes of powerful radio galaxies. I finally go on to discuss the particle content and magnetic fields of radio galaxies.

1.3.1 Non-thermal radiative processes

Two key radiative processes are responsible for the observed radio and X-ray emission in the jets and lobes of radio galaxies; synchrotron and inverse-Compton (IC) radiation. Here, I describe the theory behind these processes which form the foundation for the investigations undertaken within this thesis.

1.3.1.1 Synchrotron radiation

Synchrotron radiation is due to the interaction between relativistic, charged particles and a magnetic field. This emission is dependent on the mass of the particle but, for clarity, here I assume an electron-positron population. In a fixed magnetic field, a single particle will emit a spectrum that is strongly peaked around the critical frequency given by

$$\nu_c = \left(\frac{E}{m_e c^2}\right)^2 \frac{eB_\perp}{2\pi m_e} \tag{1.1}$$

where E is the total particle energy, m_e is electron mass and B is the magnetic field strength (e.g. Rybicki & Lightman, 1979; Longair, 2011). These electrons are subject to losses such that

$$-\frac{dE}{dt} = \frac{4}{3}\sigma_T c \left(\frac{E}{m_e c^2}\right)^2 \frac{B^2}{2\mu_0} \tag{1.2}$$

where σ_T is the Thomson cross-section, and μ_0 is the permeability of a vacuum. As this loss rate is a function of the Lorentz factor, $\gamma = E/(m_e c^2)$, the synchrotron losses increase as γ^2; hence there is a preferential cooling of high-energy electrons. The resulting observed curvature in the spectrum of older regions of plasma is known as spectral ageing, and is key to the determination of the age of an electron population radiating through synchrotron emission. I discuss the process in greater detail in Section 1.3.2.

Using Equation 1.2 we define the radiative lifetime of a particle, τ_{rad}, to be

$$\tau_{rad} = E/(-dE/dt) \propto E^{-1}B^{-2} \tag{1.3}$$

hence, for synchrotron radiation peaked around the critical frequency given by Equation 1.1, X-ray emission has a radiative lifetime $\sim 10^5$ time shorter than that at radio wavelengths. The short radiative lifetime of X-ray relative to radio emission, and the proportional dependency on the magnetic field strength, may play a key role in explaining the acceleration processes responsible for this emission and this is discussed further in Chapter 6.

For an observed spectrum which is well described by a power law to be produced (as is often the case in the acceleration regions of radio galaxies, see Section 1.4), the underlying electron energy distribution must also be a power law of the form

$$N(E) = N_0 E^{-\delta} \tag{1.4}$$

where N_0 is a normalization factor and δ the power law index of the initially injected electron energy distribution. Integrating over a range of electron energies between E_{min} and E_{max}, we

find the emissivity as a function of frequency, $J(\nu)$, is given by

$$J(\nu) = \int_{E_{min}}^{E_{max}} j(\nu) N(E)\, dE = \int_{E_{min}}^{E_{max}} j(\nu) N_0 E^{-\delta}\, dE \tag{1.5}$$

where $j(\nu)$ is the emissivity of a single electron (also see Section 2.3). Expressing Equation 1.1 in terms of E and substituting to Equation 1.6, under the assumption that $j(\nu)$ is strongly peaked around ν_{crit}, we find that

$$J(\nu) \propto N_0 \nu^{-\frac{\delta-1}{2}} B^{\frac{\delta+1}{2}} \tag{1.6}$$

It is conventional to express the power law index of the electron energy distribution as $\alpha = (\delta - 1)/2$ where α describes the spectral index of the observable spectrum. Hence, the observed flux can be expressed as

$$S_\nu \propto \nu^{-\alpha} \tag{1.7}$$

It should be noted that a low-energy cutoff may occur such that $S_{\nu,cutoff} \propto \nu^{\frac{1}{3}}$ at extremely low frequencies, or synchrotron self-absorption processes may also become important changing this relation to $S_{\nu,SSC} \propto \nu^{\frac{5}{2}}$. However, throughout this thesis, I assume that Equation 1.7 holds for any non-aged plasma.

1.3.1.2 Inverse-Compton scattering

Emission due to inverse-Compton radiation is the result of the collision between photons and charged particles. For particles with a sufficiently high energy, some of that energy is imparted to the photon, up-scattering it to higher frequencies. In the case of relativistic particles, such as may be found in the jets of radio galaxies, photons can be scattered, for example, from radio to X-ray energies. Within this thesis, I am primarily concerned with one form of inverse-Compton emission; the up-scattering of cosmic microwave background photons (iC/CMB) by the relativistic electrons that also give rise to synchrotron emission.

Analogous to the arguments given for synchrotron emission in Section 1.3.1.1, for an isotropic photon field such as one would expect from the CMB, the energy loss rate of the scattering particles is given by

$$-\frac{dE}{dt} = \frac{4}{3}\left(\frac{E}{m_e c^2}\right)^2 u_{CMB}\sigma_T \tag{1.8}$$

where u_{CMB} is the energy density of the CMB. Note the similarity between the inverse-Compton losses and the synchrotron losses of Equation 1.2. This is due to the loss rate being dependent on the electric field in the electron's rest frame, but not on the origin of that field. In the case

of synchrotron losses this is due to the electric field from the motion of the charged particles through the magnetic field. In the case of inverse-Compton radiation, it is the sum of the electric fields from the CMB incident upon the electrons which are responsible. As inverse-Compton radiation only makes a small contribution to the work undertaken here a full derivation of the emissivity is beyond the scope of this thesis, and I refer the interested reader to the fuller analysis given by Rybicki & Lightman (1979) and Longair (2011).

1.3.2 Spectral ageing

Determining the shape of the energy spectrum for an electron population can often give important insights into the underlying physics of the radio source. As described in Section 1.3.1.1, a region producing synchrotron radiation in a fixed magnetic field will have energy losses which scale as $dE/dt \propto \nu^2$; hence, in the absence of additional particle acceleration, we expect preferential cooling of higher energy electrons leading to a steeper, more strongly curved spectrum in older regions of plasma. Models of this 'spectral ageing' have therefore become a useful tool when describing the processes involved in these galaxies. In the following sections I describe the models used within this thesis, including two of the most commonly models of spectral ageing along with a more complex, but potentially more realistic model.

1.3.2.1 The standard models of spectral ageing

Two of the most widely used models of spectral ageing are those first proposed by Kardashev (1962) and Pacholczyk (1970) (the KP model) and by Jaffe & Perola (1973) (the JP model) which both assume a single injection electron energy distribution. At the point of acceleration, discussed further in Section 1.5, this distribution is assumed to be initially described by the power law given by Equation 1.4. The flow of plasma is then subject to synchrotron losses as it propagates along the lobes and plumes, potentially allowing the age and hence power of these outflows to be derived. For the KP model, an electron energy distribution, N, subject to synchrotron and inverse-Compton losses is given by Pacholczyk (1970) to be

$$N(E, \theta, t) = N_0 E^{-\delta}(1 - E_T E)^{-\delta - 2} \tag{1.9}$$

and the intensity at a given frequency by

$$I_\nu(t) = 4\pi C_3 N_0 s B \int_0^{\pi/2} d\theta \sin^2\theta \int_0^{E_T^{-1}} dE F(x) E^{-\delta}(1 - E_T E)^{\delta - 2} \tag{1.10}$$

where

$$E_T \equiv C_2 B^2 (\sin^2 \theta) t \tag{1.11}$$

with energy E, pitch angle θ and time since initial acceleration t. The constants C_2, C_3, ν_c and the function $F(x)$ are defined by Pacholczyk (1970) where $x \equiv \nu/\nu_c$. We see from Equation 1.11 that for the KP model the pitch angle θ is assumed to be both isotropic and constant over the radiative lifetime of the electrons. The JP model proposed by Jaffe & Perola (1973) instead assumes that the pitch angle is only isotropic on short time scales relative to the radiative life time, so giving

$$E_T \equiv C_2 B^2 \langle \sin^2 \theta \rangle t \tag{1.12}$$

where $\langle \sin^2 \theta \rangle$ represents the time averaged pitch angle. This leads to a distinctive exponential cutoff, compared to the KP model where electrons which maintain a small pitch angle continue to radiate at high frequencies. Examples of the KP and JP spectrum are shown in Figure 1.4 and I refer the interested reader to Leahy (1991) for further discussion of these models.

1.3.2.2 The Tribble model of spectral ageing

Both the KP and JP models discussed in the previous section assume a fixed magnetic field strength throughout the source, but this is unlikely to be the case on the large scales of which radio galaxies are observed. A model in which an electron population ages in a spatially non-uniform magnetic field was therefore proposed by Tribble (1993) (herein the Tribble model). This family of models attempts to account for a more realistic magnetic field structure by instead assuming a Gaussian random field, allowing electrons to diffuse across regions of varying field strength. In the weak field, high diffusion case in which electrons are free-streaming, the spectrum can be modelled by integrating the standard JP losses over a Maxwell-Boltzmann distribution (Hardcastle, 2013; Harwood et al., 2013; this thesis). Tribble (1993) noted that the pitch angle scattering of the JP model is a more likely scenario than that of the fixed pitch angles of the KP model and that in a varying magnetic field such as this, the spectrum more closely resembles the KP model than the classical JP case. They suggested that this might explain results where the KP model provides the best fit, such as those of Carilli et al. (1991) in their investigation of Cygnus A.

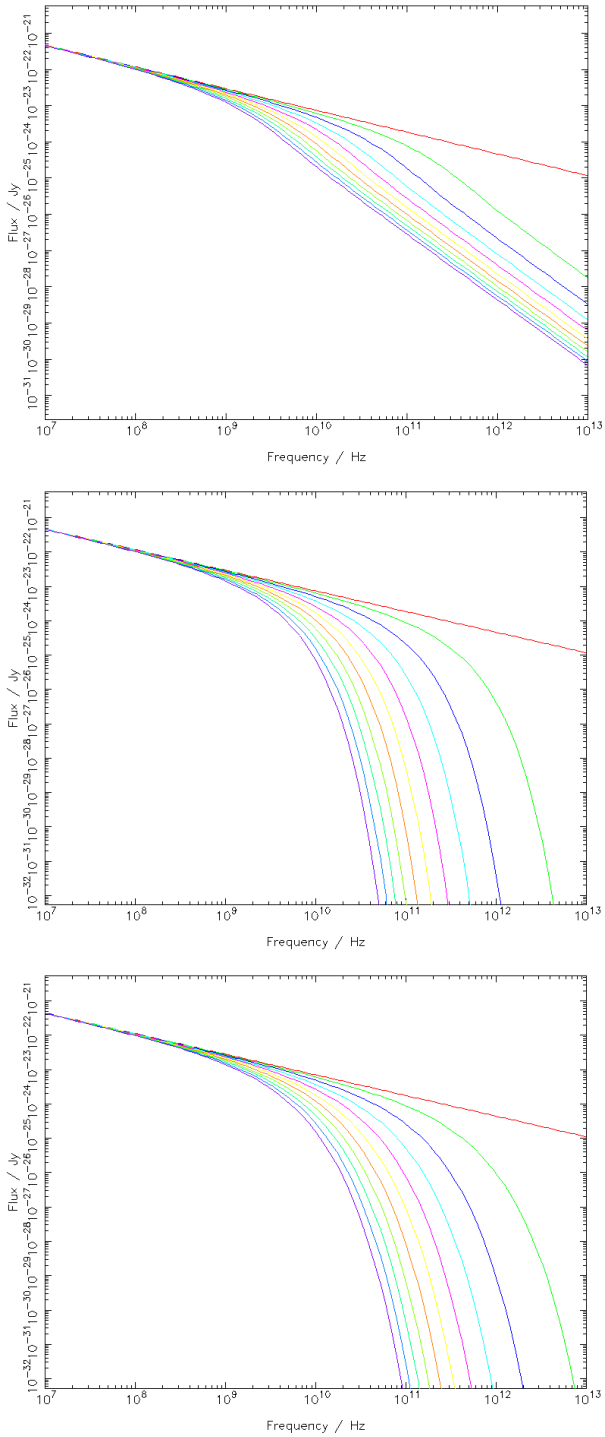

Figure 1.4: Example KP (top), JP (middle) and Tribble (bottom) models between 10 MHz and 10 THz for an arbitrary normalization with 0.6 injection index. Each plot shows model ages between 0 (red) and 10 (purple) megayears.

Integrating the JP losses over a Maxwell-Boltzmann distribution (Hardcastle, 2013) Equation 1.10 becomes

$$I_{\nu,Trib}(t) = 4\pi C_3 N_0 s \int_0^{\infty} \int_0^{\pi/2} \int_0^{E_T^{-1}} B \sin^2\theta \, F(x) \, E^{-\delta}(1 - E_T E)^{\delta-2} \times \frac{B^3 \exp\left(-B^2/2B_0^2\right)}{B_0^3} \, dE \, d\theta \, dB \quad (1.13)$$

where B_0 is the mean magnetic field strength. I consider the computational details of the Tribble model further in Section 2.3.

1.3.3 Particle content

It has so far been assumed that electrons are solely responsible for the processes discussed; however, the collimated nature of the jets within these sources mean that they must be electrically neutral. The radio jets, and the downstream lobes and plumes, must therefore contain a significant fraction of particles which hold an opposite charge, such as protons or positrons. Despite a wide range of studies having been undertaken, both particle types can produce similar pressures given appropriate assumptions about the low-energy particles, so the exact particle content of these sources has yet to be determined. The composition of the jet has potential implications for the dynamics, energetics and magnetic field strength within both high- and low-powered radio-loud AGN. In this section I discuss the arguments for both electron-proton and electron-position jets and outline the reasoning behind the assumptions made within this thesis.

Entrainment of material from the surrounding medium may also play a role in the composition and dynamics of radio galaxies (Bicknell, 1984). This entrainment is thought to be less significant in the more powerful FR-II galaxies (Leahy, 1991), hence, it is plausible that the two galaxy types have a non-negligible difference in particle content. In Section 1.3.3.3 I discuss the theory and observational evidence behind this assertion.

1.3.3.1 Electron-proton jets

Under the assumption that particle pairs originate from the inner regions of the AGN accretion flow, it has been argued by Ghisellini et al. (1992) that the jet content may consist of an electron-proton plasma due to annihilation constraints. Through studies at X-ray energies, they compare a lower limit on the particle density of small-scale jets to synchrotron self-Compton models. They argue that the theoretical upper limit for the number of particle pairs which could escape

annihilation from the dense inner regions of the jet requires a cutoff in the radiative particles at $\gamma \sim 100$. As synchrotron losses are a function of particle mass (Equation 1.2), much higher energies are required for electron-positron pairs to explain the observed emission, hence a plasma consisting of a significant proton fraction is preferred. These results are further supported by Celotti & Fabian (1993) who compare the particle number flux and kinetic energy and who also argue that that the kinetic power of the lobes cannot be provided by an electron-positron plasma, hence favour a electron-proton model. However, electron-proton pairs have so far struggled to explain results such as the polarization of parsec scale jets (Wardle et al., 1998) and Very Long Baseline Interferometry (VLBI) observations of synchrotron self-absorption in radio cores (Reynolds et al., 1996). It is therefore the electron-positron composition detailed below which is the currently preferred explanation for the initial particle content of the jets of radio-loud AGN.

1.3.3.2 Electron-positron jets

One of the strongest arguments for a electron-positron pair composition comes from polarization measurements, specifically, the Faraday rotation and depolarization of observed emission. Faraday rotation occurs when linearly polarized light travels through a magnetized plasma causing the plane of the observed polarization to rotate, the degree of which is determined by the electron density of the plasma, magnetic field strength and the direction. The strength of this effect can be characterized by what is known as the rotation measure (RM). The change in polarization angle (β) is dependent on RM such that $\beta = RM\lambda^2$, hence, can be determined through multi-wavelength observations. If the RM can be accurately determined, one can gain information about the medium through which the observed emission has passed. If the polarized emission traverses a sufficiently large region of magnetized plasma and the density of that plasma is non-uniform along the line of sight, the rotation within the beam of any radio observation will cancel, producing depolarization effects.

Using these RM and depolarization effects, it is possible to infer the properties of the jets seen in radio-loud AGN. Parsec-scale jets are known to have a high fractional polarization (e.g. Wardle, 1977; Jones & Odell, 1977) which is unexpected if a magnetized thermal plasma is present, such as would be provided by a low-gamma ($\gamma < 100$) electron-proton jet. There are therefore two plausible explanation for the lack of observed depolarization: 1) An electron energy cutoff exists such that no particles with $\gamma < 100$ are present to cause such depolarization, or, 2) the jets are electron-positron in nature. As positrons orbit in the opposite direction to electrons, any changes in the propagation speed of the left- and right-hand circular polarizations

due to one of the particles will, on average, be countered by that of the other. Hence, in the case of an electron-positron plasma no significant overall depolarization will be observed. The need for a low-energy cutoff in an electron-proton jet also means that γ_{min} potentially plays a key role in determining the jet composition. Investigations by Wardle et al. (1998) and Homan & Wardle (1999) show that circular polarization is observed in their sample of quasar jets, likely due to the Faraday conversion between linear and circular polarizations. For this to occur a large population of low-energy ($\gamma \leq 20$) electrons is required, implying that electron-positron pairs are the main constituent of radio-loud AGN jets.

Recent work also supports this picture of an electron-positron jet plasma. Through investigations into double-double radio galaxies as a result of episodic AGN activity, Konar & Hardcastle (2013) argue that if a significant fraction of protons are present, then in FR-II galaxies they must travel with the bulk Lorentz factor of the jet to avoid the separation of charge and maintain their collimated nature. For this to occur, it is required that the kinetic energy of the proton be higher than that of the paired electron. However, it has been argued by Croston et al. (2005) that protons are not energetically dominant in the lobes, and so cannot be accelerated to greater energies than the electron population.

The case of the low-power radio galaxies is less clear cut, with recent work (e.g. McNamara & Nulsen, 2012) suggesting a non-negligible proton population is present within the jets. It is most likely that in the case of FR-I galaxies the initial composition is inherently comprised of electron-positron pairs (Dunn et al., 2006), but it is the entrainment of thermal material from the surrounding medium which contributes to the observed proton population (Croston et al., 2008b). It is this entrainment of material which I discuss in the following section.

1.3.3.3 Entrainment

Irrespective of the particle content of the jets discussed in previous sections, additional material may also be entrained from the surrounding medium, adding a thermal component to their composition. In powerful FR-II galaxies where bulk jet speeds are relativistic to large distances, hence interaction with the surrounding medium must remain low, entrainment is likely to be negligible. However, for FR-I galaxies which are known to decelerate on small scales compared to their FR-II counterparts, it has been suggested that entrainment is likely to be a major factor in the deceleration process (Bicknell, 1984; Bowman et al., 1996; Feretti et al., 1999; Laing & Bridle, 2002a; Croston & Hardcastle, 2014). If this is the case, then the jets of FR-I galaxies

are likely to contain a significant fraction of thermal material, either swept up by the interaction with the medium through which it passes or entrained from stellar winds.

Observations at X-ray energies have also given insight into the entrainment of material in radio galaxies. Assuming the minimum energy condition (the minimum energy required for the observed emission), studies find that FR-Is are typically underpessured compared to the surrounding gas (Morganti et al., 1988; Worrall & Birkinshaw, 2000; Hardcastle & Worrall, 2000a). These findings support a picture in which entrained thermal material may provide the additional pressure required (e.g. Croston et al., 2008a; Wykes et al., 2013). In the well studied case of Centaurus A, Wykes et al. (2013) place a conservative estimate on the entrainment rate of $\sim 3.0 \times 10^{21}$ g s^{-1}, which they suggest provides a significant, although not dominant, proton population capable of supporting the radio lobes. The entrainment of material is therefore likely to play a key role in the overall dynamics of FR-I radio galaxies.

1.3.4 Magnetic fields

Along with charged particles, it is required that a magnetic field be present for synchrotron emission to occur. Measurements of synchrotron emissivity do not, however, tell us anything about the strength of that field and so values must be derived through alternate means. A common assumption made about the field strength in these sources is that of equipartition between the particle energy density and the magnetic field (e.g. Leahy, 1991; Croston et al., 2005, also see Chapter 3 for further discussion on this assumption).

Assuming the power law distribution given by Equation 1.4, the total energy of the electron content over a finite energy range is given by

$$u_e = \int_{E_{min}}^{E_{max}} N_0 E^{1-\delta} dE \tag{1.14}$$

From Equation 1.2 we see that $-dE/dt \propto \gamma^2 B^2$; hence, where S is the integrated flux of an electron population with energies between E_{min} and E_{max}

$$\frac{u_e}{S} \propto \frac{\int_{E_{min}}^{E_{max}} E^{1-\delta} dE}{B^2 \int_{E_{min}}^{E_{max}} E^{2-\delta} dE} \tag{1.15}$$

As emission is peaked around a frequency given by Equation 1.1 such that $E \propto B^{-1/2}$, over a finite frequency range the limits of integration of Equation 1.15 are both proportional to $B^{-1/2}$, therefore

$$\frac{u_e}{S} \propto \frac{(B^{-1/2})^{2-\delta}}{B^2 (B^{-1/2}) E^{3-\delta}} = B^{-3/2} \tag{1.16}$$

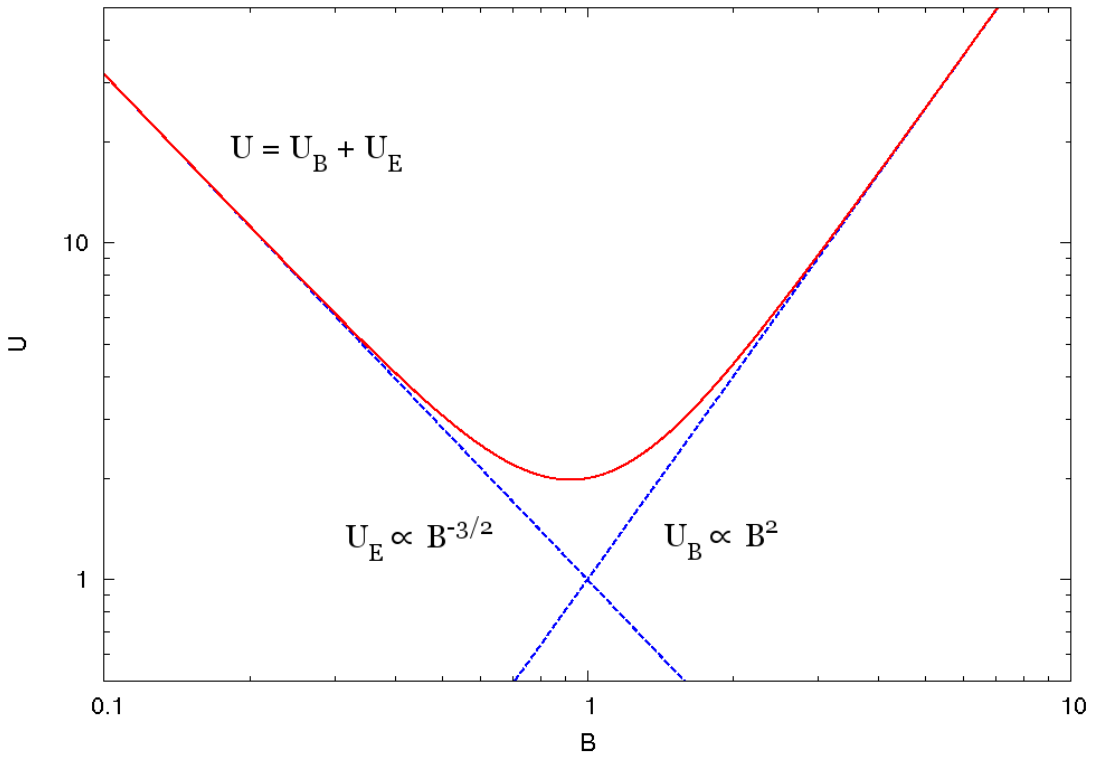

Figure 1.5: Plot of the total energy content (arbitrary units) of a radio source as a function of magnetic field strength as detailed in Section 1.3.4. The total energy content (solid red line) is given by the sum of the electron energy content U_E and the magnetic field energy U_B (dashed blue lines). Note that the minimum energy occurs close to the equipartition value ($B = 1$).

hence,

$$u_e \propto B^{-3/2} \tag{1.17}$$

The energy density of the magnetic field scales as $u \propto B^2$ so, assuming equal filling factors of the magnetic field and electrons, the minimum energy required for a given luminosity radiating through the synchrotron process has a sharp minimum close to the equipartition value (Figure 1.5).

Under the minimum energy condition, equipartition therefore provides a good proxy for the magnetic field strength. This measure is particularly useful due to it being easily measurable but, as was discussed in Section 1.3.3.3, its validity when applied to FR-Is is not clear (e.g. Tashiro et al., 1998). In FR-II galaxies, there is some suggestion that this approximation may be close to being correct. Inverse-Compton emission, which is dependent on the relativistic

electron density rather than the magnetic field (Section 1.3.1.2), can provide an estimate of the field strength if the photon field is known. In FR-II galaxies, X-ray emission is thought to result from the upscattering of the well known, isotropic, CMB photons (see Section 1.4.4) and it is therefore theoretically possible to determine the magnetic field strength. Using inverse-Compton modelling constrained by X-ray observations of this iC/CMB emission, and measurements at radio wavelengths of the (magnetic field dependent) synchrotron emission, Croston et al. (2005) find, using a sample of 33 FR-II radio galaxies and quasars, magnetic field strengths between 0.3 and $1.3B_{eq}$ with a strong peak at $\sim 0.7B_{eq}$. In most cases equipartition therefore provides an adequate approximation for FR-IIs, but the difficulties in directly determining magnetic field strengths has meant that many uncertainties still exist as to their true properties. I discuss the role of magnetic fields and their possible departure from equipartition further in Chapters 3 and 6.

1.4 The observational properties of radio galaxies

Both FR-I and FR-II radio galaxies are observed to possess a wide range of large morphologies and small scale features. In the following sections, I describe the observational properties of radio galaxies at radio and X-ray wavelengths and highlight some of the questions which have arisen from empirical investigations.

1.4.1 FR-I galaxies at radio wavelengths

Although the FR-I/II classification of radio galaxies is primarily morphological in nature (Section 1.2.1), a break in radio luminosity is also observed. It is clear from Figure 1.6 that a dichotomy exists between the two radio galaxy types (Fanaroff & Riley, 1974; Owen & Ledlow, 1994). The majority of FR-Is are observed to display 178 MHz luminosity densities below $\lesssim 2 \times 10^{25}$ W Hz^{-1} sr^{-1} (Fanaroff & Riley, 1974; Owen & Ledlow, 1994), and have a surface brightness dominated by the inner jet region ("core brightened").

FR-I galaxies are observed to have structure which can extend from parsec to megaparsec scales (e.g. Jones & Odell, 1977; Birkinshaw et al., 1981; Andernach et al., 1992; Marscher & Jorstad, 2011) and are known to display a range of morphologies (Figure 1.7). Head-tail and wide-angle tail FR-I sources are commonly thought to be due to environmental effects, although jet opening angle may also play a role in determining the large scale morphology of these sources (Krause et al., 2012). Jets are also often observed to contain bright, localized

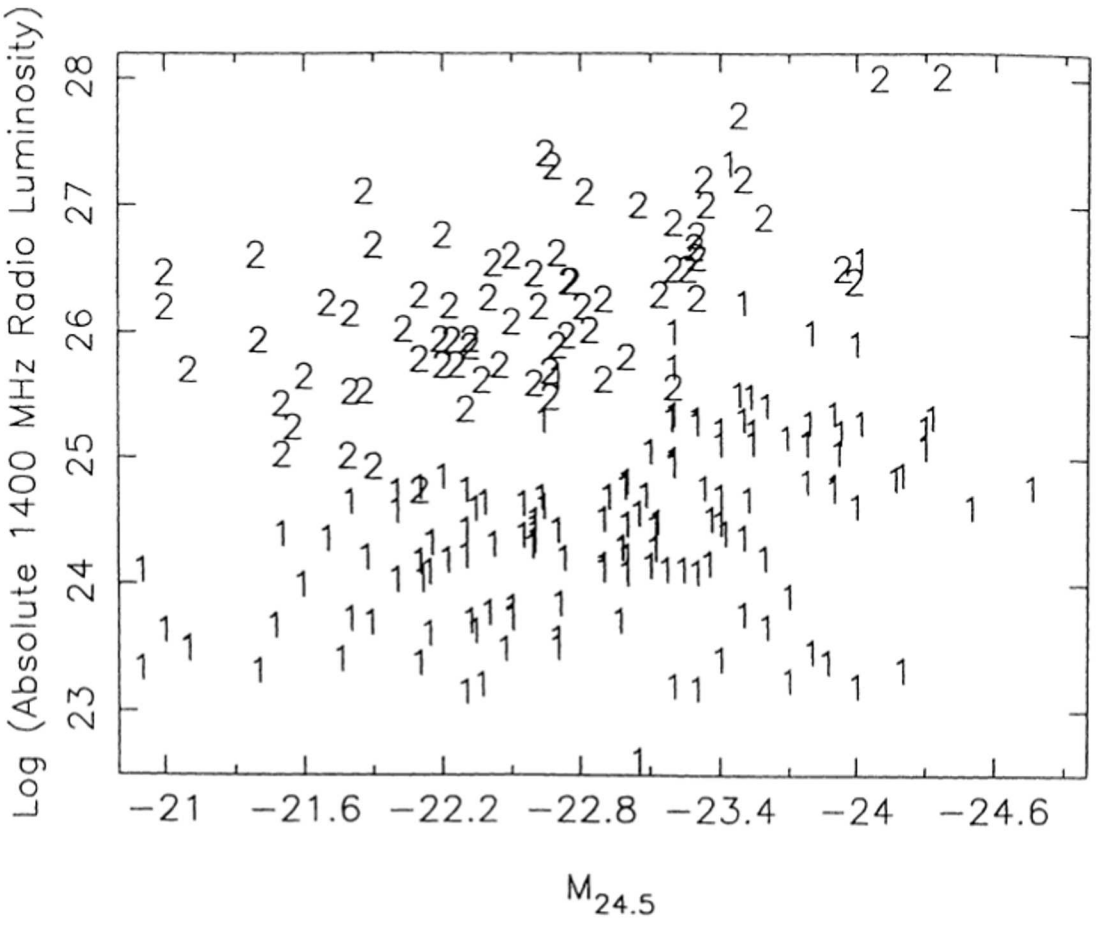

Figure 1.6: Plot by Owen & Ledlow (1994) of 1.4 GHz radio versus R-band luminosity for a sample of radio galaxies. Radio units are W $Hz^{-}1$. FR-I's and FR-II's are denoted by 1's and 2's respectively.

regions of increased brightness known as knots (e.g. Kraft et al., 2002a; Hardcastle et al., 2003). These common features are plausibly due to weak shocks caused by the interaction between the jet plasma and slow or stationary objects within the flow (Goodger et al., 2010).

On small scales ($\lesssim 1$ kpc), FR-I jets are highly relativistic with speeds close to the AGN of 0.7 – $0.9c$, but decrease to bulk flow speeds of around only $\lesssim 0.2c$ on the order of tens of kpcs (e.g. Laing et al., 1999; Giovannini et al., 2001; Laing & Bridle, 2002a; Jetha et al., 2006). This rapid deceleration is thought to be due to low jet power, entrainment, environmental effects (e.g. Bicknell, 1992) and possibly jet opening angle (Krause et al., 2012). The overpressure of the jets relative to the surrounding medium (e.g. Bicknell, 1984; Laing & Bridle, 2002b) results in a low-density cavity which is inflated by the buoyant gas (Gull & Northover, 1973; Fabian et al., 2000) giving rise to the characteristic plumes of FR-I galaxies. I discuss the dynamics behind these features further in Section 1.5.2.

1.4.2 FR-II galaxies at radio wavelengths

FR-II galaxies are observed to have structure which can extend to scales of hundreds of kiloparsecs to megaparsecs (e.g. Alexander, 1987; Konar et al., 2006; Mullin et al., 2006; Machalski et al., 2009) with luminosity densities generally in excess of $\gtrsim 2 \times 10^{25}$ W Hz^{-1} sr^{-1} (Fanaroff & Riley, 1974; Owen & Ledlow, 1994). In contrast to the core brightened FR-Is, hot spots dominate the surface brightness and the sources are therefore often referred to as "edge brightened". The average bulk advance speeds of these hot spots is observed to be on the order of ~ 0.02 – 0.2c (e.g. Myers & Spangler, 1985; Alexander & Leahy, 1987; Liu et al., 1992; this thesis), although uncertainties in determining how long a radio-loud AGN has been active in FR-IIs has meant that deriving precise advance speeds has proved difficult. I discuss hot spots and the various methods of determining their advance speed further in Section 1.5.3.

The jets of FR-IIs are thought to remain relativistic out to large distances (see Section 1.5.3) but their properties at radio wavelengths are much less well understood than their FR-I counterparts. One of the main reasons for this has been their low luminosity and the inability to resolve jets across their width, meaning the transverse spectral profile is largely unknown. For the handful of objects where analysis is possible along the length of the jet (e.g. Schilizzi et al., 2001 for 3C236, Katz-Stone et al., 1993 for Cygnus A and Treichel et al., 2001 for 3C438) spectral variations are sometimes observed, although this appears not to be a universal feature, since in 3C401 (Treichel et al., 2001) and 3C353 (Swain et al., 1998) a constant spectral index is observed (Treichel et al., 2001). The cause of such spectral variation is not clear, but could

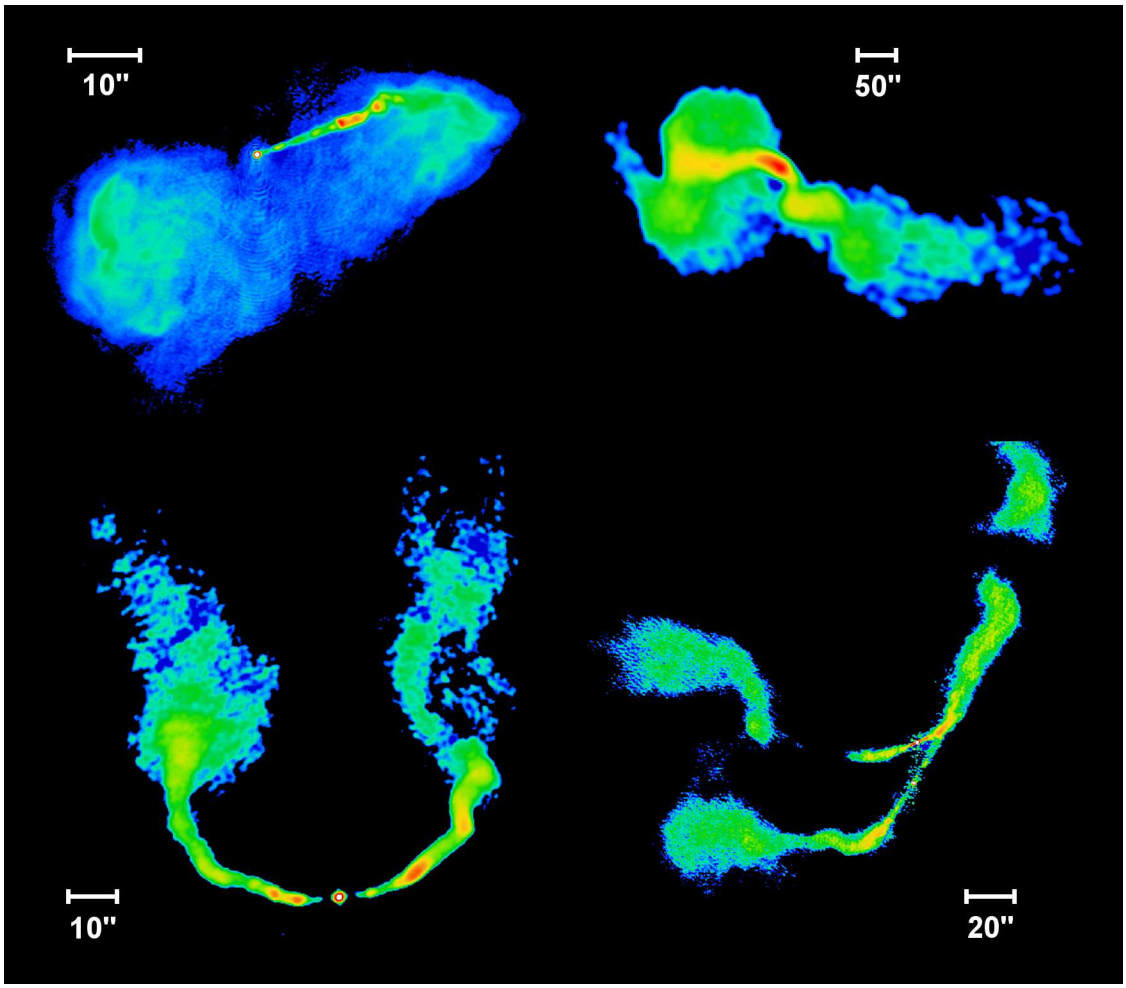

Figure 1.7: A collection of FR-I morphologies at radio wavelengths. Top left, M87 (Owen et al., 2000): Residing at only ~ 20 Mpc, M87 is one of the brightest radio sources in the sky. Although being core dominated and displaying the plumes associated with an FR-I morphology, only a single jet is observed at radio wavelengths. Top right, 3C66B (Hardcastle et al., 1996): A classic FR-I radio galaxy with twin radio jets and plumes. Bottom left, 3C83.1B (O'Dea & Owen, 1986): A head-tail source with clear bending of the jets and plumes, most likely due to ram pressure as the galaxy moves through its environment. Bottom right, 3C75 (Hardcastle et al., 2004b): A peculiar FR-I source containing two radio cores. It displays two sets of twin jets and plumes. 1 arcsecond on the sky represents a physical distance of 0.088 kpc for M87 ($z = 0.00428$), 0.44 kpc for 3C66B ($z = 0.0215$), 0.51 kpc for 3C83.1B ($z = 0.0255$) and 0.47 kpc for 3C75 ($z = 0.0232$).

plausibly arise from magnetic field variations, shocks within the jet driven by lobe turbulence (Jones et al., 1999) or jet-lobe interactions (Treichel et al., 2001).

Like their low-power counterparts FR-IIs display a wide range of morphologies, a selection of which are shown in Figure 1.8. X-shaped and double-double FR-IIs are thought to occur due to episodic AGN activity. They are therefore thought to be key in the investigation of AGN history, but it has also been shown that a shift in the orientation of the central black hole's axis can also result in the observed morphology (e.g. Merritt & Ekers, 2002; Dennett-Thorpe et al., 2002). Wide-angle tailed radio galaxies have a morphology intermediate between types FR-I and FR-II. These peculiar objects are observed to have two highly collimated FR-II type jets out to scales of tens of kiloparsecs (Hardcastle & Sakelliou, 2004) but appear to become disrupted causing FR-I type plumes to form. These galaxies are almost exclusively associated with central cluster galaxies. Hardcastle & Sakelliou (2004) suggest that the jet disruption is due to the environment in which they reside, but the details of this process has yet to be determined.

To determine the dynamics and energetics of these complex sources, it is the archetypal double radio galaxies which must be considered. These FR-II objects display clear hot spots and lobes which often extend back to the AGN core. They are therefore ideal for investigating the underlying physics of powerful radio galaxies. Further details of the dynamics of these sources are given in Section 1.5.3.

1.4.3 FR-I galaxies at X-ray energies

With the launch of high-resolution X-ray telescopes such as the *Chandra* X-Ray observatory in 1999, it quickly became apparent that emission at X-ray wavelengths was a common (e.g. Worrall et al., 2001a; Sambruna et al., 2004), if not a universal (Hardcastle et al., 2002b) feature of the jets in FR-I galaxies. It is generally argued that the emission of X-rays in most FR-Is can be well modelled as synchrotron emission (e.g. Hardcastle et al., 2001; Wilson & Yang, 2002; Brunetti et al., 2003; Perlman & Wilson, 2005; Harris & Krawczynski, 2006) from a single electron population (a 'one-zone' model) (e.g. Laing et al., 2008). The smooth transition of observed spectra from the radio and optical components of the jets to those observed in the X-ray gives good empirical support to this model (Figure 1.9). However, the lifetime over which a particle will radiate through the synchrotron process (Section 1.3.1.1) depends on the Lorentz factor of the emitting particle and the magnetic field in which it resides (e.g. Longair, 2011). For emission in an FR-I jet at 1 keV in a 10 nT magnetic field, and assuming a magnetic field that is approximately in equipartition with the radio emissions (e.g. Leahy, 1991), the expected

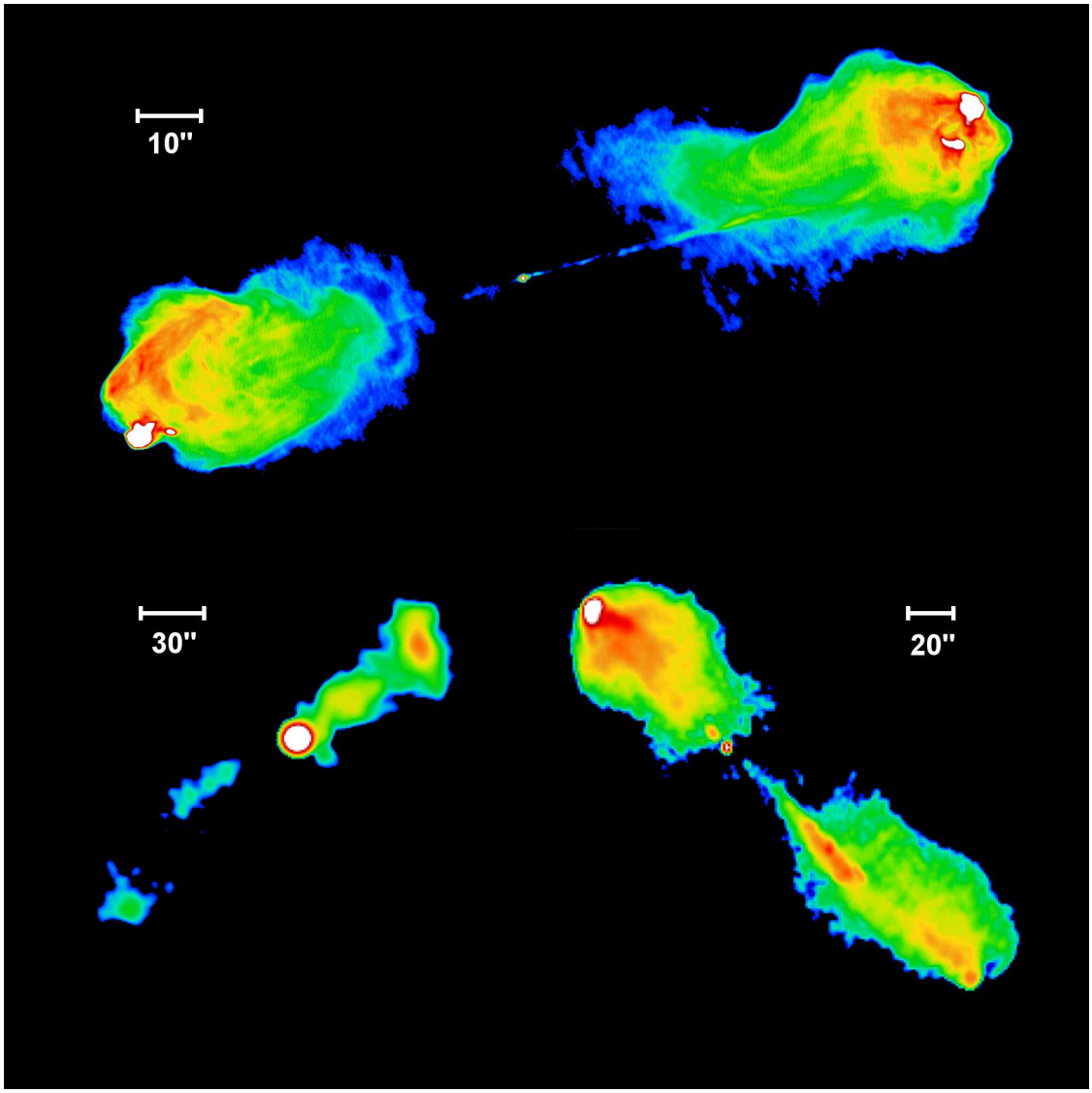

Figure 1.8: A collection of FR-II morphologies at radio wavelengths. Top, Cygnus A (Dreher et al., 1987): One of the brightest and well studied FR-IIs in the sky. Cygnus A is an archetypal FR-II galaxy displaying clear hot spots and lobes. Bottom left, 3C293 (Bridle et al., 1981): Example of a FR-II source with a highly asymmetric morphology. Bottom right, 3C33.1 (Leahy, Bridle and Strom, unpublished (http://www.jb.man.ac.uk/atlas/): An FR-II radio galaxy with an asymmetric morphology. A classical FR-II structure is seen to the north of the core, but only a weak hot spot and brightened emission along the jet length are observed in the southern lobe. 1 arcsecond on the sky represents a physical distance of 1.1 kpc for Cygnus A ($z = 0.0561$), 0.89 kpc for 3C293 ($z = 0.0450$) and 3.1 kpc for 3C33.1 ($z = 0.181$).

radiative lifetime of an electron is expected to be only of the order of hundreds of years. If we compare this to the approximate size of the X-ray jet of the FR-I radio galaxy Centaurus A, which extends to a distance of approximately 4.5 kiloparsecs from the active galactic nucleus (AGN), it would take a particle travelling at the speed of light around 15000 years to travel from the central region to its furthest extent (also see Burns et al., 1983; Harris & Krawczynski, 2006; Hardcastle, 2007 and references therein for similar arguments). This is much greater than the expected lifetime of an electron radiating via the synchrotron process and leads to the conclusion that the X-ray emission cannot be due to particles accelerated near the AGN, but instead the emitting particles must be accelerated *in situ* in the jet (e.g. Biretta & Meisenheimer, 1993; Brunetti et al., 2003; Hardcastle, 2007; Goodger et al., 2010).

It is generally agreed (e.g. Hardcastle et al., 2003; Kataoka et al., 2006) that at least two forms of particle acceleration are present within the jets of radio galaxies. There is growing evidence, particularly in the case of Centaurus A (Goodger et al., 2010), that emission relating to small scale features such as X-ray-bright knots is due to shock acceleration caused by interaction with a compact stationary or slow moving body. This acceleration is seen to dominate emission from the innermost sections of the jet in galaxies such as Centaurus A (e.g. Hardcastle, 2007); however, the particles responsible for the more diffuse emission which dominates the outer jet regions cannot be explained in the same manner. Particles radiating at these energies must therefore be accelerated by a second process (Hardcastle et al., 2004b; Kataoka et al., 2006). The inability to resolve all but the closest FR-I jets to this level of detail means it is uncertain whether this is the case for all FR-I galaxies; however, it is likely that diffuse emission will be present in the majority, if not all cases, based on those objects in which they can currently be resolved. Various theoretical models exist for the cause of this diffuse *in situ* acceleration, such as second order Fermi acceleration (Stawarz & Ostrowski, 2002; Rieger et al., 2007), magnetic reconnection (Birk & Lesch, 2000) and decaying beams of ultra high-energy neutrons (Atoyan & Dermer, 2004); however, each contains its own set of problems which have yet to be resolved. Further discussion of this diffuse emission and results from my investigations of these sources are presented in Chapter 6.

1.4.4 FR-II galaxies at X-ray energies

X-ray emission from the jets and lobes of FR-II galaxies, although common (e.g. Tashiro et al., 1998; Wilson et al., 2000; Isobe et al., 2002; Hardcastle & Worrall, 2000b; Hardcastle et al., 2004b), is on the whole still poorly understood. Whereas the observed spectrum of X-ray jets

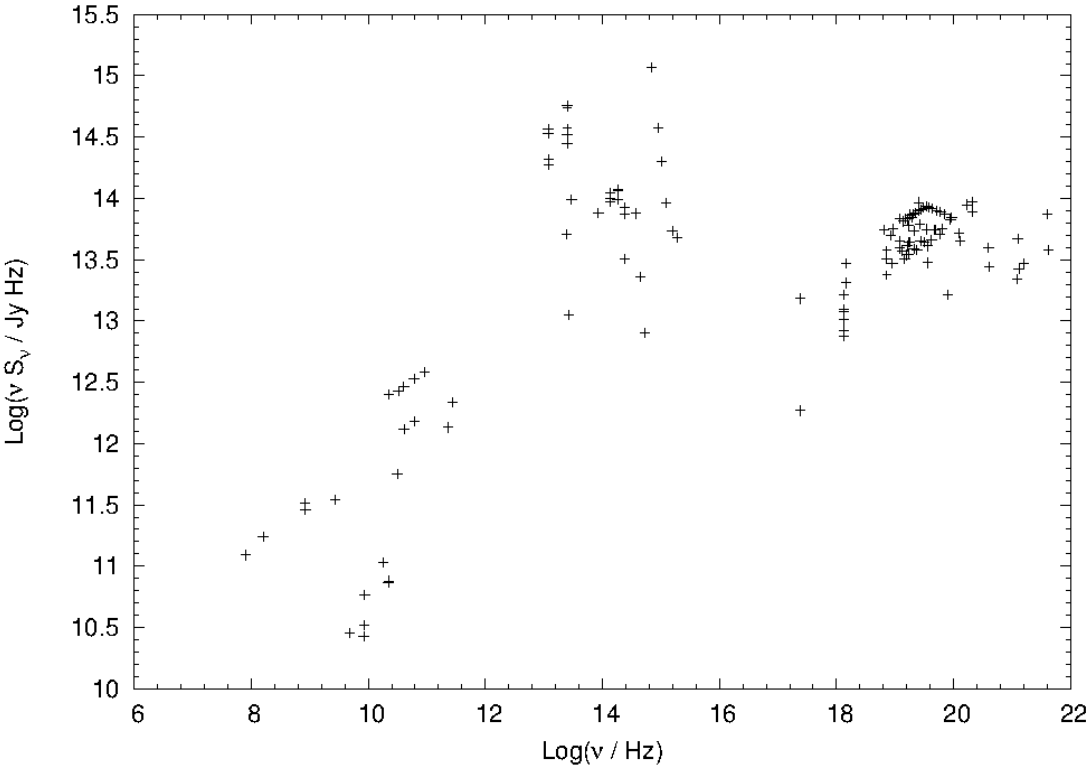

Figure 1.9: Plot of log($\nu\ S_\nu$) versus log(ν) for the FR-I radio galaxy Centaurus A. Data taken from the NASA extragalactic database (NED) and references therein. Note the large scatter at optical wavelengths is due to differing aperture sizes and optical core variability.

of FR-I radio galaxies between radio and X-ray are found to be described well by a simple synchrotron spectrum (Section 1.4.3), the jets in FR-II galaxies are not well described by such models beyond optical wavelengths. It is therefore commonly assumed that the observed X-ray emission is a result of the inverse-Compton process due to the upscattering of either low-energy synchrotron photons (synchrotron self-Compton), or, of cosmic microwave background photons (iC/CMB) (Tavecchio et al., 2000; Celotti et al., 2001; Kataoka & Stawarz, 2005; also see the review by Hardcastle, 2005). However, for these inverse-Compton models to properly describe the broadband spectrum of the X-ray emission in FR-II jets, large departures in the magnetic field strength from equipartition are required (e.g. Chartas et al., 2000). One alternative suggestion made by Tavecchio et al. (2000) and Celotti et al. (2001) for the jet of PKS 0637-752 is the boosting of the CMB photons in the rest frame of the jet. This requires the jet to be highly relativistic and to be orientated close to the line of sight, which for PKS 0637-752 is known to be the case, but X-ray jets are known to exist in FR-IIs which lie at much larger angles (e.g. Kraft et al., 2002b). This model's applicability to the general FR-II population is therefore not yet clear. In some cases, particularly in low-power FR-IIs, it has been suggested that a second synchrotron component may provide a more plausible explanation for the X-ray jet emission (e.g. Jester et al., 2002). No consensus has yet been reached as to a universal mechanism for the observed emission from X-ray jets and therefore remains an open question.

In the lobes of FR-II galaxies, diffuse X-ray emission is observed in a number of objects (e.g. Feigelson et al., 1995; Brunetti et al., 2001; Hardcastle et al., 2002a; Isobe et al., 2002). This emission is generally attributed to two processes; soft X-rays ($\lesssim$ 3 keV) arising from a thermal component, and hard X-rays ($\gtrsim$ 3 keV) from inverse-Compton emission, although the boundary at which this division occurs is not entirely clear. The photon field which is accelerated to hard X-ray energies is still some matter of debate. In most cases upscattering of the CMB provides good agreement with observations for sources with a magnetic field strength close to equipartition, but some evidence exists (e.g. Brunetti et al., 2001) that scattering of infrared photons may play an important role. The dependence on model parameters and the difficulty in separating the thermal and inverse-Compton components of the observed spectra mean that many ambiguities exist in out understanding of this emission.

1.5 The dynamics of radio galaxies

Determining the dynamics of radio galaxies has been a long standing problem. Their often complex morphology, and structure which ranges from parsec to megaparsec scales, have meant that making a model which can adequately describe the observed features has proved challenging, leaving many outstanding questions unanswered. In this section, I outline the standard model of radio-loud active galaxies and our current understanding of radio galaxy dynamics.

1.5.1 The beam model of radio-loud active galaxies

The beam model, first suggested by Longair et al. (1973) and later refined by Blandford & Rees (1974) and Scheuer (1974), is commonly accepted as explaining the observed large scale structure of radio-loud active galaxies. Collimated jets are the primary transport mechanism of material from the central AGN out to large distances in the form of a fluid flow, which pierces through the external medium and, where interaction occurs, forms a working surface. The details of this interaction are dependent on galaxy type; however, both FR-I and FR-II galaxies are observed to contain parsec-scale jets with apparent superluminal motion implying relativistic speeds (see Zensus, 1997 for a review). It is therefore likely that both radio galaxy types are similar on small scales (i.e. prior to deceleration) with factors such as jet power, opening angle and the intervening medium determining the eventual development of the large scale structure. In the following sections I describe our current understanding of these type-specific dynamics.

1.5.2 FR-I dynamics

On kiloparsec scales the well collimated inner jets of FR-I galaxies are observed to flare, resulting in an increase in surface brightness. This brightening is thought to be due to a reconfinement shock (Laing & Bridle, 2002b) and a low efficiency of energy transport through the medium. These jets are thought to be turbulent and, as noted in Section 1.3.3.3, may entrain the surrounding material leading to the observed deceleration. The first model of this form was proposed by Bicknell (1984), and has been refined over the subsequent decades by Laing & Bridle (2002a,b), Canvin & Laing (2004) and Laing et al. (2008). For conciseness, I refer to this model as the standard model for the remainder of this section.

With only a limited number of highly resolved sources available for which investigations can be undertaken, determining the generality of detailed FR-I properties has always proved a

limiting factor. Nevertheless, the standard model has proved successful in describing the observational properties in those few sources for which studies can be made. This model predicts a deceleration of the initially relativistic jets to speeds of $\lesssim 0.2$c on scales of $\sim$10 kpc. The jet speed is therefore likely to be subrelativistic for the majority of their length. The observed symmetry of the jets in FR-I galaxies supports this picture of a slow-moving jet. If high speeds were maintained out to large distances, relativistic effects would cause an asymmetry to be seen in a high fraction of these sources, such as is observed in FR-II galaxies (Section 1.5.3).

The diffuse plumes and lobes of emission which occur after the deceleration of the jet are observed to have a wide range of morphologies (Figure 1.7). These variations are likely to be due to a combination of environmental and jet power effects but the manner in which this material propagates through the surrounding medium does appear, at least in part, to be determined by the current evolutionary stage of the radio galaxy. Young and recently restarted FR-I galaxy lobes are thought to be overpressured and expand supersonically through the medium. In the well studied source Centaurus A, Kraft et al. (2003) observe shock-heating of the interstellar medium (ISM) due to expansion with a Mach number of approximately 8.5 and greatly over pressured lobes. These findings are supported by recent investigations such as those by Croston et al. (2007) and Heesen et al. (2014) of NGC 3801 and of PKS B2152-699 by Worrall et al. (2007), which both support a picture of supersonic lobe expansion, even under minimum energy conditions.

In older, more developed FR-I galaxies, lobes and plumes are thought to expand through the external medium subsonically (e.g. Leahy, 1991). As was noted in Section 1.3.3.3, X-ray observations of the surrounding gas suggest that these lobes are underpressured by up to an order of magnitude under the assumption of the minimum energy condition (e.g. Croston et al., 2008a). There must therefore be either a departure from the minimum energy condition, or additional mechanisms must be included to maintain the required pressure balance. A non-unity lobe filling factor provides a possible solution to this problem, although what material could fill the remaining volume whilst remaining undetectable remains a mystery (e.g. Hardcastle & Worrall, 2000a). An alternative solution is that of a dominant proton population. As discussed in Section 1.3.3.3, entrainment is thought to be the primary mechanism for the addition of protons to the jets, hence lobes, of FR-I galaxies. Perhaps the most compelling argument for this entrainment is given by Croston et al. (2008a) who find a link between lobe pressure, morphology and expected entrainment rates. It is therefore likely that this entrainment plays a pivotal role in providing the proton population required to maintain pressure balance.

1.5.3 FR-II dynamics

In contrast to FR-Is, the jets of FR-II galaxies are thought to remain relativistic out to large distances. Evidence for these high speeds come mainly from arguments of jet sidedness, the apparent difference between the primary and counter-jet, and jet prominence, the brightness compared to the total source flux. Using a combination of these methods, studies such as those undertaken by Hardcastle et al. (1999), Arshakian & Longair (2004) and Mullin & Hardcastle (2009) find jet speeds between ~ 0.55–0.75c ($\gamma \approx 1.15 - 1.5$). An alternative method for inferring jet speed can be made through inverse-Compton modelling of the X-ray emission (e.g. Tavecchio et al., 2000; Celotti et al., 2001). Constraining these models through X-ray and radio observations, speeds of in the region of ~ 0.98c have been derived (e.g. Tavecchio et al., 2000; Sambruna et al., 2004). Although these speeds are much higher than those found from sidedness arguments, the derivation of these speeds is highly model-dependent. The reliance on X-ray observations also causes a bias towards bright sources oriented close to the line of sight, hence this method cannot be applied to a statistically complete sample. This disparity may also be resolved if the jet has velocity structure (e.g. Hardcastle, 2006; Mullin & Hardcastle, 2009), although how jet velocity varies as a function of its radius remains unknown. A consensus on the precise jet speeds has therefore yet been reached. Regardless of the disparity between the two methods, it is apparent that jet speeds remain high along their length implying efficient energy transfer. To maintain these speeds, these highly collimated jets must only interact weakly with the surrounding medium and are therefore much less well understood than their FR-I counterparts.

The jets of FR-IIs must eventually decelerate. This occurs when the fast moving jet plasma encounters slower moving material in its path. As these jets are supersonic, they cannot know about the material into which they are advancing. In the rest frame of the jet, they are therefore unexpectedly hit by a wall of fast moving material causing shock acceleration to occur forming a termination point in the jet known as a hot spot (e.g. Myers & Spangler, 1985; Meisenheimer et al., 1989; Carilli et al., 1991). Note that it is not a requirement that the jet terminates at the tip of the radio lobe, and jet termination is observed elsewhere e.g. at the base of the plumes in wide angle tailed sources (e.g. Hardcastle & Sakelliou, 2004), but this is generally the natural termination point of the jets, hence hotspots, of most FR-II sources. In these hotspots, the bulk kinetic energy of the jet is dissipated but as not all of the energy provided by the jet is lost in the form of radiation, a back-flow of material populates the area behind the hot spot (Longair et al., 1973; Scheuer, 1974). The regions of plasma previously accelerated in the hot

spots are constrained by the external medium to form the characteristic lobes associated with FR-II type radio galaxies (e.g. Scheuer, 1974; Begelman & Cioffi, 1989; Kaiser & Alexander, 1997; Krause et al., 2012). This material, which forms a cocoon of plasma, is thought to aid in the confinement of the jet (e.g. Kaiser & Alexander, 1997). Numerical modelling of radio lobe dynamics has shown reasonably good agreement with observations (see Ferrari 1998 for a review) and continues to this day (Tregillis et al., 2001; Heinz et al., 2006; Krause et al., 2012; Mendygral et al., 2012; Hardcastle & Krause, 2013; Morsony et al., 2013). However, there is some disagreement about the pressure of the lobes. Kaiser & Alexander (1997) required the lobes in their models to be highly overpressured, but Hardcastle & Worrall (2000a) found that for a sample of 63 FR-II galaxies, these lobes are typically underpressured at minimum energy. X-ray observations have since shown that many FR-IIs are, at best, in pressure balance with the external medium, but fall well short of the high pressure difference required for such models to be consistent. Similar arguments as were made in Section 1.5.2 for FR-I type galaxies can also be made here, such as non-minimum energy conditions, additional particles and non-unity filling factors. Inverse-Compton measurements provide empirical support for non-equipartition fields in at least some of these sources (e.g. Tashiro et al., 1998; Isobe et al., 2002; Croston et al., 2005) but it is not yet clear if this departure is either typical in powerful radio galaxies or would be able to provide the highly overpressured lobes required by the self-similar models.

The advance speed of hot spots, which can be thought of as analogous to the expansion speed of FR-I lobes, is a long-standing area of investigation. Through arguments of lobe symmetry, Mackay (1973) first estimated hot spots to advance at speeds to be < 0.08c; however, further investigations have since led to a much wider range of plausible values. The advance speeds of FR-II sources can also be considered through arguments of lobe asymmetry. Scheuer (1995) proposes that assuming the brightest jet is observed in the approaching lobe, then for a source which is intrinsically symmetric an advance speed can be derived from the ratio of apparent lobe lengths (see also Chapter 3). From his sample of 43 sources, he finds a typical advance speed of only a few percent of the speed of light, but this form of analysis is only suitable for finding the 'typical' advance speed over a large sample and so cannot be directly applied to individual target sources. If the age of a source is known, the average advance speed over the lifetime of the outflow can also be derived. Spectral ageing analysis suggests advance speeds on the order of ~ 0.2c (e.g. Myers & Spangler, 1985; Alexander & Leahy, 1987; Liu et al., 1992) in agreement with asymmetry arguments. However, when ages are derived from a dynamical view point (e.g. Eilek, 1996), these speeds are up to an order of magnitude lower than when found spectrally

(~ 0.02c). I discuss this age and speed disparity in the context of results presented within this thesis in Section 3.4.

1.6 Galaxy evolution and the role of radio-loud AGN

Due to the sheer size and energy of radio-loud AGN, it is perhaps no surprise that they are thought to have an impact on their surrounding medium; however, recent investigations have suggested that it is not only the local environment on which they impact, but on the evolution of galaxies as a whole. In the following sections I describe the environment in which radio-loud AGN reside, their impact on that environment and models of AGN feedback which attempt to explain observations and their role in galaxy evolution.

1.6.1 The environment of radio-loud AGN

As previously mentioned, for all but a few well known exceptions (e.g. Ledlow et al., 1998; Keel et al., 2006), radio-loud AGN are hosted by elliptical galaxies where the most super-massive black holes capable of powering the most luminous AGN reside. This therefore suggests that the host galaxy and the environments in which they are found may play an important role in the formation of radio-loud AGN. Early studies by Lilly & Prestage (1987) and Owen & Laing (1989) found that optical emission from FR-I galaxies exceeds that of their FR-II counterparts which they suggested could be indicative of higher dust extinction in FR-IIs. Later investigations have also shown that that around 75 per cent of powerful radio galaxy host galaxies are morphologically disturbed (e.g. Gonzalez-Serrano et al., 1993) and are on average more blue than normal ellipticals (e.g. Govoni et al., 2000). Best (2004) also finds that neither the black hole or host galaxy properties are primarily responsible for triggering of nearby AGN activity and therefore suggest that galaxy mergers or interactions may instead be responsible. This empirical evidence supports the long-standing idea (e.g. Heckman et al., 1986) that galaxy mergers may be responsible for the onset of powerful AGN activity. However, more recent investigations have shown that evidence of post-merger disruptions in these galaxies are not observed when compared to field galaxies (e.g. Cisternas et al., 2011; Schawinski et al., 2011). Secular processes have therefore been suggested as an alternative to galaxy mergers for the triggering of AGN at redshifts $\lesssim 2$ (e.g. Orban de Xivry et al., 2011; Kocevski et al., 2012), although mergers are still the preferred mechanism at higher redshifts.

The environment in which these elliptical galaxies reside is also thought to be key in the formation of these sources. Radio-loud AGN are found in most galaxy clusters, where the intracluster medium (ICM) is typically observed to be high temperature ($\sim 10^7$ – 10^8 K), low density ($\sim 10^{-3}$ ions / cm^{-3}) and primarily composed of ionized hydrogen (Sarazin, 1986; Sarazin et al., 1992; Fabian, 1994 and references therein). The pressure of this hot gas, trapped in the group or cluster's potential well, is thought to aid in the confinement and regulation of the lobe expansion of radio galaxies. At moderate to high redshifts, both high- and low-power radio-loud AGN are observed to inhabit rich clusters (e.g. Hill & Lilly, 1991). However, low-redshift studies have shown (e.g. Prestage & Peacock, 1988; Hill & Lilly, 1991; Best, 2004) that powerful radio-loud AGN are found more commonly in galaxy groups and poor cluster environments with low-power radio galaxies generally residing in denser environments. The cause of this preference is still unclear, but there are two likely scenarios; the environment of central group galaxies are suited to hosting radio-loud AGN, or, interactions caused by the proximity of nearby galaxies are responsible for the onset of AGN activity.

The high temperatures observed in the ICM can be partially explained through shock-heating of material as it falls into the cluster's potential well but, in hierarchical models of cluster formation, this process alone cannot account for the high temperatures observed and additional mechanisms are required. In addition to explaining the high temperatures in group and cluster environments, an additional problem exists in reconciling the theory and observation of galaxy cluster cores. At the centre of clusters, the short radiative lifetime of the X-ray emitting gas is expected to cause gas to cool, contract and flow towards the centre of the cluster (Cowie & Binney, 1977; Fabian & Nulsen, 1977; Mathews & Bregman, 1978; also see Fabian, 1994 and McNamara & Nulsen, 2007 for comprehensive reviews). These so-called cooling flows are nearly always found in clusters with a central radio galaxy (Eilek, 2004) and give rise to an important question. If cool, dense gas is cooling on to central cluster galaxies, why is less star formation observed when compared to normal galaxies, where gas is less abundant?

Supernova winds were originally thought to provide the required energetic input for both heating the ICM and the quenching of star formation in these galaxies (e.g. Ponman et al., 1999). However, recent investigations have found (Wu et al., 2000; Croton et al., 2006; Bower et al., 2006) that radio-loud active galaxies are likely to be the primary cause. In the following section I detail the impact of radio-loud AGN on their environment.

1.6.2 The impact of radio-loud AGN on their environment

As discussed in the previous section, it has become increasingly apparent that radio-loud AGN have a significant impact on their environment, but the details of *how* these sources provide the required energetic input is less clear. X-ray observations provide perhaps the strongest evidence of these interactions. X-ray cavities, regions of low thermal emission co-incident with radio galaxy lobes is observed, were first discovered in the 1990s using the *ROSAT* telescope (Boehringer et al., 1993; Hardcastle et al., 1998) but have become of particular interest (e.g. Birzan et al., 2004; Rafferty et al., 2006) since the launch of the *Chandra* X-ray observatory (Section 2.1.1). These cavities imply a deficit in thermal material relative to the external medium, hence, work must have been performed on the ICM. Studies of X-ray cavities not only provide strong evidence in support for radio-loud AGN having a significant impact on their environment but can also be used to determine lower limits for the internal pressure of radio galaxy lobes.

Evidence of ICM heating due to more complex mechanisms has also been found. In some of the most well studied objects, shocks driven by radio galaxy lobes are observed to propagate through the external medium (e.g. Smith et al., 2002; Nulsen et al., 2005; Croston et al., 2011) which, in at least some cases, is observed to accelerate particles in a manner consistent with diffusive shock acceleration (e.g. Croston et al., 2009). This strongly suggests that radio-loud AGN provide energy transfer to the external medium via a variety of mechanisms, rather than simply through the displacement of cluster gas. It has recently been shown that the jets of radio-loud AGN may also drive outflows of neutral hydrogen (e.g. Oosterloo et al., 2004). This process may be important in removing the cold, dense gas in galaxies at high redshifts, so reducing the material available for star formation.

Radio-loud AGN are also thought to have an effect on the cooling flow described in Section 1.6.1. Displacement of gas described previously in this section is one possible mechanism by which these cooling flows could be disrupted; however, it was suggested early on (Binney & Tabor, 1995) that the mechanical energy of radio galaxy jets could dramatically affect their properties. Using self-similar models of supersonically expanding radio cocoons, Kaiser & Alexander (1999) show that shocked material has a cooling time much larger than the lifetime of the radio source. Basson & Alexander (2003) later suggested that once the radio jet is turned off, the remnant of the AGN activity rises buoyantly through the ICM, dragging cool material with it. All of these mechanisms potentially affect the expected gas cooling time when compared

to the naive view of a simple inflow of cooling gas, and so may explain the low star formation rates observed in these galaxies.

It is therefore clear that radio-loud AGN play an important role in the dynamics and energetics of the ICM. In the following section I provide details of the self-regulating AGN feedback model, which is widely believed to provide a solution to the problem of low star formation rates and which affects the process of galaxy evolution as a whole.

1.6.3 AGN feedback and its role in galaxy evolution

The growing body of evidence detailed in the previous sections for the heating of the ICM and the disruption of cooling flows has recently seen a dramatic shift in our view of the importance of radio galaxies in galaxy evolution. Previous attempts to explain this heating and subsequent suppression of star formation have traditionally involved mechanisms such as supernova feedback (e.g. White & Rees, 1978; White & Frenk, 1991); however, such models rely on a large supply of massive stars in suppressed systems to provide the required energetic input. Recent investigations have found that models of AGN feedback in which kinetically powerful outflows control the supply of gas available for star formation have proved particularly successful. In the following sections, I present the currently favoured model of AGN feedback and the modes under which it operates.

1.6.3.1 Quasar mode

Galaxy mergers are thought to play a major role in the hierarchical formation of galaxies. Bower et al. (2006) and Croton et al. (2006) present 'quasar mode' models of AGN feedback in which these interactions both trigger the onset of AGN activity and regulate the star formation rate. In this model, mergers cause high accretion rates on to the central supermassive black hole either due to disruption of bulge gas, or by directly depositing matter to the AGN core. The resulting radiative winds (and perhaps also strong jets) drive cold gas from the galaxy greatly reducing or even halting star formation. At high redshifts ($z \gtrsim 2$), quasar mode is thought to be of particular importance in giving rise to the 'red and dead' characteristics of massive ellipticals. The physics of this mode of AGN feedback is still poorly understood and observational evidence is at best limited, but simulations provide good agreement with current models of galaxy formation and the observational properties of massive ellipticals. However, as noted in Section 1.6.1 cooling flows and the in-fall of ejected material should replenish the gas supply leading to the resumption

of star formation. An additional 'maintenance mode' must be present to produce the observed properties of massive ellipticals.

1.6.3.2 Radio mode

In explaining the maintenance mode mentioned above, Croton et al. (2006) suggest a 'radio mode' feedback model with lower accretion rates than their quasar mode counterpart. In this model, cool molecular clouds that condense into star forming regions also feed the central supermassive black hole. This triggers the onset of AGN and their mechanically powerful radio jets which subsequently heat cooling flows and suppress the supply of cold gas for further star formation. As detailed in Sections 1.6.1 and 1.6.2, observational evidence for this radio mode heating of the ICM and cooling flows is strong, and hence it has become the preferred explanation for the lack of star formation in massive ellipticals. These model of AGN feedback have gained support not only because of its ability to account for observations in a self regulating manner, but because it is also independent of star formation on which many previous feedback models have relied. Figure 1.10 emphasizes this models success with radio mode feedback agreeing well with observations compared to the poorly fitting non-feedback model.

It is the nearby, well resolved radio galaxies which are key to determining the dynamics and energetics of radio galaxies, hence it is this radio mode which is of greatest interest to this thesis. In the following section I summarize the issues raised within this introduction and outline the questions which this thesis aims to answer.

1.7 Outstanding questions and thesis aims

In this chapter, I have detailed the theory behind radio-loud AGN, their observational properties and the environment in which they reside. I have highlighted many of the outstanding problems surrounding the physics of these objects and to their impact on galaxy evolution. If one is to begin addressing these issues it is of the utmost importance that the dynamics and energetics of these sources are understood.

The total power output of these radio sources is one question of particular importance if the impact of radio-loud AGN is to be fully understood. Whilst a (model dependent) total energy can be estimated (Falle, 1991; Kaiser & Alexander, 1997; Godfrey, 2013), if one is to determine the total jet power the age of the source must be known. Models of spectral ageing (Section 1.3.2) are commonly used for this purpose; however, limitations imposed by the previous generation

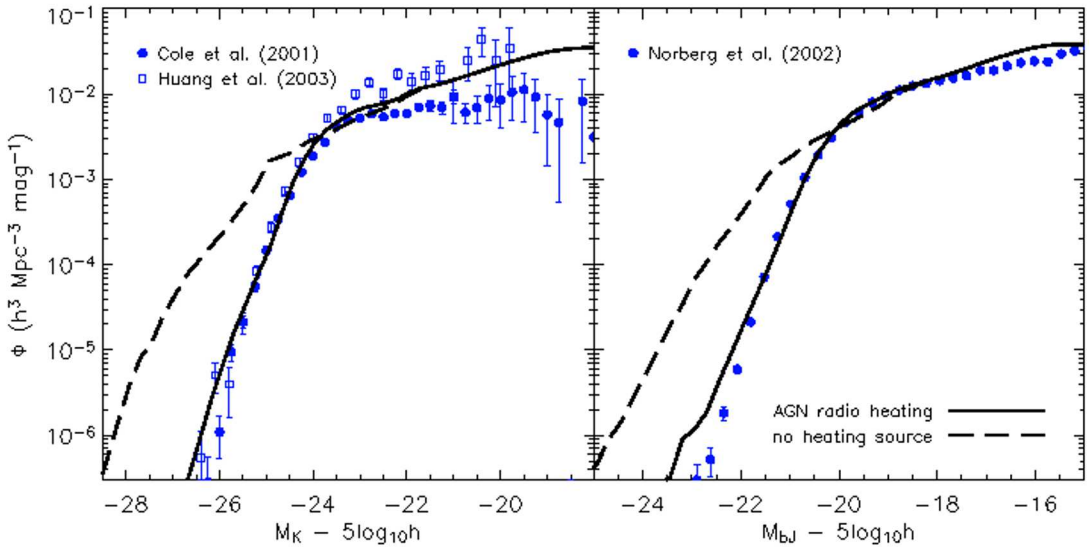

Figure 1.10: Plot by Croton et al. (2006) of luminosity functions in the K (left) and B (right) photometric bands. Overlaid are models including (solid line) and excluding (dashed line) radio mode feedback. When this feedback model is included, the predicted luminosity of massive ellipticals is in good agreement with observations.

of radio telescopes have left the reliability of these ages in question (Eilek, 1996). The historical inability of radio interferometers to produce high sensitivity, large bandwidth observations with good UV coverage has meant that investigations of the radio spectrum of radio-loud active galaxies have traditionally relied on the use of large spatial regions or integrated fluxes leaving a significant uncertainty in the key parameters of these models. During this thesis I therefore use innovative techniques and methods to exploit the expanded capabilities of new generation radio interferometers to address these crucial problems. In doing so, I consider specifically these outstanding questions:

- How can one best exploit the new generation radio interferometers for the determination of spectral age?
- Are the commonly assumed parameters of spectral ageing models valid when considered on small spatial scales?
- Is spectral ageing a physical reality in the lobes of powerful radio sources?

- Do models of spectral ageing currently provide reliable intrinsic ages for powerful radio sources?

The limited resolution available at metre wavelengths have meant that the spectral profile and energetics of radio galaxies are currently poorly understood at low-frequencies. However, with the commissioning of LOFAR (see Section 2.2.2) this is set to change. In this thesis I therefore use LOFAR early science data of FR-II radio galaxies to address the following key questions:

- What is the spectral profile of powerful radio galaxy lobes at low frequencies?
- What impact does this have on calculations of the energetics of these sources?

As mentioned in Section 1.4.3, observations of X-ray jets of FR-I galaxies imply *in-situ* particle acceleration, but details of the mechanism behind particle acceleration to these high-energies is at best limited. Previous studies have mainly focused around the properties of individual galaxies with no large scale sample available for comparison. It has therefore been hard to determine if a given property is common across all FR-I galaxies or whether it is unique to that target. With the growing number of galaxies in which X-ray jets are known to be present, enough data now exist for larger sample investigations to be undertaken. I therefore use archival data from the *Chandra* X-ray observatory (see Section 2.1.1) to provide insight into the following questions:

- What relationships are present between the properties of X-ray jets and their host galaxies?
- Do any of the current models adequately describe particle acceleration in the X-ray jets of FR-I galaxies?

In the next chapter, I detail the instrumentation, data reduction techniques and methods used in the analysis of radio and X-ray observations. I go on to present the software package developed in answering the question of determining reliable spectral ages using new generation, broad-bandwidth, radio interferometers. In Chapter 3, I present results from initial investigations of spectral ageing at GHz frequencies of two bright, nearby FR-II sources and discuss the implications for the questions outlined above. In Chapter 4, I expand this study to an additional FR-II source using the fully upgraded Jansky Very Large Array (JVLA, see Section 2.2.1) which tightly constrain models of spectral ageing. In Chapter 5, I present a study of a powerful radio

source at low-frequencies using LOFAR and discuss the findings implications for radio galaxy energetics. In Chapter 6, I present the first large sample study of X-ray jets using the *Chandra* X-ray telescope and test these findings against current models of particle acceleration. In Chapter 7, I summarize these findings and discuss their implications with respect to answering the questions laid out within this chapter and conclude with my planned future work which aims to resolve new issues which have been raised within this thesis. Sections of this thesis (including this introduction) are taken from material published in Harwood & Hardcastle (2012) and Harwood et al. (2013). Joint publications and any material provided by collaborators are referenced accordingly throughout.

2

Instrumentation and methods of analysis

2.1 X-ray observations

The launch of NASA's flagship X-ray observatory, *Chandra*, in 1999 on the space shuttle Columbia ushered in a new era of high resolution X-ray astronomy, allowing the study of small scale objects and features. In this section I give a brief overview of *Chandra* and the methods of reduction used in Chapter 6.

2.1.1 *Chandra*

Due to the high energies involved, X-ray telescopes cannot simply reflect incoming photons in the manner one would with an optical telescope; they must be deflected by a series of grazing-incidence mirrors to a focal point where a series of detectors are located (Figure 2.1). There are 4 available scientific instruments which can be used by *Chandra*; High- and Low-Energy Transition Gratings (HETGS and LETGS respectively), the High Resolution Camera (HRC) and the Advanced CCD Imaging Spectrometer (ACIS). The HETGS and LETGS are mounted near the front of the telescope, diffracting incoming X-rays. Used in combination with either the HRC or ACIS they provide two dedicated high resolution spectroscopy instruments. The High Resolution Camera (HRC) is located in the Science Instrument Module (SIM) at the telescope's focal point and provides a high resolution ($\sim$ 0.5 arcsec) imaging capability. The ACIS, of which this thesis makes use, is also mounted in the SIM and consists of an array charged couple devices. This detector provides high resolution images ($\sim$ 0.7 arcsec) but also benefits from

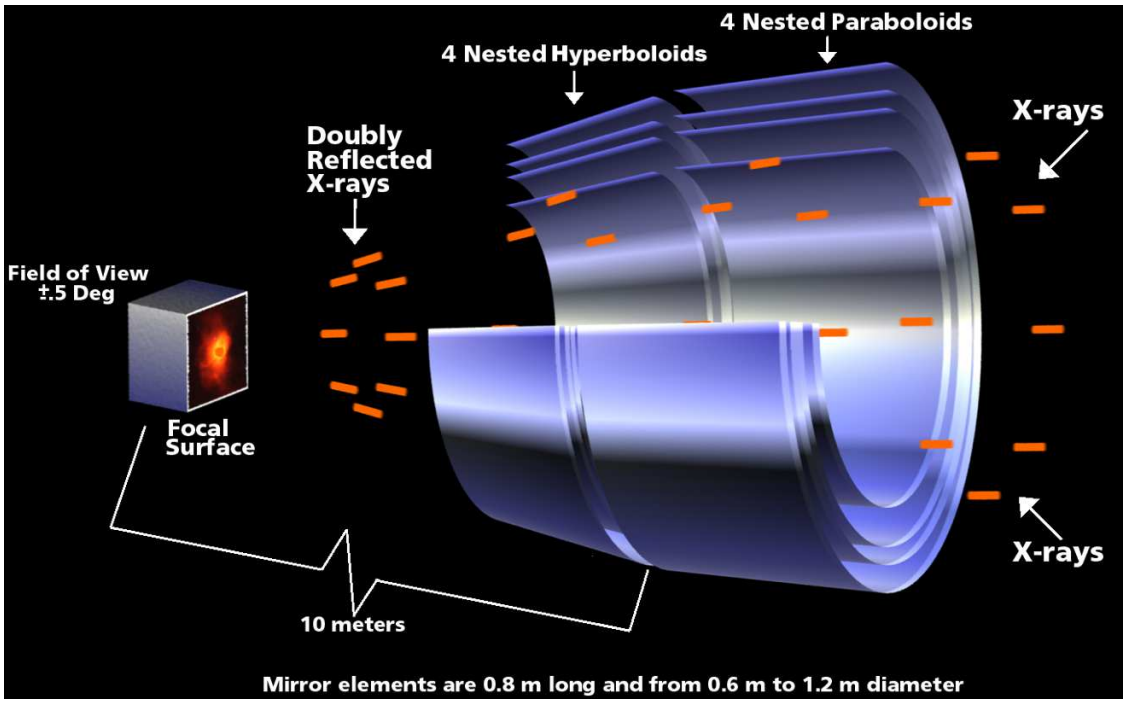

Figure 2.1: Schematic view of the *Chandra* grazing mirror design. Image courtesy of NASA/CXC/D.Berry.

greater sensitivity and higher energy resolution than the HRC. Except where the highest spatial resolution is critical, ACIS is therefore the preferred instrument for the majority of observations. A schematic overview of *Chandra* and its instrument locations is shown in Figure 2.2. In the following section I detail the reduction methods used for the X-ray observations of Chapter 6.

2.1.2 Data reduction

Prior to being made available to the end user, all *Chandra* observations are initially reduced using a system known as standard data processing (herein the *Chandra* pipeline). This pipeline (and *Chandra* data reduction in general) can be broken down in to 3 stages:

- Level 0: Raw data is transferred from *Chandra*, separated into Flexible Image Transport System (FITS) files and then divided along observational boundaries.
- Level 1: Instrument and time dependent corrections (e.g. aspect solutions) are applied to Level 0 data.

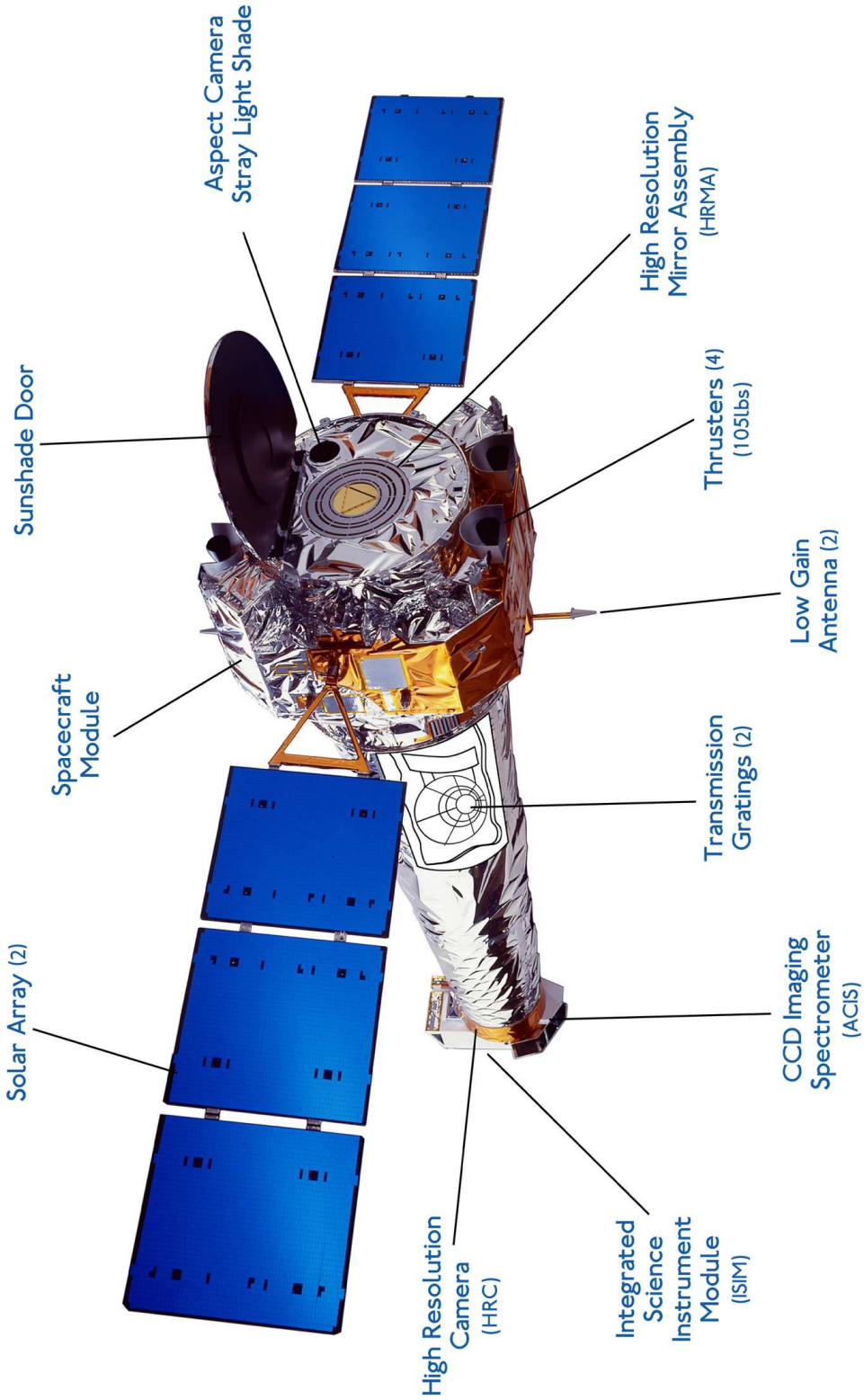

Figure 2.2: Schematic view of the *Chandra* X-ray observatory with instruments labelled. Image courtesy of NASA/CXC/NGST.

- Level 2: Filters and transformations, such as cosmic ray detection and conversion to celestial coordinates, are applied to Level 1 data.

In order to obtain the highest quality possible, the observations used in this thesis were reprocessed with the most up to date calibration data using the CIAO data analysis system[1]. Using a C-shell script, the level 1 events file was first processed using the DESTREAK command and output to a revised data file. This corrects for the ACIS chip serial readout[2] which causes a random but significant charge to be placed upon pixel rows. The status flags of the data were then reset by use of the DMTCALC before removal of hot pixels via the ACIS_RUN_HOTPIX. This acts to remove two forms of spurious data; hot pixels as defined by the CALDB database and those pixels which have an unusually high or low localized value when compared to the bias images. This hot pixel detection aims to remove any instrumentation error within the chip along with any other hot pixel sources such as cosmic-ray after glows. A new level 1 events file was then output via the ACIS_PROCESS_EVENTS command which creates a new file with updated parameters such as coordinates and energy range. The DMCOPY command was then used to create a level 2 event files with known bad data removed and filtered to the desired energy range. Unless otherwise stated, this will be the standard method of X-ray data reduction throughout this thesis.

2.2 Radio observations

Over the last few years, huge advancements have been made in the capability of radio telescopes to provide high resolution, high fidelity, large bandwidth observations. This has allowed for research to be undertaken in previously poorly understood areas of astronomy. In this section, I provide details of two such ground breaking instruments used within this thesis and the methods applied in the reduction of this data.

2.2.1 Karl G. Jansky Very Large Array (JVLA)

First becoming operational in 1980, the Very Large Array (VLA) is a 27 element interferometer located on the San Agustin plains in New Mexico, USA (Figure 2.3). Operated by the National Radio Astronomy Observatory (NRAO), the VLA is capable of observations between 74 MHz

[1] http://cxc.harvard.edu/ciao/

[2] http://cxc.harvard.edu/ciao/why/destreak.html

Table 2.1: Comparison of VLA and JVLA capabilities

Parameter	VLA	JVLA	Factor Increase
Sensitivity (12 hour observation)	10 μJy	1 μJy	10
Maximum bandwidth	0.1 GHz	8 GHz	80
Spectral windows	2	64	32
Maximum Channels	512	4194304	8192
Finest frequency resolution	381 Hz	0.12 Hz	3180
Frequency coverage (1 – 50 GHz)	22%	100%	5

and 50 GHz and consists of a Y-shaped array of 25 metre parabolic dishes mounted on railroad tracks. This allows for the antennas to be arranged in wide variety of predetermined array configurations. In its most compact form (D-configuration) the VLA has a maximum baseline length of 1 km and minimum baseline of 35 meters, allowing for the detection of diffuse emission such as is detected in the lobes of radio galaxies. In its most extended form (A-configuration) the VLA can achieve baselines of up to of 36 km (680 meters minimum baseline), allowing for the study of compact structure. As radio interferometers are only sensitive to emission on scales of λ/B_{min}, where B_{min} is the length of the shortest baseline, the ease in combining array configurations in order to sample both large and small scale structure means that the VLA has proved vital in the study of radio galaxies over the last 30 years.

In January 2000, a proposal was made for a major overhaul to improve the key capabilities of the telescope by at least an order of magnitude by upgrading its receiver and processing systems. 2010 marked a key point in the upgrade of the VLA with the installation of a Wideband Interferometric Digital ARchitecture (WIDAR) correlator, which expanded the instantaneous bandwidth from a maximum of 100 MHz to 8 GHz per polarization. The WIDAR correlator, combined with new wide-band receivers, has allowed for near complete frequency coverage between 1 and 50 GHz. Improvements to the low-frequency receivers (74 – 500 MHz) also make it the ideal instrument for complementary studies with new low-frequency interferometers such as LOFAR which I discuss in the following section. I show for comparison the old and new VLA capabilities in Table 2.1. For conciseness, I refer to observations taken prior to the 2010 as the VLA and observations post-WIDAR installation as the JVLA throughout this thesis.

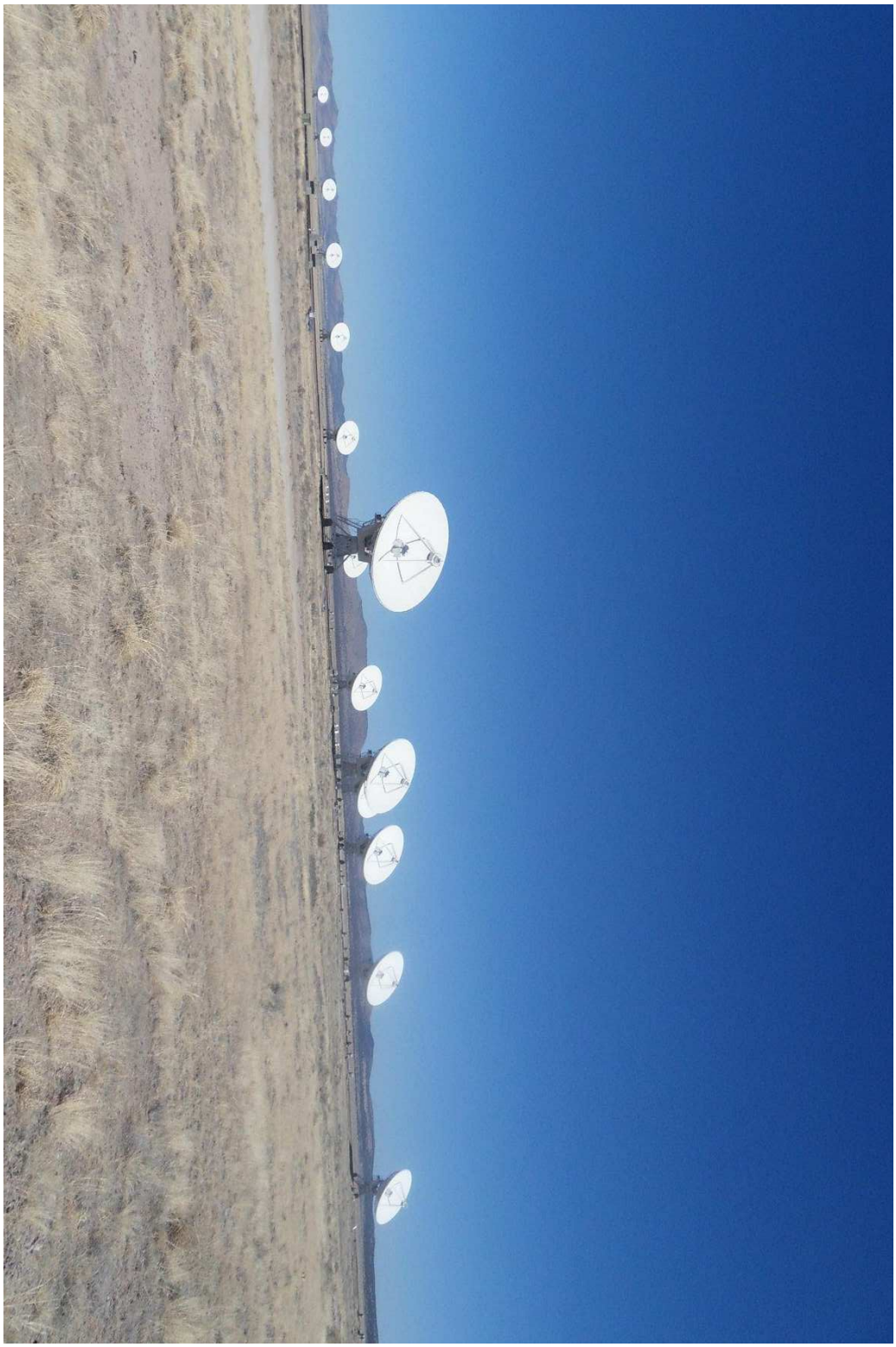

Figure 2.3: The Jansky Very Large Array (JVLA) in New Mexico, USA. Array shown in the compact D configuration.

2.2.1.1 Typical JVLA continuum observations

For standard JVLA continuum observations (and for standard interferometric observations in general) at least 3 sources are required; a flux calibrator, a phase calibrator and the target source. While the JVLA systems are very well characterized, if one is to determine the absolute flux of a source on the sky it must be calibrated against a reference source of known flux density. This source must be both bright, vary very little (if at all) with time and either unresolved in the observed frequency and array configuration, or, a well defined model of the calibrator source must exist to ensure all of the observed flux is accounted for, which limits the potential sources available for use. The NRAO provides details of a handful of well studied standard flux calibrator sources[1] which have been the subject of long term studies (e.g. Perley & Butler, 2013) and it is these sources which I use in this thesis. I use the standard practice of observing the flux calibrator at the very start and very end of the observing run.

A phase calibrator must also be observed to correct for instrumental phase drifts and atmospheric effects. This calibrator must be a point source at the observed frequency and array configuration with constant amplitude. As one uses this source to correct for atmospheric effects it must be located close to the target source and, as atmosphere varies on relatively short time scales, observed frequently throughout the observing run, though self calibration (discussed in Section 2.2.3.5) reduces this requirement. As the phase calibrator does not have the high brightness and stability requirement of the flux calibrator, suitable sources are much more common. The NRAO again maintains a list of sources suitable for use for a range of frequencies and array configurations. In this thesis, I again use the standard practice of interlacing observations of the target source with regular phase calibrator observations. An example JVLA observing plan is shown in Figure 2.4.

2.2.2 LOw-Frequency ARray (LOFAR)

In 2006, construction began on an ambitious project to provide high sensitivity, broad bandwidth observations at long wavelengths, the LOw-Frequency ARray (LOFAR). Consisting of ~ 25000 dipole antennas arranged into 46 stations spread throughout Europe (Figure 2.5), LOFAR is currently the world's largest connected interferometer. Operated by the ASTRON radio observatory in the Netherlands, LOFAR consists of 2 antenna types; the low band antennas (LBA) which operate between 10 and 90 MHz, and high band antennas (HBA) capable of observations between

[1] https://science.nrao.edu/facilities/vla/docs/manuals/oss2013a/performance/cal-fluxscale

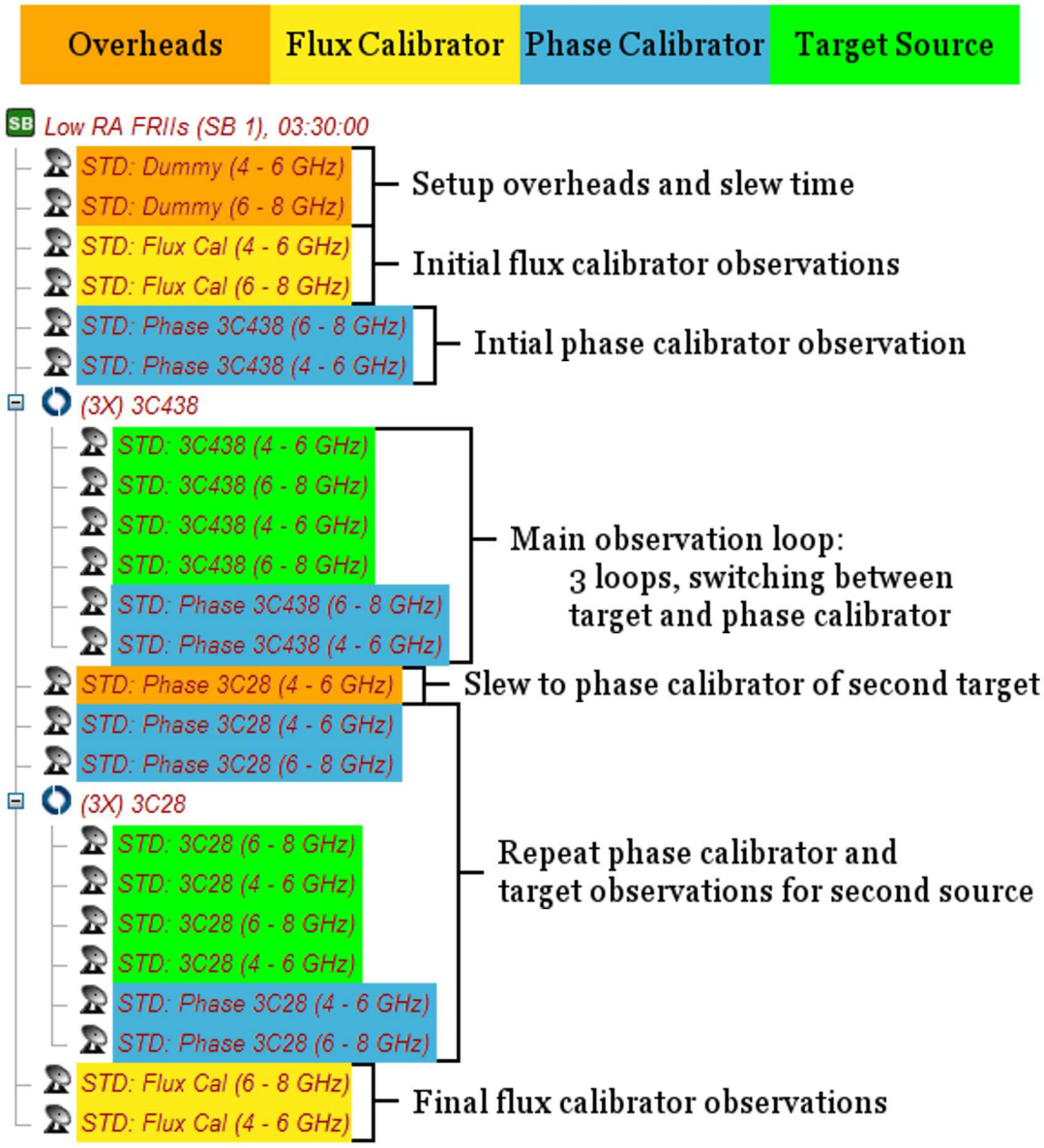

Figure 2.4: Example of a typical JVLA observing plan as detailed in Section 2.2.1.1 of two target sources, 3C438 and 3C28.

110 and 240 MHz (Figure 2.6). The LOFAR antennas can be roughly split into 3 categories. 24 core stations are densely packed within a 2 km radius known as the Superterp located near Exloo in the Netherlands and provide excellent short baseline coverage for the study of extremely extended structure, such as epoch of reionization studies. 14 remote stations spread throughout the Netherlands provide baselines of up to 100 km allowing for the study of more compact structure up to ~ 2 arcsec resolution at 240 MHz. Finally, 8 international stations provide baselines of up to 1500 km giving unprecedented sub-arcsecond resolution at low frequencies.

One of the major benefits of a dipole antenna system such as LOFAR is its extremely large field of view (up to ~ 45 degrees at 15 MHz) and the capability to take multiple simultaneous pointings. As LOFAR observes a large fraction of the entire sky during any given observation, ones ability to observe the visible sky is only limited by the computing power available to handle the data. LOFAR therefore initially utilized an IBM Blue Gene for the correlation of observations which, at the time of installation, was the second most powerful supercomputer in the world. (The correlator system has since been upgraded to the COBALT system which uses graphic processing units (GPUs) to provide an increased data throughput compared to standard CPU systems; data in this thesis used the original correlator.) This allows for LOFAR to be highly flexible in its observations by either splitting its bandwidth to make up to a maximum of 450 beams across the sky, or, using its full bandwidth capabilities to provide deep, high fidelity, low noise observations.

In 2012, LOFAR officially began scientific observations allowing, for the first time, the low-frequency spectrum of radio galaxies to be determined on small spatial scales. Within this thesis I use LOFAR in the single beam mode as part of the nearby AGN key science project to obtain high fidelity, broad-bandwidth observations of powerful radio sources and determine the dynamics and energetics of these sources at these low frequencies.

2.2.2.1 Typical LOFAR continuum observations

Typical LOFAR observations are based on similar principles to those described in Section 2.2.1.1, but vary in the way in which they are undertaken. In contrast to the two separate calibrator sources used for the JVLA, LOFAR generally uses one object selected from a list of reference sources (Scaife & Heald, 2012) to acts as both a flux and phase calibrator (although note it is not uncommon for secondary or tertiary flux calibrators to be observed). For HBA observations, the calibrator source is interlaced with the target observations in a similar manner as is used for the JVLA phase calibrator. At LBA frequencies, where correcting for changes in

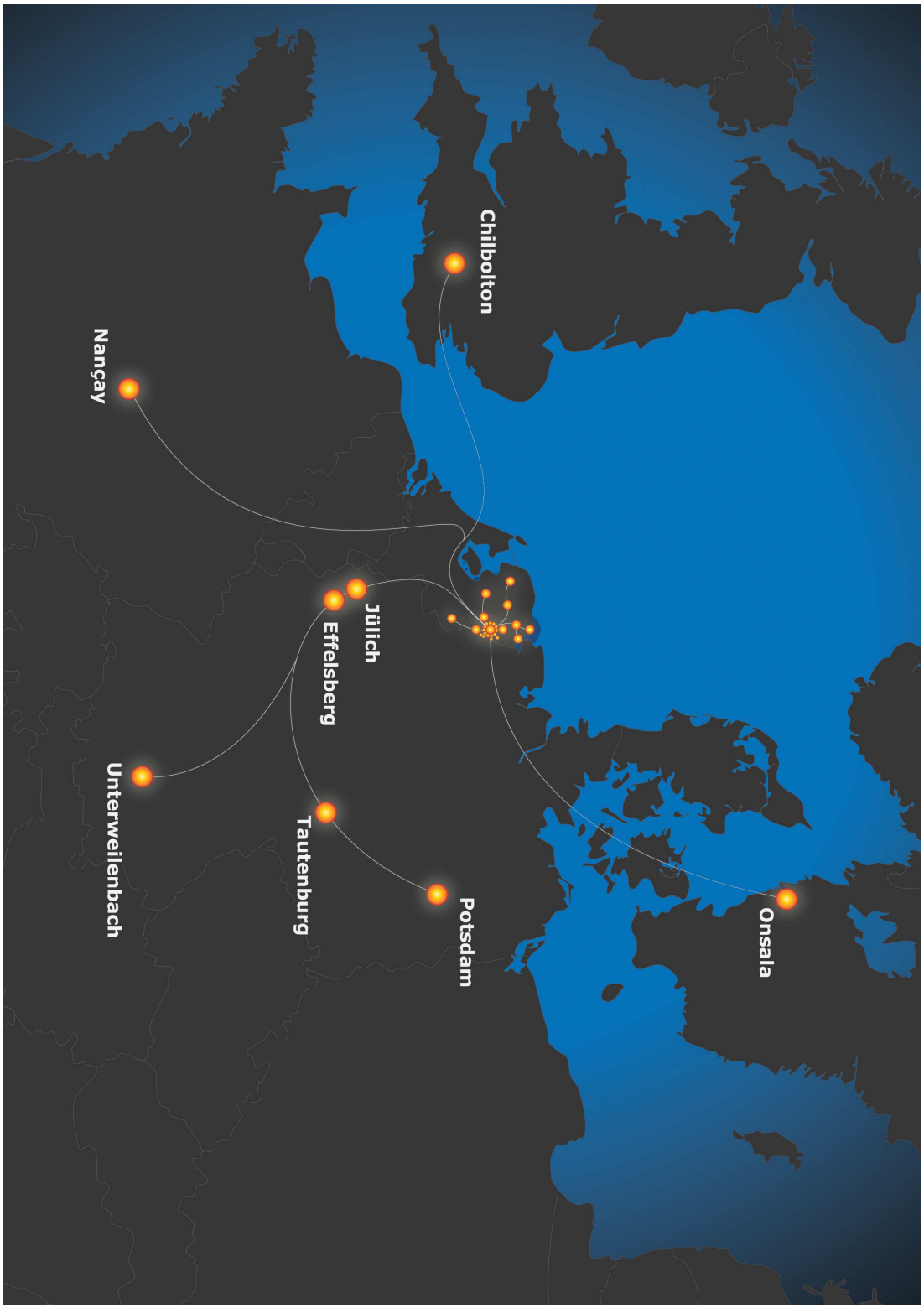

Figure 2.5: Location of LOFAR stations throughout Europe. Image courtesy of ASTRON.

Figure 2.6: Images of a LOFAR LBA (left) and HBA (right) station. Note the HBA antennas are located within the observed black casings. Images courtesy of ASTRON.

the atmosphere is of great importance, the calibrator source is observed concurrently with the target. This is achieved by using some of the available bandwidth to form a second beam on the sky which constantly monitors the calibrator source.

2.2.3 Radio data reduction

Since the 1970s, the Astronomical Image Processing System[1] (AIPS) has been the standard reduction package for interferometric radio observations. However, a new data reduction software is currently being developed by a consortium of the National Radio Astronomical Observatory (NRAO), the European Southern Observatory (ESO), the National Astronomical Observatory of Japan (NAOJ), the CSIRO Australia Telescope National Facility (CSIRO/ATNF) and the Netherlands Institute for Radio Astronomy (ASTRON). The Common Astronomy Software Applications[2] (CASA) aims to be better suited to the reduction of the broad bandwidth observations of the new generation of radio telescope and allow for the easier integration of automated pipelines and of end user developed tasks.

These two reduction software packages require data in two separate formats; AIPS compatible UVFITS files and CASA measurement sets (MS). The difference between the two (at least in the context of this thesis), is purely of a structural nature and converting between UVFITS and MS formats is a relatively trivial process. As the data format has no significant impact on the reduction methods employed within this thesis, I refer the interested reader to the relevant technical documentation[3,4] for further information.

In this thesis, I use both AIPS (Chapter 3) and CASA (Chapters 4 and 5) for the reduction of radio observations. Although very different in appearance, the underlying methods behind the reduction of radio data remain the same in both software packages. The reduction used within this thesis generally follows the methods detailed within the cookbook of each reduction package[5,6] but, for ease of reference, I provide in this section a summary of the general data reduction techniques and methods specific to the reduction of LOFAR data used.

[1] http://www.aips.nrao.edu/index.shtml
[2] http://casa.nrao.edu/
[3] http://casa.nrao.edu/docs/UserMan/UserManse7.html
[4] ftp://ftp.aoc.nrao.edu/pub/software/aips/TEXT/PUBL/AIPSMEM117.PS
[5] AIPS: http://www.aips.nrao.edu/cook.html
[6] CASA: http://casa.nrao.edu/ref_cookbook.shtml

2.2.3.1 AIPS calibration

Built in FORTRAN, AIPS is operated through a system of 'tasks' with five-letter names. These tasks access the main functions of the software (e.g. the flagging of bad data) and are parameterized by adverbs (e.g. specifying the range of data you wish to flag). Before the calibration of a data set can begin, AIPS requires that the UVFITS data are loaded into the software through the UVLOD task. Because the JVLA antennas are movable, corrections must be made to account for any changes in antenna positions which have been recorded in the system after the observations were made. This is achieved using the VLANT task which connects to the NRAO servers and corrects the antenna table to the latest available information for a given observation time and date. For instruments where the antenna positions are fixed (such as for LOFAR), this stage is not required for their reduction. Once these corrections have been made, the absolute values for the flux calibrator must be obtained. In this thesis, common calibration sources are used in all observations, hence known values can be loaded using the SETJY task and OPTYPE 'CALC' to determine the expected calibrator fluxes at any given frequency. For broad bandwidth JVLA data, a bandpass calibration is required to determine the response of each antenna over the observed frequency range. The BPASS task is therefore run on the flux calibrator observation with the antenna position and total flux calibration, determined via SETJY, applied. With these initial values determined the main calibration of the observations can be undertaken.

An initial flagging of the raw data is next undertaken using the automated RFLAG task along with manual flagging of bad time ranges, baselines and channels using the UVFLG task. A standard model of the flux calibrator is then loaded using the CALRD task allowing the position and morphology to be known. Using the CALIB task, this model is used along with the values determined above to produce a solution table for the flux calibrator. If a large number of solution are found to fail, additional flagging is performed and the calibration is rerun. This process is then repeated without the use of a model to provide solutions for the phase calibration sources. It is next necessary to determine the flux of the phase calibration sources using the flux calibration solutions via the GETJY task. These gain solutions are then applied to the calibration table and temporarily applied to the target source. The data are then inspected through the visual inspection task UVPLT, which allows various data parameters such as time, UV distance and amplitude to be plotted. Additional flagging is then performed on the flux calibrator, phase calibrators and the target source, repeating this calibration process until all possible radio-frequency interference (RFI) has been removed. To allow future investigations to be undertaken without the need

for a second reduction of the observations, polarization calibration was also performed. As for this thesis only Stokes I images have been produced, I do not detail the reduction method here but instead refer the interested reader to appendix E of the AIPS cookbook.

Once the calibrated data is of sufficient quality, the target source is separated from the main data set and calibration permanently applied using the SPLIT task and, where required, the data are averaged over time or frequency using the SPLAT task. Once complete concatenation with further observations (e.g. from other array configurations) and imaging can be undertaken. I describe the imaging process and further self and cross calibration techniques in Sections 2.2.3.4 through 2.2.3.5.

2.2.3.2 CASA calibration

Written in C++, CASA is controlled through an iPython interface either interactively or through the use of Python scripts. The calibration of interferometric data with CASA is similar to that described in Section 2.2.3.1 but unlike AIPS, MS data sets are referenced directly by each command, hence a loading phase is not required. As the original data set is modified, care must be taken that suitable backups are taken where the original data are not easily accessible, such as is often the case with LOFAR observations.

For (J)VLA data, automated flagging of the raw data is first made using the FLAGDATA command in RFLAG mode to remove any high amplitude RFI. Corrections for changes in antenna position are then determined using the GENCAL command. This works in a similar manner to the AIPS VLANT task, retrieving the latest positional information from the NRAO servers and creating a table of corrections. SETJY is then run which loads both a model of the flux calibrator source and the expected flux values.

An initial phase calibration is then performed on a small range of central channels of the flux calibrator on a per time integration basis. Once complete, the residual antenna delays are then solved for using the GAINCAL command with GAINTYPE = K. Using these calibration tables, the bandpass is next determined for the flux calibrator using the BANDPASS command. The final phase and amplitude calibrations are then calculated, again using GAINCAL with CALMODE = AP. The final calibration tables are then applied using the APPLYCAL function and the data inspected using the PLOTMS command. Flagging of the data is then performed, the applied calibration cleared using the CLEARCAL function and the process repeated until the data are clear of RFI. As with the AIPS data reduction, I also performed polarization calibration for the benefit of future projects following the standard techniques outlined in the CASA cookbook, but

as no polarization images have yet been produced do not detail the process here. Once initial calibration and flagging is complete, the target source is again separated from the main data set in preparation for concatenation, self or cross calibration and imaging.

One of the major advantages of CASA is its capacity to easily automate much of the data reduction process. In Chapter 4 where a large number of radio maps are required this is of particular benefit. The reduction process described in this section, with the exclusion of the flagging of RFI, has therefore been coded into a Python script.

2.2.3.3 LOFAR calibration

The calibration of LOFAR data used in this thesis follows the guidelines set out in the standard imaging cookbook[1]; however, due to the high volume of data produced by LOFAR a complete manual reduction of observations is less than desirable. In this thesis, I therefore use Southampton University's automated LOFAR pipeline written by Adam Stewart[2]. In this section, I detail LOFAR specific programs and how they are applied within this pipeline.

Whilst the calibration of LOFAR observations follow the general processes outlined in the previous sections, LOFAR specific functions have been written (generally based on core CASA tasks) for the handling of these low-frequency data. One key difference is the need for the removal of bright radio sources. As LOFAR always sees the entire sky (Section 2.2.2), the 5 brightest radio sources (Cassiopeia A, Cygnus A, Hydra A, Taurus A and Virgo A) must be subtracted from the data if they are expected to interfere heavily with a given observation. These so-called A-team sources, the properties of which have been well characterized, are therefore removed in a process known as demixing prior to the data being made available to the end user. However, if this demixing is performed when interference from A-team sources is not present, the data quality can deteriorate. Simulations are therefore run using CASA to determine the impact on any given observation and this information passed to the observing staff at ASTRON.

Flagging of bad data is first performed on the raw data using the AOFlagger of Offringa et al. (2010) which has been designed primarily for LOFAR observations. Models of the calibrator sources are next created using the Global Sky Model (GSM) function which uses the VLA Low-frequency Sky Survey (VLSS), Westerbork Northern Sky Survey (WENSS) and NRAO VLA Sky Survey (NVSS) surveys to determine their properties. Amplitude calibration solutions are then determined using the BlackBoard Selfcal (BBS) package and the solutions applied. A phase

[1] https://www.astron.nl/sites/astron.nl/files/cms/lofar_imaging_cookbook_v13.pdf
[2] Adam.Stewart@astro.ox.ac.uk

only calibration is then undertaken using BBS and solutions transferred to the target source. Further automated flagging is then performed on the corrected data. Finally, the individual subbands of the LOFAR observation are concatenated using the New Default Pre-Processing Pipeline (NDPPP) package and a manual inspection of the data made using CASA. Any remaining RFI is then flagged manually using the techniques of Section 2.2.3.2. Once free of bad data the observation is ready to be imaged, the methods of which I detail in the next section.

2.2.3.4 Imaging

Imaging of the calibrated data in this thesis has been undertaken using both the AIPS IMAGR task (Chapter 3) and CASA CLEAN function (Chapters 4 and 5). It is worth noting that a dedicated LOFAR software package (AWIMAGER) tailored for wide-field imaging is also available. However, as this imager is computationally expensive and in this thesis I am only interested in bright sources at the centre of the field of view, CASA provides a functionality better suited to the observations made.

Three forms of deconvolution are used in this thesis; CLEAN, multi-scale CLEAN (MSCLEAN) and the maximum entropy method (MEM). The CLEAN algorithm is probably the most commonly used method for the deconvolution of radio data. First presented by Högbom (1974), this algorithm assumes the sky can be represented by a series of point sources known as CLEAN components which are restored with a Gaussian CLEAN beam to create the final image. The cycle of this algorithm can be summarized as follows:

1. Determine the position and intensity of peak flux in the dirty map
2. Subtract the dirty beam, weighted by the peak intensity and a user defined gain factor, from the location of the peak flux
3. Repeat processes 1 and 2 until the remaining peak intensity falls below a user defined level
4. Convolve the CLEAN components with an idealized elliptical Gaussian CLEAN beam
5. Restore the dirty image residuals to the CLEAN image

A further development of this algorithm was made by Clark (1980) who proposed that as the majority of the computational time required to perform a CLEAN cycle was used in shifting and scaling the dirty beam, a 2 dimensional Fast Fourier Transform (FFT) could be instead used.

Clark (1980) therefore introduced major and minor cycles to the algorithm to address this issue. The minor cycle proceeds as follows:

1. A section of the beam is selected so as to include the highest exterior sidelobe
2. Peaks in the dirty image which have a intensity greater than the highest exterior sidelobe relative to the image peak are selected
3. A Högbom CLEAN is performed using the peaks and beam determined in the previous steps

A major cycle is then performed where the CLEAN model determined by the minor cycle is transformed via a FFT, multiplied by the inverse transform of the beam, transformed back again and subtracted from the dirty image.

A further modified version of CLEAN known as the Cotton-Schwab algorithm (Schwab, 1984) provides the preferred method of CLEANing in this thesis. This version builds on that of Clark by during the major cycles, subtracting the CLEAN components from the un-gridded visibilities allowing gridding errors to also be corrected. The Cotton-Schwab algorithm is also generally found to be faster than that of Clark, reducing the computational time required.

A more recent evolution of these deconvolution algorithms is the multi-scale CLEAN. Where the methods described above assume a Gaussian beam on fixed scales, MSCLEAN instead uses a range of user defined sizes. The beam shapes are determined by convolving the dirty beam with implementation-dependent shapes which are then used simultaneously to CLEAN the image. The scale size which is found to subtract the most flux is then used within that cycle. This is particularly useful for sources such as radio galaxies with extended structure as the diffuse emission will first be removed from the dirty map reducing the residuals on large scales, before working down to the smaller structure on subsequent cycles.

The final deconvolution method used within this thesis is the maximum entropy method. In contrast to CLEANing, the MEM works in the image plane and attempts to produce the smoothest possible positive image with the minimum possible pixel range compared to some *a priori* knowledge of the source structure (e.g. a shallow CLEANed map). This typically produce highly smooth images and has had success in deconvolving extended radio emission, but at the sacrifice of small scale structure. Hybrid methods which use both MEM and CLEAN in an attempt to resolve this issue are also possible, and I discuss these further in Chapter 3.

The resolution of an interferometer is given by $\theta \approx \lambda/b$, where b is the distance of the maximum baseline. In this thesis, I shall generally refer to the frequency of a given observation, rather than its wavelength, hence for ease of reference define the resolution in arcseconds to be given by

$$\theta \approx \frac{Ac}{b\nu} \tag{2.1}$$

where ν is the frequency and $A = 180 \times 3600/\pi$ is the conversion factor from radians to arcsecond. I take the cell size to be one fifth of this value, except where matched images are required, in which case the resolution and cell size of the lowest-frequency map is used. All images within this thesis are made in Stokes I (i.e. total intensity) and are CLEANed to convergence using a gain factor of 0.1. I define the other imaging parameters, such as weightings and iterations, where appropriate throughout the thesis. In Chapter 4, I use the scripting capability of CASA to process the large number of images required, using Equation 2.1 to automatically determine the resolution.

2.2.3.5 Self and cross calibration

Even with careful calibration, residual phase errors are likely to remain. If a good signal to noise can be achieved for a given target, self calibration can be undertaken to improve this situation and lower the RMS noise of the radio map. Using a shallow image of the source, a CLEAN component model is produced on which further phase calibrations can be based. A deeper image can then be made with these solutions applied creating an improved model of the target. This process is then repeated until no further improvement is observed.

As the aim of self calibration is to produce an improved model on each cycle, this process can be simplified if a reliable model of a target is already known. This is often the case where multiple observations of the same source in the same frequency range have been taken. These new data can instead be cross calibrated with the existing CLEAN component model to calculate the required solutions. This process is also useful in the calibration of data over multiple array configurations by using a model made at a higher resolution, where the spatial location of the peak flux is well constrained, to calibrate the lower resolution data. However, care must be taken when performing cross-calibration as if the original model is of low quality, these errors will propagate across all of the observations.

Whilst self and cross calibration can prove a powerful tool in improving the dynamic range and overall quality of an image, it is key that the underlying assumptions are met. Along with a

high signal to noise level, a single phase correction over the entire field must also be assumed. As the targets discussed in the following Chapters are bright sources in the centre of the field, one can be confident that these assumptions hold. Self and cross calibration are therefore used extensively throughout this thesis.

2.3 The Broadband Radio Astronomy ToolS (BRATS)

The broad-bandwidth capabilities of next generation telescopes such as the JVLA and LOFAR mean that the spectrum of any given source varies significantly within the bandwidth of any given observation. Detailed spectral analysis taking this variation into account is set to become standard practice when dealing with any new broadband radio observations but, as with any new technology, there is often a lack of software and appropriate methods of analysis to use these new data to their maximum potential. I have therefore developed the Broadband Radio Astronomy ToolS software package (BRATS) to overcome this problem.

As BRATS is available to and in use by the wider astronomical community, this section serves two purposes; to outline the analysis methods used within this thesis and to act as a reference of the software's main functionality for end users.

2.3.1 Overview

Written in C, BRATS is a terminal-based Linux software package which provides a wide range of model fitting, visualization and statistical tools for the analysis of radio maps with good frequency coverage over a large frequency range. This is most often applicable to broadband radio maps where multiple images can be produced within a single pointing, but can also be used for simple analysis of narrowband observations or where a large number of narrowband images are available. The primary function of the software is to provide a set of analysis tools for determining the spectral profile of radio sources, with a particular emphasis on models of spectral ageing (Section 1.3.2). At the time of writing, BRATS has around 30 functions and over 100 individual commands, hence here I provide an overview of only the most commonly used features and their usage. A full list of commands including usage descriptions is available by typing '*help*' in BRATS.

2.3.2 Obtaining BRATS and installation

In order to ensure a smooth roll-out and so that adequate support can be provided, BRATS is currently available directly from the author[1]. A publicly downloadable version is scheduled for release in late spring / early summer of 2014 and will be available at the BRATS website[2] where information on the latest software features can also be obtained.

BRATS has successfully been installed on a range of Linux desktop distributions (Debian, Fedora, Mint), as well as in stand-alone server and cluster environments. The majority of pre-requisites come as standard in most Linux distributions (e.g. a C compiler such as GCC) but is dependent on two non-standard libraries, both of which must first be obtained before installation; PGPLOT[3] and FUNTOOLS[4]. I have generally found that using standard repository tools (e.g. yum or apt-get) to obtain these libraries causes the least compatibility issues and provides the easiest method of installation.

The BRATS tar file should next be extracted (the location here is not important but should be easy to locate), and the Makefile modified to account for the dependencies and the desired install location. Environment variables pointing to the PGPLOT libraries should then be set, for example in a CSH environment

```
setenv LD_LIBRARY_PATH /usr/local/pgplot/
setenv PGPLOT_DIR /usr/local/pgplot/
```

These are required whenever BRATS is run and I therefore recommend entering these variables into a shell profile (e.g. .cshrc). These instructions along with example installation parameters are detailed within the Makefile for ease of reference. Once completed, BRATS can then be installed by running the '*make brats*' command. At this point it is recommended that an alias is made to the BRATS executable, for example in a CSH environment

```
alias brats '/soft/brats/brats'
```

The software should now be installed and can be accessed by typing '*brats*' in a terminal window.

Before analysis of a data set can begin, BRATS also requires two directories to be created. By default, these are assumed to be named *images* and *data* and to be located in the folder from

[1] Jeremy.Harwood@physics.org
[2] http://www.askanastronomer.co.uk/brats
[3] http://www.astro.caltech.edu/%7Etjp/pgplot/
[4] https://www.cfa.harvard.edu/%7Ejohn/funtools/

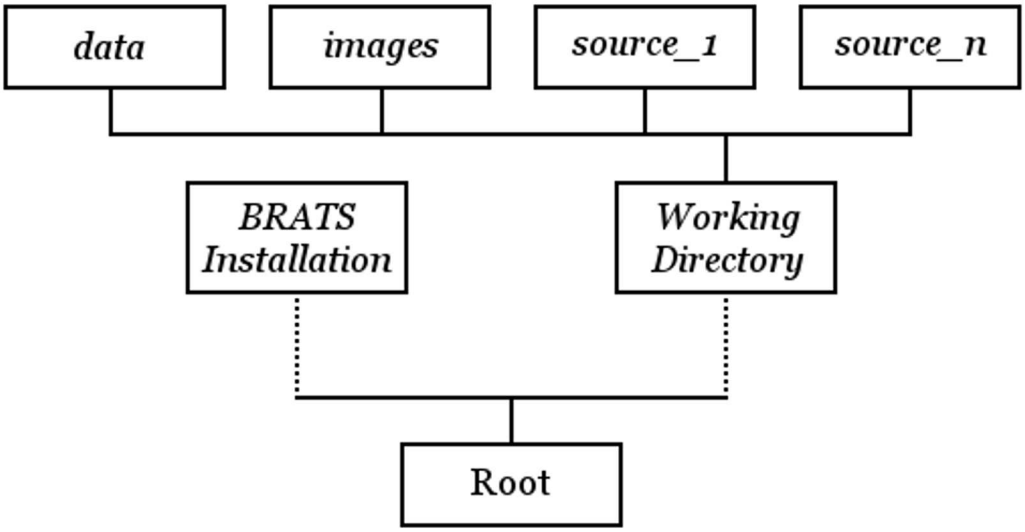

Figure 2.7: Recommended directory structure for BRATS usage. Dotted lines represent the users preferred path, solid lines indicate directories located within the preceding level. Region files should ideally be contained within the working directory. Source directories should contain only the FITS files to be loaded.

which the software was launched (the working directory). It is recommended that the working directory also contains the region files and subfolders containing the radio maps, which I discuss further in the next section. More complex setups can be also be achieved through use of the '*dataloc*' and '*imageloc*' commands. The recommended structure for standard use is shown in Figure 2.7.

2.3.3 Loading data and image requirements

To begin using BRATS a series of FITS images of the source at varying frequencies are required. The software acts independently of the method of reduction of the data but the images must contain compatible FITS headers (currently AIPS or CASA). The radio maps should be at a minimum matched in dimensions, coordinate system and beam size and be well aligned (Section 2.3.3.1). These images should be located in a folder containing only the FITS files that are to be loaded and ideally, easily locatable (e.g. Figure 2.7). Any additional files in this directory will cause a failure of the data to load.

A region file is also required to identify where a value for background RMS noise should be calculated. This file must be in DS9[1] format and WCS coordinates. A second region file is also recommended, loosely encompassing the area in which the target of interest is located. This additional region file is vital where other bright sources are located within the image, but also reduces the computational time required in all images by ignoring the area outside of the defined region. This secondary region may also be used to exclude areas within the source which are not of interest, or that may interfere with later statistical analysis (e.g. AGN cores in analysis of radio galaxy lobes). Background and source region selections can be made using any software capable of saving region files in DS9 format such as DS9 itself or in CASA. Once the data and region files are in place a set of (optional) parameters may be adjusted before loading, such as the sigma cut-off level ('*sigma*').

The radio data are loaded into BRATS by specifying the location of the FITS directory and the region files described above, along with the redshift of the target source to the '*load*' task. When run, the FITS header information is loaded using the FUNTOOLS library to access the image files and checks are undertaken to identify potential problems (e.g. identical map frequencies). The RMS noise of each map is then calculated and the flux values which fall within the defined region (if specified) and above the specified sigma cut-off level are loaded into memory. A flux map of the first image in the array is then displayed to screen as a visual check that the expected data have loaded successfully. If required, this processes can be repeated to load multiple data sets which can be acted on either individually or as a whole by subsequent tasks. Unless otherwise stated, the functions described in the following sections act only on the data stored in memory, leaving the original FITS images unchanged.

2.3.3.1 Image alignment

Highly accurate alignment of the images used is of the utmost importance when fitting spectral ageing models and spectral indices on small spatial scales. If not corrected these positional shifts can lead to the measurement of unrealistic spectra, particularly where a steep flux gradient exists (e.g. at the edge of the source).

In this thesis, I align images based on the position of the AGN core. Defining a region around the core in CASAVIEWER, a Gaussian is fitted using the CASA IMFIT task. The location of the peak is recorded and the process repeated for each radio map. Based on these values, a sensible

[1] http://ds9.si.edu/site/Home.html

central pixel is determined and the required shift calculated for each image. The maps are next loaded into AIPS and the OGEOM task used to make the required corrections. The resulting images are then output and Gaussians again fitted to check the alignment.

2.3.4 Adaptive regions

Once a data set has been loaded, regions which define the source and the area over which subsequent commands will be applied must be set (these should not be confused with the broad regions defined in Section 2.3.3). The spectral analysis of radio sources, particularly in the context of spectral ageing, has traditionally required the use of large spatial regions in order to obtain the required signal to noise levels. With the increased performance of the new generation of radio interferometer and the consequent improvement in image fidelity, it is possible to consider much smaller regions than has previously been viable. In the case of bright sources with good *uv* coverage, it is often possible to consider the source spectra on a pixel by pixel basis; however, for old or poor quality data, one may need to consider larger regions to get the required signal to noise. The '*setregions*' function is therefore used to group pixels in to regions based on a specified set of parameters. These adaptive regions are constrained in two primary ways; signal to noise ratio and maximum search area.

For each pixel for which a region has not yet been defined, and has not been excluded by one of the bad pixel detection techniques (see below), its flux density S_{reg} was compared to a minimum flux density given by

$$S_{reg} \geq R_{SN} \left\{ (J \times S_{RMS}) \sqrt{n_{reg}/a_{beam}} \right\} \tag{2.2}$$

where R_{SN} is a user defined signal to noise ratio, J is the on-source noise multiplier (discussed further in Chapter 3), S_{RMS} is the thermal noise, n_{reg} is the number of pixels currently in a given region and a_{beam} is the primary beam area. If the pixel flux density is below that of the minimum value, an adjacent pixel is added to the region and the test repeated with an increased value of n_{reg}. This process was then repeated adding the closest unused pixel until either the inequality of Equation 2.2 is satisfied, or n_{reg} is greater than a defined maximum search area. In the case that a pixel failed to satisfy these criteria it was marked as bad and was no longer considered in any subsequent analysis.

The adaptive regions function also provides additional bad pixel detection techniques above those of the signal to noise ratio and sigma level detections. In this thesis, I apply the BRATS 'hot' and 'cold' pixel detection function. When a pixel was tested for inclusion within a region

its flux density value was compared with the surrounding pixels. If the tested flux density differs from those surrounding it by a specified multiple more then 50 per cent of the time, or, too many of the surrounding pixels were already marked as bad so the test cannot be performed reliably, the tested pixel was also excluded. It is important that the parameters for this detection method are set so as to only exclude large variations in flux density which are nonphysical and highly likely to be a result of spurious data. I discuss further the criteria which should be met in the context of spectral ageing further in Chapter 3.

2.3.5 Model fitting and parameter determination

The BRATS software provides a number of tools designed specifically for the analysis of spectra and fitting of spectral ageing models to broadband radio data. These range from the fitting of a simple power law as a function of position, through to the much more complex spectral ageing models of Sections 1.3.2.1 and 1.3.2.2. In this Section, I describe the most commonly used fitting functions and those used for the minimization of model parameters.

2.3.5.1 Spectral index mapping

The most straight forward form of analysis that can be performed is the fitting of spectral indices to the observed flux values. BRATS uses a linear least squares regression in log space to determine the spectral index for each region by the equation

$$\alpha_r = \frac{N\sum_{i=0}^{N}(\log\nu_i \log S_{i,r}) - \sum_{i=0}^{N}\log\nu_i \sum_{i=0}^{N}\log S_{i,r}}{N\sum_{i=0}^{N}(\log\nu_i)^2 - \left(\sum_{i=0}^{N}\log\nu_i\right)^2} \tag{2.3}$$

where N is the total number of radio maps, i is the individual map index, r is the region number, ν is the map frequency and S is the region flux.

The results are then plotted as a function of position to form a spectral index map. As well as being a useful analysis tool on their own right, these maps provide a good initial check for the data quality and to identify any potential problems such as alignment issues without the need for use of the more computationally expensive spectral age model fitting. It is in this context that spectral index maps are used within this thesis.

2.3.5.2 Colour-colour plots

An further method of analysis often referred to within this thesis, and also available in BRATS, is the creation of colour-colour plots ('*colourcolour*'). This technique uses two, two-point power laws to describe the spectral curvature of a source over a large frequency range. Measurements are made over various regions of the source and the results compared to the paths expected to be taken by models of spectral ageing. An example of one such a plot created by Stroe et al. (2013) is shown in Figure 2.8. This method of determining spectral age has met with some success (e.g. Katz-Stone et al., 1993; Hardcastle & Looney, 2001); however, its inability to tightly constrain model parameters or easily differentiate between model types has left many open questions. In the next section, I describe the method of direct fitting of spectral ageing models to observations used in this thesis.

2.3.5.3 Spectral age fitting

Currently, 3 models of spectral ageing can be fitted by BRATS; the JP, KP and Tribble models ('*fitjpmodel*', '*fitkpmodel*' and '*fitjptribble*' respectively). In contrast to classical methods of determining spectral age such as the colour-colour plots described in the previous section, BRATS is capable of carrying out the full numerical integrations required to determine the flux values at a given frequency and age. For a user defined magnetic field strength ('*bfield*') and injection index ('*injectindex*'), these model fluxes are then compared to the observations and a χ^2 value calculated to determine the goodness-of-fit (see Section 2.3.6). This process is then repeated over a range of ages and a best fitting spectral age determined for each region within the source.

To determining the model fluxes, the standard synchrotron equations outlined in Section 1.3.1.1 (also see Longair, 2011) are used, where the emissivity of a single electron as a function of frequency is given by

$$J(\nu) = \frac{\sqrt{3}Be^3 \sin\alpha}{8\pi\epsilon_0 c m_e} F(x) \tag{2.4}$$

To reduce computational time, a look-up table of the single-electron synchrotron radiation spectrum values, $F(x)$, is made between $x = 1 \times 10^{-4}$ and 22 at 100 logarithmic intervals. The function $F(x)$ is taken as defined by Rybicki & Lightman (1979) to be

$$F(x) = x \int_x^\infty K_{5/3}(z) dz \tag{2.5}$$

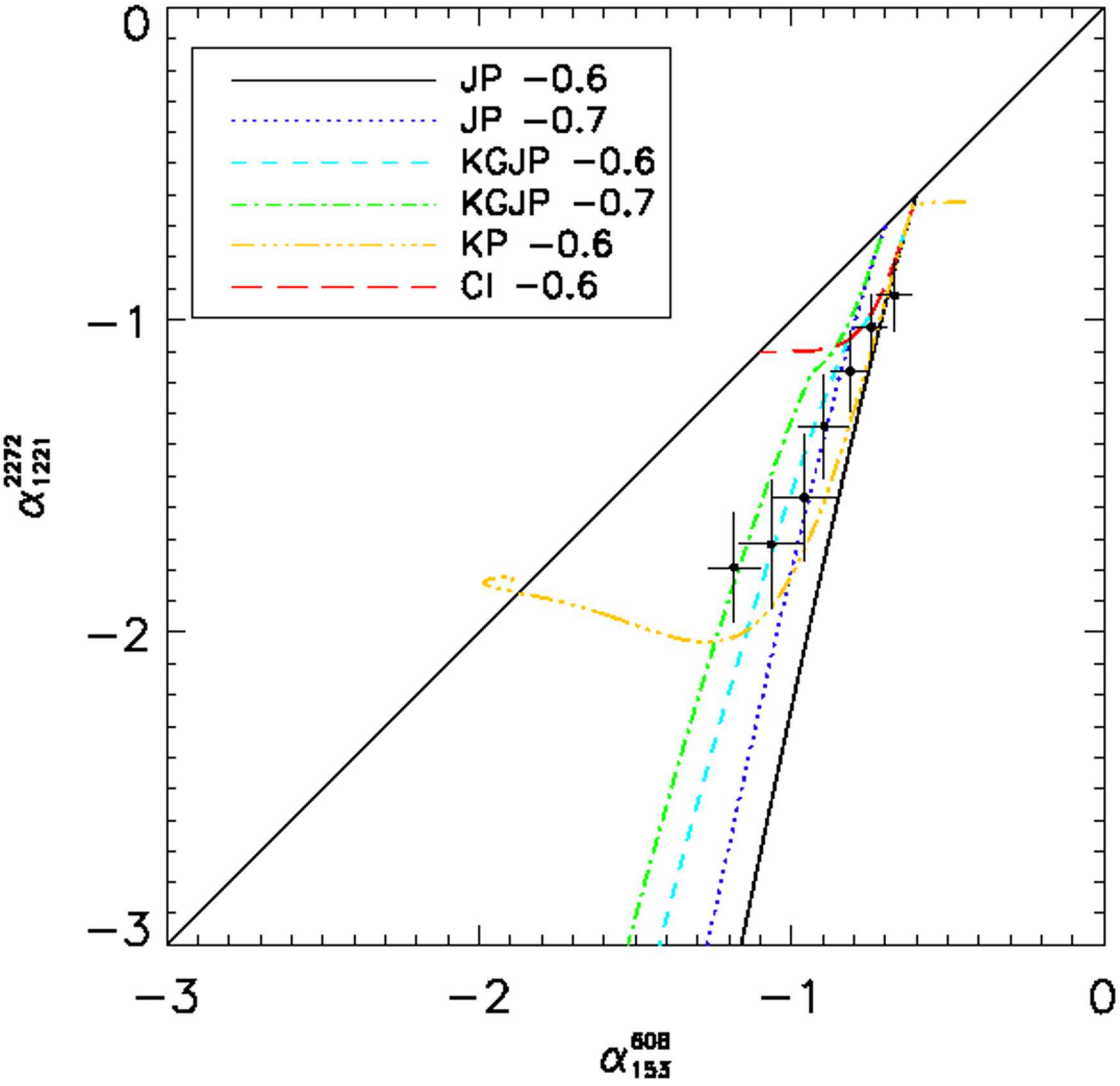

Figure 2.8: Colour-colour plot of the radio relic CIZA J2242.8+5301 by Stroe et al. (2013). Black dots are the data points at various regions downstream of the source. Overlaid are various models of spectral ageing with varying injection indices. 'JP' and 'KP' refer to the models described in Section 1.3.2, 'CI' to the continuous injection model (Pacholczyk, 1970) in which a supply of freshly accelerate electrons are injected to the region of plasma, and 'KGJP' to the hybrid Komissarov-Gubanov model (Komissarov & Gubanov, 1994) in which freshly accelerated electrons are injected to the JP model for a finite time period.

where K is the Bessel function of order $5/3$, $x \equiv \nu/\nu_c$ and $\nu_c = \gamma^2 eB_\perp/2\pi m_e$ is the critical frequency. These points are then used to find any value of x using a log-linear two-point interpolation. For cases where x falls outside of the minimum tabulated range, the asymptote of Pacholczyk (1970)

$$F(x) = 2.15x^{1/3} \tag{2.6}$$

is used and for large values of x it is assumed that $F(x) = 0$. The pitch angles are taken to be isotropic, hence integrating over the probability distribution $(1/2)\sin\alpha$ and between the minimum (E_{min}) and maximum (E_{max}) electron energies the total model emission is found by

$$S_{model}(\nu) = \frac{\sqrt{3}e^3 B}{8\pi\epsilon_0 c m_e} \int_0^\pi \int_{E_{min}}^{E_{max}} F(x)\frac{1}{2}\sin^2\alpha\, n_e(E)\, de\, d\alpha \tag{2.7}$$

where n_e is the electron energy distribution subject to losses given by

$$n_e(E) = N_0 E^{-2\alpha+1}(1-\beta)^{(2\alpha+1)-2} \tag{2.8}$$

and β are the model dependent losses. For the KP model

$$\beta_{KP} = B^2 E t \left(\frac{4\sigma_T \sin\alpha}{6m_e^2\nu_c^3\mu_0}\right) \tag{2.9}$$

is analogous to Equation 1.11 and for the JP model

$$\beta_{JP} = B^2 E t \left(\frac{4\sigma_T}{6m_e^2\nu_c^3\mu_0}\right) \tag{2.10}$$

is analogous to Equation 1.12.

In the case of the free-streaming Tribble model (Section 1.3.2.2), the JP losses are integrated over a Maxwell-Boltzmann distribution (Hardcastle, 2013), hence where B_0 is the mean magnetic field strength of the source Equation 2.7 becomes

$$S_{model}(\nu) = \sqrt{\frac{2}{\pi}}\frac{\sqrt{3}e^3}{8\pi\epsilon_0 c m_e} \int_0^\infty \int_0^\pi \int_{E_{min}}^{E_{max}} F(x)\sin^2\alpha\, n_e(E) \times \frac{B^3 \exp\left(-B^2/2B_0^2\right)}{B_0^3}\, dE\, d\alpha\, dB \tag{2.11}$$

Using the GNU Scientific Library[1] (GSL) for the required numerical integration, unnormalized flux density values are determined between a user defined minimum and maximum age

[1] http://www.gnu.org/software/gsl/

range controlled via the '*myears*' command. These values are then normalized (see below) and a χ^2 statistical test performed using the standard equation

$$\chi^2 = \sum_{\nu=1}^{N} \left(\frac{S_{i,\nu} - S_{model,\nu}}{\Delta S_{i,\nu}} \right)^2 \tag{2.12}$$

where N is the total number of observed frequencies, $S_{i,\nu}$ is the observed flux density of region i at frequency ν, $S_{model,\nu}$ is the model flux and $\Delta S_{i,\nu}$ is the total uncertainty of the observed region given by

$$\Delta S_{i,\nu} = \sqrt{\left\{ (J \times S_{RMS}) \sqrt{n_{reg}/a_{beam}} \right\}^2 + (S_{i,\nu} \times \Delta S_E)^2} \tag{2.13}$$

where ΔS_E is the flux calibration error for a given observation and J is the on-source noise multiplier.

As one cannot be certain that in all cases the spectral age will not contain local minima, a grid search is used to find the best fitting spectral age for each model. In order to obtain a high accuracy, but at a reasonable computing cost, a broad search is first run using large age intervals. This process is then automatically repeated over a series of decreasing age intervals bounded by the best fitting model of the previous cycle until the required accuracy is obtained. These search parameters are controlled by using the '*ageres*' and '*levels*' commands respectively. For each spectral age tested the normalization is determined by a golden ratio search based on the methods of Press et al. (2007). Using this approach over a 2-dimensional grid search vastly improves the speed of the model fitting and allowed accuracy to be achieved to the floating point limit.

As the method described above provides the χ^2 curve of each region as a function of age, the uncertainty in the spectral age can also be calculated. Avni (1976) shows that a 1σ error is given by a deviation of $\Delta\chi^2 = 1$ from the minimum χ^2 value. These errors are therefore calculated during the fitting process and can then be mapped and exported for further analysis using the 'errormap' and 'exportdata' commands respectively.

Once fitting has complete, a range of statistical values (see Section 2.3.6) are output to screen and spectral age mapping becomes available. Using the '*specagemap*' and '*chisquaredmap*' functions, the spectral age and goodness-of-fit values can be plotted as a function of position. An example spectral age map (from simulated data) is shown in Figure 2.9.

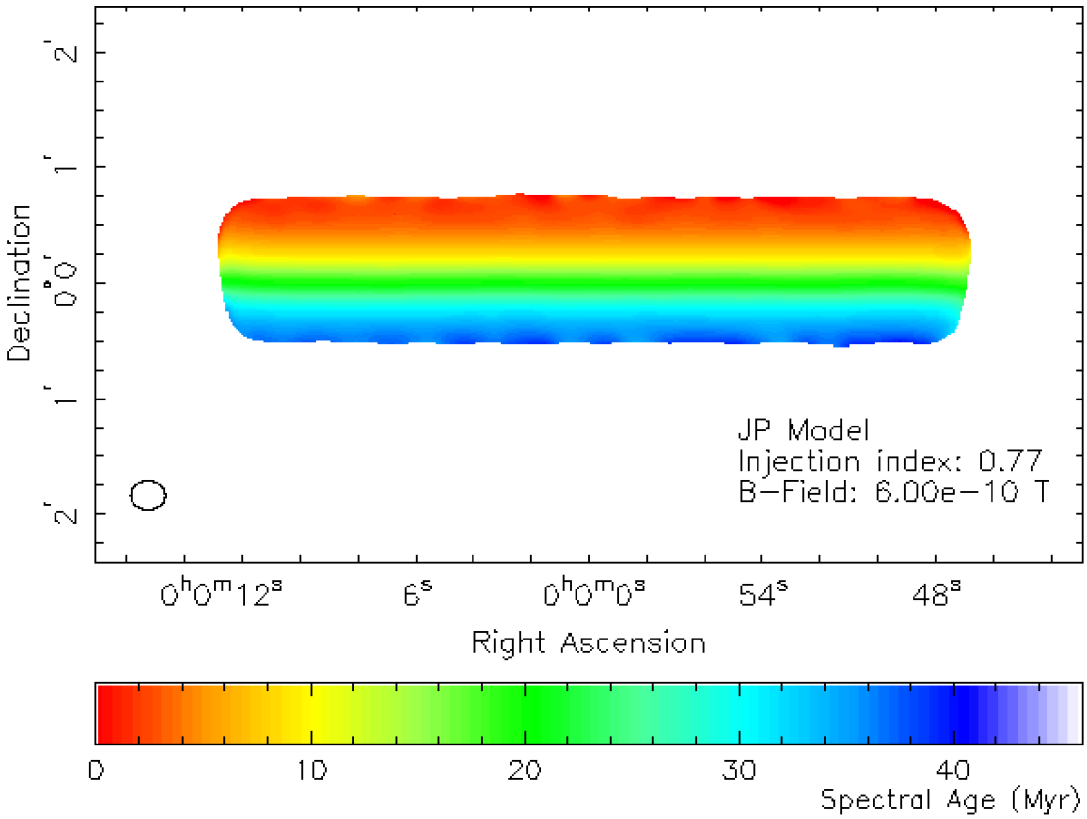

Figure 2.9: Fitting of the JP model of spectral ageing to simulated observations. The simulated data consist of seven images between 153 MHz and 2.27 GHz determined from an ideal JP model with $\alpha_{inj} = 0.77$. Flux values are determined on a pixel by pixel (1 arcsec) basis between 0 and 40 Myrs, then convolved with a 15 arcsec beam. The resulting images were then analyzed with the BRATS '*fitjpmodel*' command to produce the above spectral ageing map, which recovers the input ages well.

2.3.5.4 Injection index determination

BRATS also provides the ability to determine the injection index of a given source through the '*findinject*' command. This function fits models using the methods in the previous section, but in addition also varies the injection index over a range defined by the '*injectmin*', '*injectmax*' and '*injectintervals*' commands. On completion, the sum of the χ^2 over all regions for each injection index can be output via the '*exportdata*' command, allowing a goodness-of-fit curve to be determined as a function of injection index. The minimum of this curve in turn gives the best fitting injection index for a given model and source. As this method of determining the injection index can use all of the observed flux, it is not reliant on measurements made of the relatively small particle acceleration regions, or the assumed location at which this particle acceleration occurs.

The errors for the injection index can be calculated in a similar manner to those described for the spectral ages in Section 2.3.5.3. However, as here one uses the sum of χ^2 over all regions for each injection index, the values are over weighted by a factor of the beam area. Assuming the injection index is approximately constant across any given source, the injection index errors are therefore determined by finding where $\Delta\chi^2 = 1$ for the corrected χ^2 values (χ^2_{cor}) such that

$$\chi^2_{cor} = \frac{\chi^2}{A_{beam}} \tag{2.14}$$

where A_{beam} is the beam area. The use of these methods and their implications are discussed further in Chapters 3 and 4.

2.3.6 Statistics

BRATS provides a number of statistics to aid in the interpretation of the model fitting described in Section 2.3.5.3. The primary measure for an individual fit of a region is given by its χ^2 value (Equation 2.12). Although the plotting of these χ^2 values as a function of position (Section 2.3.5.3) is an important tool in determining the goodness-of-fit for regions within a source and identifying area that are poorly described by a model, additional statistical tests are required to infer the goodness-of-fit of a given model over the source as a whole.

The sum of the χ^2 for an entire source can provide an initial indication of the overall goodness-of-fit; however, regions where there are high χ^2 values for known, non-physical reasons (such as dynamic range effects) can cause the average to be biased toward the rejection of a model. Two additional statistical checks are therefore available to account for this bias. The

χ^2 cumulative distribution function is first calculated at 68, 90, 95 and 99 per cent confidence levels using the computational techniques of Press et al. (2007) and the GNU Scientific Library functions. The χ^2 value of each region is then binned to a given confidence level with a cut-off for the rejection of the region set at ≥ 95 per cent confidence. If more than half of the regions fall above this rejection cut-off, the model over the source is classed as a poor fit and rejected. The median of the individual rejected or non-rejected interval bins is then taken to give a level at which the (non-) rejection is made. For example, if the median of the non-rejected regions falls within the 68 to 90 per cent interval bin, we can say that the model for the source as a whole cannot be rejected at greater than a 90 per cent confidence level. This method of analysis allows the goodness-of-fit to be weighted towards the area over which a model is well or poorly fitted rather than a bias towards high χ^2, but potentially small, regions of poor fit.

2.3.7 Image combination

A useful tool available in BRATS is the ability to easily combine radio maps in the image plane. The '*combineimages*' command first loads images into memory using the same methods as detailed in Section 2.3.3. The flux values are then scaled to a given frequency by a user defined spectral index and the values combined on a pixel by pixel basis. The fluxes are then averaged and the FUNTOOLS library is then used to export a new combined image. It should be noted that the proper alignment of the radio maps (Section 2.3.3.1) is an important factor in ensuring good quality in the resulting image. I use this method of image combination in Chapters 3 and 5.

2.3.8 Image reconstruction and difference maps

The final two features which I discuss in this chapter are the image reconstruction ('*mapfrom-model*') and the difference map ('*diffmap*') functions. For a radio source well described by a spectral ageing model of known age and normalization, it is theoretically possible to produce an image at any given frequency. Once a spectral ageing model has been fitted using the methods of Section 2.3.5.3, the BRATS image reconstruction function can be used to perform such a task. Using the best fitting spectral ages and normalization, BRATS determines the flux values of a given model for any user defined frequency. This is particularly useful for the prediction of source behaviour at previously unobserved frequencies and, as used in this thesis, for comparison to combined or alternative images to determine the model accuracy.

BRATS facilitates such comparisons by providing the difference map function. This task loads two FITS images (these do not have to have been produced or fitted by BRATS) through the standard method detailed in Section 2.3.3. The fluxes of the first map are then subtracted from the second and a FITS image with the residual flux values is output. This is particularly useful in determining how well a 'pure' spectral ageing model describes a source and is used in Chapters 3 and 4 of this thesis.

3

Spectral ageing in the lobes of FR-II radio galaxies

3.1 Introduction

It has long been recognised (e.g. Eilek & Arendt, 1996) that multi-frequency observations for which spectra can be determined over a large number of regions within the source can provide vital advances in determining which, if any, of the current models of spectral ageing (Section 1.3.2) are correct. However, this has largely been limited by the fact that only three or four narrow-band frequencies have been available at GHz wavelengths where the curvature is expected to be most obvious. The historic inability of radio interferometers to produce high sensitivity, high bandwidth observations with good *uv* coverage has meant that many ambiguities exist in the current understanding of radio-loud active galaxies. Indirect methods such as the colour-colour diagrams used by Katz-Stone et al. (1993) and Hardcastle & Looney (2001) have therefore been required to determine the validity of these spectral ageing models. The new generation of radio telescopes currently becoming operational is set to change this situation dramatically. As noted in Section 2.3 the broad-bandwidth capabilities of instruments such as the JVLA mean that the spectrum of any given source can be determined within the bandwidth of any given observation, producing a detailed spectral shape and highlighting any curvature present. In the case of the JVLA, current capabilities allow curvature across the entire C-band (4-8 GHz) to be observed. This type of detailed spectral analysis is set to become standard practice when dealing with any new broadband radio observations; hence it is vital that methods are developed to handle this new type of data.

Table 3.1: List of target sources and galaxy properties

Name	IAU Name	Redshift	5 GHz Core Flux (mJy)	Spectral Index (178 to 750 MHz)	LAS (arcsec)
3C436	J2144+281	0.215	19	0.86	109.1
3C300	J1422+195	0.272	9	0.78	100.9
3C234	J1001+287	0.1848	90	0.86	112

'Name' and 'IAU Name' list the 3C and IAU names of the galaxies as used within this chapter. 'Spectral Index' lists the low frequency spectral index between 178 to 750 MHz and 'LAS' the largest angular size of the source. The 'Redshift', '5 GHz Core Flux', 'Spectral Index' and 'LAS' column values are taken directly from the 3CRR database (Laing et al., 1983) (http://3crr.extragalactic.info/cgi/database). Note that due to correlator issues, 3C234 has an insufficient number of radio maps for a full spectral analysis to be performed.

The improved bandwidth capabilities of instruments such as the JVLA also provide the first opportunity of investigating more complex, but possibly more realistic, spectral ageing models. Both the KP and JP models assume a fixed magnetic field strength throughout the source (Section 1.3.2.1), but this is unlikely to be the case. A model in which an electron population ages within a variable magnetic field was therefore proposed by Tribble (1993) (Section 1.3.2.2). Historically, the small number of narrow-bandwidth frequencies available have not been sufficient to discern between the classical cases and the more complex models proposed by Tribble, but with broadband data now available, we are in a position to investigate the viability of these potentially more realistic models.

Within this Chapter I therefore address two primary aims; I test the new methods of analysis for broad-bandwidth radio data detailed in Section 2.3 and present the results of this analysis for the lobes of FR-II radio galaxies comparing JP, KP and Tribble models of spectral ageing. I go on to discuss the implications of my results in the context of spectral ageing and the dynamics of FR-II radio galaxies as a whole. Section 3.2 gives details of target selection, data reduction and the spectral analysis methods used. In Section 3.3 I present my results and in Section 3.4 I discuss the implications for the current understanding of the dynamics of FR-II radio galaxies.

Table 3.2: Observation Details

Name	JVLA Project ID	Frequencies (GHz)	Target TOS (hrs)	Flux Calibrator	Calibrator TOS (mins)
3C436	AC0138	1.47	6.9	3C48	9.7
	10B-137	4.04, 4.47, 4.92, 5.41	2.0	3C48	2.5
		5.86, 7.21, 7.95	2.0	3C48	2.5
	AR0294	8.47	0.97	3C286	9.5
3C300	AH0179	1.49	0.73	3C286	12.2
	10B-137	4.04, 4.47, 4.92	1.9	3C286	4.3
		5.86, 7.21, 7.94	1.9	3C286	4.3
3C234	10B-137	4.92, 5.86, 7.21	1.9	3C286	4.3
	AR0294	8.42	1.0	3C48	7.7

'Name' list the 3C name of the galaxies as used within this chapter. 'JVLA Project ID' refers to the project identifier as used by the NRAO archive search facility (https://archive.nrao.edu/). Where two identical frequencies are listed for a single source, the data sets have been combined in the *uv* plane during reduction. 'Frequencies' lists the final image frequencies. 'Target TOS' lists the time on source at each frequency (total for all array configurations). 'Calibrator TOS' lists the time on source at each frequency for the corresponding 'Flux Calibrator'. Note that due to correlator issues, 3C234 has an insufficient number of radio maps for a full spectral analysis to be performed.

3.2 Data reduction and spectral analysis

3.2.1 Target selection and observations

I selected targets from the 3CRR sample (Laing, Riley, & Longair, 1983), which contains many well-studied FR-II sources. Previous studies have shown (Alexander & Leahy, 1987; Alexander, 1987; Carilli et al., 1991; Perley, Röser, & Meisenheimer, 1997; Hardcastle & Looney, 2001) that spectral steepening becomes observable at frequencies above a few GHz. The resolution obtained by the JVLA at C-band frequencies (4.0-8.0 GHz) was therefore a natural choice for making the required observations. In choosing my targets it was important that I was confident of seeing all known structure and so the largest angular size (LAS) of my targets must be well sampled by the shortest spacing available at the top of C-band. This restricted me to sources with angular sizes ≤ 180 arcsec. At the same time, I required a reasonably large angular size in order to be able to make well-resolved images with the resolution available at the bottom of the C-band. In order to extend my investigation beyond the C-band range, I restricted myself to $z < 0.3$, since the sources of appropriate angular sizes also have good X-band (8.0 - 8.8 GHz) VLA observations (Leahy et al., 1997; Hardcastle et al., 1997) as well as archival VLA L-band (1.34 - 1.73 GHz) data available. Within this redshift range, there were 6 3CRR sources with $100 < \theta_{LAS} < 180$ arcsec. In order to obtain the best signal to noise ratio the brightest three sources were chosen for observation (Table 3.1).

At the time of proposal the JVLA was still at an intermediate stage of development. In order to simulate the broadband nature of the fully upgraded instrument, observations were made using 128-MHz bandwidth spread logarithmically throughout the whole C-band. In order to ensure both compact and diffuse emission was sampled, observations were obtained in both C and D configurations. Details of the data sets obtained along with the archival VLA data sets used can be found in Table 3.2. Observations at X-band frequencies used data reduced previously by Hardcastle et al. (1997). Unfortunately, due to issues with the JVLA WIDAR correlator at the time of observation, 3C234 has an insufficient number of radio maps available for a full spectral analysis to be performed; however, I include details of these observations and present combined radio map images in Section 3.2.2 for those frequencies which were available, as these still provide the broadest frequency radio maps of the source to date.

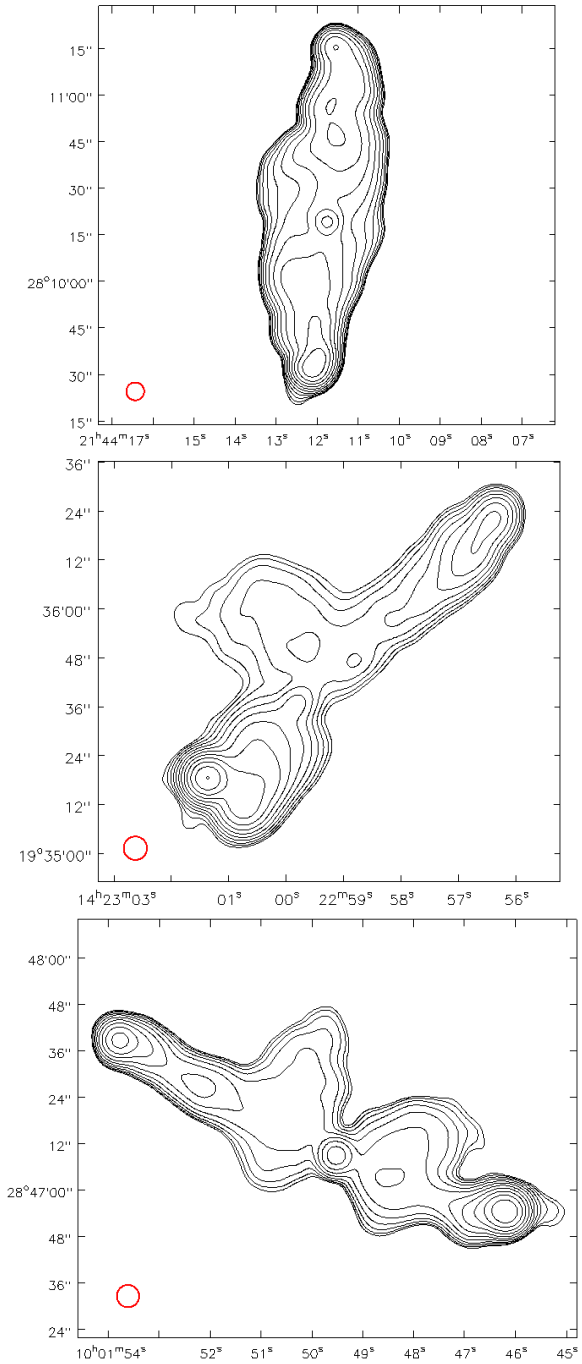

Figure 3.1: Combined frequency radio maps of 3C436 (top), 3C300 (middle) and 3C234 (bottom) between 4 and 8 GHz scaled to 6.0 GHz. The off-source RMS of the combined maps is 27, 33 and 89 μJy beam^{-1} with peak fluxes of 68.5, 280 and 369 mJy beam^{-1} for 3C436, 3C300 and 3C234 respectively. 12 contours are spaced logarithmically between 5σ based on the on-source RMS noise and the peak flux. The restoring beam (red) is indicated in the bottom left corner of each image. 1 arcsecond on the sky represents a physical distance of 3.49 kpc for 3C436 ($z = 0.215$), 4.17 kpc for 3C300 ($z = 0.272$)and 3.11 kpc for 3C234 ($z = 0.185$).

3.2.2 Data Reduction

The C- and D-band configuration data were downloaded from the NRAO archive and reduced using AIPS in the standard manner described in Section 2.2.3.1 accounting for the special considerations for JVLA data calibration in Appendix E of the AIPS cookbook. Before the data were ready for analysis, the C and D configuration observations first had to be combined in the *uv* plane and the final images created. The D configuration data were re-calibrated in phase only using the higher resolution C configuration map as a model. The data sets were then combined in the *uv* plane using the DBCON task. As I require all of the maps to be well matched in terms of both image and beam size, the combined data were imaged to the resolution of the lowest frequency C-band data. A summary of parameters used for imaging is shown in Table 3.3.

The X-band data of Hardcastle et al. (1997) were already pre-calibrated to a high standard; however, regridding to J2000 co-ordinates was required along with re-imaging to match the parameters of Table 3.3. For reduction of the archival VLA L-band observations, standard methods were used as per Section 2.2.3.1. The parameters used in reduction of the C-band observations were applied where appropriate and the array configurations combined in the *uv* plane. Note that B and C configurations were used to allow comparable resolution to be obtained at these longer wavelengths.

Ensuring the radio maps were accurately aligned across all frequencies was of the utmost importance in allowing spectral features as a function of position to be determined. The core and hot spots were therefore used as reference and each frequency aligned using the method described in Section 2.3.3.1 to correct for small deviations in position between maps.

Alignment of the radio maps is always liable to introduce uncertainty to the fitting of spectral ageing models and one must therefore be confident that these effects will be negligible. Fitting Gaussians to the core and hotspots of the aligned maps, I find the standard deviation between maps to be only 0.10 and 0.09 pixels for 3C436 and 3C300 respectively. These effects will therefore only have a significant effect where a sharp change in flux occurs e.g. the edge of the source (also see Section 3.3.2) and in the analysis of fine structure within the lobes. As within this thesis I am primarily concerned with the oldest regions of plasma where flux is approximately constant over many pixels, these errors are negligible compared to the larger uncertainty introduced by, for example, the flux calibration.

Now that of the JVLA upgrade is complete, fully broadband observations will partially resolve this issue (e.g. Chapter 4) as all frequencies within a given band will be taken in a single

Table 3.3: Summary of imaging parameters

Parameter	AIPS Name	Value	Units
Polarization	STOKES	I	
Image Size	IMSIZE	512 512	Pixels
Cell Size	CELLSIZE	0.8 0.8	Arcsec
Weighting	ROBUST	-0.5	
Beam Major Axis	BMAJ	5.75	Arcsec
Beam Minor Axis	BMIN	5.75	Arcsec

'Parameter' refers to the imaging parameter used in making of radio maps within this chapter. 'AIPS Name' refers to the AIPS parameter taking the value stated in the 'Values' column.

pointing; however, it is still be necessary to correct for these errors due to frequency-dependent phase shifts causing offsets and when combining data over more than one frequency band.

3.2.3 Spectral Analysis

In this Chapter, I use the BRATS software for the analysis and fitting of spectral ageing models following the methods detailed in Section 2.3. The radio maps at each frequency were first loaded in to BRATS and, to save on processing time at later stages of analysis, a region fully encompassing the source (but excluding the core) was defined using DS9, along with a background region for determining the off-source thermal noise. Initial source detection was then performed, for which a 5σ cut-off was used based on this RMS value.

The radio maps at each C-band frequency were also combined in BRATS (Section 2.3.7) in order to give the widest bandwidth images of these sources available to date. The integrated fluxes of the source at each frequency were first plotted using the BRATS *'totalflux'* command and a suitable scaling factor between frequencies determined based on a power law model. The flux was taken from the raw data and this scaling factor applied on a pixel by pixel basis to correct to an intermediate frequency of 6 GHz. The flux was then averaged across the number of maps merged and a FITS image produced. The details of the individual maps are given in Table 3.4, with the resultant combined radio maps shown in Figure 3.1.

3.2.3.1 Region selection

Although it has so far been assumed that the off-source RMS is a good approximation to the background noise, it is likely to be the case that the noise on-source is considerably higher due to the increased uncertainty in the modelling of the extended emission. This has implications for both region selection and for statistical testing of models. For all but the lowest flux regions this effect is likely to be negligible with the off-source noise being at least an order of magnitude smaller than the standard 2 per cent flux calibration error for C-band observations with the JVLA. However, the most diffuse, low flux regions should also contain the oldest electron population. To correct for this uncertainty, the flux and spectral index maps were carefully inspected to locate areas of diffuse emission within the source for which one could be confident that flux was approximately constant and free from any significant structure. Two, 2 by 8 pixel long regions were then selected for the northern and southern lobes of each source using DS9 and an RMS of the deviation from the mean flux obtained at 4.4, 5.8 and 7.2 GHz. Dividing each region through by the off-source RMS I find a tight clustering of values ~ 3 times the RMS for both sources. This multiplier was then applied during both the region selection and the the model fitting process through the BRATS '*onsource*' command. Region selection was performed using the BRATS '*setregions*' command using the standard procedure detailed in Section 2.3.4.

Caution is also necessary when selecting the parameters for this method of region selection, which is of particular importance when one wishes to consider each as a potential fit to a spectral ageing model. As models of spectral ageing have multiple free parameters (see Section 2.3.5), the superposition of two JP or KP synchrotron spectra will not always result in the expected spectrum for a simple variation in age. If one considers the extreme case in which a region is defined such that it covers an area over which there is a sharp gradient between a very old spectrum with a high normalization and a young region with a low normalization, the superposition of these two ages will only provide a JP or KP 'like' spectrum rather than the true spectrum which was intended to be observed. This will depend heavily on the frequencies of the observations that have been used in the fitting process and can lead to unreliable ages and inflated χ^2 values for the model fits. In reality, we are nearly always observing the sum of different synchrotron spectra in this way as one is integrating along the line of sight through the source, but it is assumed that these variations will be small enough to be negligible. For the most part, this is also likely to be true of the point to point variations across the length and width of the lobes for most sources; however, it is in general best practice to use the smallest possible regions for the

Table 3.4: Summary of maps by frequency

Source	Frequency (GHz)	Off-source RMS (μJy beam^{-1})	On-source RMS (μJy beam^{-1})
3C436	1.47	247	741
	4.04	141	423
	4.47	78.5	236
	4.92	111	334
	5.41	98.5	295
	5.86	68.1	204
	7.21	63.1	189
	7.95	64.3	193
	8.47	49.9	150
3C300	1.49	266	799
	4.04	107	321
	4.47	67.6	203
	4.92	67.7	203
	5.86	69.7	209
	7.21	79.2	237
	7.94	90.4	271
3C234	4.92	219	657
	5.86	125	375
	7.21	103	309
	8.42	114	342

'Frequency' refers to the frequency of the map listed in the 'Source' column. 'Off-source RMS' refers to RMS noise measured over a large region well away from the source and 'On-source RMS' the noise used for region selection and statistics as per Section 3.2.3.1.

Table 3.5: Summary of adaptive region parameters

Parameter	Value	Units	Description
Signal to noise	1		SNR (pixel to pixel)
Search area	1	Pixels^2	Max. search area
On-source noise	3		On-source noise multiplier
Hot pixel limit	20	Per cent	Max. pixel variation
Map variations	-1		Maximum map variation (off)

'Value' refers to the values applied within BRATS for the corresponding 'Parameter'. The 'Description' column provides further details of the value meaning. Note that a signal to noise of 1 is still subject to the 5σ cutoff and the on-source noise multiplier.

given quality of data available to minimize these effects. It should be noted that although one cannot consider structure on scales smaller than the beam size, each pixel will still be weighted towards the true spectrum at its position, hence by using the smallest regions possible for a given set of observations, the overall reliability of the results in terms of model fitting will be increased. As my observations were planned specifically with these considerations in mind (e.g. good *uv* coverage for high image fidelity) in the analysis that follows I considered each source on a pixel by pixel basis to minimize the risk of the superposition of spectra affecting the results in this way. A summary of the values chosen for this region selection is shown in Table 3.5.

3.2.3.2 Model fitting and parameter determination

In this chapter I have tested two of the most commonly used JP and KP models, along with the more complex Tribble model with free-streaming JP losses as detailed in Section 1.3.2. For both the JP and KP models, I assumed a fixed magnetic field which is in equipartition across the lobes (although see Section 3.4.3 for discussion on the validity of this assumption). I made use of the SYNCH code of Hardcastle, Birkinshaw, & Worrall (1998) and the parameters of Table 3.6 to determine the magnetic field strength for each source. As both the JP and KP models assume an initial electron energy distribution described by a power law, previous attempts to fit such models to observations have assumed an injection index of between ~ 0.5 and 0.7 (Jaffe & Perola, 1973; Carilli et al., 1991; Katz-Stone et al., 1993; Orru et al., 2010). However, whilst this has historically been a reasonable assumption, the improved radio data provided by the JVLA both in terms of both quality and quantity gave us an ideal opportunity to investigate this

Table 3.6: Summary of SYNCH parameters

Source	Parameter	Value	Units	Comments
3C436	Length, Radius	110, 10.5	Arcsec	
3C300	Length, Radius	115, 12.0	Arcsec	
3C436	δ	2.72		$\delta = 2\alpha_{inj} + 1$
3C300	δ	2.64		$\delta = 2\alpha_{inj} + 1$
All	E_{min}	5×10^6	eV	$\gamma \approx 10$
All	E_{max}	1×10^{11}	eV	$\gamma \approx 1 \times 10^6$

'Source' lists the target name for which the listed parameters were applied. 'Parameter' refers to the parameter name where; E_{min} is the minimum energy of the electron distribution; E_{max} is the maximum energy of the electron distribution; 'Length, Radius' are the source dimensions; and δ is the electron energy power law index given by $\delta = (\alpha_{inj}/2) - 1$ where α_{inj} is the injection index of the source determined in Section 3.3.1.

assumption. I therefore use the '*findinject*' command to determine the best fitting injection index for each model and source. A lower limit for the injection index of 0.5 is given by synchrotron theory, therefore both the KP and JP models were initially fitted at intervals of 0.1 between this value and a reasonable upper limit of 1.0. Once the best injection index had been determined at this level of accuracy, the *findinject* command was run for a second time in a range around the minimum value at intervals of 0.01. The resulting values were then plotted and the minimum injection index found.

Once the model parameters had been determined, the final model fitting of the sources was performed. The combination of normalization and spectral age which provided the lowest χ^2 value for each region were recorded. Plots of model against observed flux along with mapping of spectral ages and corresponding χ^2 values as function of position were produced using the BRATS software package. The statistical values detailed in Section 2.3.6 were also recorded to aid in the final analysis of the data.

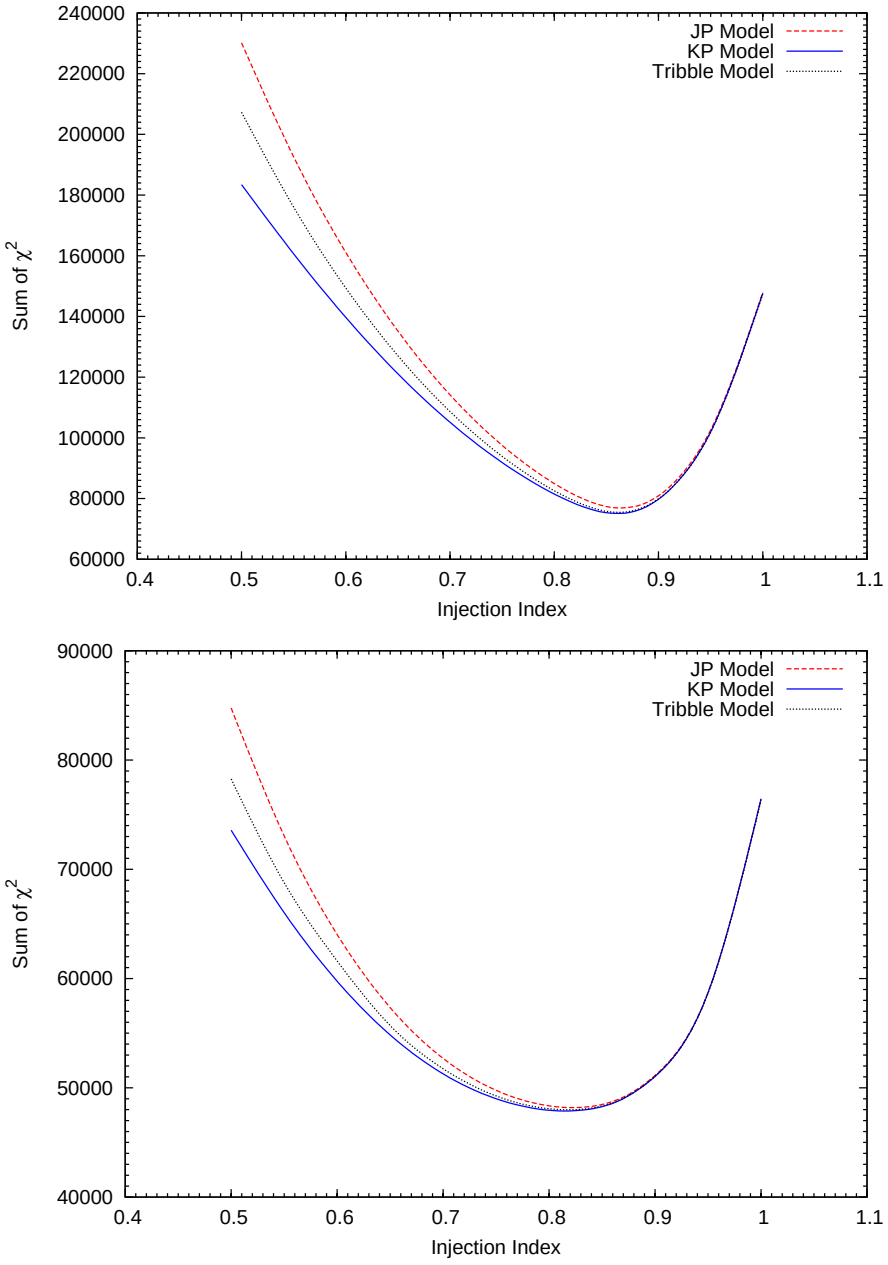

Figure 3.2: χ^2 values for 3C436 (top) and 3C300 (bottom) for varying injection index values fitted with a natural cubic spline. The solid blue line represents the KP model, the red dashed line the JP model and the black dotted line the Tribble model. Data points are taken at intervals of 0.1 between 0.5 and 1.0 inclusive and intervals of 0.01 between 0.8 and 0.92 for 3C436 and between 0.8 and 0.87 for 3C300. As all data points lie on the fitted spline, they are not plotted for clarity. Note that minima occur at 0.86 for 3C436 and at 0.82 for 3C300 for all models.

Table 3.7: Model Fitting Results

Source	α_{inj}	Model	Mean χ^2	Mean χ^2_{red}	Confidence Bins					Rejected	Median
					< 68	68 - 90	90 - 95	95 - 99	≥ 99		Confidence
3C436	0.86	KP	15.64	2.23	1300	1057	437	663	1337	No	< 68
		JP	16.03	2.29	1238	1042	427	674	1413	No	< 68
		Tribble	15.74	2.25	1286	1055	429	670	1354	No	< 68
	0.60	KP	29.21	4.17	472	372	227	567	3156	Yes	> 99
		JP	33.61	4.80	360	313	179	491	3451	Yes	> 99
		Tribble	31.16	4.45	395	347	194	542	3316	Yes	> 99
3C300	0.86	KP	11.65	2.33	1705	724	276	476	931	No	< 68
		JP	11.72	2.34	1705	709	280	462	956	No	< 68
		Tribble	11.67	2.33	1706	719	273	476	938	No	< 68
	0.60	KP	14.55	2.91	1593	728	254	388	1149	No	< 68
		JP	15.58	3.12	1544	748	246	374	1200	No	< 68
		Tribble	14.91	2.98	1574	743	239	375	1181	No	< 68

'Source' lists the target name of the listed results. 'α_{inj}' refers to the injection index used for fitting of the 'Model' column. Mean χ^2 lists the average χ^2 over the entire source with an equivalent reduced value shown in the 'Mean χ^2_{red}' column. 'Confidence Bins' lists the number of regions for which their χ^2 values falls within the stated confidence range. 'Rejected' lists whether the goodness-of-fit to the source as a whole can be rejected as per Section 3.2.3.2 and 'Median Confidence' the confidence level at which the model can or cannot be rejected.

3.3 Results

3.3.1 Model Parameters

The plot of χ^2 values for varying injection indices are shown in Figure 3.2 where one can see that clear minima occur for all models and sources. In the case of 3C436 the JP, KP and Tribble models give an injection index of $0.86^{+0.003}_{-0.002}$ with 3C300 having minima at $0.82^{+0.013}_{-0.005}$ in all cases. It is immediately clear that these represent a much steeper injection index than has previously been assumed[1]; however, given that there is no *a priori* knowledge of the injection indices of FR-IIs at this level of spectral resolution, particularly at the low frequencies at which the power law distribution is assumed to occur, these best-fit values were used for model fitting and the determination of δ for the magnetic field strength as listed in Table 3.6. Fits were also performed using the commonly used injection index of 0.60 to allow comparison. This deviation from the standard assumption of injection index and its implications are discussed further in Section 3.4.2.

Where $\delta = 2\alpha_{inj} + 1$ relates the injection index α to the initial electron energy power law distribution δ, for the best-fitting injection indices I derive values of $\delta_{3C436} = 2.72$ and $\delta_{3C300} = 2.64$ respectively. Assuming equipartition and the parameters of Table 3.6, I find magnetic field strengths of 1.04 nT for 3C436 and 1.10 nT for 3C300. For the commonly assumed $\alpha_{inj} = 0.6$ where $\delta = 2.2$, I derive magnetic fields strengths of 0.648 nT for 3C436 and 0.755 nT for 3C300. These values agree well with commonly assumed values of around 10^{-9} T for lobes of FR-II radio galaxies (e.g. Jaffe & Perola, 1973; Alexander & Leahy, 1987; Alexander, 1987; Carilli et al., 1991; Croston et al., 2005).

3.3.2 Spectral age and model comparison

Figures 3.3 and 3.4 show the spectral age of the two sources and their corresponding χ^2 values as a function of position. One can see that although spectral age does change with distance along the lobe, this variation is not restricted to one axis and many unexpected features are present. Given the complexity and dynamics of these sources this is perhaps not surprising, but this is the first time these variations have been observed in great enough detail to be fully analyzed. The spectral morphology between models only differs by ~ 15 per cent with respect to age with the main spectral features remaining independent of model type. This is also the case for the more

[1] It is interesting to note that in the recent LOFAR study of the nearby FR-I source M87 by de Gasperin et al. (2012), a similar high injection index was observed

commonly used injection index of 0.60. I find that spectral age increases by a factor of around 3, consistent with expectations, but also observe an increase of around 50 per cent in the χ^2 in regions of both diffuse and small scale emission (Table 3.7).

One can see from Figure 3.3 that 3C436 has a spectral morphology close to that of the classical case, with the lowest age regions located close to the hot spots and a general trend of increasing age as one moves towards the galaxy core. However, I note that there is also a non-negligible variation in age across the width of both the northern and southern lobes. For 3C300 this asymmetry is even more pronounced. Not only does one observe age variations across the width of the southern lobe, one also see discrete low age regions spread along the length of the northern lobe (A of Figure 3.5). Comparing their location to features observed on the high resolution maps of Figure 3.12, I find that they coincide with the likely location of the northern jet. In the southern lobe of 3C300, one can also see an extended region with a spectral age of ~ 1 Myr (B of Figure 3.5) well away from the hot spot. This region is likely to be the result of either the relic of an old hot spot, or a fast outflow as noted by Hardcastle et al. (1997). What is clear is that these cross-lobe age variations have implications for previous studies of spectral ageing where cross-lobe variations are assumed to be small. I discuss these points further in Section 3.4.3.

The goodness-of-fit of the models to these sources also provide some interesting results. The χ^2 values for 3C436 of Figure 3.3 and Table 3.7 show that for $\alpha_{inj} = 0.86$, one cannot reject any of the three models for the majority of the central lobe. However, there are also a significant number of regions for which the models do not provide a good fit. The worst fitting regions where $\chi^2_{red} \approx 16$ lie at the very edge of the southern lobe (C of Figure 3.5). I note from the high-resolution map of Figure 3.12 that within these regions an extended area of high intensity and low spectral age is present well away from the location of the classical hot spot. As these regions of high χ^2 are so close to the edge of the source, to the hot spot and to this extended region of high intensity, I suggest that the poor model fits are likely due to edge effects and dynamic range issues resulting in large flux variations. It can be seen from the plot of one of these regions in Figure 3.7 (top left) that the variation is noise like, with such large variations unlikely to be physical in nature. Examples of well-fitted regions for both sources are shown in Figure 3.8 for comparison. Interestingly, Figure 3.3 also shows that an elongated region (D of Figure 3.5) of the southern lobe, which one would expect to be well fitted, instead has a high χ^2 value. Comparing these regions to the high resolution maps of Figure 3.12 one can see a clear correlation between the jet and the poor model fits. This is a somewhat unexpected

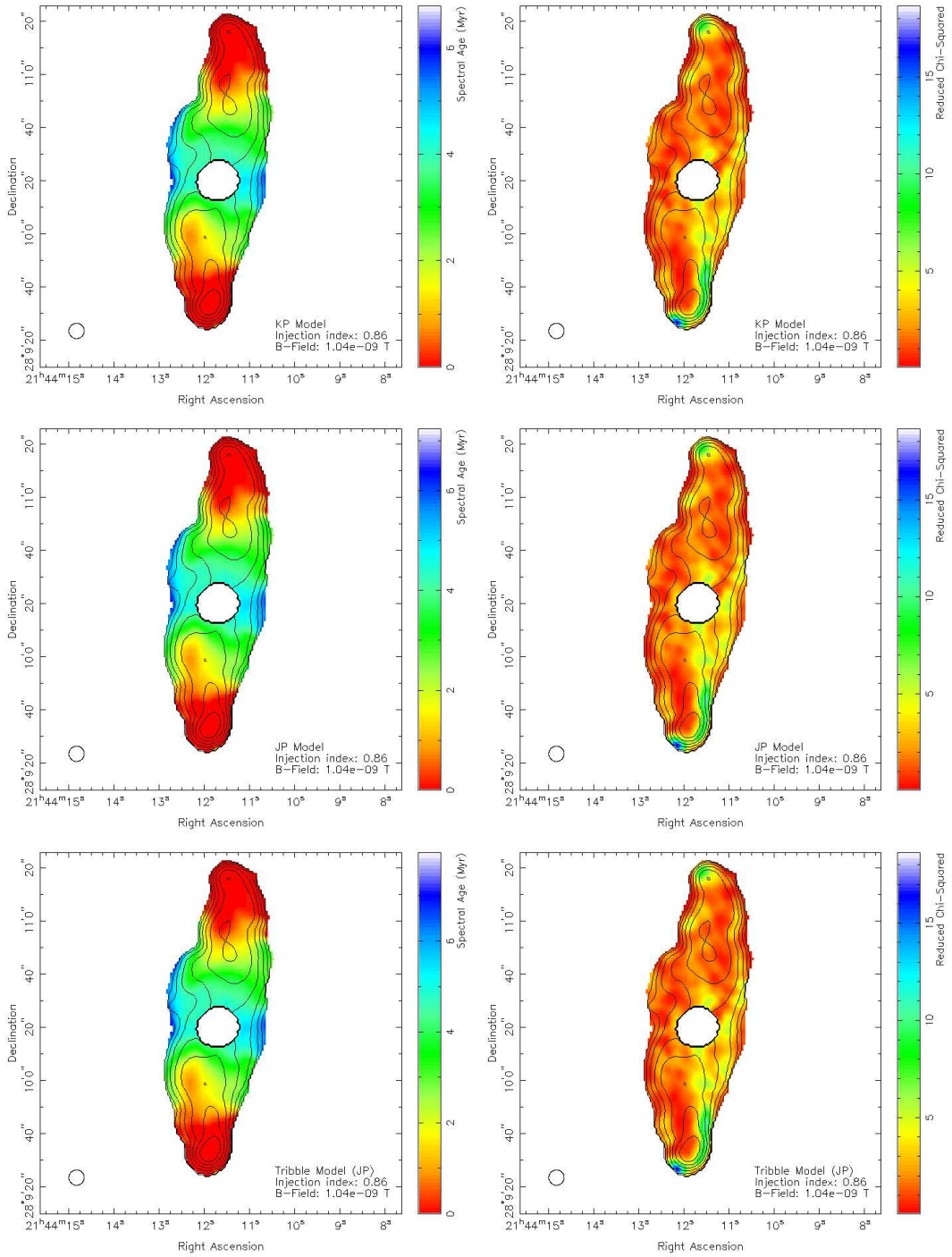

Figure 3.3: Spectral ageing maps (left) and corresponding χ^2 maps (right) of 3C436 with 7.2 GHz flux contours. Three model fits are shown; KP model (top), JP model (middle) and Tribble model (bottom) with injection index 0.86.

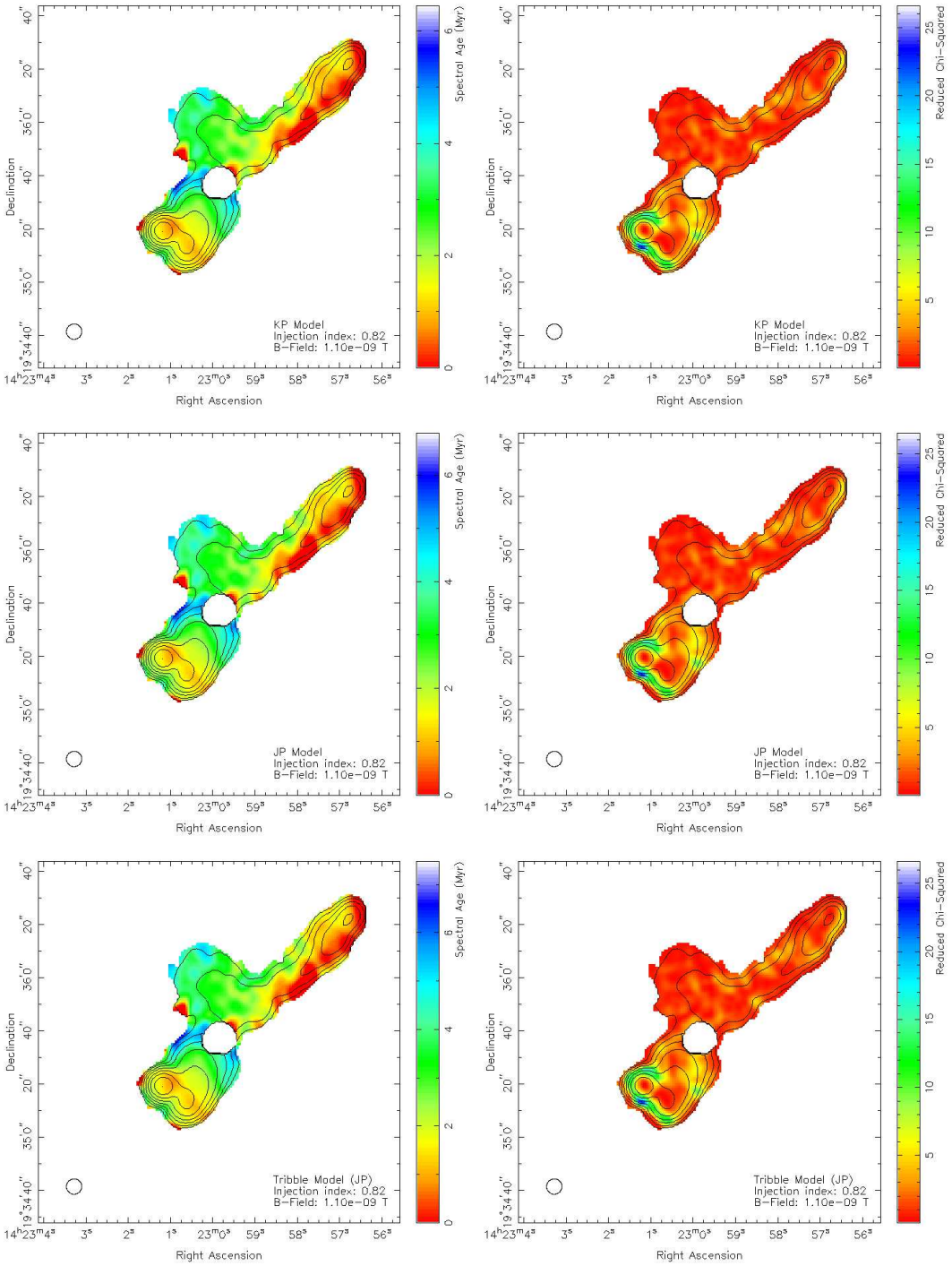

Figure 3.4: Spectral ageing maps (left) and corresponding χ^2 maps (right) of 3C300 with 7.2 GHz flux contours. Three model fits are shown; KP model (top), JP model (middle) and Tribble model (bottom) with injection index 0.82.

result given the resolution at which these observations were made as the jet is barely visible in the individual total intensity maps. The spectral distinction between jet and lobe may provide a means of inferring the location of bright jets in future broadband investigations where high resolution maps are not available.

The χ^2 values for 3C300 of Figure 3.4 and Table 3.7 again provided good model fits for the central regions of the lobes for the best-fitting $\alpha_{inj} = 0.82$, but one can also see many regions where the model fits can be rejected of at least the 95 per cent significance level which must be accounted for. The area around the southern hot spot and along the southern edge of the source where $\chi^2_{red} \approx 15$ are the regions of greatest intensity (Figure 3.1) and it is therefore again likely that these regions are affected by dynamic range issues (e.g. Figure 3.7, middle). I also observe that the more diffuse emission of the southern lobe provides a worse fit than is expected in comparison to the diffuse emission of the northern lobe. Being well separated from the hot spot it is unlikely to be subject to any significant dynamic range effects but the overall source morphology and its location within the lobe does allow for possible orientation effects which are discussed further in Section 3.4.1. Model fits to the diffuse emission which are observed to the side of the source are in good agreement with the models; however, from Figure 3.3 I find an unexpected low age region is present (E of Figure 3.5). Comparing these regions to the high resolution maps of Figure 3.12, I find no corresponding small scale structure which can account for these low ages but note that these are the lowest flux regions of the source. From Figure 3.7 (bottom) which shows the plot of one of these regions, noise-like variations can be seen with large error bars which will tend to push the best-fit to that of a power law. I am therefore likely pushing the limit of image fidelity within this area and so believe that these low age regions are likely not physical in nature.

The error maps shown in Figure 3.6 can also provide insight into the effects of uncertainty on the results presented within this section. For 3C436, the errors are roughly constant across the majority of the source taking values < 0.5 Myrs in both freshly accelerated and aged regions of plasma. 3C300 displays a similar distribution of errors with a fairly constant distribution of age errors. The unexpected low age region discussed previously (E of Figure 3.5) is seen to have very large error bars (~ 2.75 Myrs) giving further support that the limits of image fidelity are being reached within this area. In both sources, an increase in the size of the errors is seen towards the edge of the sources can again most likely be attributed to the edge effects discussed above.

Table 3.8: 3C436 Lobe Advance Speeds

Source	α_{inj}	Model	Lobe	Max Age (Myrs)	$+$	$-$	Distance (kpc)	Speed (v/c)	$+$	$-$
3C436	0.86	KP	North	5.90	0.73	0.60	208	0.168	0.021	0.017
		JP	North	6.30	0.83	0.57	208	0.157	0.021	0.014
		Tribble	North	6.91	0.69	0.52	208	0.144	0.014	0.011
		KP	South	5.90	0.73	0.60	180	0.136	0.018	0.015
		JP	South	6.30	0.83	0.57	180	0.146	0.018	0.012
		Tribble	South	6.91	0.69	0.52	180	0.124	0.012	0.0094
	0.60	KP	North	17.4	3.09	2.40	208	0.0570	0.010	0.0079
		JP	North	16.4	1.06	0.85	208	0.0605	0.0039	0.0031
		Tribble	North	18.2	0.80	1.18	208	0.0545	0.0024	0.0035
		KP	South	17.4	3.09	2.40	180	0.0494	0.0088	0.0068
		JP	South	16.4	1.06	0.85	180	0.0524	0.0034	0.0027
		Tribble	South	18.2	0.80	1.18	180	0.0472	0.0021	0.0031

'Source' lists the target name of the listed results. 'α_{inj}' refers to the injection index used for fitting of the 'Model' column. 'Max Age' is the maximum ages of the corresponding 'Lobe' in Myrs. 'Distance' gives the separation between the oldest age population in the lobe and the hot spot in Kpc.'Speed' lists the derived speed as a fraction of the speed of light as detailed in Section 3.3.3.

Table 3.9: 3C300 Lobe Advance Speeds

Source	α_{inj}	Model	Lobe	Max Age (Myrs)	$+$	$-$	Distance (kpc)	Speed (v/c)	$+$	$-$
3C300	0.82	KP	North	4.50	0.59	0.73	293	0.311	0.041	0.050
		JP	North	5.20	0.67	0.73	293	0.269	0.035	0.038
		Tribble	North	5.60	0.73	0.81	293	0.250	0.033	0.036
		KP	South	5.60	0.84	0.75	140	0.120	0.018	0.016
		JP	South	5.90	0.63	0.72	140	0.114	0.012	0.014
		Tribble	South	6.50	0.69	0.81	140	0.103	0.011	0.013
	0.60	KP	North	10.5	0.98	1.33	293	0.133	0.012	0.017
		JP	North	11.0	0.63	1.15	293	0.127	0.0073	0.013
		Tribble	North	12.8	1.36	1.18	293	0.114	0.012	0.010
		KP	South	13.8	0.92	1.24	140	0.0486	0.0069	0.0063
		JP	South	13.0	1.96	1.78	140	0.0515	0.0036	0.0049
		Tribble	South	14.4	0.95	1.38	140	0.0465	0.0031	0.0045

'Source' lists the target name of the listed results. 'α_{inj}' refers to the injection index used for fitting of the 'Model' column. 'Max Age' is the maximum ages of the corresponding 'Lobe' in Myrs. 'Distance' gives the separation between the oldest age population in the lobe and the hot spot in Kpc.'Speed' lists the derived speed as a fraction of the speed of light as detailed in Section 3.3.3.

An alternate view of these errors can also be taken by considering the fractional, rather than absolute, error values. The roughly even distribution of (absolute) errors over the sources means that the fractional errors in older regions of plasma are much lower than those in regions of freshly accelerated plasma. It is therefore harder to discern between relatively small variations in low age regions. As this chapter is primarily concerned with the total age of the source (i.e. the highest age regions of plasma), this effect is unlikely to impact upon the results presented here. However, any future investigations that wish to investigate age variations in plasma close to the hotspot should carefully consider this effect.

The model fitting using the commonly assumed value of $\alpha_{inj} = 0.60$ fare much worse than those of the best-fitting injection indices. Table 3.7 shows that for 3C436 all models can be rejected through median binning at greater than the 99 per cent confidence level. For 3C300 the model fits cannot be rejected at the 68 per cent confidence level, but I note that this is heavily weighted by the larger northern lobe where the models are well fitted. In the southern lobe I find that all models can be rejected at the 99 per cent confidence level in the vast majority of regions. I note that even in the well fitted northern lobe the χ^2 values are still significantly worse than those where $\alpha_{inj} = 0.82$. It is also interesting to note that from Figure 3.2 as one moves to lower injection index values, the difference in the sum of χ^2 between models increases, making the determination of the best-fitting model much more distinct. This again has implications for both past and future studies of spectral ageing discussed further in Section 3.4.2.

Although the majority of model fits cannot be rejected at any reasonable confidence level, one can see from Table 3.7 that there is a consistency as to which of those tested provides the best description of the source. I find that for both sources and injection indices, the JP model provides a significantly worse fit to the two sources compared to those of the KP and Tribble. The KP model always provides the best fit regardless of injection index, with the Tribble model giving very similar statistical values both in terms of mean χ^2 and median binning by confidence level. Given that the JP model has historically been considered the more physically realistic description of spectral ageing this is perhaps surprising; I discuss this finding further in Section 3.4.4.

3.3.3 Lobe speeds

Assuming an initial acceleration of an electron population in the region of the hot spot which then ages freely over time, one is able to determine a characteristic speed of a given lobe, v_{lobe}, using the spectral age of oldest material and the current distance of the hot spot from the core. Defining a characteristic lobe speed in this way was the method used by two of the largest

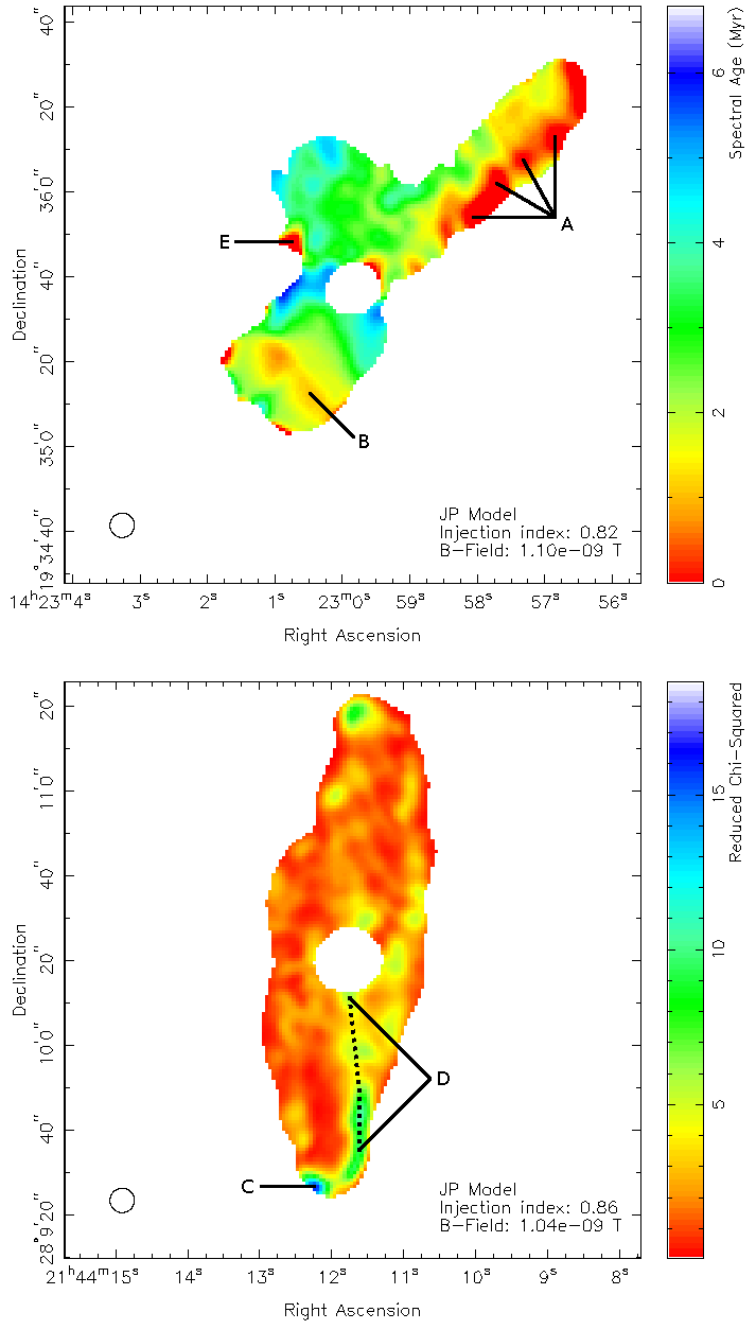

Figure 3.5: Spectral age map of 3C300 (top) and reduced χ^2 map of 3C436 (bottom) for the JP model fitting with a 0.86 injection index. Locations of significant interest are marked as discussed in Section 3.3.2.

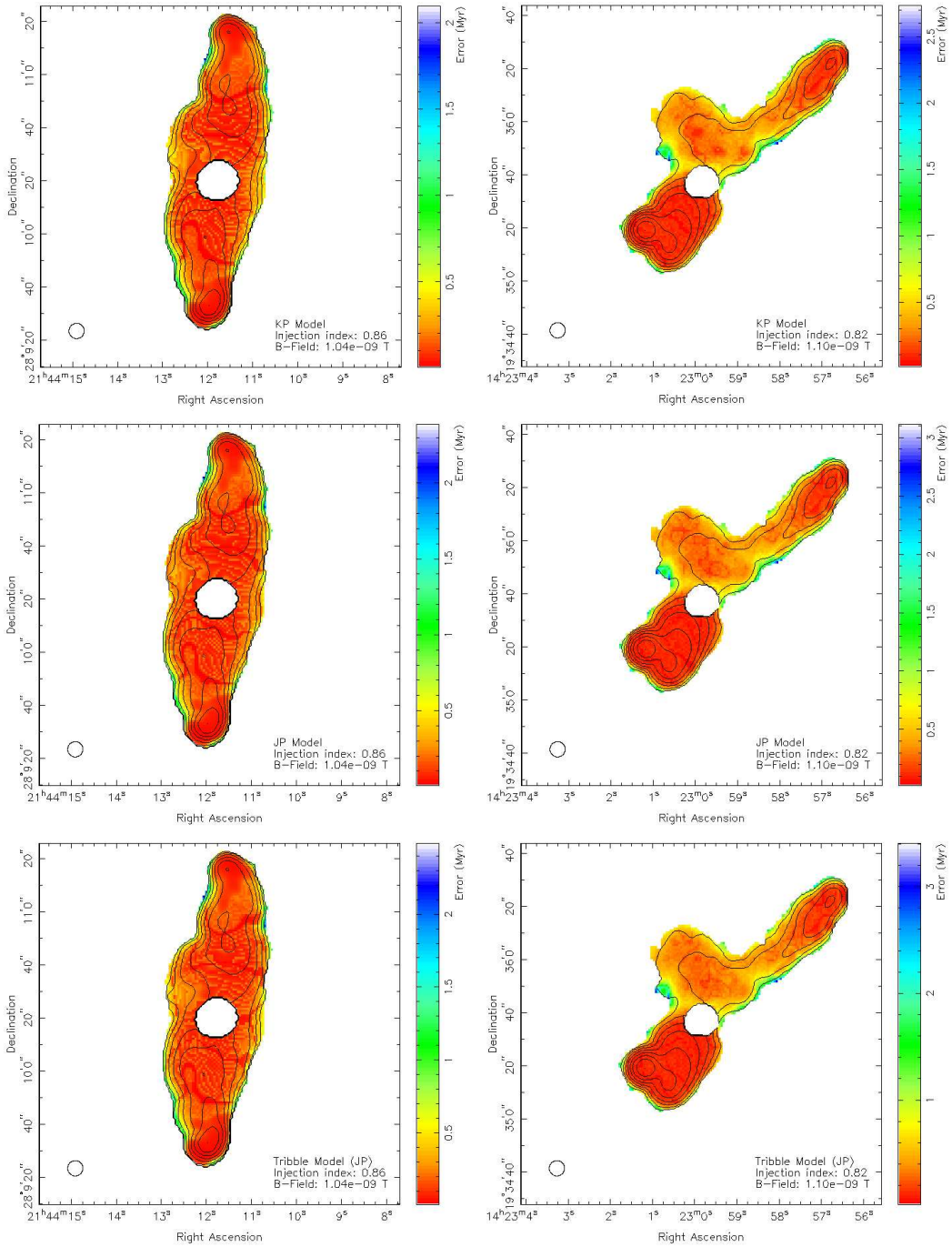

Figure 3.6: Errors for 3C436 (left) and 3C300 (right) for the KP (top), JP (middle) and Tribble (bottom) models of spectral ageing mapped as a function of position with 7.2 GHz flux contours overlaid. Positive error bars for the are shown for each model. Errors are determined using the methods described in Section 2.3.5.3.

spectral ageing samples by Alexander & Leahy (1987) and Liu et al. (1992), allowing a direct comparison to be made between our results and lobe speeds of similar FR-II sources.

From Tables 3.8 and 3.9 it can be seen that for 3C436, the best-fitting injection index provides a lobe speed of between 0.144 (Tribble) and 0.168 c (KP) which are in good agreement with those found by Myers & Spangler (1985) and Liu et al. (1992) for similar FR-II sources. Considering the case where $\alpha_{inj} = 0.6$, I find that due to the increased curvature (hence age) required in fitting the models, the lobe speeds drop considerably to between 0.0545 (Tribble) and 0.0605 c (JP), in line with the work of Alexander & Leahy (1987) who find significantly lower lobe speeds over their sample.

For 3C300, I find the speed of the northern lobe to be much higher than would be expected with values between 0.250 (Tribble) and 0.311 c (KP) in the best-fitting case. Although I find that if $\alpha_{inj} = 0.6$ these values drop to between 0.109 (Tribble) and 0.133 (JP), these speeds are still notably higher than those presented by Alexander & Leahy (1987) where they find for the northern lobe a speed of 0.026 ± 0.045 c. Assuming initial acceleration of the oldest regions of plasma occurred when the hot spot was located near the core, I am also able to derive a lower limit of the drift speed for the emission found in the side lobe of 3C300. Using the Tribble model (which provides the oldest ages) and where $\alpha_{inj} = 0.82$, I find a lower limit for the average speed of 0.113 c. Where $\alpha_{inj} = 0.60$ an average speed of 0.0493 c is required to reach its current location. Whilst quite high, these speeds are not physically implausible. For the southern lobe of 3C300 I find for the best-fitting injection index the lobe advance speeds lie between 0.103 (Tribble) and 0.120 c (KP) while if $\alpha_{inj} = 0.6$, speeds range between 0.0465 (Tribble) and 0.0515 c (JP). The large variation in advance speed between the northern and southern lobes is likely to be due to possible effects of both orientation and jet environment which are discussed further in Sections 3.4.1 and 3.4.3 respectively.

3.3.4 Source reconstruction

In principle, if the spectral age and normalization of a region within a source are known, then the flux of that region can be determined for any given model at any given frequency. Within this chapter, the regions of the source are taken on a pixel by pixel basis; hence, it was possible to reconstruct the source as a whole producing images comparable to the combined radio maps of Figure 3.1. The flux of each pixel at 6 GHz was therefore calculated using the best-fitting model, age and normalization values as determined in Section 3.3.2 for both 3C436 and 3C300. In reality, differences will exist between the image reconstructed from the model and what is

observed in regions where it does not provided an exact description of the source. The reconstructed image was therefore subtracted from the combined frequency images using BRATS to provide a goodness-of-fit map as a function of position and to highlight any large scale correlations which exist. Two images were then produced for each source showing regions where flux has been over- and underestimated, the results of which are shown in Figure 3.9.

I find, as expected, that there are slight variations between the combined frequency maps and those determined through reconstruction of the source for the best fitting KP model. From Figure 3.1 I note that the off-source RMS of the combined frequency maps is 27 and 33 μJy beam^{-1} for 3C436 and 3C300 respectively. Comparing these values to the subtracted images, I find that the model reconstruction agrees well across the majority of both sources but note some distinct regions where flux variation is well above the RMS noise.

For 3C436, I notice that the reconstructed image considerably underestimates the flux at the tips of both the northern and southern lobes. These correspond to the brightest regions of the source, but note from the high resolution images of Figure 3.12 that for the southern lobe, this region may not be the location of the primary hot spot. A similar discrepancy can also be seen in the southern hot spot of 3C300, although in this case the model overestimates the source flux. As discussed in Section 3.3.2, this is unlikely to be due to the high injection indices as the model fits improve within these regions when compared to fits at lower injection indices. It is therefore possible that these bright regions were again subject to dynamic range effects. An underestimate in flux of the reconstructed source is also seen in regions close to the core and in the side lobe of 3C300. These flux differences are much smaller than those found at the tips of the lobes and are found in the oldest regions of plasma. Figures 3.3 and 3.4 show that both of these areas of the source provides a good fit to the model. Bearing in mind that here I am not correcting for the on-source noise described in Section 3.2.3.1, it is likely that these underestimates are due to the large fractional error present in these fainter regions. In the case of 3C300, one can also see an underestimate of flux along the bright southern edge of the source and in regions of the southern lobe close to the core. Comparing the location of these areas to those of Figure 3.4 this is not surprising as they correlate closely to the poor fitting of the model within these regions. This is likely due to possible dynamic range and orientation issues discussed further in Sections 3.4.1 and 3.4.3.

Probably the most interesting result found within these maps are the extended regions of overestimated model flux in the southern lobe of 3C436 and the northern lobe of 3C300. These regions closely correlate with the suspected location of the jets in both the high resolution maps

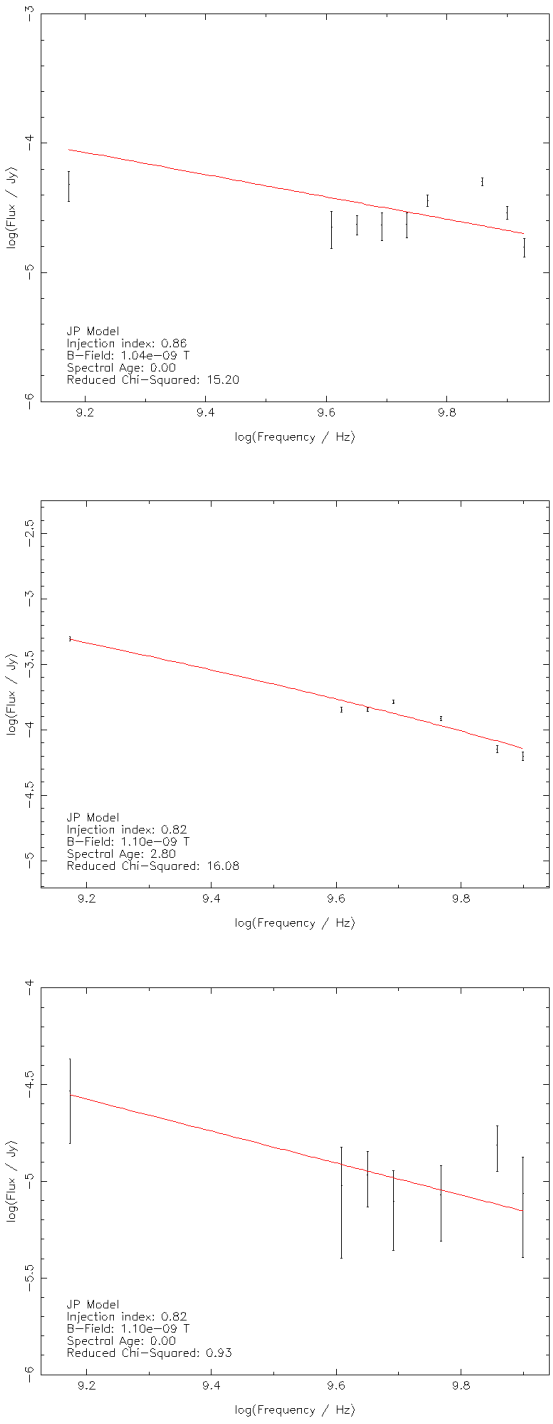

Figure 3.7: Plots of flux against frequency for the high χ^2 regions of 3C436 (top) and 3C300 (middle) and the unexpected low ages region of 3C300 (bottom) as discussed in Section 3.3.2. Red lines indicate the best-fitting JP model with parameters as noted on each plot.

of Figure 3.12. If these are indeed the location of the jets, then it is not surprising that the model does not successfully reproduce the observed flux, as one would not expect the spectral ageing models and the assumptions therein to be valid under such conditions.

Source reconstruction was also performed at 4.47 and 7.21 GHz and subtracted from the individual observations, the results of which are shown in Figures 3.10 and 3.11. 3C436 follows the general trend of the combined map subtraction described above, but note a tendency at both 4.47 and 7.21 GHz for the model to overestimate the observed source flux. In the southern lobe, these are again closely correlated with the suspected location of the jet which may be the cause of this discrepancy. 3C300 is particularly well described at both frequencies by the model, with overestimation of the source flux only observed in the southern hotspot and underestimation limited to small, localized regions of plasma, many of which are associated with the known poorly fitted regions discussed in Section 3.3.2.

The implications of these findings, in conjunction with those of Section 3.3.2 with respect to determining the age, and hence power, of sources, are discussed in detail in Section 3.4.

3.4 Discussion

The dependency of spectral ageing on a number of assumptions (e.g. equipartition) and poorly constrained parameters (e.g. magnetic field strength) have historically called in to question both its reliability as a measure of age (hence power) as well as the validity of the spectral age models as a whole (e.g. Eilek, 1996; Eilek & Arendt, 1996; Blundell & Rawlings, 2001). The results I present within this chapter provide the first opportunity to further investigate previously held assumptions and to constrain some of these parameters to unprecedented levels. In the following sections I discuss these parameters, results and the influence they have on the current understanding of the dynamics of these sources.

3.4.1 Source morphology

So far, I have assumed that the viewing angle of these galaxies is side-on. From the high resolution maps (Figure 3.12) of 3C436, I see that only a one-sided jet is observed from which one can infer that the source must, to at least some degree, be tilted towards the line of sight. However, the symmetry in terms of lobe size and classical double structure suggests that this angle is likely to be small and so the assumption of a side-on viewing angle is probably still a good approximation. The irregular morphology of 3C300 means that this assumption is far less

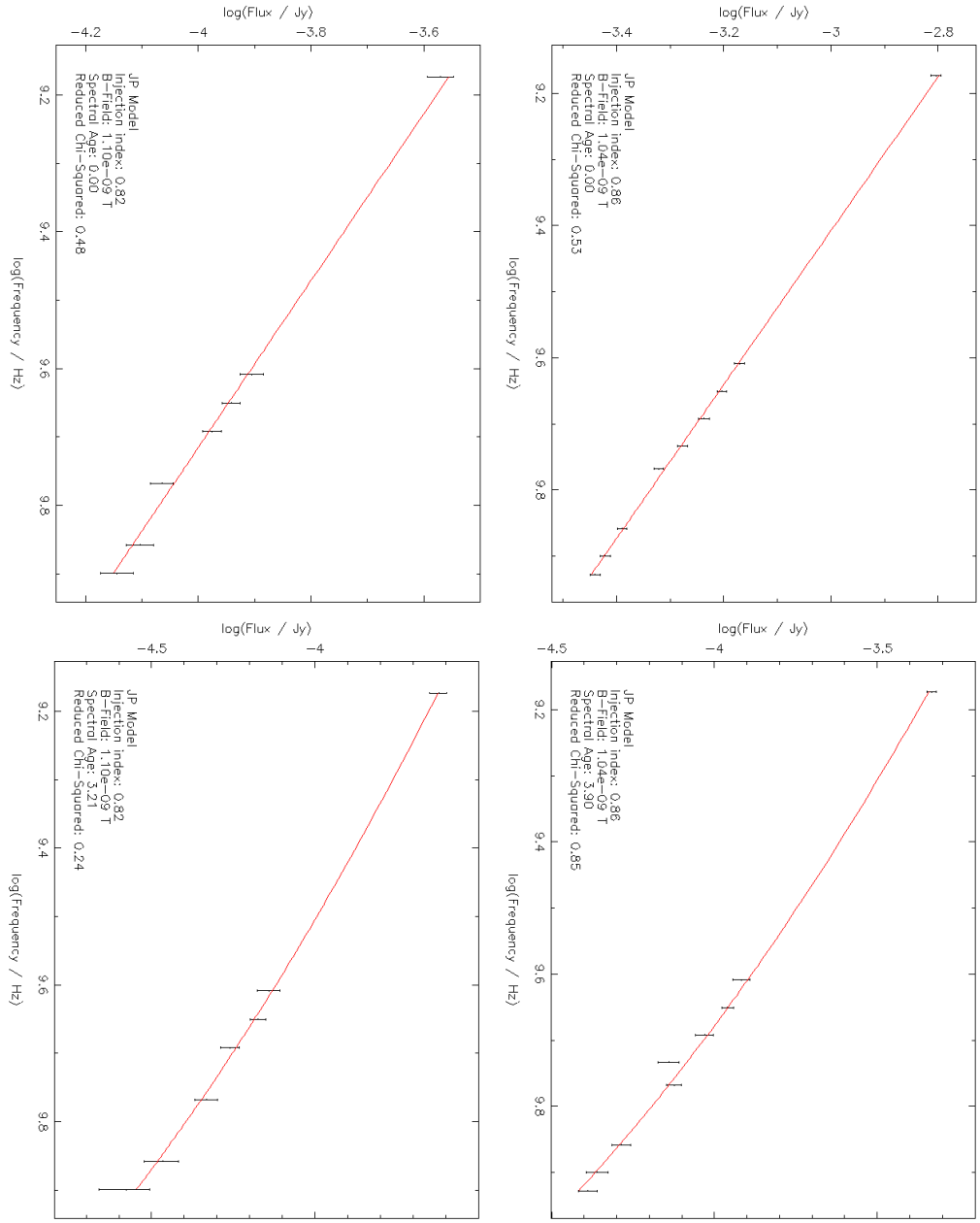

Figure 3.8: Plots of flux against frequency for two well fitted regions of 3C436 (top) and 3C300 (bottom) showing low (left) and high (right) spectral ages. Red lines indicate the best-fitting JP model with parameters as noted on each plot.

clear cut. One can see from Figure 3.1 that the southern lobe of 3C300 is significantly shorter than than that of the northern lobe and contains bright emission away from the hot spot (B of Figure 3.5). One also clearly observe a distinctive region of diffuse emission to the side of the source, which I assume to be associated with the northern lobe.

One strong possibility for this asymmetric morphology is the environment in which the galaxy resides. If the external gas density of the medium through which the jet passes differs significantly between the northern and southern lobes, then one would also expect to observe differing lobe morphologies. If a jet resides in a low density environment, the jet can easily propagate through the medium, hence one would expect an elongated structure as is observed in the northern lobe of 3C300. Conversely, if the external gas density is high one would expect a much shorter, wider lobe to be present. Unfortunately, determining whether 3C300 resides in such an asymmetric environment would require X-ray observations of the surrounding medium; however, the derived jet speeds and spectral ages, discussed further in Section 3.4.3, do provide some indirect evidence that this may be the case.

Although the observations made within this chapter do not allow us to directly determine the cause of this irregular morphology, the possible observable effects must be considered. As mentioned in Section 3.3.2, the poorly fitted regions within the southern edge of the lobe of 3C300 could be a result of the angle of the source to the line of sight. The general assumption for all investigations of spectral analysis of this type is that the point to point age variations along the line of sight will be small enough to be negligible (Section 3.2.3.1). For a classical double such as 3C436 this assumption is likely to hold as one can see from Figure 3.3 that age variations are small for any region size (i.e. one pixel deep) slice across the width of the lobe. Age variations along the line of sight would therefore remain small for any side-on viewing angle. However, if the viewing angle of the source is rotated so that one is looking significantly 'head on', such as may be the case for 3C300, one will observe the effects of non-negligible variation in age that are known to exist along the length of the source. One would therefore encounter the problems of modelling a superposition of ages as outlined in Sections 3.2.3.1 but along the line of sight, rather than along the length or width of the source. In areas such as the hot spot, the observed flux will be dominated by the young, bright emission of a given (small) region with only a minor fraction contribution being made from any aged regions present, so a good fit will still be found. For more diffuse and low flux regions such as the southern edge of 3C300, this will not be the case and the effects of superposition can no longer be ignored. It is also possible that if the source lies significantly away from the plane of the sky, then the

asymmetry between the lobes may be due to light travel time effects. In this scenario, one would observe the southern lobe at a much earlier time than its northern counterpart; hence, it may not yet have evolved in to the extended structure seen in the northern lobe.

The absence of diffuse emission to the side of the southern lobe of 3C300 may also be due to the effects of orientation. If the southern lobe does in fact have a morphology similar to the characteristic L-shape of the northern lobe, but is rotated either towards or away from the line of sight, it would not be immediately evident that such a feature exists. Given the potentially large age variations and size of this region, this emission could add considerably to the superposition of spectra observed, so invalidating the underlying assumption that along any given line of sight, age variations are small. I therefore believe that in the southern lobe of 3C300, both dynamic range effects caused by the extended region of high intensity emission, along with a possible contribution from the observing angle effects mentioned in this section are likely to be the cause of poor fits in the southern lobe, rather than any physical property of the source.

The observed regions of low age (3C300) and poor χ^2 (3C436) which correlate closely to the suspected location of the jets, is an unexpected result at such moderate resolutions and is the first observation that I am aware of such features in FR-II galaxies. As the jet spectra are thought to take the form of a power law (Bridle & Perley, 1984; Treichel et al., 2001) similar to those found in the jets of more extensively studied FR-I jets (Laing et al., 2006, 2008; Laing & Bridle, 2013), it is likely that these regions are a superposition of the aged and jet spectra. In the case of 3C300 the low age regions correlate closely to bright features along the jet, hence, the jet emission is likely to dominate the spectral profile in these areas. In the case of 3C436 the jet is not observed in either flux or spectral age, therefore the regions must still be dominated by the aged plasma at these resolutions. As the flux of the aging spectra decreases faster with increasing frequency than a power law of the jet, this leads to a flattening of the spectral profile at higher frequencies. It is therefore possible for an age to be well fitted at lower frequencies, but increasingly deviate from the model as one increases in frequency, leading to poor χ^2 values (particularly when the spectral age is also low such as is seen in 3C436). In either case, these results provide a possible method for inferring the location of jets where no high resolution images are available. The jet also gives rise to a potentially significant source of cross lobe age variations which should be carefully considered in future investigations.

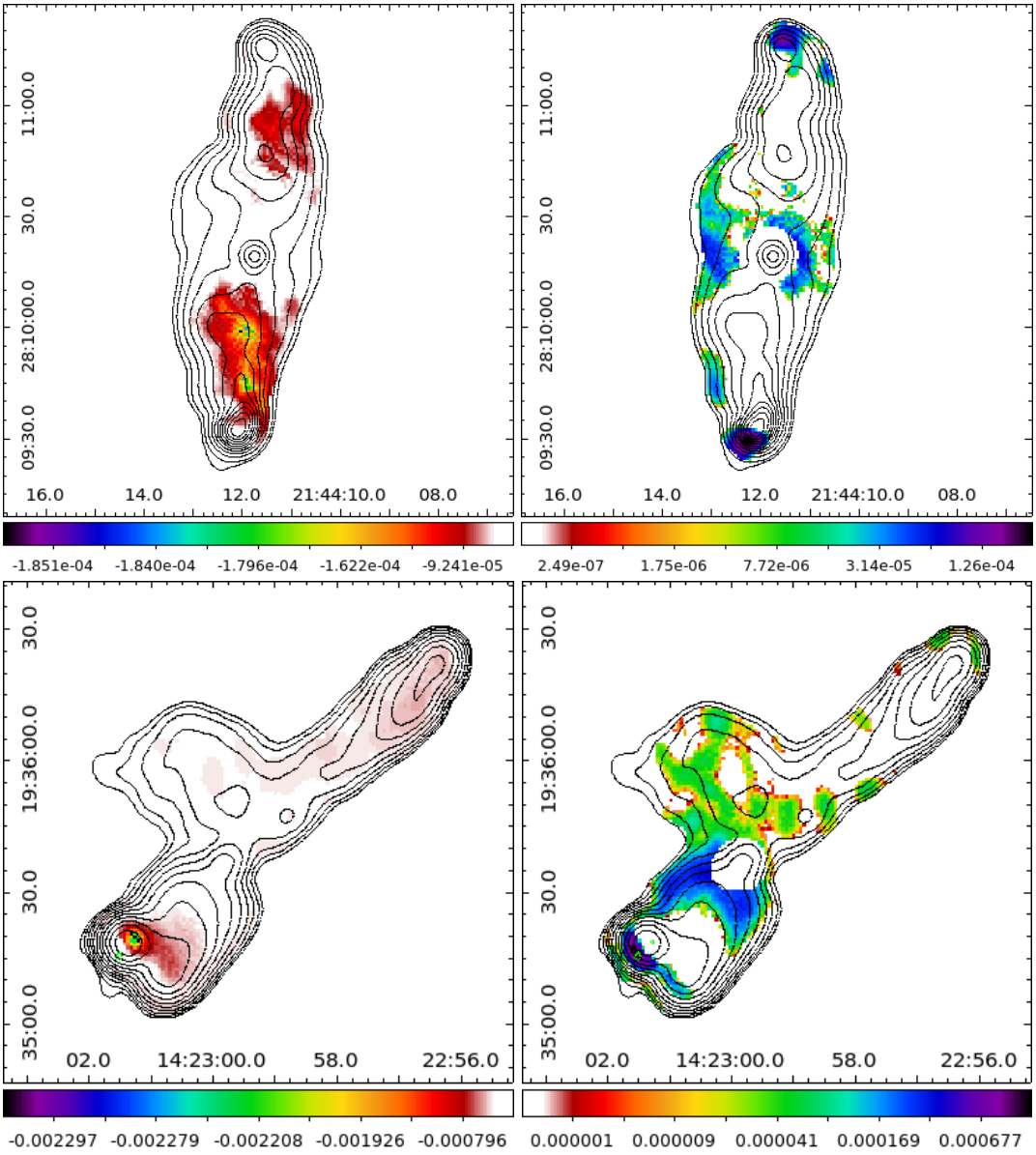

Figure 3.9: Maps of residual flux from the subtraction of the reconstructed model source from the observed source using the combined 6 GHz map described in Section 3.3.4. Model subtracted maps of 3C436 (top) and 3C300 (bottom) showing regions of model flux overestimation (left) and underestimation (right) are shown. Scale is in units of Jy beam^{-1}. Here the KP model has been used in reconstruction of the source using the best fitting spectral ages and normalizations. Maps are limited to the regions used in the model fitting of Sections 3.2.3.2 and 3.3.2. Overlaid are the 6 GHz contours of the combined frequency maps of Figure 3.1.

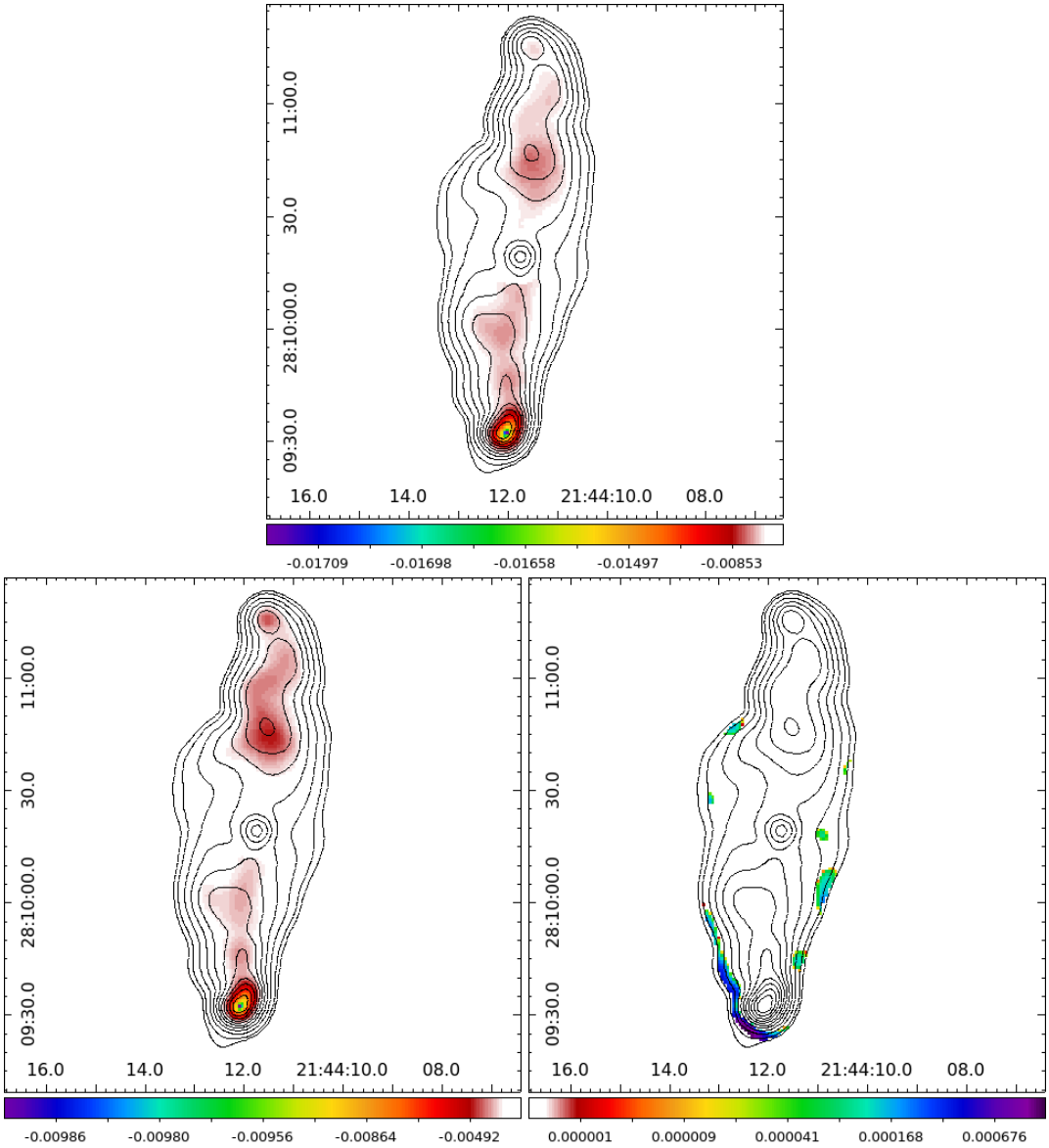

Figure 3.10: Maps of residual flux from the subtraction of the reconstructed model of 3C436 from 2 of the observed frequencies as described in Section 3.3.4. Model subtracted maps at 4.47 GHz (top) and 7.21 GHz (bottom) show regions of overestimation (left) and underestimation (right) of the model flux. Note that there are no underestimated regions at 4.47 GHz. Scale is in units of Jy beam^{-1}. Here the KP model has been used in reconstruction of the source using the best fitting spectral ages and normalizations. Maps are limited to the regions used in the model fitting of Sections 3.2.3.2 and 3.3.2. Overlaid are the 6 GHz contours of the combined frequency maps of Figure 3.1.

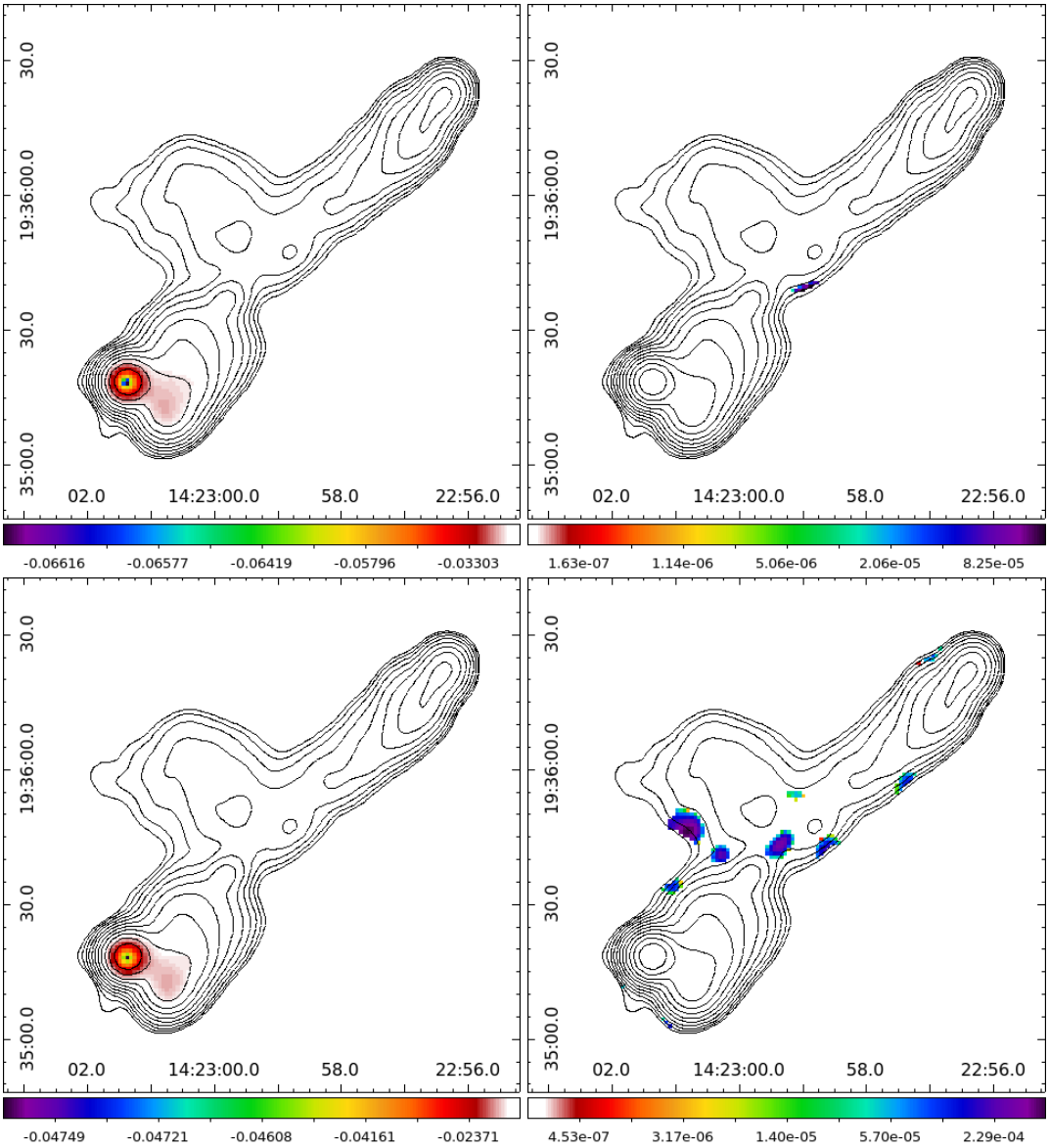

Figure 3.11: Maps of residual flux from the subtraction of the reconstructed model of 3C300 from 2 of the observed frequencies as described in Section 3.3.4. Model subtracted maps at 4.47 GHz (top) and 7.21 GHz (bottom) show regions of model flux overestimation (left) and underestimation (right). Scale is in units of Jy beam^{-1}. Here the KP model has been used in reconstruction of the source using the best fitting spectral ages and normalizations. Maps are limited to the regions used in the model fitting of Sections 3.2.3.2 and 3.3.2. Overlaid are the 6 GHz contours of the combined frequency maps of Figure 3.1.

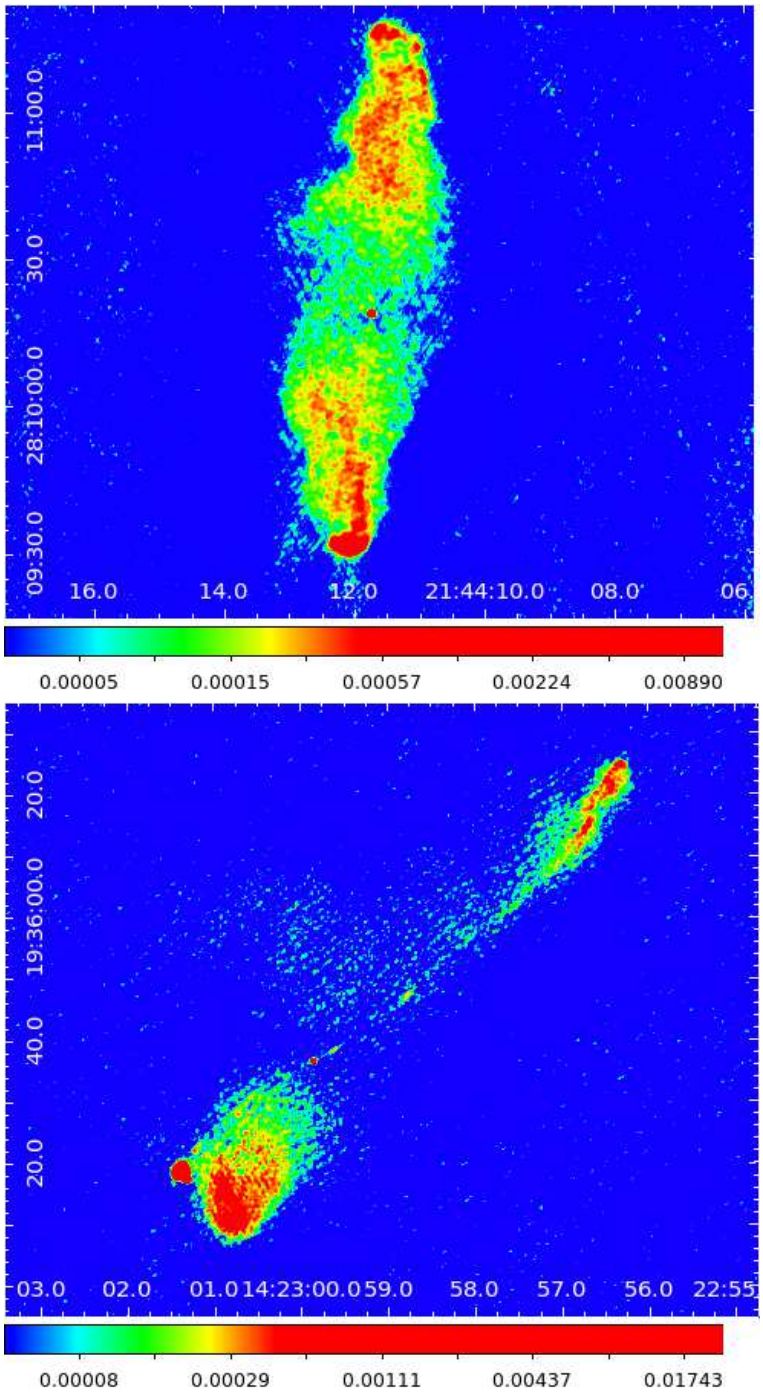

Figure 3.12: High resolution total intensity maps of 3C436 (left) and 3C300 (right) by Hardcastle et al. (1997). The resolution of the maps are 0.75 and 0.50 arcseconds for 3C436 and 3C300 respectively. The flux scale has been adjusted to enhance the bright small scale features and jets described in Section 3.3.2.

3.4.2 Injection index

In determining the spectral age of FR-II sources through the two most commonly used single injection JP and KP models, as well as the more complex Tribble model, a key assumption is made about the initial electron energy distribution and radiative losses. It is assumed that the initial distribution (Equation 1.4), takes the form of a power law of index δ. If one is to assume these models to be correct, then by extension the observable initial spectral energy distribution of these models given by $\alpha_{inj} = 2\delta + 1$, should also take the form of a power law; the so-called injection index. As noted in Section 3.2.3.2, previous studies have assumed the injection index to take values ~ 0.5 to 0.7 (Jaffe & Perola, 1973; Carilli et al., 1991; Katz-Stone et al., 1993; Orru et al., 2010) but it is clear from the results of Section 3.3.1 that these values do not provide the best fits for any of the commonly used models tested within this chapter. It is interesting to note that the study of spectral index at low frequencies by Laing & Peacock (1980) as well as subsequent early studies of spectral ageing based on these works (e.g. Alexander 1987) all find spectral indices at low frequencies of around 0.8 for FR-II sources of a similar redshift. However, given the assumptions and finding of recent investigations, this is a highly unexpected result which could be due to several causes that must be explored if one is to believe such a large discrepancy.

One possibility is that the derived injection indices are being driven to high values through lack of curvature in the models at low-frequencies. If one considers the spectral profiles of the Tribble model and the JP model on which it is based, at very low frequencies (i.e. a few tens of MHz) one can see from Equation 2.7 that for any given age the Tribble model produces a more highly curved spectrum due to the integration of losses over a Maxwell-Boltzmann distribution. One would therefore expect a lower best-fitting injection index value to be found for the Tribble model compared to that of the JP model if the high values were due to a lack of low-frequency curvature, rather than the convergence of all models to a single injection index value within a source. In theory, this can also be reproduced by increasing the age of a given region so a greater low-frequency curvature is present; however, this would also force the model at GHz frequencies to be poorly fitted. As it is already well established that these models can provide a good description of FR-II sources, I find that this is unlikely to be the case.

The low-age regions (particularly those of zero age) also provide insight into the injection index values found within this chapter. These regions are well described by spectra close to that of a power law; hence, if the injection index was somehow being forced by the ageing models

to higher values through a lack of low-frequency curvature, one would expect these regions to still provide the best-fit around the commonly assumed value of 0.6 as they are less heavily influenced by loss effects. From Figure 3.3 and Table 3.7, one can see this is clearly not the case. Across all sources and models, the χ^2 values within these low age regions are better fitted by the higher injection indices. I therefore find it unlikely that a lack of low-frequency curvature in the models is the underlying cause of this unexpected result. It should be noted that this does not preclude a need for increased curvature at low frequencies in providing the best description of spectral ageing as a whole, but it does not appear to be influencing the determination of the initial electron energy distribution.

Probably the most likely cause of such a bias to high injection indices comes from the data itself. The large frequency gap between the archival VLA observations and the higher frequency JVLA observations mean that the 1.4 GHz data hold a higher weighting in the determination of an injection index. I find that when only the JVLA data are considered the best-fitting injection index falls to the more commonly assumed values; however one cannot reject these variations based on selectively excluding data points solely to fit with convention. Historically, spectral ageing has been determined through colour-colour plots (e.g. Katz-Stone et al., 1993; Hardcastle & Looney, 2001), or, through spectral break analysis (e.g. Burch, 1979; Alexander, 1987; Liu et al., 1992; Konar et al., 2006) which suffer from the same frequency space limitations. As these studies are also limited to large spatial regions, injection index values can only be determined reliably in regions of particle acceleration i.e. the hot spots, where ageing effects should be negligible. As I find no valid reason to exclude these low-frequency data points and, within this chapter, I am able to determine the injection index based on many small regions, over multiple sources, fitted to multiple models, all of which converge to a common injection index, I cannot confidently reject these findings. This leaves three plausible solutions to the problem; 1) the injection indices do conform to the assumed values of ~ 0.6 but are forced to higher values by erroneous 1.4 GHz data; 2) the higher injection indices found within this chapter are correct and previous studies are biased towards lower values; or, 3) the models themselves are poorly fitted at low frequencies, resulting in an observed injection index which is higher than the physical reality.

What is clear is that these findings call into question what has previously been held to be a reliable assumption. As I can find no cause of a bias towards higher than expected injection indices, one must consider the possibility that there may be either some physical reality behind these values or that previous studies where a lower injection index has been assumed may also be

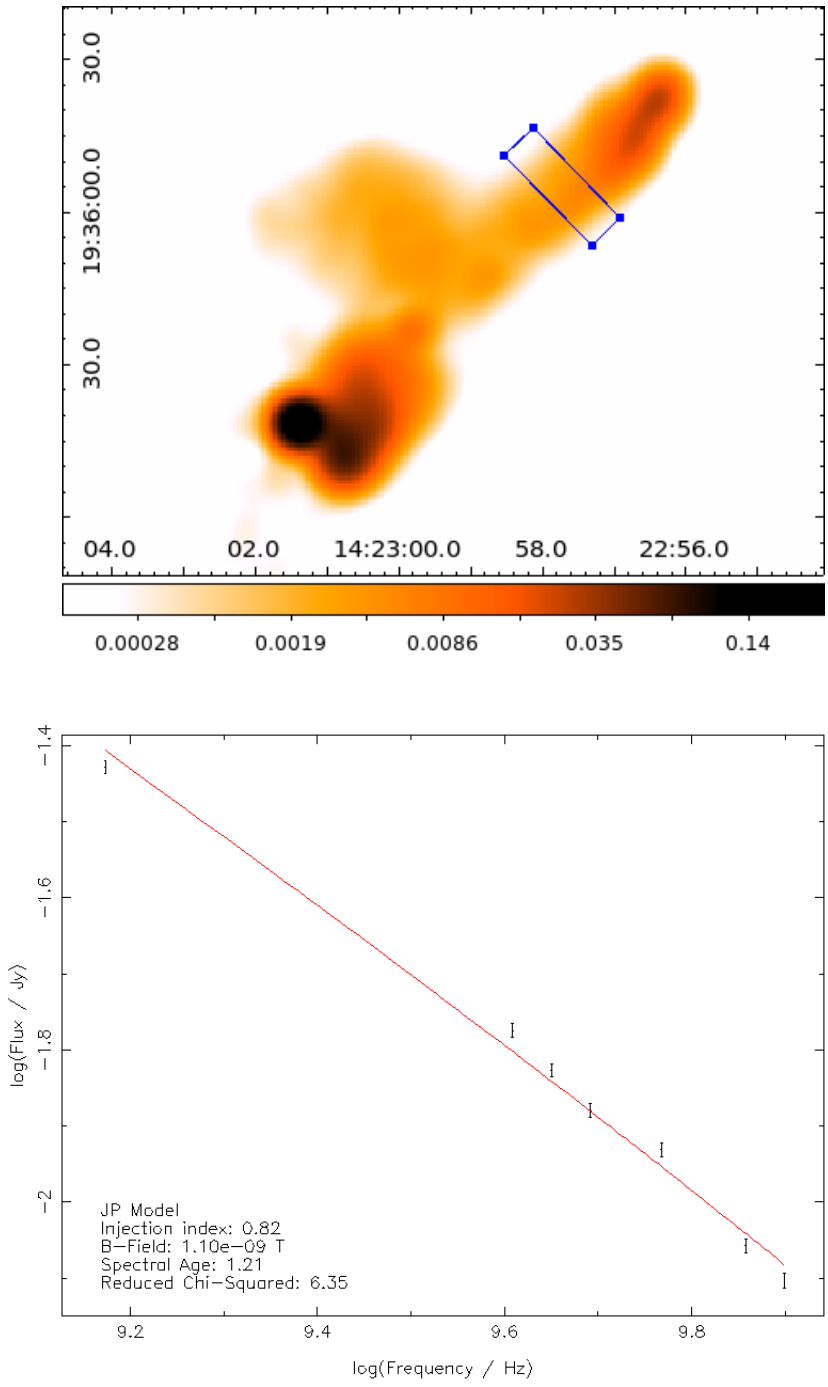

Figure 3.13: Example of how spatially large regions can bias the true spectral age. Top: Combined frequency map of 3C300 at 5 GHz with a single, spatially large region overlaid. Bottom: A plot of the resulting JP model fit and statistics.

subject to this same effects leading to biased statistics in model fitting. One can see from Figure 3.2 that with an injection index of 0.6, there is a large variation in the goodness-of-fit between models but when considering these fits for the best-fitting injection index, they become far less pronounced. Therefore regardless of the underlying reason for the high injection indices, a given model may be favoured over another due to an incorrect assumption, rather than its ability to describe a given source. This is a particular risk when combined with the cross-lobe variations in age discussed in subsequent sections.

Most importantly, this uncertainty in injection index has major consequences in determination of the underlying jet power and dynamics. As the injection index influences the spectral ages both directly through a reduced need for curvature at the oldest ages, and indirectly through the determination of the magnetic field strength, there is also a considerable variation in any derived values. Although I cannot draw any definitive conclusions with respect to the FR-II population as a whole based on such a small sample, finding the cause of this discrepancy is key if one is to determine the validity of spectral ageing models.

3.4.3 Spectral ages and lobe speeds

It has been known since the mid 90's (Eilek, 1996), that spectral ages of both FR-I and FR-II radio sources underestimate the ages as determined from a dynamical view point. Later works such as those by Blundell & Rawlings (2000) suggest that spectral and dynamical ages may be reconciled, but only for sources with ages $\ll 10$ Myrs. Many alternative models such as *in situ* acceleration (Eilek, 1996; Carilli et al., 1991) and magnetic field variations (Katz-Stone et al., 1993; Eilek & Arendt, 1996; Eilek et al., 1997) have therefore been proposed as possible explanations for the observed spectra of these sources. However, as has been discussed by many authors (e.g. Rudnick et al., 1994; Blundell & Rawlings, 2000; Hardcastle & Croston, 2005; Goodger et al., 2008) these methods are still unable to fully account for what is observed. Although previous determination of spectral ages on which these differences are inferred have a good physical basis, they are derived from a somewhat naive view of the source. As the capabilities of the older generation of radio telescopes only allow large regions of the lobe to be considered, often spanning across its entire width (e.g. Alexander & Leahy, 1987; Machalski et al., 2009), a uniform age and normalization across the width of the lobe (or at minimum within the specified region) has to be assumed to avoid the problems associated with the superposition of synchrotron spectra raised in Section 3.2.3.1. It is clear from Figures 3.3 and 3.4 that this is not the case and there will be a non-negligible superposition of electron energy distributions

from electron populations of varying ages. This is especially prevalent in the northern lobe of 3C300 where from the flux maps of Figure 3.1 it is not immediately evident that multiple low age regions exist. If one considers a reasonably large cross section of the lobe as a single region (as has historically been the case), the integrated spectra for a large number of ages are observed ranging between 1 and 3 Myrs. This superposition creates a deviation from the true model spectrum (Section 3.2.3.1), leading to an unreliable measure of the spectral age of the source. Figure 3.13 shows the effects of these large regions when applied to the data in this chapter. It can be clearly seen that when measured in this way, the observed spectral age does not provide an accurate representation of the true spectral age. One also sees that the goodness-of-fit is far worse for the single region when compared to the multiple small regions used within this chapter, as one would expect if this were a result of the issues associated with superposition. A similar, although less pronounced, situation is also present in the lobes of 3C436. In this case although this new form of analysis allows us to see that notable age differences are present across the width of the source, taking large regions based on the flux maps of Figure 3.1 may again cause a superposition of electron populations leading to an unreliable estimate of the age. I therefore strongly suggest that future investigations of spectral ageing should carefully consider spectral morphology of a sample if large regions are to be considered, or preferably, and if the data allow, use small regions such as within this chapter to account for any small scale variations.

I find that the lobe speeds of 3C436 are consistent with those found by Myers & Spangler (1985); Alexander & Leahy (1987) and Liu et al. (1992) for similar FR-II sources which use similar characteristic lobe speeds to those derived within this chapter; however, it initially appears that the northern lobe of 3C300 is advancing much faster than one might expect. As discussed in Section 3.4.1, it is possible that the northern lobe resides in a region of low external gas density, with the southern lobe in a much denser environment. As a shock front moving through a low density medium is able to travel faster than one which is slowed by interaction with a dense external medium, the high advance speed observed in the northern lobe is perhaps not surprising. The complementary low advance speed of the southern lobe and high drift speed of the northern side lobe also provides good support for this dichotomy in environment. It is currently not possible to conclusively deconvolved the effects of orientation, light travel time effects and interaction with the external medium; however, given that well aged regions of plasma (~ 4 Myrs for the KP model) are located are ~ 20 arcsec from the core (as measured along the line of the jet) in both the northern and southern lobes, orientation effects with respect to 'head-on' viewing angle are unlikely to be the cause of such a large difference in lobe length. Combined

with the irregular morphology of the source, I therefore suggest that a difference in external gas density is the most likely cause for both the morphological asymmetry and advance speeds of 3C300.

The advance speeds of FR-II sources can also be considered through arguments of lobe asymmetry. Scheuer (1995) proposes that assuming the brightest jet is observed in the approaching lobe, then for a source which is intrinsically symmetric the ratio of apparent lobe lengths, Q, is related to the viewing angle θ by

$$Q = \frac{(1 + v_a \cos\theta)}{(1 - v_a \cos\theta)} \tag{3.1}$$

where $v_a \equiv v/c$ (β of Scheuer 1995) is the lobe advance speed. From his sample of 43 sources, he finds a typical advance speed of only a few percent the speed of light. This is much slower than either of my sources, but note from Figure 5 of Scheuer (1995) that these values range from between -0.2 and 0.4c, well within the range of my derived values. This form of analysis is only suitable for finding the 'typical' advance speed over a large sample and so cannot be directly applied to individual target sources. This is particularly evident from those considered within this chapter, where the possible non-intrinsic asymmetry of 3C300 makes it immediately unsuitable for this type of analysis, and the inverted lobe asymmetry of 3C436 (i.e. the jet is located in the shorter of the two lobes) means an advance speed cannot be derived reliably in this way. However, their analysis does raise an important issue in determination of advance speeds derived through spectral ageing analysis. Scheuer (1995) suggests that the speeds determined from spectral age could be dominated by the back flow of ageing plasma, rather than the advance of the lobe. If this is the case, the inferred speeds of a source would be much greater than the physical reality.

The possible causes of low ages and fast advance speeds discussed above do not, however, fully account for the difference of up to 10 times the dynamical age found by Eilek (1996). This issue is further complicated by the fact that the high injection indices found within this chapter only serves to increase this discrepancy. The widely used self-similar analytic model of Kaiser & Alexander (1997) which assumes an atmosphere where the density, ρ, decreases as a power law such that

$$\rho_x = \rho_0 \left(\frac{d}{a}\right)^{-\beta} \tag{3.2}$$

where d is the distance from the AGN, a is the scale length and β is the density power law index, can provide a basis for determining the dynamical age of my sources as a test of this discrepancy. Through numerical modelling Hardcastle & Krause (2013) (herein H&K) determine the

range over which the Kaiser & Alexander (1997) lobe length / time relations hold. Under the assumptions laid out by Kaiser & Alexander (1997) that the lobe head advance speed is set by ram pressure balance between the momentum flux of the jet and the external medium (with a power law dependence between density and radius described above) they find that the lobes of sources similar to those studied within this chapter grow as

$$L \sim 2.0 t^{3/(5-3\beta)} \tag{3.3}$$

where L is the lobe length in kpc and t is the ages of the source in Myrs (Figure 3 of H&K and discussion therein). The possible asymmetric environment of 3C300 means that this relation may be unreliable, but for 3C436 one is able to find the dynamical age. Using the model of H&K where $\beta = 0.75$ and considering the northern lobe, I find the dynamical age to be ~ 62 Myrs. This gives to a dynamical advance speed of only $\sim 0.016c$; around one tenth the advance speed derived from the oldest spectral ages of the Tribble model with the best fitting injection index. It should be noted that the average value for β in clusters is ~ 0.6 (Mohr et al., 1999; Sand et al., 2004; Croston et al., 2008b; Newman et al., 2013) and is unlikely to be any greater than the assumed value, hence one can take this to be a lower limit for the advance speed.

One possible solution to the large difference in spectral and dynamical ages lies in the assumptions I have so far made with respect to the magnetic field. Across all models, I have assumed that the field strength is in equipartition, but this may not be the case. X-ray studies by Croston et al. (2005) of FR-II sources find that the strength in the lobes varies between ~ 0.3 and 1.3 B_{eq}, with a peak around 0.7 B_{eq}, hence if the lobe field strength is lower than equipartition, much younger spectral ages will be derived. The spectral break frequency, ν_T, is related to the age of the source, t, by (Hughes, 1991)

$$\nu_T = \frac{(9/4)c_7 B}{(B^2 + B_{CMB}^2)^2 t^2} \tag{3.4}$$

where B is the field strength in the lobe, $B_{CMB} = 0.318(1+z)^2$ nT is the equivalent magnetic field strength for the CMB and $c_7 = 1.12 \times 10^3$ nT^3 Myr^2 GHz is a constant defined by Pacholczyk (1970). Rearranging Equation 3.4 in terms of t and differentiating, one can see that a maximum age occurs when $B = B_{CMB}/\sqrt{3}$, which in the case of 3C436 equates to a field strength of ~ 0.25 B_{eq}; however, even with a magnetic field strength below the lower bound of Croston et al. (2005), the oldest regions of plasma still only rise to ~ 15 Myrs for the best fitting injection indices and ~ 40 Myrs where $\alpha_{inj} = 0.6$. I therefore find it unlikely that magnetic

field strength in isolation can account for the difference between the dynamical and spectral ages, although they potentially play a major role in reconciling these values.

An alternative solution to this disparity in age is that the lobes of these sources are instead best modelled by a continuous supply of newly accelerated particles, rather than through the single injection models used within this thesis. The most widely used model of this continuous injection (CI) is that detailed by Pacholczyk (1970). Within this model it is assumed that a constant supply of particles are injected into the lobes which then subsequently age through standard JP losses. In order to fit this model to observations one must assume that the injected particles are confined to the fitted region; hence only the integrated fluxes can be considered. Consequently, one would expect to observe that a CI model is well-fitted to all lobe spectra since the integrated flux encompasses both aged emission (the lobes) and a source of continuously injected particles (the hotspot). I therefore do not consider fitting of the CI model within this thesis but it is still possible to infer the effect of the CI model from *in situ* particle acceleration, from sources such as turbulence within the lobes, on the measured spectral age. As within these models particles are constantly being accelerated throughout the lobes, the supply of high energy electrons is replenished and the spectra should be observed to be flatter than those given by the single injection models. Higher ages are therefore required to account for the observed curvature, potentially closing the gap between the spectral and dynamic ages, but the physical reality of such a model is not so clear cut. If there is indeed a significant underlying contribution from *in situ* particle acceleration, then as the flux observed from high energy electrons in aged regions of plasma will decreases faster than the power law distribution of newly accelerated particles, one would expect to observe a flattening of the spectrum at high frequencies (~ 90 GHz). However, no such flattening is observed at these short wavelengths (Hardcastle & Looney, 2008) and the data are instead well fitted by a JP model of spectral ageing. As no specific physical process provides a clear means of causing such acceleration in the lobes of such sources, and the only evidence for such a model is the discrepancy itself, I do not favour *in situ* acceleration models.

Irrespective of this age disparity, one feature which is common to all lobes and across all sources is the distinctive transition from low to high ages which are a clear prediction of the single injection model. It therefore appears that spectral ageing does have a physical basis. Whether the dynamical ages are currently being over estimated or the lobes are somehow being kept spectrally young remains an outstanding question; however, it is apparent that determination of intrinsic properties such as jet power will require careful consideration to account for the points raised within this chapter if one is to ultimately determine the dynamics of these sources.

3.4.4 Model comparison

The KP and JP models of spectral ageing have been a longstanding basis for the spectral analysis of the lobes of FR-II radio galaxies. It is therefore not surprising that for the best-fitting injection indices, neither model can be fully rejected based purely on the statistical tests performed within this chapter. However, as noted in Section 3.3.2 there is a clear disparity in which model provides the best description of the source. Across all models and injection indices, the KP model provides a significantly better fit to the observations than the JP model. Previous studies have also shown, most notably Carilli et al. (1991), that this is not an isolated case and may be common in many other sources. Whilst this in itself is not a cause for concern, the time averaged pitch angle of the JP model is a much more physically realistic case than the fine tuning of parameters that would be required to maintain the fixed pitch angle of the KP model. Should one believe the consistently better fitting KP model, or the worse fitting but probably more realistic JP model?

Thankfully, the low-field-strength, high-diffusion Tribble model tested within this chapter may be able to provide the first steps towards answering this question. As this model is based on the original JP electron energy distribution and losses, one is able to maintain the physically realistic case that the JP model provides. The results are also comparable to that of the KP model in all statistical tests undertaken but the Tribble model is more physically realistic. Although I do not suggest that the assumption made by the Tribble model is a highly accurate description of the field throughout the source, I do propose that it is likely to be much closer to the true case than a simple uniform field. The Tribble model therefore appears to bridge the gap between the JP and KP models, providing a basis for determining a more accurate description of the FR-II population as a whole.

3.5 Conclusions

I have presented within this chapter a variety of new methods which are implemented by the BRATS software package for the analysis of the new generations of broadband radio data. Using new JVLA observations along with archival data at GHz frequencies, I have applied these methods to address many of the outstanding issues of spectral ageing in the lobes of FR-II radio galaxies. I have tested two of the most commonly used single injection models of spectral ageing (KP and JP) along with the Tribble model, which attempts to account for magnetic field variations throughout the source. The key points made within this chapter are as follows:

1. I present the first high spectral resolution analysis of spectral ageing in FR-II galaxies. My analysis further supports that spectral ageing has at least some physical basis in reality, although I suggest that classical (JP and KP) models provide a somewhat naive view of the source.

2. Lobe advance speeds agree well with previous studies of similar FR-II sources. I suggest the elongated morphology and fast advance speed of the northern lobe of 3C300 is environmental in nature.

3. Using dynamical models, I confirm the findings of Eilek (1996) that a discrepancy exists between those ages determined spectrally and those determined dynamically. I place an upper limit on this discrepancy of 10 times the spectral age for my sources. I find that although lower magnetic field strengths cannot in isolation fully account for this disparity, they potentially play a major role in reconciling these values.

4. In both sources observed, the KP model provides a better fit than the (more physically realistic) JP model of spectral ageing: However, I find that the model first suggested by Tribble (1993) and subsequently investigated by Hardcastle (2013), provides an equivalent goodness-of-fit to the KP model whilst maintaining the physical reality of the JP model. I therefore suggest that the Tribble model may provide the next step towards accurately describing spectral ageing in the lobes of FR-II galaxies.

5. I strongly suggest that many of the assumptions previously held when undertaking spectral ageing investigation must be viewed with caution and, going forward, methods should be adapted to take in to consideration the finding within this chapter. In particular:

    - The best-fitting injection indices of the JP, KP and Tribble models all converge to 0.86 for 3C436 and 0.82 for 3C300. This is much higher than the commonly assumed values of between 0.5 to 0.7. I discuss possible causes for this variation but suggest further investigations are made at low frequencies in an attempt to determine a reliable range of injection index values.
    - I find that even in the close to ideal case of 3C436, non-negligible age variations are present across the width of the lobe. I show how determining a lobe's spectra based on large regions spread along the length of the lobe (as has historically been the case) can bias model fitting towards low ages and poor fits.

- A non-negligible contribution from the jet of FR-II sources is observed even at moderate resolutions. Whilst this may provide a method of jet location where high resolution maps are not available, this can again result in significant age variations over the width of the source and poor model fits.

In the next chapter, I carry out investigations using truly broadband data in which many more frequency points are available and attempt to constrain many of the findings summarized in this section, particularly discerning between spectral ageing models. Extension of this work to low frequencies is presented in Chapter 5 addressing the issue of low-frequency curvature and the energetics of radio galaxies.

4

Further investigations of spectral ageing at GHz frequencies

4.1 Introduction

The investigations undertaken in Chapter 3 have given the first insights into the spectral structure of FR-II radio galaxies on small spatial scales, and have shown the methods of analysis which allow for the detailed analysis of broad-bandwidth radio observations. However, in doing so it has become apparent that many of the previously held assumptions made in the application of models of spectral ageing are, at least in some cases, less reliable than previously thought. It is therefore important that further sources are investigated to determine if these findings are common to all FR-II galaxies and if the methods developed remain robust when applied to fully broad-bandwidth observations.

In this chapter, I use JVLA observations of an additional FR-II radio galaxy with full C-band frequency coverage to begin answering these questions and address five primary aims. I investigate whether significant cross-lobe variations are likely to be common and if the injection index of the source remains higher than expected when tightly constrained by full bandwidth observations. I investigate whether emission from the jet significantly affects spectral ageing analysis and test whether the Tribble model of spectral ageing provides a similar goodness-of-fit and realism to that discussed in the previous Chapter. In Section 4.2 I give details of target selection, data reduction and the analysis undertaken. Section 4.3 presents my results and in Section 4.4 I discuss these findings in the context of the aims outlined above.

Table 4.1: List of target sources and galaxy properties

Name	IAU Name	Redshift	5 GHz Core Flux (mJy)	Spectral Index (178 to 750 MHz)	LAS (arcsec)
3C438	J2153+377	0.290	7.1	0.88	22.6

'Name' and 'IAU Name' list the 3C and IAU names of the galaxies as used within this chapter. 'Spectral Index' lists the low frequency spectral index between 178 to 750 MHz and 'LAS' the largest angular size of the source. The 'Redshift', '5 GHz Core Flux', 'Spectral Index' and 'LAS' column values are taken directly from the 3CRR database (Laing et al., 1983) (http://3crr.extragalactic.info/cgi/database).

4.2 Data reduction and spectral analysis

4.2.1 Target selection and observations

The method of target selection broadly follows the methods laid out in Chapter 3, using the 3CRR sample (Laing, Riley, & Longair, 1983) of well-studied FR-II sources as reference. As spectral curvature becomes most easily observable above a few GHz, the resolution obtained with the JVLA at C-band frequencies (4.0-8.0 GHz) again made it the natural choice for making the required observations. In order to ensure that the targets are both well sampled by the shortest baselines at the highest C-band frequencies and to ensure a reasonable resolution at the lowest frequencies, I restricted the size of the sources on the sky to $LAS \leq 50$ arcsec at a redshift of $z < 0.5$. In addition to the criteria used in Section 3.2, I also imposed a spectral index cut-off for the integrated spectrum of $\alpha > 0.8$, where 0.8 is the average of the 3CRR sample. This ensures that the physically smaller sources that we will be studying in this chapter are likely to show significant spectral ageing. From the eight remaining sources, I excluded the peculiar source 3C171 and 3C305 where the radio structure plausibly results from strong interaction with cold gas within the host galaxy (Hardcastle et al., 2010), and 4C14.27 which is likely to be a relic system. 17.5 hours of observing time was awarded for 2 of the remaining 5 sources, which I split equally between 3C438 and 3C28.

In order to ensure that all known compact and diffuse emission was sampled, observations were made using the A, B and C array configurations. At the time of observation the maximum bandwidth capability of the JVLA was 2 GHz. I therefore used two 2 GHz observations to give full frequency coverage between 4 and 8 GHz (also see Figure 2.4). In this Chapter, I present the

Table 4.2: Observation Details

Name	JVLA Project ID (Array Config)	Frequencies (GHz)	Target TOS (mins)	Flux Calibrator	Calibrator TOS (mins)
3C438	12B-097 (A)	4 – 8	36	3C48	9
	12A-153 (B)	4 – 8	50	3C48	8
	12A-153 (C)	4 – 8	48	3C48	7

'Name' list the 3C name of the galaxies as used within this chapter. 'JVLA Project ID' refers to the project identifier as used by the NRAO archive search facility (https://archive.nrao.edu/) with the array configurations used given in brackets. 'Frequencies' lists the frequency coverage of the observations. 'Target TOS' lists the time on source at each frequency for each array configuration. 'Calibrator TOS' lists the time on source at each frequency for the corresponding 'Flux Calibrator'.

observations and analysis of 3C438 which was found to have the higher data quality of the two sources, the details of which are given in Tables 4.1 and 4.2. 3C28 will form part of the future investigations detailed in Section 7.6.

4.2.2 Data Reduction

The A, B and C configuration data were downloaded from the NRAO archive and reduced using CASA in the standard manner described in Section 2.2.3.2. As I require multiple images for my analysis rather than just a single broadband data cube each of the 32, 125 MHz spectral windows were individually calibrated and imaged to avoid any bias introduced by, say, the spectral indices used by higher term (e.g. $nterms = 2$) multi-frequency synthesis (MFS) imaging used by CASA. Once reduced, the A-configuration data were self-calibrated and imaged to the resolution of the lowest frequency. Note that in Section 4.3 I exclude the two lowest spectral windows, and hence use the resolution of the lowest frequency used in the analysis, rather than the lowest frequency observed. Once self-calibrated and CLEANed to convergence, the A configuration images were used to cross-calibrate (Section 2.2.3.5) the B-configuration observations. The A and B configurations were then combined and imaged, then in turn used to cross-calibrate the C configuration data. All array configurations were then combined and the final radio maps produced using MSCLEAN. A summary of parameters used for the imaging described in this section is shown in Table 4.3.

Table 4.3: Summary of imaging parameters

Parameter	CASA Name	Value	Units
Polarization	STOKES	I	
Image Size	IMSIZE	4098 4098	Pixels
Cell Size	CELL	0.084 0.084	Arcsec
Weighting	ROBUST	-0.5	
Beam size	RESTORINGBEAM	0.42 0.42	Arcsec
Multiscale	MULTISCALE	[0, 5, 15, 45]	Pixels

'Parameter' refers to the imaging parameter used in making of radio maps within this chapter. 'CASA Name' refers to the CASA parameter taking the value stated in the 'Values' column.

In contrast to the radio maps in Chapter 3, the observations here were taken for each array configuration in a single pointing and are therefore inherently well aligned. However in order to correct for small, sub pixel variations in position, Gaussians were fitted to the radio core using CASAVIEWER. A reference pixel was then decided upon and each map aligned using the methods of Section 2.3.3.1. Fitting Gaussian to the aligned maps in a similar manner to that described in Chapter 3, I find the standard deviation in the alignment between maps to be only 0.007 pixels, and are therefore again unlikely to make any significant contribution to the uncertainty in the fitting of models to the oldest regions of plasma. These images were then copied to the BRATS working directory ready for further analysis.

In order to extend my frequency coverage the combined VLA / MERLIN L-band data presented by Treichel et al. (2001), which are of comparable resolution to the C-band observations, were also obtained. These data were already calibrated to a high standard, hence only regridding to J2000 coordinates, re-imaging to match the parameters of Table 4.3 and alignment in the standard manner was required.

An additional image was also created using the full 4 GHz bandwidth centered at a frequency of 6 GHz. As for this combined data the flux changes significantly over the bandwidth, the data must be suitably scaled in order to produce a realistic image of the source. As any (reasonable) assumption made about this frequency dependence will not bias my analysis, I use the CASA CLEAN parameter $nterms = 2$ which scales the flux by a spectral index value fitted over the observed bandwidth. The resulting image is shown in Figure 4.1.

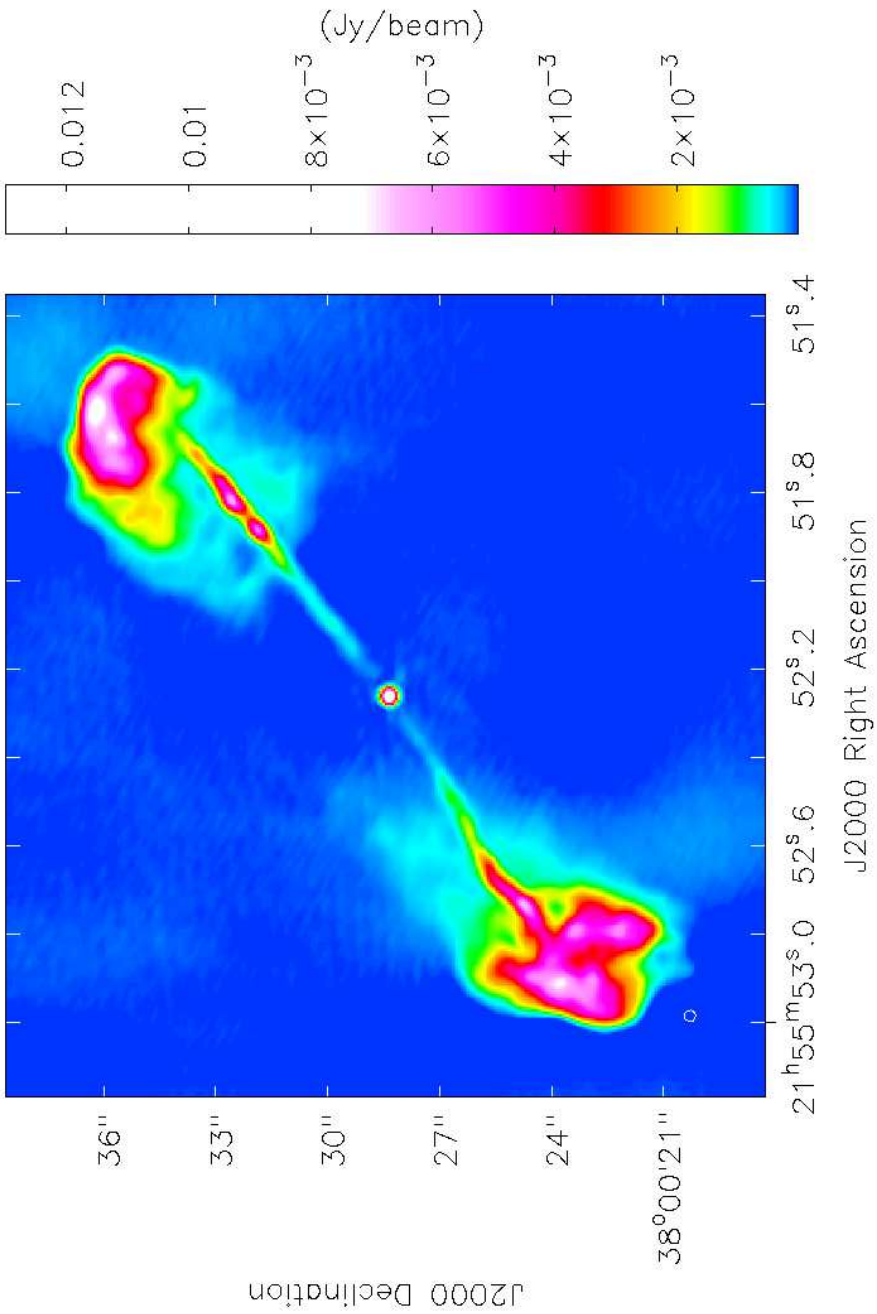

Figure 4.1: Combined A, B and C configuration radio map of 3C438 between 4 and 8 GHz. Imaged using multiscale CLEAN and CASA nterms = 2 to a central frequency of 6 GHz. The off-source RMS of the combined maps is 8μJy beam^{-1}. The restoring beam is indicated in the bottom left corner of the image.

Table 4.4: Summary of maps by frequency

Frequency (GHz)	Off-source RMS (μJy beam^{-1})	On-source RMS (μJy beam^{-1})
1.42	70.6	212
4.33	34.1	102
4.45	33.5	101
4.58	35.6	107
4.71	34.1	102
4.84	33.8	101
4.97	32.1	96.4
5.07	38.8	116
5.20	33.5	100
5.33	32.2	101
5.45	30.9	96.7
5.58	28.8	92.7
5.71	28.7	86.4
5.84	28.7	86.0
5.97	31.6	94.8
6.03	36.0	108
6.29	25.8	77.3
6.54	25.7	77.0
6.67	27.6	82.9
6.80	25.5	77.6
6.93	26.3	79.0
7.03	29.6	88.8
7.16	23.9	71.7
7.29	23.8	71.3
7.41	23.9	71.8
7.54	25.7	77.1
7.67	24.8	74.5
7.80	23.8	71.4
7.93	24.7	74.2

'Frequency' refers to the frequency of the map, 'Off-source RMS' refers to RMS noise measured over a large region well away from the source and 'On-source RMS' the noise used for region selection and statistics as per Section 4.2.3.

4.2.3 Spectral analysis and region selection

In this Chapter, I again use the BRATS software package for the analysis and fitting of spectral ageing models as detailed in Section 2.3. As the method used is identical to that described in Chapter 3 I do not repeat the process here, but instead detail the data quality, exclusions and the uncertainties which are specific to this investigation.

From the 32 JVLA spectral windows between 4 and 8 GHz, I find that 28 have good quality data in all array configurations. Of the remaining four, the spectral window at 6.10 GHz (SPW 17) is of extremely poor quality in all configurations (most likely due to an instrumental issue at the time of observation) and is therefore excluded from my analysis. At 4.02 GHz (SPW 0), heavy flagging of RFI was required in all array configurations leading to poor data quality and so this image was excluded from further analysis. The observations at 4.14 and 6.36 GHz (SPW 1 and 19 respectively) are of reasonable quality, but significant RFI was present in the B and C configuration data. These two frequencies were therefore excluded from the spectral analysis, but included in the making of the combined image shown in Figure 4.1.

A region fully encompassing the source (but excluding the core) was defined using DS9, along with a background region for determining the off-source thermal noise in the standard manner. Initial source detection was then performed, for which a 5σ cut-off was used based on this RMS value. I adopt the same practice as in Section 3.2.3.1 and apply an on-source multiplier of 3 to this value for the determination of statistical values and region selection. As each JVLA image is taken within a single pointing, one can be confident that the relative flux calibration error between images is small. I therefore take the flux calibration error to be 1 per cent for the JVLA images between 4 and 8 GHz. As the L-band observations were made with MERLIN and the old VLA system, the flux calibration error relative to the JVLA is not immediately clear. I therefore opt for the conservative value of the standard absolute flux calibration error value for VLA L-band observations of 5 per cent.

Following the arguments of Section 3.2.3.1, and as these data are of good quality, in the analysis that follows I again considered each source on a pixel by pixel basis to minimize the risk of the superposition of spectra affecting the results. A summary of the values chosen for the region selection is shown in Table 4.5.

Table 4.5: Summary of adaptive region parameters

Parameter	Value	Units	Description
Signal to noise	1		SNR (pixel to pixel)
Search area	1	Pixels^2	Max. search area
On-source noise	3		On-source noise multiplier
Hot pixel limit	20	Per cent	Max. pixel variation
Map variations	-1		Maximum map variation (off)

'Value' refers to the values applied within BRATS for the corresponding 'Parameter'. The 'Description' column provides further details of the value meaning. Note that a signal to noise of 1 is still subject to the 5σ cutoff and the on-source noise multiplier.

4.2.3.1 Model fitting and parameter determination

In this chapter, I have tested the broad bandwidth data described above against the three models of spectral ageing used within this thesis (Section 1.3.2). I have again assumed a magnetic field which is in equipartition using the SYNCH code of Hardcastle, Birkinshaw, & Worrall (1998) (also see Section 3.2.3.2) with the parameters of Table 4.6 to determine the magnetic field strength of the source.I took the minimum and maximum electron Lorentz factor to be $\gamma = 10$ and $\gamma = 1 \times 10^6$ respectively to determine the best fitting injection index I used the '*findinject*' command between $\alpha_{inj} = 0.5$ and 1.0 at intervals of 0.1. A second run was then performed around the minimum with a smaller step size of 0.01. The resulting values were then plotted and the minimum injection index found. Final model fitting of the sources was then performed using the derived values. The statistical values for each model (Section 2.3.6) were recorded and spectral ageing and χ^2 maps were then exported ready for further analysis.

4.3 Results

4.3.1 Model Parameters

The plot of χ^2 values for varying injection indices are shown in Figure 4.2 where one can see that a clear minimum occurs at an injection index of $\alpha_{inj} = 0.78^{+0.002}_{-0.001}$. Although not as high as those values discussed in Chapter 3, it remains much steeper than the previously assumed values of 0.6 to 0.7 traditionally used. I use this best fitting value for model fitting and the determination of δ for the magnetic field strength as listed in Table 4.6. An interesting point to

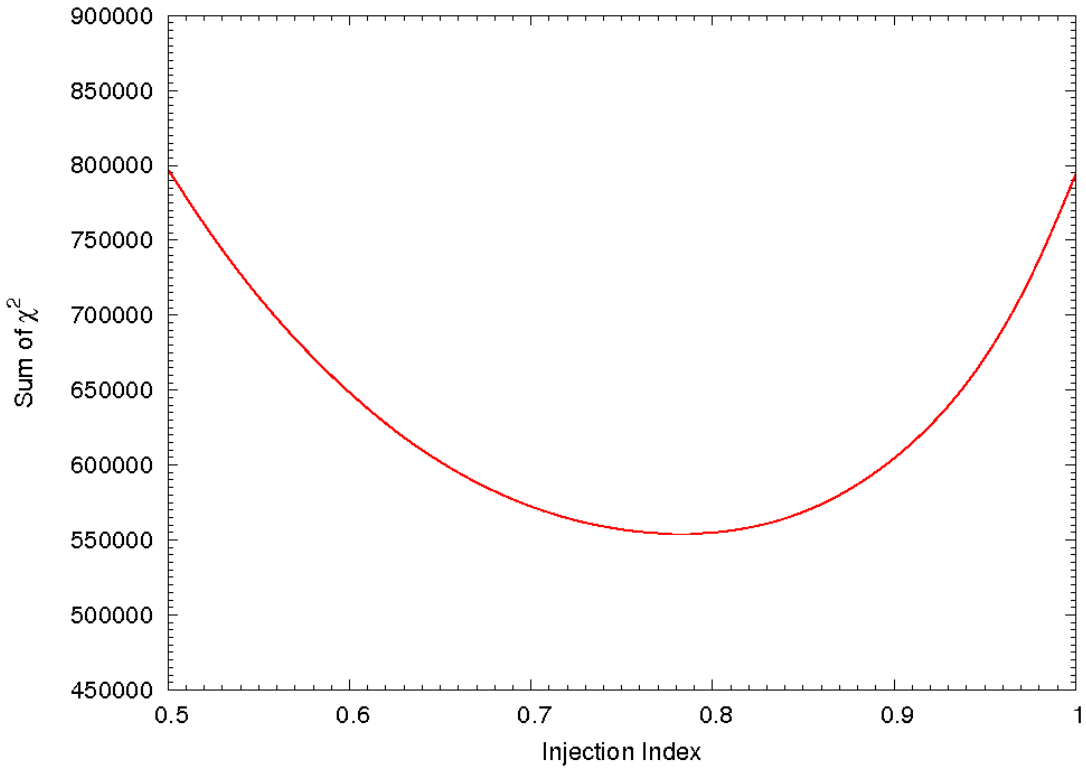

Figure 4.2: χ^2 values for 3C438 including the jet region for varying injection index values using the JP model of spectral ageing. Data points are taken at intervals of 0.1 between 0.5 and 1.0 inclusive and intervals of 0.01 between 0.72 and 0.82 and fitted with a natural cubic spline. As all data points lie on the fitted spline, they are excluded for clarity. Note that a minimum occurs at 0.78.

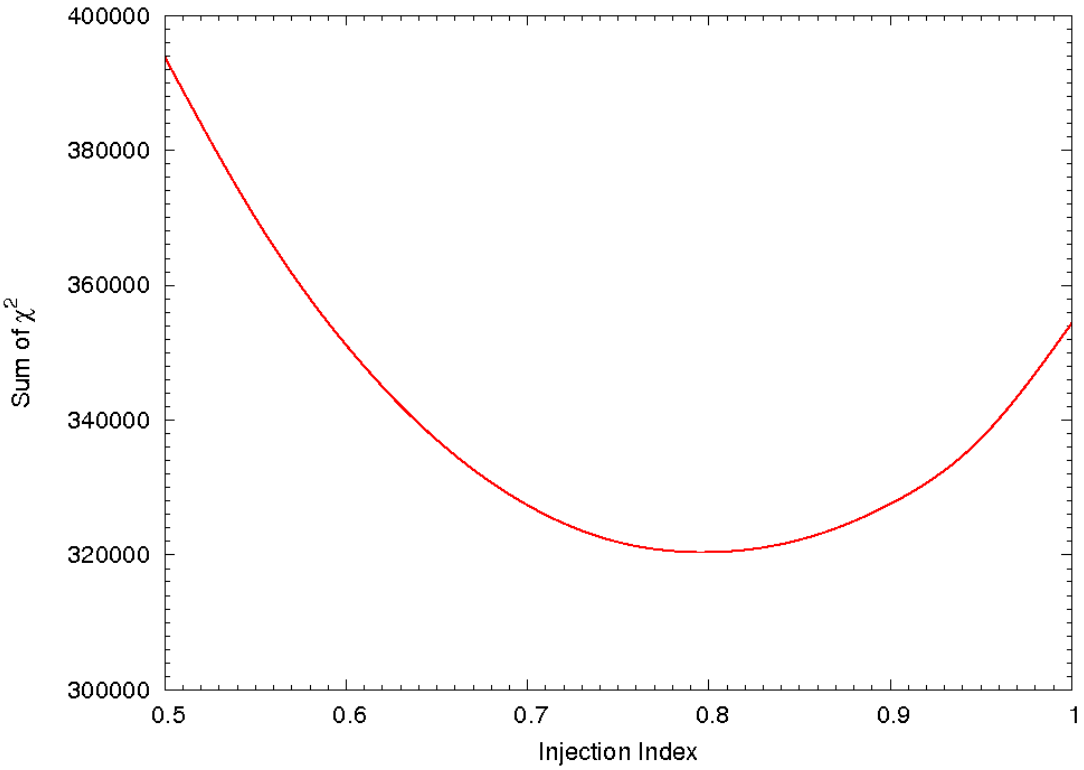

Figure 4.3: χ^2 values for 3C438 with the jet region excluded for varying injection index values using the JP model of spectral ageing. Data points are taken at intervals of 0.1 between 0.5 and 1.0 inclusive and intervals of 0.01 between 0.75 and 0.85 and fitted with a natural cubic spline. As all data points lie on the fitted spline, they are excluded for clarity. Note that a minimum occurs at 0.80.

Table 4.6: Summary of SYNCH parameters

Parameter	Value	Units	Comments
Length, Radius	17.5, 2.62	Arcsec	
δ	2.56		$\delta = 2\alpha_{inj} + 1$
E_{min}	5×10^6	eV	$\gamma \approx 10$
E_{max}	1×10^{11}	eV	$\gamma \approx 1 \times 10^6$

'Parameter' refers to the parameter name, where E_{min} is the minimum energy of the electron distribution; E_{max} is the maximum energy of the electron distribution; 'Length, Radius' are the source dimensions; and δ is the electron energy power law index given by $\delta = (\alpha_{inj}/2) - 1$ where α_{inj} is the injection index of the source determined in Section 4.3.1. Note that the length stated is the sum of the lengths of the northern and southern emitting regions and should not be confused with the LAS of the source.

note is that in contrast to 3C436 and 3C300 discussed in Chapter 3, emission coincident with the jet is clearly visible (Figure 4.1). Where $\delta = 2\alpha_{inj} + 1$ relates the injection index α to the initial electron energy power law distribution δ, for the best-fitting injection indices I derive a value of $\delta = 2.56$. Assuming equipartition and the parameters of Table 4.6, I find a magnetic field strength of 3.7 nT.

As discussed in Section 1.5.3, the jets of FR-II sources are still poorly understood and it is therefore not clear if the plasma responsible for this emission is due to reaccleration of lobe material at a jet-lobe boundary, or if it is accelerated internally within the jet itself. In either case, there is no *a priori* reason to believe that the observed jet emission should be well described by a spectral ageing model and I therefore ran a second minimization with the jet excluded from consideration. From Figure 4.3, one can clearly see that with the jet excluded a minimum occurs at a slightly increased injection index of $\alpha_{inj} = 0.80$. I use this value for the fitting of spectral age models where the jet has also been excluded in Section 4.3.2.

4.3.2 Spectral age and model comparison

Figure 4.4 shows the spectral age and the corresponding χ^2 values as a function of position for the JP, KP and Tribble models. One can see, even when the obvious variations due to the jet are

Table 4.7: Model Fitting Results (Full Source)

α_{inj}	Model	Mean χ^2	Mean χ^2_{red}	Confidence Bins					Rejected	Median
				< 68	68 - 90	90 - 95	95 - 99	≥ 99		Confidence
0.78	KP	45.88	1.70	2413	1229	548	1173	3889	Yes	> 99
	JP	47.51	1.76	2212	1227	568	1182	4163	Yes	> 99
	Tribble	46.78	1.73	2207	1278	544	1186	4037	Yes	> 99

'α_{inj}' refers to the injection index used for fitting of the 'Model' column. Mean χ^2 lists the average χ^2 over the entire source with an equivalent reduced value shown in the 'Mean χ^2_{red}' column. 'Confidence Bins' lists the number of regions for which their χ^2 values falls with the stated confidence range. 'Rejected' lists whether the goodness-of-fit to the source as a whole can be rejected as per Section 2.3.6 and 'Median Confidence' the confidence level at which the model can or cannot be rejected.

Table 4.8: Model Fitting Results (No Jet)

α_{inj}	Model	Mean χ^2	Mean χ^2_{red}	Confidence Bins					Rejected	Median
				< 68	68 - 90	90 - 95	95 - 99	≥ 99		Confidence
0.80	KP	43.48	1.61	2059	1003	412	954	2705	Yes	> 99
	JP	44.92	1.66	1793	1021	448	969	2902	Yes	> 99
	Tribble	44.32	1.64	1885	1044	426	961	2817	Yes	> 99

'α_{inj}' refers to the injection index used for fitting of the 'Model' column. Mean χ^2 lists the average χ^2 over the entire source with an equivalent reduced value shown in the 'Mean χ^2_{red}' column. 'Confidence Bins' lists the number of regions for which their χ^2 values falls with the stated confidence range. 'Rejected' lists whether the goodness-of-fit to the source as a whole can be rejected as per Section 2.3.6 and 'Median Confidence' the confidence level at which the model can or cannot be rejected.

ignored, that significant cross-lobe age variations exist in a manner consistent with the results of Chapter 3. Low age regions in the northern and southern lobe are coincident with the hot spots as one would expect, with older regions of plasma residing closer to the core. The maximum age of the source only differs by ~ 20 per cent between models with the main spectral features remaining independent of model type. From Tables 4.7 and 4.8, which show the statistical results of the model fitting, one sees that the spectral ages are reduced by ~ 0.2 Myrs in the case where the jet is not considered due to the higher injection index used.

A particularly interesting spectral feature which is observed in Figure 4.4 is the low age region at the edge of the southern lobe. It is not immediately obvious why particle acceleration should be occurring over such an extended region of the source, hence, further testing is required. I therefore used BRATS and the L- and X-band presented by Treichel et al. (2001), reimaged at 0.42 arcsec resolution, to produce a two point spectral index map. Figure 4.6 shows the resultant image zoomed to the southern lobe. Although a small region of low spectral index is observed, there is a distinct lack of the extended flat spectrum emission which one would expect if significant particle acceleration was occurring. The χ^2 maps of Figure 4.4 also provide some insight into this spectral feature. The small area of flat spectrum / low age seen in both the spectral index and ageing maps is a very poor fit, with the remainder of this region having higher χ^2 values compared to the source as a whole. From Figure 4.1 one can see a sharp gradient in flux on which this edge lies and it is likely that this low age region is due to the sharp edge of the lobe. I therefore consider the spectral ages derived not to represent the true age of the plasma within this elongated region for the remainder of this thesis.

In addition to the lobes, 3C438 has significant emission coincident with the assumed location of the jet. As was discussed in Section 4.3.1, there is no reason to believe that it should be well described by a spectral ageing model; however, it does provide a good proxy for changes in the steepness of this emission's spectrum. In the southern lobe, changes in the spectrum are observed to be relatively smooth with an increase in brightness and flattening of the spectrum occurring as the jet passes into the observed lobe emission. At this same location, a change in direction of the jet emission is also seen to occur. In the northern lobe, the observed jet emission remains straight along its length, but is seen to be 'knotty' with sharp changes in the spectrum. The errors associated these regions (Figure 4.5) are higher than the surrounding plasma, however, from the χ^2 maps in Figure 4.4 one can see that bright regions of the jet emission are well fitted by spectral ageing models, although they are a poor fit in lower flux regions. This is perhaps not surprising as if the accelerated particles take the form of a power law, it will be well described

by a spectral ageing model of zero age, regardless of any subsequent processes. I discuss this jet emission further in Section 4.4.

Although the distribution of age errors (Figure 4.5) is consistent with those presented in Chapter 3, the goodness-of-fit of the models to these sources is far less clear. From Figure 4.4 one can see that the overall χ^2 values are fairly consistent over the lobe emission ranging between values of $\chi^2_{reduced} \sim 1$ and 2.5. The northern lobe provides a noticeably better fit compared to the southern lobe which may give a hint towards the cause of these high χ^2 values, which I discuss further in Section 4.4. The northern hot spot is also poorly fitted by all 3 models of spectral ageing, a feature which appears to be common in the sources investigated in this thesis. The two southern hot spots do not show these high values but I note they appear to be much weaker than their northern counterpart. I discuss this further in Section 4.4 and it will also form part of my future work (Section 7.6). From Tables 4.7 and 4.8 I find that goodness-of-fit of the 3 models follows the pattern seen in Chapter 3, with the KP providing the best fitting model, the JP model providing a noticeably poorer model of the source and the Tribble model providing an intermediate goodness-of-fit. However, all 3 models are rejected at the 99 per cent significance level in both the cases where the jet has been included and excluded. Given the overall consistency of the fit to the lobes this is somewhat surprising; however, effects which I discuss further in Section 4.4 may be causing the χ^2 values to be systematically high.

4.3.3 Lobe Speeds

Using the same method described in Section 3.3.3, and assuming that the initial acceleration of the electron population occurs in the region of the hot spot, I derive the characteristic lobe speeds, v_{lobe}, for 3C438. The results of this are shown in Figures 4.9 and 4.10 for the source with and without the jet included respectively. With the jet included, the best fitting injection index implies an advance speed of between 0.0377 c (KP) and 0.0456 c (JP) for the northern lobe and 0.0344 c (KP) and 0.0415 c (JP) for the southern lobe. These values increase slightly where the jet is excluded, as one would expect for a high injection index to 0.0395 c (KP) and 0.0462 c (JP) for the northern lobe and 0.0360 c (KP) and 0.0412 c (JP) for the southern lobe. The ages fall well within the expected range described in the previous chapter and with other investigations (e.g. Alexander & Leahy, 1987). I discuss these speeds and their implications further in Section 4.4.

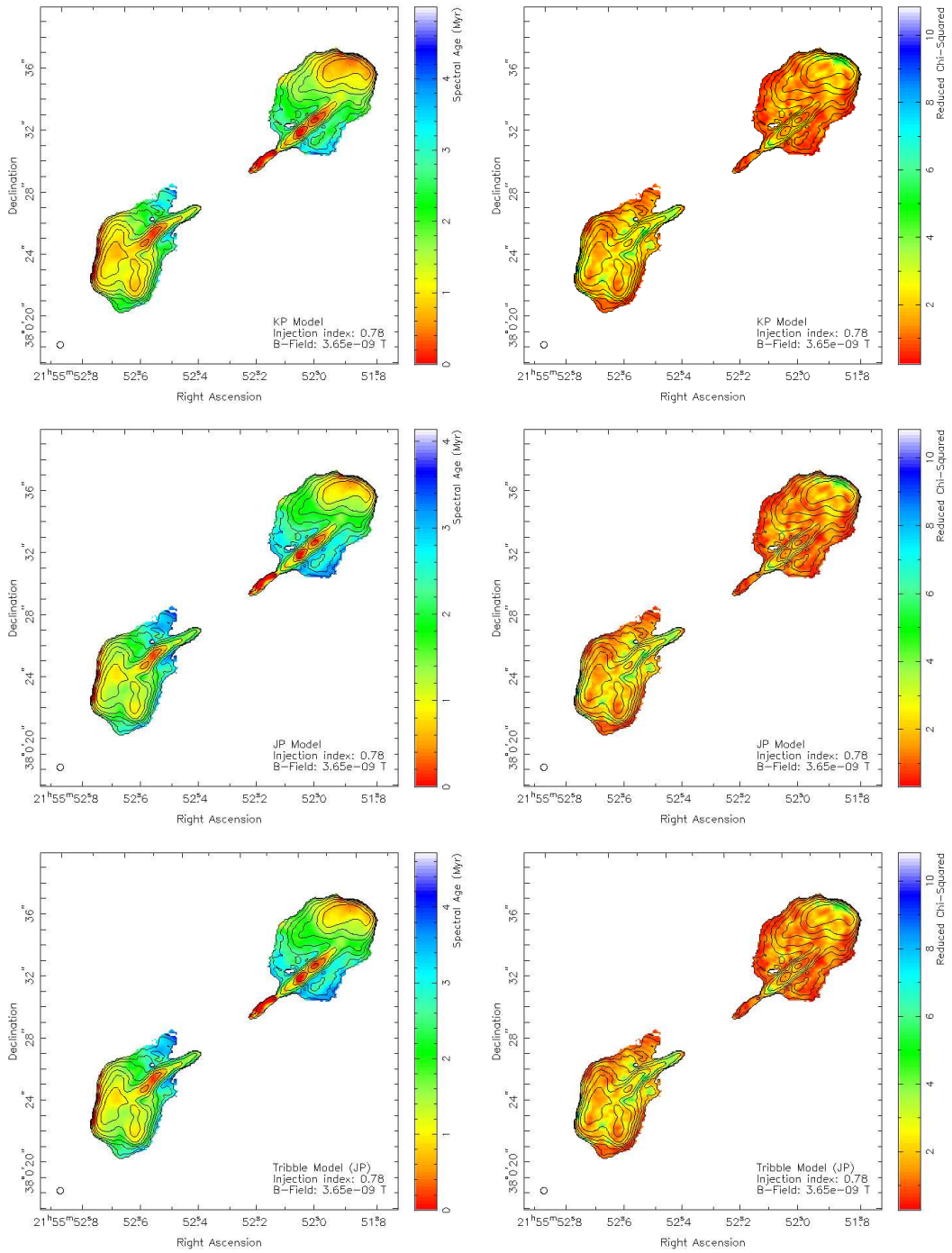

Figure 4.4: Spectral ageing maps (left) and corresponding χ^2 maps (right) of 3C438 with 7.9 GHz flux contours. Three model fits are shown; KP model (top), JP model (middle) and Tribble model (bottom) with injection index 0.78

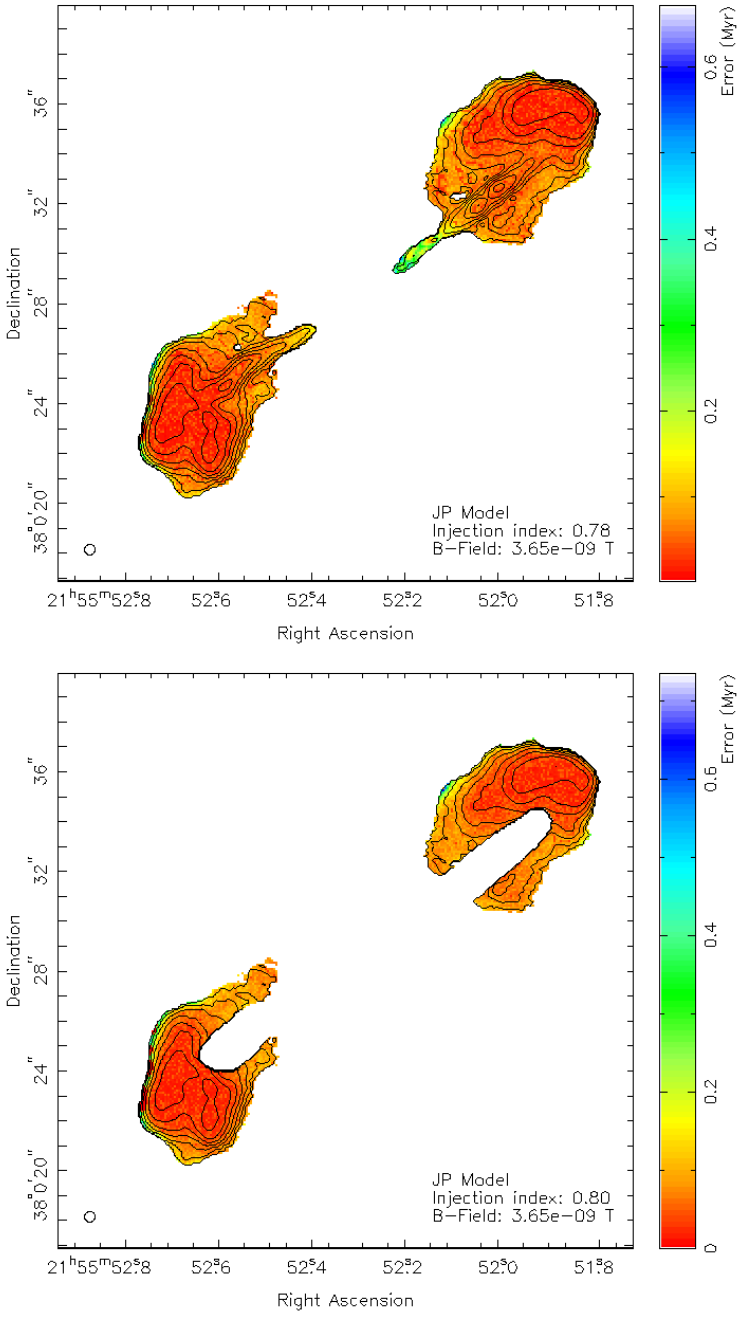

Figure 4.5: Spectral age errors of 3C438 including (top) and excluding (bottom) the jet region, mapped as a function of position with 7.9 GHz flux contours overlaid. Positive errors for the JP model are shown. Errors are determined using the methods described in Section 2.3.5.3.

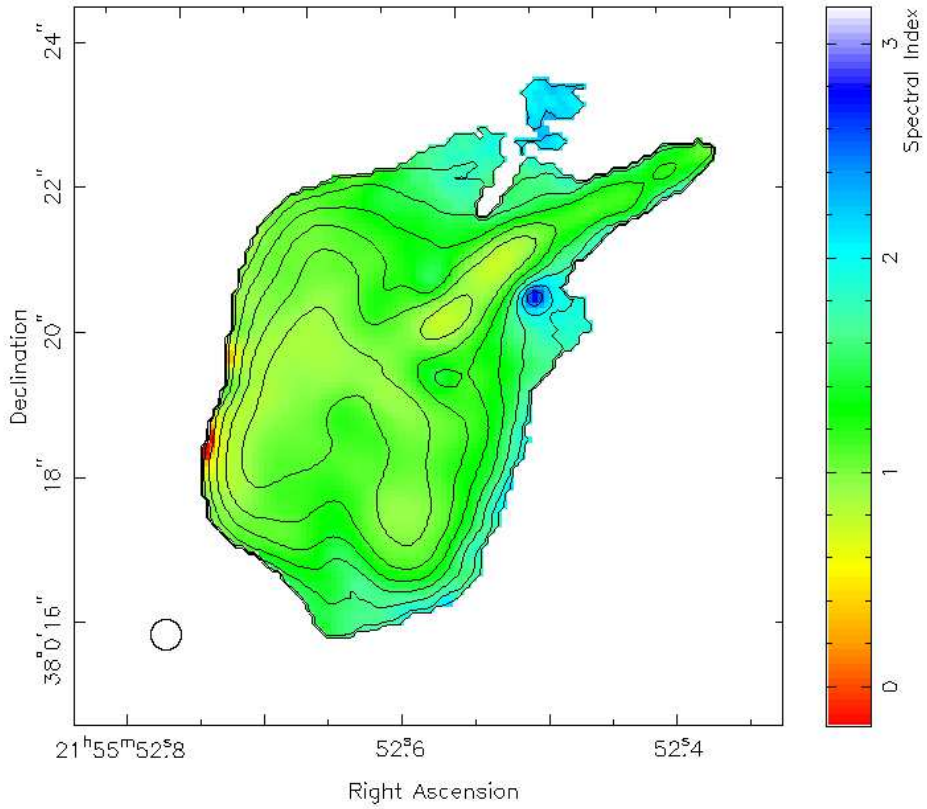

Figure 4.6: Two-point spectral index map created in BRATS of the southern lobe of 3C438 between 1.4 and 8 GHz. The data used is that presented by Treichel et al. (2001), reimaged at 0.42 arcsec resolution.

Table 4.9: 3C438 Lobe Advance Speeds (Full Source)

α_{inj}	Model	Lobe	Max Age (Myrs)	+	-	Distance (kpc)	Speed (v/c)	+	-
0.78	KP	North	4.35	0.40	0.29	27.75	0.0377	0.0038	0.0028
	JP	North	3.60	0.06	0.10	27.75	0.0456	0.00078	0.0028
	Tribble	North	4.10	0.08	0.11	27.75	0.0400	0.00078	0.0013
	KP	South	4.35	0.40	0.29	25.97	0.0344	0.00035	0.0025
	JP	South	3.60	0.06	0.10	25.97	0.0415	0.00071	0.0012
	Tribble	South	4.10	0.08	0.11	25.97	0.0365	0.00073	0.0010

'α_{inj}' refers to the injection index used for fitting of the 'Model' column. 'Max Age' is the maximum age of the corresponding 'Lobe' in Myrs. 'Distance' gives the separation between the oldest aged population in the lobe and the hot spot in kpc.'Speed' lists the derived speed as a fraction of the speed of light as detailed in Section 4.3.3.

Table 4.10: 3C438 Lobe Advance Speeds (No Jet)

α_{inj}	Model	Lobe	Max Age (Myrs)	+	-	Distance (kpc)	Speed (v/c)	+	-
0.78	KP	North	4.15	0.37	0.24	27.75	0.0395	0.0032	0.0021
	JP	North	3.55	0.06	0.10	27.75	0.0462	0.00071	0.0012
	Tribble	North	4.05	0.08	0.12	27.75	0.0405	0.00080	0.0012
	KP	South	4.15	0.37	0.24	25.97	0.0360	0.0035	0.0023
	JP	South	3.55	0.06	0.10	25.97	0.0421	0.00078	0.0013
	Tribble	South	4.05	0.08	0.08.12	25.97	0.0369	0.00073	0.0011

'α_{inj}' refers to the injection index used for fitting of the 'Model' column. 'Max Age' is the maximum age of the corresponding 'Lobe' in Myrs. 'Distance' gives the separation between the oldest aged population in the lobe and the hot spot in kpc.'Speed' lists the derived speed as a fraction of the speed of light as detailed in Section 4.3.3.

4.4 Discussion

The results of Chapter 3 have brought into question many of the previously held assumptions about the models of spectral ageing and have confirmed that, for at least some sources, a large age disparity exists between the spectral and dynamical ages of powerful radio sources. In this chapter, I have presented results which further expand my sample of these sources and tightly constrain curvature at frequencies of a few GHz. In the following sections I discuss if these truly broad bandwidth observations impact upon my findings of the previous chapter, and how this impacts on the overall understanding of radio galaxy dynamics.

4.4.1 Source orientation

As discussed in Section 3.4, the angle at which the radio galaxy is viewed can have a major impact on the interpretation of aging measurements. From Figure 4.1, jets are clearly visible in both the northern and southern lobes hence, assuming these jets are relativistic, the source must be viewed close to side on. As noted in Section 4.3.2, an increase in emission is observed in the jet emission close to the region where the jet transitions into the lobe material. I discuss this further in Section 4.4.2, but if this increase in brightness is due to a jet-lobe boundary interaction, the close alignment with the edge of the lobe in the 1.4 GHz image again suggests that 3C438 is observed close to the plane of the sky. The symmetry of the source and its classical double structure also gives credence to this assertion and I therefore assume effects such as those of beaming and the superposition of material of different ages along the source's length as negligible for the remainder of this section (although a superposition of spectra through the source will still exist).

4.4.2 Jets

As emission coincident with the location of the jets is observable in 3C438, the bias they may cause to the overall study of the lobe emission must be considered. Comparing Tables 4.7 and 4.8 one finds that when the jet is included, $\sim$42 per cent of the fits are rejected at $\geq$ 99 percent confidence, and without the jet only $\sim$37 per cent of model fits are rejected at this level. Conversely, $\sim$26 per cent of the regions show a good fit at the $<$ 68 percent confidence level, compared to $\sim$29 per cent when the jet is removed. It therefore appears that the inclusion of the jet may give rise to at least some poorly fitted regions of the source, but at a level which cannot

explain the rejection of the models as a whole. I discuss further possible causes of the overall model rejection in Section 4.4.5.

The observed jet emission also provides the opportunity to consider the dynamics of the jets themselves. As noted in Section 4.3.1, brightening of the jet occurs in both the northern and southern lobes coincident with where the jet enters the lobe. One possible explanation of such features is therefore an interaction between the lobe material and the jet itself. The exact cause of such an interaction is unclear, but it could plausibly be due to either lobe material being reaccelerated at the jet-lobe boundary, or the onset of turbulence within the jet resulting in localized shock acceleration. The observed curvature in the jet found in the southern lobe may possibly be evidence of this interaction, but due to the presence of two hot spots, I suggest that the more likely cause is transverse movement of the jet between the two regions. Regardless of the cause, the presence of clear hotspots in both lobes implies that a large fraction of the jet material must proceed uninhibited by this unknown acceleration process; however, the results presented in this chapter do not allow us determine the underlying reason for the jet emission, especially in light of the fact that there is no *a priori* reason to assume it should be well described by the spectral ageing models used here. Note that here we use the term hotspot to refer to the regions of bright emission at the end of the radio lobes, although acknowledge that this does not fit the strict definition laid out by, for example, Leahy et al. (1997).

4.4.3 Injection index

One of the key findings of Chapter 3 is the deviation of the injection index from previously assumed values and it is again clear from the results presented in Section 4.3,that this discrepancy remains in the case of 3C438.

Whilst these findings reinforce the idea that these higher injection indices are widespread, the question of a systematic offset (Section 3.4.2) between the new flux scale used in these new observations and those used in reduction of old VLA/MERLIN data where reliable models of the calibrator sources were not available remains. To provide a more definitive answer to this important question, low-frequency observations are required. I therefore address this question further through the use of LOFAR observations in Chapter 5.

4.4.4 Spectral ages and lobe speeds

A further question raised in Chapter 3 is the well known discrepancy between dynamical and spectral ages. Thanks to X-ray investigations by Kraft et al. (2007), the environment in which 3C438 resides is well known and one is able to determine a well constrained dynamical age. Kraft et al. (2007) find that the cluster in which 3C438 resides has a core density out to ~ 30 arc seconds, hence the source resides entirely within this region of approximately constant density. Using the models described in Section 3.4.3 with a value of $\beta = 0$, I derive a dynamical age for 3C438 of 3.2 Myrs.

Comparing these values to the spectral ages shown in Tables 4.9 and 4.10, one sees that they are in much better agreement to the dynamical ages that those sources studied in the previous chapter. The JP and Tribble models provide good agreement with the dynamical age. The KP model overestimates the age of the source by ~ 30 per cent but still provides a reasonable age compared to the difference of up to an order or magnitude found in previous studies (e.g. Eilek, 1996; Chapter 3).

There are various possible explanations for this good agreement in age compared to those found for 3C436 and 3C300. The X-ray studies performed by (Kraft et al., 2007) of the environment in which 3C438 resides provides observational constraints on β which are directly related to the source, rather then a value inferred from the observation and simulation of similar cluster environments. One can therefore be more confident that the dynamical model is representative of the source. However, it is unlikely that the values of β used in Chapter 3 will vary to such an extent to correct for the order of magnitude difference. An alternative, possibly complementary, explanation is given by Blundell & Rawlings (2000) who suggest that it is possible to reconcile the dynamical age of source with ages $\ll 10$ Myrs *and* where the magnetic field history is well approximated. In the case of 3C300 and 3C436, although the spectral ages are well below this value the dynamical ages suggest they are in fact much older, whereas for 3C438, they suggest a young source. Although it is not possible to trace the history of the magnetic field, the uncertainty introduced from these effects to a low age source such as 3C438 are likely to be small compared to those in older radio lobes. The tighter constraints placed on the spectral curvature, at GHz frequencies by the truly broad bandwidth observations used in this chapter is also likely to play a key role in providing more accurate ages, but determining which of these factors is the most significant requires a larger sample of galaxies to be considered. Regardless of the cause,

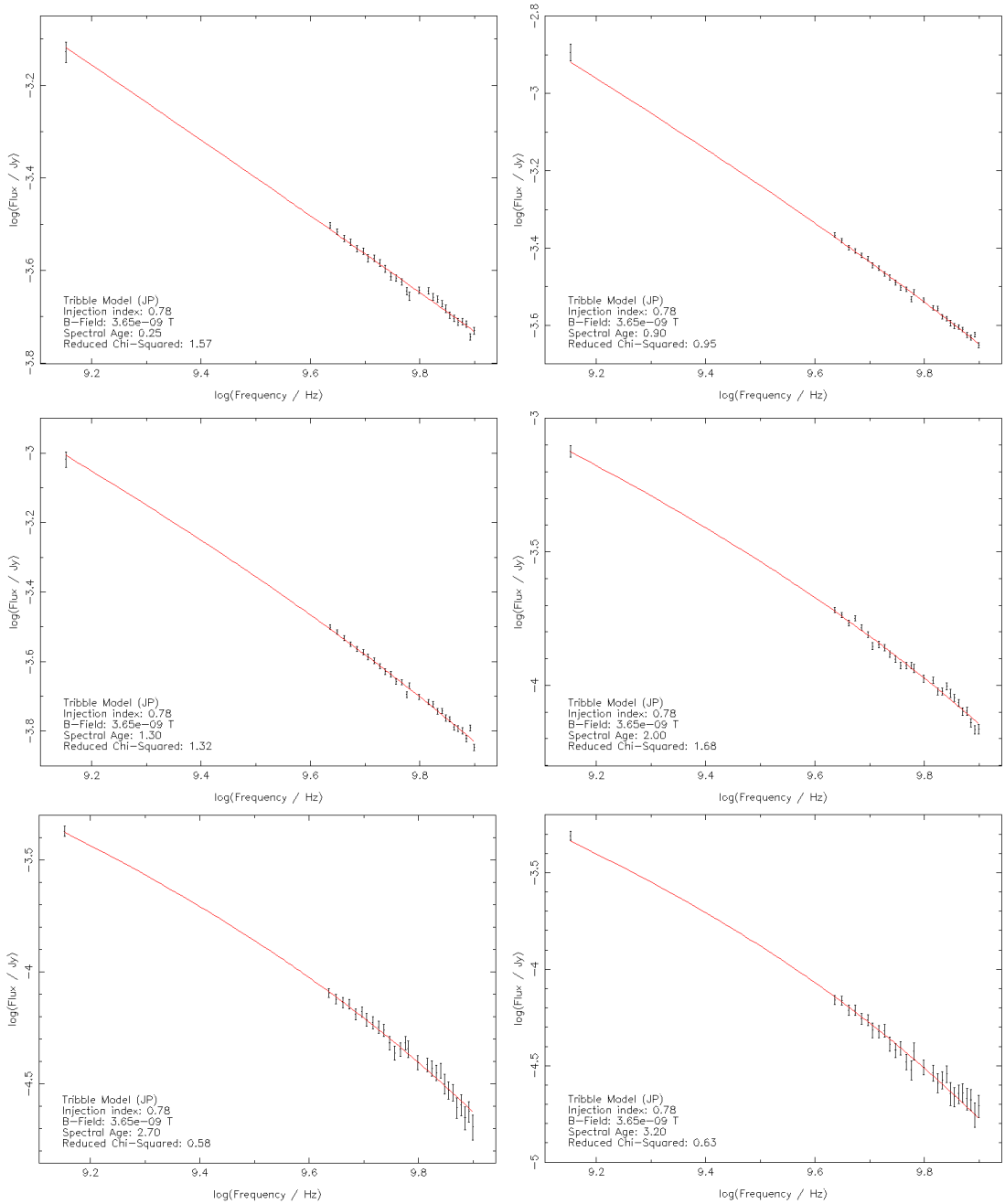

Figure 4.7: Plots of flux against frequency for six well fitted regions of 3C438 at low (top), moderate (middle) and high (right) spectral ages. Red lines indicate the best-fitting Tribble model with parameters as noted on each plot.

the good agreement between the two values means that one can be confident that the ages of 3C438 presented in this chapter, provide a good estimate of the true source age.

The characteristic lobe speeds of 3C438 shown in Tables 4.9 and 4.10 agree well with previous studies of similar FR-II sources (e.g. Myers & Spangler (1985); Alexander & Leahy (1987)). Although they are much lower than those found in this thesis for 3C436 and 3C300, this may be due to the large age disparity found between the spectral and dynamical ages suggesting that the lobe speeds in Chapter 3 are an overestimate. As was discussed in the previous section, the good agreement between the spectral and dynamical ages mean that for 3C438 one can be confident that the speeds derived provide a physically realistic estimate.

With reliable advance speeds determined and the external environment well known, a Mach number can also be derived. The sound speed of the medium through which the lobes are advancing is given by $c_{sound} = \sqrt{\gamma kT/m}$ where $\gamma = 5/3$ is the adiabatic index, $m = 0.5m_p$ is the mass of the particles and T is the gas temperature, which in turn one can use to derive the Mach number by the standard equation $M = v/c_{sound}$. Kraft et al. (2007) find that the cluster environment in which 3C438 resides has a gas temperature of 17 keV, hence using the advance speeds listed in Table 4.9, I find Mach numbers between 4.85 (KP) and 5.87 (JP) for the northern lobe, and 4.43 (KP) and 5.34 (JP) for the southern lobe. This implies that the lobes are therefore expanding supersonically and must therefore be overpressured with respect to the external medium. However, the pressure of these lobes suggest a different scenario. Given the assumed magnetic field strength of 3.65 nT, I find using the SYNCH code described in Section 3.2.3.2 a total energy density for each radio lobe of 5.3×10^{-12} J m^{-3} and a subsequent internal pressure, given by $P = U/3$ where U is the total energy density, of 1.8×10^{-12} Pa. The gas pressure of the external medium can also be derived by the standard equation $P = nkT$ where $n \approx 2.2n_0$ is the number density of particles. Using the gas temperature of 17 keV and number density of protons of 3.4×10^{-2} cm^{-3} presented by Kraft et al. (2007), I therefore derive the pressure of the external medium to be 2.0×10^{-10} Pa. These calculations therefore imply that the lobes are *underpressured* on the order of approximately 2 magnitudes. Similar sources such as Cygnus A that are found in rich cluster environment have also been observed to display such discrepancies (e.g. Hardcastle & Croston, 2010). One possible explanation for this difference is that the lobe energy density is dominated by non-radiating particles, although the origins of such a population remains unknown. In such a scenario, the minimum energy condition would no longer apply causing a departure from equipartition, affecting the spectral ages of the source.

Determining the cause of such disparities is therefore vital for both the dynamics and energetics powerful radio sources.

4.4.5 Model comparison

In Chapter 3, although they potentially underestimated the ages of the sources considered, the overall model fits were in good agreement with the data; however, the model fitting data for 3C438 (Tables 4.7 and 4.8) give some surprising results. Given the good agreement between the dynamical and spectral ages discussed in the previous section, one would expect the three models of spectral ageing tested to be well fitted to the observations but are all instead rejected at the 99 per cent confidence level. As was discussed in Section 4.4.2 emission coincident with the jet may cause some bias towards higher χ^2 values but is unable to fully account for the model rejections.

A further possible cause may lie in the hot spot regions. In the northern hot spot where strong emission is observed, the models provide a poor fit. One possible cause of this is a differing injection index in the hot spot and the lobes, as has been observed in other FR-II source (e.g. Hardcastle & Looney, 2001). If particle acceleration occurs over an extended region rather than at a single point, the lobe emission may be best described by the electron distribution as it leaves the hotspot, rather than in the hot spot itself where turbulence and the mixing of electron populations is likely to be high. The hot spots in the southern lobes do not display such a reduction in the goodness-of-fit, but given their emission is much weaker than their northern counterpart, this is perhaps not surprising. As in Chapter 3 I suggest that high resolution detailed studies of the hot spot regions will form an integral part of determining reliable spectral ageing models. One such investigation which I will undertake is detailed in Section 7.6.

Although jet and hot spot emission are likely to cause some bias to high χ^2 values, insight in to the underlying reason for the overall model rejection can also be found by comparing the goodness-of-fit between the two lobes. The extended emission in the northern lobe is generally well described by the spectral ageing models compared to its southern counterpart which overall has much higher χ^2 values. The worst fitting regions of extended emission in the southern lobe appear to be located between the two hot spots and close to the path of the jet. As the jet and hotspot sweep across the lobe between the two areas, freshly accelerated particles will become mixed with older regions of plasma. This mixed electron population will not be well described by the single injection models used within this thesis, and I therefore suggest this to be the primary cause of poor model fits, rather than any inherent problem with the models themselves.

Detailed numerical modelling of spectral ages in radio galaxy lobes may be able to reproduce such effects in the future.

4.5 Conclusions

I have presented within this chapter the spectral ageing study of the FR-II source 3C438. Using broad bandwidth JVLA observations to tightly constrain spectral curvature at GHz frequencies, I have investigated whether significant cross-lobe variations are likely to be common in powerful radio sources and if the high injection indices found in Chapter 3 are still observed when tightly constrained by full bandwidth observations. I have investigated whether emission from the jet affects spectral ageing analysis and test whether the Tribble model of spectral ageing provides a similar goodness-of-fit and realism to that discussed in the Chapter 3. The key points made within this chapter are as follows:

1. Significant cross-lobe age variations are again observed in the lobes of 3C438. I suggest that these variations are a common feature of FR-II sources and so should be considered carefully in all future studies.

2. I find a best-fitting injection index for 3C438 to be $\alpha_{inject} = 0.78$, consistent with higher injection indices found in the previous chapter.

3. Jet emission causes a slight bias towards flatter injection index values but, even for the strong jet emission observed in 3C438, does not account for large difference between the commonly assumed values and those found within this thesis.

4. A brightening of jet emission coincident with the approximate location that the jet enters the lobe, although the cause of emission due to jet-lobe interaction is not clear.

5. The goodness-of-fit of the spectral ageing models mirrors that found in the previous chapter. I again suggest that Tribble model currently provides most likely scenario when both goodness-of-fit and physically plausibility are considered.

6. I derive a Mach number of between 4.43 and 5.87 implying that radio lobes are expanding supersonically. However, I find that the lobes are are underpressured on the order of approximately 2 magnitudes, similar to what is observed in other rich cluster sources (e.g. Cygnus A).

7. In contrast to Chapter 3, the spectral ages of 3C438 agree well with those determined from a dynamical view point. I suggest that this is due to improved constraints provided by the fully broad bandwidth data, the young age of the source and the improve reliability of the dynamical model due to the availability of studies at X-ray wavelengths.

In the next chapter, I use low-frequency observations to investigate the physical reality of the high injection indices found this the previous two chapters. I also address the issue of low-frequency curvature and the energetics of powerful radio galaxies.

5

The energetics of radio galaxies at LOFAR wavelengths

5.1 Introduction

As was mentioned in Section 1.7, the limited resolution provided by the previous generation of radio interferometer at metre wavelengths have meant that the spectrum and energetics of radio galaxies are currently poorly understood at low-frequencies. With the commissioning of LOFAR (2.2.2) this is set to change. In this chapter, I present results from work I have done as part of the LOFAR nearby AGN key science project.

One key question which has arisen from the investigations presented in Chapters 3 and 4 is why do the sources studied have such unexpectedly high injection index values? At low frequencies, the effects of spectral ageing are known to be small (Figure 1.4), hence the electron energy distribution should remain close to the originally injected power law. If one can therefore determine the spectrum of a radio galaxy at low frequencies as a function of position, it is possible to determine if the injection indices derived in the previous chapters are reliable, or simply an artefact of the methods used. The high resolution, broad bandwidth observations provided by LOFAR are therefore ideal for addressing this issue.

A further important question which LOFAR is ideally suited to answer relates to the energetics of powerful radio galaxies. The calculation of the total energy content of FR-II sources generally relies on synchrotron and inverse-Compton modelling constrained by measurements at X-ray and radio wavelengths (e.g. Croston et al., 2004, 2005). Whilst integrated flux densities at low frequencies have long been available, the limited number of data points at these wavelengths

Table 5.1: List of target sources and galaxy properties

Name	IAU Name	Redshift	5 GHz Core Flux (mJy)	Spectral Index (178 to 750 MHz)	LAS (arcsec)
3C223	J0939+355	0.137	8.5	7.4	306

'Name' and 'IAU Name' list the 3C and IAU names of the galaxies as used within this chapter. 'Spectral Index' lists the low frequency spectral index between 178 to 750 MHz and 'LAS' the largest angular size of the source. The 'Redshift', '5 GHz Core Flux', 'Spectral Index' and 'LAS' column values are taken directly from the 3CRR database (Laing et al., 1983) (http://3crr.extragalactic.info/cgi/database).

has meant that the spectrum of this emission must be assumed. LOFAR observations therefore provide the ability to constrain these models and evaluate the previously used assumptions about low-frequency spectrum.

In this chapter, I use LOFAR observations of the FR-II source 3C223 to address three key questions. What is the low-frequency spectrum of FR-II radio galaxies on small spatial scales? Are the injection indices derived at low frequencies consistent with those derived in Chapters 3 and 4? How do these measurements impact upon the total energy content of FR-II sources? In Section 5.2 I give details of target selection, data reduction and the analysis undertaken. Section 5.3 presents my results and in Section 5.4 I discuss these findings in the context of the aims outlined above.

5.2 Data reduction and spectral analysis

5.2.1 Target selection and observations

Observing time for thirteen targets was requested as part of the cycle-0 nearby AGN KSP cycle-0 proposal covering various stages in the life-cycle of radio-loud active galaxies. Of these thirteen targets, two nearby powerful radio galaxies suitable for the detailed spectral analysis detailed above were observed, 3C223 and 3C452. To ensure good uv coverage was obtained, 10 hour observations were made of each target at HBA and LBA frequencies using the core and remote stations. This provides baselines out to $\sim$ 100 km which, at the lowest HBA frequency (110 MHz), give a resolution of $\sim$ 7 arcseconds, allowing small scale spectral variations to be investigated.

Table 5.2: Observation Details

Name	Array	Frequencies (MHz)	Target TOS (mins)	Flux Calibrator	Calibrator TOS (mins)
3C223	HBA Inner	110 – 180	429	3C196	78
	LBA	30 – 80	600	3C196	600

'Name' list the 3C name of the galaxies as used within this chapter. 'Array' refers to the LOFAR array configurations used. 'Frequencies' lists the frequency coverage of the observations. 'Target TOS' lists the time on source at each frequency. 'Calibrator TOS' lists the time on source at each frequency for the corresponding 'Flux Calibrator'.

Of the two sources observed, 3C452 has been of recent interest due to the suggestion by Sirothia et al. (2013) that it may be a previously unknown double-double radio galaxy (Section 1.4.2). However, although the LOFAR data were initially calibrated, an error in the LOFAR antenna tables at the time of observation meant they were of poor quality. Although this issue is relatively easy to solve, the renewed importance of this source and the ongoing debate over the physical reality of the additional structure observed by Sirothia et al. (2013) due to its absence from JVLA observations (R.Perley, private communication), mean that I have opted to save this source for a future, extended investigation. I therefore restrict my analysis to 3C223 for which the data are of good quality and not affected by these additional concerns. Details of 3C223 and the observations made are given in Tables 5.1 and 5.2.

5.2.2 Data reduction

Prior to observation, simulations were run in order to determine if the demixing of A-team sources was required (Section 2.2.3.3). I found that at both LBA and HBA frequencies, Cygnus A and Cassiopeia A heavily affect the observations, hence demixing of these sources was undertaken by the LOFAR support staff prior to the data being made available. The observations were then downloaded from the archive to the LOFAR server at Southampton University and calibrated using the Southampton pipeline and the methods detailed in Section 2.2.3.3. In order to obtain the required number of data points to determine the spectral profile of the source, but also maintain a good signal to noise ratio, these data were split into four 12 MHz bands at LBA frequencies and into nine 7-MHz bands at HBA frequencies. Imaging was then undertaken for each of these bands in CASA using MSCLEAN (Section 2.2.3.4). The images were mapped at

Table 5.3: Summary of HBA imaging parameters

Parameter	CASA Name	Value	Units
Polarization	STOKES	I	
Image Size	IMSIZE	4098 4098	Pixels
Cell Size	CELL	1.4 1.4	Arcsec
Weighting	ROBUST	-0.5	
Beam size	RESTORINGBEAM	7.0 7.0	Arcsec
Multiscale	MULTISCALE	[0, 5, 15, 45]	Pixels

'Parameter' refers to the imaging parameter used in making of radio maps within this chapter. 'CASA Name' refers to the CASA parameter taking the value stated in the 'Values' column.

the resolution appropriate to the lowest LBA and HBA frequencies with a cell size one fifth of that value. A summary of parameters used for the imaging described in this section is shown in Tables 5.3 and 5.4.

In order to extend my frequency coverage,the L-band VLA data presented by Leahy & Perley (1991) were also obtained. These data are comparable in resolution to the LOFAR HBA and reduced to a high standard, hence only regridding to J2000 coordinates and re-imaging to match the parameters of Table 4.3 was required. As a bright core is observable at all frequencies, the images were then aligned to the northern hotspot using the methods of Section 2.3.3.1 where I find a standard deviation in alignment between maps of 0.09 pixels. It should be noted that use of hotspots provides a less robust method of alignment than the radio core used in the previous chapters; however, the lack of significant edge effects and the large uncertainty introduced by the noise in the LOFAR observations mean that this method should prove sufficient for the analysis undertaken within this chapter. The images were then copied to the BRATS working directory ready for further analysis. Examples of the resulting LBA and HBA images are shown in in Figure 5.1.

5.2.3 Spectral analysis and region selection

In this Chapter, I again use the BRATS software package for the fitting of spectral ageing models and production of spectral index maps as detailed in Section 2.3. As the method used is identical to that described in previous chapters I do not describe the process again here, but instead detail

Table 5.4: Summary of LBA imaging parameters

Parameter	CASA Name	Value	Units
Polarization	STOKES	I	
Image Size	IMSIZE	4098 4098	Pixels
Cell Size	CELL	7.0 7.0	Arcsec
Weighting	ROBUST	-0.5	
Beam size	RESTORINGBEAM	49.7 35.4	Arcsec
Position Angle	RESTORINGBEAM	89.8	Degrees
Multiscale	MULTISCALE	[0, 5, 15, 45]	Pixels

'Parameter' refers to the imaging parameter used in making of radio maps within this chapter. 'CASA Name' refers to the CASA parameter taking the value stated in the 'Values' column.

the quality of the data, exclusions and the uncertainties which are specific to this investigation.

From the 9 HBA bands imaged, I find that 6 have good quality data suitable for spectral ageing analysis. HBA bands 3, 7 and 8 are of extremely poor quality and are therefore excluded from my analysis. At LBA frequencies, only one band at 51 MHz is currently suitable for use in my analysis. Due to the lack of international baseline, the LBA data are currently unsuitable for investigations of the spectrum on small spatial scales and are instead used within this thesis to provide an integrated flux density measurement at very low frequencies, and to constrain the synchrotron / inverse-Compton modelling described in Section 5.2.3.1.

A region fully encompassing the source (but excluding the core) was defined using DS9, along with a background region for determining the off-source thermal noise in the standard manner. Initial source detection was then performed, for which a 5σ cut-off was used based on this RMS value. Due to dynamic range issues which particularly affect the northern lobe (see Section 5.3) I apply an on-source multiplier of 10 to ensure that the effects of these high noise levels are minimized. This value is then used for the determination of statistical values and region selection in the standard manner described in previous Chapters.

The relative flux calibration errors of the LOFAR observations discussed here are still poorly constrained (also see Section 7.6); however, using the integrated flux values and spectral index presented by Orru et al. (2010) who use VLA observations at 74 and 327 MHz and extrapolating to LOFAR LBA and HBA frequencies, I find total integrated flux values of 37.4 Jy at 51.66 MHz and 17.9 Jy at 161 MHz. As a secondary check, the same process can be carried out

Table 5.5: Summary of maps by frequency

Frequency (MHz)	Off-source RMS (mJy beam^{-1})	On-source RMS (mJy beam^{-1})	Integrated Flux (Jy) Northern	Southern	Total
51.6	12.4	$--$	19.00	15.41	34.14
118	1.08	10.8	13.69	11.02	24.71
125	0.947	9.47	12.89	10.28	23.17
133	0.910	9.10	12.03	9.76	21.79
147	0.784	7.84	10.88	8.85	19.73
154	0.840	8.40	10.38	8.40	18.78
161	0.834	8.34	9.63	7.84	17.47

'Frequency' refers to the frequency of the map, 'Off-source RMS' refers to RMS noise measured over a large region well away from the source and 'On-source RMS' the noise used for region selection and statistics as per Section 4.2.3. As the 51.6 MHz image is not used in the adaptive regions selection, no on-source RMS value is given. 'Integrated Flux' values are listed at each frequency for the 'Northern' and 'Southern' lobes along with the 'Total' integrated flux of the source.

using the integrated fluxes measured by Laing & Peacock (1980) at 84 MHz and 178 MHz. These give similar values of 36.9 Jy at 51.66 MHz and 17.0 Jy at $161MHz$. Comparing these values to Table 5.5, I find good agreement to within around 5 per cent and therefore take this to be my standard flux calibration error for my LOFAR observations. As in Chapter 4, the L-band observations were made with the old VLA system, so the flux calibration error relative to LOFAR is not immediately clear. I therefore opt for the conservative value of the standard absolute flux calibration error value for VLA L-band observations of 5 per cent.

For determining the regions used in model fitting, I again follow the arguments of Section 3.2.3.1, and considered the source on a pixel by pixel basis to minimize the risk of the superposition of spectra affecting the results. A summary of the values chosen for the region selection is shown in Table 5.6.

5.2.3.1 Model fitting and parameter determination

In this chapter, I have tested my observations with two forms of model fitting; the standard spectral ageing fitting used in Chapters 3 and 4, and synchrotron / inverse-Compton modelling.

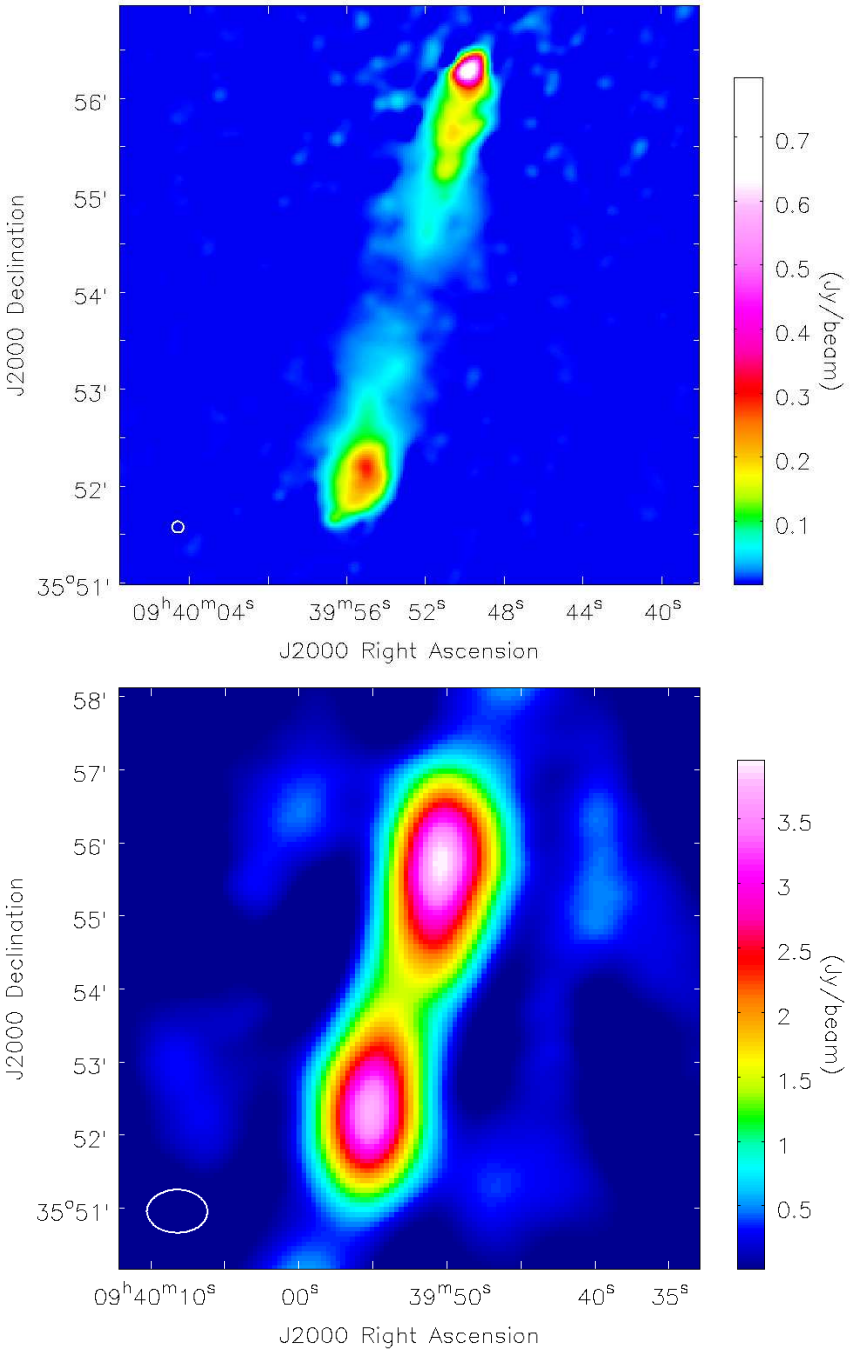

Figure 5.1: Radio maps of 3C223 at 140 MHz (top) and 51.6 MHz (bottom). Imaged using multi-scale CLEAN in CASA. The off-source RMS noise is 0.78 mJy beam^{-1} for the 140 MHz map and 12.4 mJy beam^{-1} for the 51.6 MHz map. The restoring beam is indicated in the bottom left corner of the image.

Table 5.6: Summary of adaptive region parameters

Parameter	Value	Units	Description
Signal to noise	1		SNR (pixel to pixel)
Search area	1	Pixels^2	Max. search area
On-source noise	10		On-source noise multiplier
Hot pixel limit	20	Per cent	Max. pixel variation
Map variations	-1		Maximum map variation (off)

'Value' refers to the values applied within BRATS for the corresponding 'Parameter'. The 'Description' column provides further details of the value meaning. Note that a signal to noise of 1 is still subject to the 5σ cutoff and the on-source noise multiplier.

Although the analysis method used here follows that used throughout this thesis, the choice of spectral ageing models tested differs from that of previous chapters. At GHz frequencies, the spectral age models are tightly constrained by the C-band observations with determination of the injection index weighted towards the L-band data. However, at the low frequencies used in this chapter this process is reversed, allowing better constraints to be placed on the injection index but at the cost of being able to differentiate between similar models. In particular, the Tribble model which is characterized by its additional curvature between MHz and GHz frequencies cannot be reliably separated from the standard JP model on which it is based. I therefore test only the JP and KP models of spectral ageing in this chapter.

To investigate the energetics of 3C223, we refitted the synchrotron / inverse-Compton models used by Croston et al. 2004 and 2005, constrained by the new radio observations presented here. The SYNCH code of Hardcastle et al. (1998) was used to fit a two component model consisting of a synchrotron spectrum (Section 1.3.1.1) constrained by low-frequency radio measurements, and an inverse-Compton spectrum (Section 1.3.1.2) constrained by X-ray observations. The best fitting injection index found in Section 5.3.1 of $\alpha_{inj} = 0.71$ ($\delta = 2.42$) was assumed, with an electron distribution of $\gamma_{min} = 10$ and $\gamma_{max} = 4.4 \times 10^4$. The radio lobes were modelled as cylinders using the values given in Table 5.7. Additional integrated flux densities at L-, P- and X-band band frequencies were included in the synchrotron / inverse-Compton modelling which, along with X-ray flux, were taken to be the values measured by Croston et al. (2004).

A further difference from the analysis of previous chapters is the determination of the magnetic field strength. During the Synchrotron / inverse-Compton modelling fitting, the magnetic

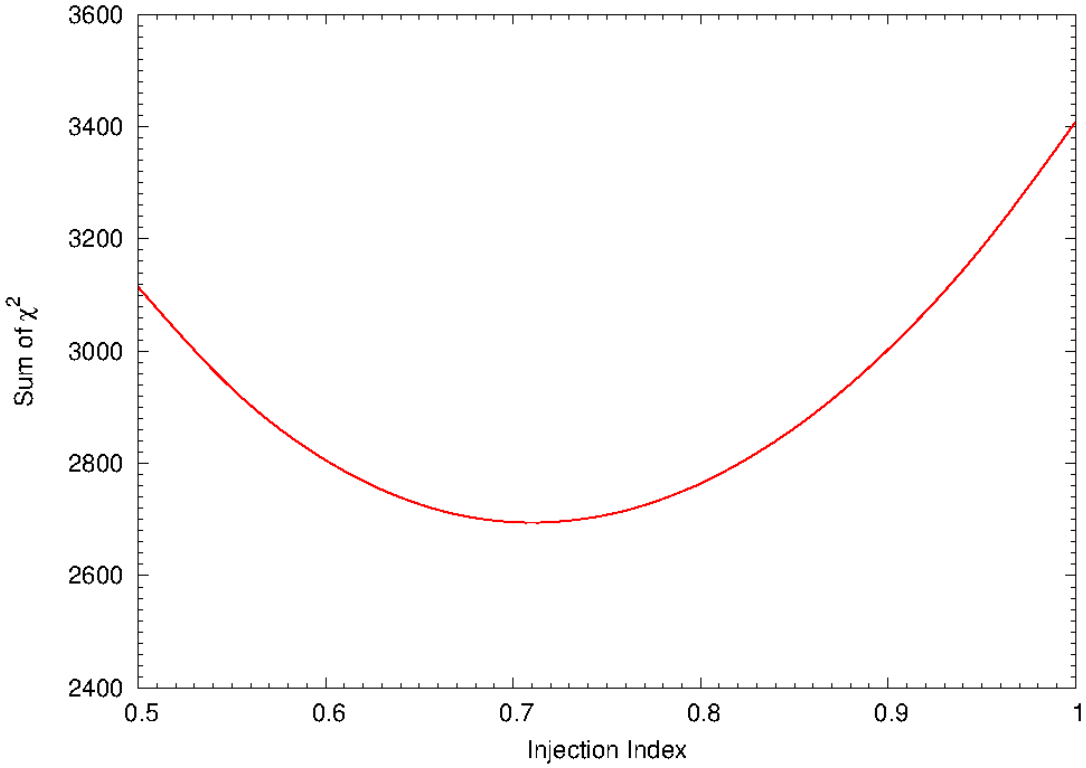

Figure 5.2: χ^2 values for 3C223 for varying injection index values fitted with a natural cubic spline. The solid blue line represents the KP model and the red dashed line the JP model. Data points are taken at intervals of 0.1 between 0.5 and 1.0 inclusive and intervals of 0.01 between 0.65 and 0.75. As all data points lie on the fitted spline, they are excluded for clarity. Note that a minimum occurs at 0.71 for all models.

field strength is adjusted to ensure that the X-ray flux measurement is reproduced by the inverse-Compton model. This methods removes the need to assume equipartition values and allows me to determine a more reliable value for the magnetic field strength. To determine the best fitting injection index I follow the method of previous chapters, using the '*findinject*' command between $\alpha_{inj} = 0.5$ and 1.0 at intervals of 0.1. A second run was then performed around the minimum at the higher resolution of 0.01. The resulting values were then plotted and the minimum injection index found. Final model fitting of the sources was then performed using the derived values. The statistical value for each model (Section 2.3.6) were recorded and spectral ageing and χ^2 maps were then exported ready for further analysis.

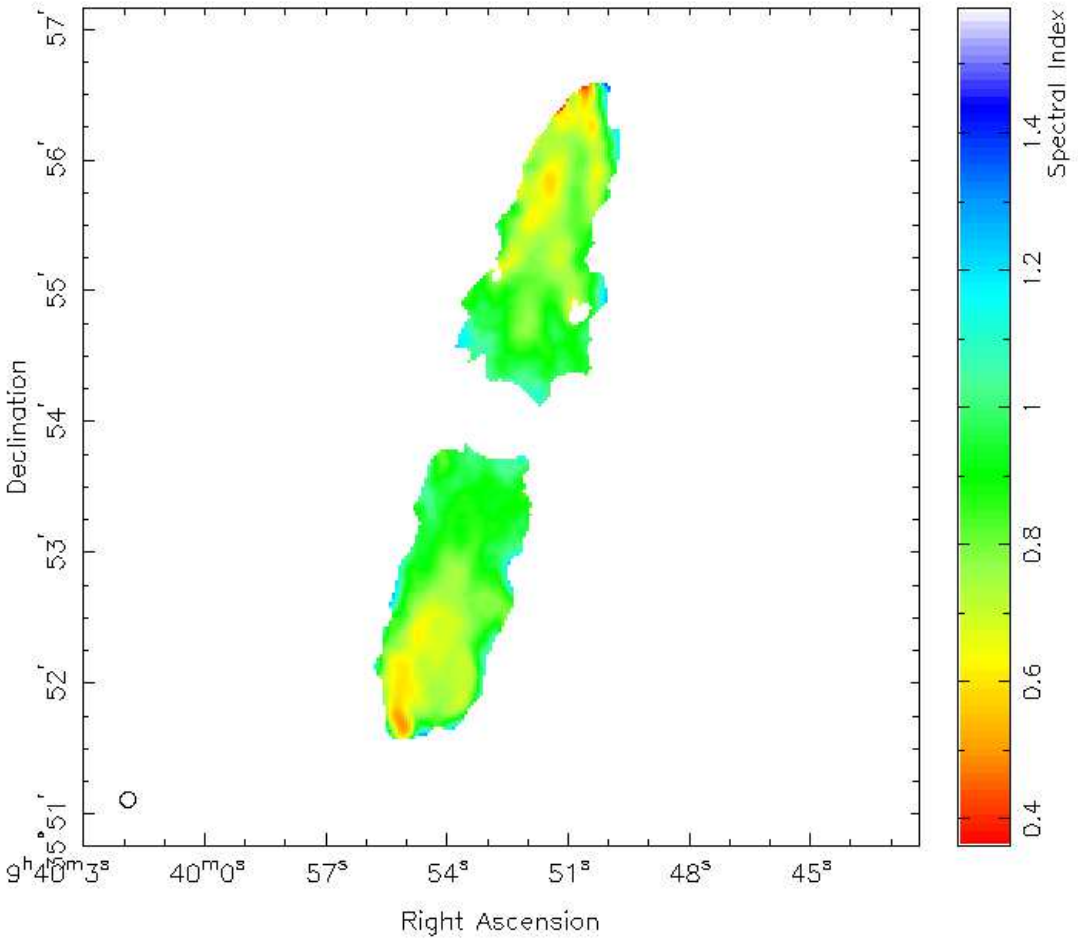

Figure 5.3: Spectral index map of 3C223 between 118 MHz and 1.48 GHz. Note the noise-like regions of flat spectrum in the northern lobe discussed in Section 5.3.3.

Table 5.7: Summary of synchrotron / inverse-Compton model parameters

Parameter	Value	Units	Comments
Length, Radius	157.5,21.5	Arcsec	Northern lobe
Length, Radius	152.0, 25.8	Arcsec	Southern lobe
δ	2.42		$\delta = 2\alpha_{inj} + 1$
E_{min}	5×10^6	eV	$\gamma \approx 10$
E_{max}	1×10^{11}	eV	$\gamma \approx 1 \times 10^6$

'Parameter' refers to the parameter name, where E_{min} is the minimum energy of the electron distribution; E_{max} is the maximum energy of the electron distribution; 'Length, Radius' are the source dimensions; and δ is the electron energy power law index given by $\delta = (\alpha_{inj}/2) - 1$ where α_{inj} is the injection index of the source determined in Section 5.3.1 The values of E_{min} and E_{max} are the same as those used by Croston et al. (2004).

5.3 Results

5.3.1 Model Parameters

As discussed in Section 5.2, the magnetic field strength of 3C223 can be determined by inverse-Compton measurements as described by Croston et al. (2004). Normalizing the spectrum of the synchrotron / inverse-Compton model to the 51.6 MHz data point and using the parameters of Table 5.7, I find a magnetic field strength of 0.36 and 0.32 nT for the northern and southern lobes respectively. I therefore take the average value of 0.34 nT for the fitting of the spectral ageing models. This magnetic field strength is much lower that those derived in Chapters 3 and 4, but this disparity is not unexpected (Croston et al., 2005) and I therefore use this value throughout this chapter. I discuss the causes of this low magnetic field strength in Section 5.4.3.

The plot of χ^2 values for varying injection indices are shown in Figure 5.2 where one can see that a clear minimum occurs at an injection index of $\alpha_{inj} = 0.71^{+0.057}_{-0.055}$. This is the lowest injection index found so far in this thesis but it is still at the highest end of the commonly assumed values for radio galaxies of 0.6 to 0.7. Where $\delta = 2\alpha_{inj} + 1$ relates the injection index α to the initial electron energy power law distribution δ, for the best-fitting injection indices I derive a value of $\delta = 2.42$, which I have used in subsequent fitting of spectral ageing models.

Table 5.8: Model Fitting Results (Spectral Ageing)

α_{inj}	Model	Mean χ^2	Mean χ^2_{red}	Confidence Bins					Rejected	Median
				< 68	68 - 90	90 - 95	95 - 99	≥ 99		Confidence
0.71	KP	3.52	0.70	5250	415	130	196	263	No	< 68
	JP	3.52	0.70	5250	415	130	196	263	No	< 68

'α_{inj}' refers to the injection index used for fitting of the 'Model' column. Mean χ^2 lists the average χ^2 over the entire source with an equivalent reduced value shown in the 'Mean χ^2_{red}' column. 'Confidence Bins' lists the number of regions for which their χ^2 values falls with the stated confidence range. 'Rejected' lists whether the goodness-of-fit to the source as a whole can be rejected as per Section 2.3.6 and 'Median Confidence' the confidence level at which the model can or cannot be rejected.

Table 5.9: Model Fitting Results (Synchrotron / Inverse-Compton)

Lobe	Volume (10^{65} m^3)	Magnetic Field Strength (nT)	Energy Density (10^{-13} J m^{-3})	Factor Increase
Northern	2.45	0.36	2.8	2.3
Southern	1.93	0.32	3.2	2.0

'Volume' refer to the volume of the lobe of 3C223 listed in the 'Lobe' column in units of 10^{65} m^3. 'Magnetic Field Strength' and 'Energy Density' list the results of the model fitting. 'Factor Increase' shows the increase in the total energy density of the lobe compared to the results of Croston et al. (2004).

5.3.2 Spectral age fitting

Figure 5.4 shows the spectral age and the corresponding χ^2 values as a function of position for the JP and KP models. Although the overall morphology of the source replicates well the spectral index map of Figure 5.3, there are a number of uncharacteristic regions which must be investigated if we are to believe these results. The first is found at the tip of the northern lobe, where one sees a small area which is best fitted by an age of ~ 80 Myrs which, due to its close proximity to the hot spot, one would expect to be low age. As noted in Section 5.2.3 the current LOFAR images, particularly the northern lobe where emission is brightest, are dynamic range limited and the high noise levels are likely to affect the measurements in some regions of the source. I therefore find it unlikely that this region provides a realistic estimate of the true source age.

A potentially more problematic characteristic of these spectral age maps is where there is a rapid increase in both the northern and southern lobes from ages < 10 Myrs to over 40 Myrs. Interpreting such sharp change is at best difficult at best given there is no obvious physical reason for such a rapid increase in age to occur. A more detailed discussion on these maps is provided in Section 5.4.1, but note here that due to the curvature being poorly constrained at higher frequencies, these maps (and by association the fitting results of Table 5.8) do not represent the true age of the source or a reliable test of the goodness of fit of the spectral ageing models.

The χ^2 maps provide a seeming contradictory picture to these non-physical ages; however, these values are weighted towards providing a measure for the goodness-of-fit to the injection index used, rather than to the ages themselves. I expand upon this reasoning further in the next section.

5.3.3 Spectral index mapping

As discussed in Section 5.1, the spectral curvature at low frequencies due to ageing is minimal, hence the spectral index at these wavelengths provides an excellent measure of the injection index. From Figure 5.3 one can see that the extended emission of the lobes (excluding any potential edge effects) is relatively smooth, ranging from $\alpha \sim 0.65$ near to the hot spot to ~ 0.8 further towards the core. It is interesting to note that in the hot spots where injection index values are often determined, flat spectral indices of $\alpha \sim 0.65$ are observed.

Whilst the spectral morphology of the southern lobe transitions smoothly as one would expect, the northern lobe displays a significantly 'knotty' structure. These features are most likely due to the dynamic range effects discussed in the previous section resulting in approximately beam sized, noise-like areas of flat spectrum being observed. I therefore focus my analysis on the southern lobe which is less likely to be affected by these issues (although many of the same arguments can still reliably be applied to both lobes).

The spectral index values of Figure 5.3 agree well with the minimization value of $\alpha = 0.71^{+0.057}_{-0.055}$. Given the findings of Section 5.3.2 where I emphasize the unreliability of the spectral ages, this may seem somewhat counter intuitive. However, as was stated in Section 5.2, the LOFAR data considered here provide tight constraints on the injection indices of the source, regardless of how well the age is constrained by higher frequency observations. It is for this same reason that the χ^2 maps shown in Figure 5.3 suggest model that fits well even though the ages are physically unrealistic. I therefore conclude that the spectral index and ageing model minimization provide a realistic picture of the injection index. I discuss the results presented here further in Section 5.4.2.

5.3.4 Synchrotron / inverse-Compton fitting

Figure 5.6 shows the results of synchrotron / inverse-Compton model fitting for the northern and southern lobes of 3C223. Within errors, the integrated LOFAR fluxes of both lobes agree well with the original observations made by Croston et al. (2004); however, the now well constrained spectrum of the emission at very low frequencies provides some interesting differences with respect to the energetics of the source. From the numerical results presented in Table 5.9, one sees that in order for the model to match the observed 1 keV inverse-Compton flux, energy densities of 2.8×10^{-13} and 3.2×10^{-13} J m^{-3} are required for the northern and southern lobes respectively. Comparing these values to those presented by Croston et al. (2004) I find an

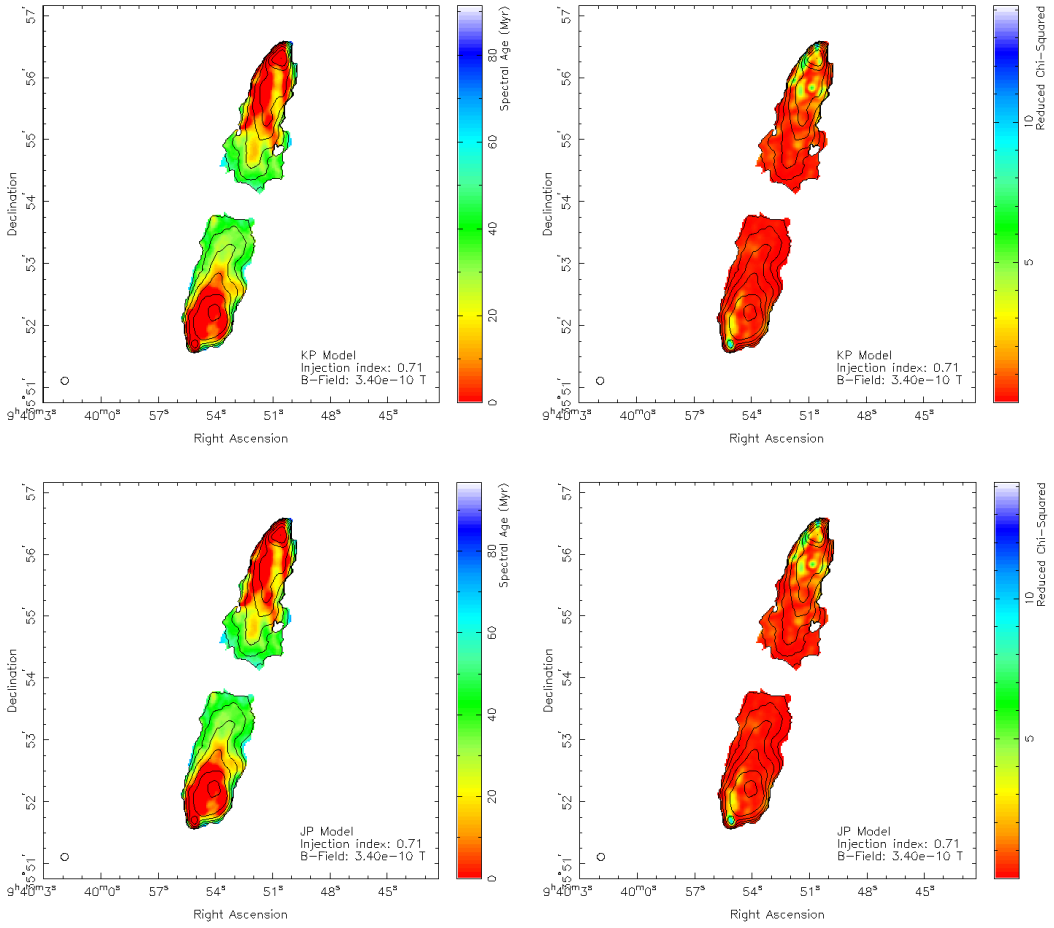

Figure 5.4: Spectral ageing maps (left) and corresponding χ^2 maps (right) of 3C223 with 1.4 GHz flux contours. Two model fits are shown; the KP model (top) and the JP model (bottom) with injection index 0.71

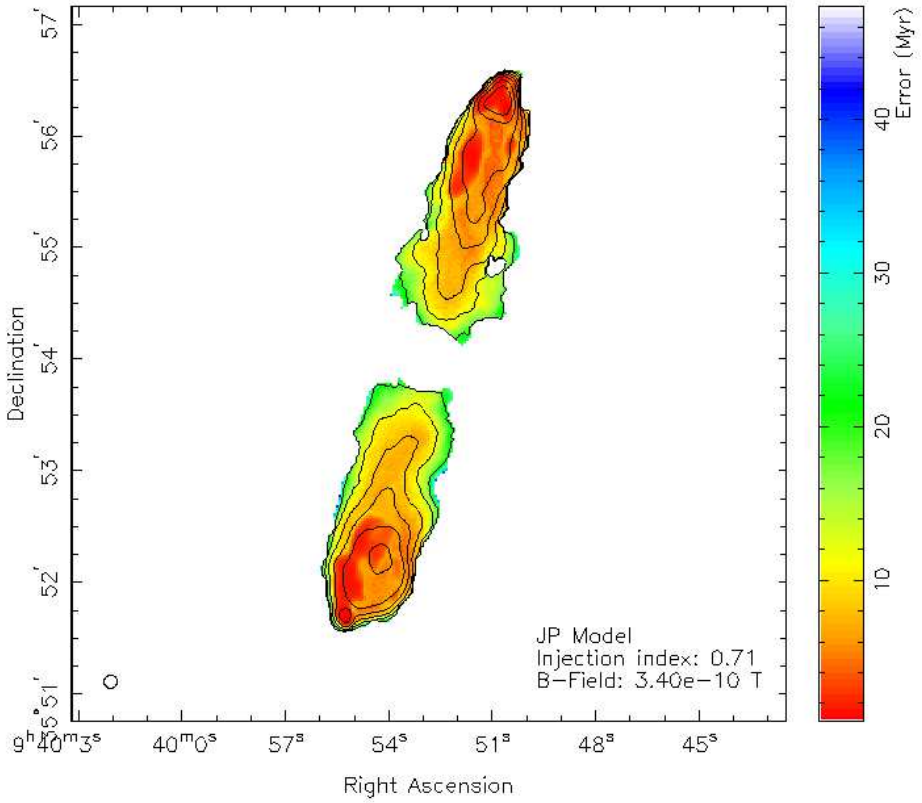

Figure 5.5: Spectral age errors of 3C223 mapped as a function of position with 1.4 GHz flux contours overlaid. Positive errors for the JP model are shown. Errors are determined using the methods described in Section 2.3.5.3.

increase in the total lobe energy density by a factor of 2.3 in the northern lobe and 2.0 in the southern lobe. I discuss the cause of this significant increase and its implications for the overall energetics of powerful radio sources further in Section 5.4.3.

5.4 Discussion

The results of Chapters 3 and 4 have shown that the injection indices required to properly describe models of spectral ageing are much steeper than previously thought. In this chapter I have used low-frequency LOFAR data, where spectral curvature due to ageing is minimal, to investigate if these high values remain present at long wavelengths, or are simply an artefact of the methods used.

These new observations have also allowed me to determine for the first time the low-frequency spectral profile of FR-II sources on small spatial scales and provide better constraints on synchrotron / inverse-Compton models. In the following sections I discuss the injection index of 3C223 and the physical reality of the injection indices and spectral ages presented within this thesis. I go on to discuss how the results of my synchrotron / inverse-Compton model fitting impacts upon the energetics of radio galaxies.

5.4.1 Spectral ages

As discussed in Section 5.3.2, the spectral ages determined in this chapter for 3C233 are not representative of the true source age. In this section I therefore discuss the reason of why the spectral ageing models tested fail to provide a realistic estimate of the source age and how this may be resolved in future studies.

One of the main benefits of the low-frequency observations used within this Chapter in the study of spectral ageing is the lack of curvature due to synchrotron and inverse-Compton losses. Whilst this makes them ideal for determining the injection index of a source, it also means that the curvature, hence age,in the 3C223 study is determined by a single 1.48 GHz data point. Given that spectral curvature is expected to be most prominent at a frequency of a few GHz, it is perhaps not surprising that the ages found here are far from reliable. The spectral ages presented in this chapter therefore emphasize that one must carefully consider where along an aged spectrum the observed data lie and which of the model's parameters are well constrained when undertaking spectral ageing studies.

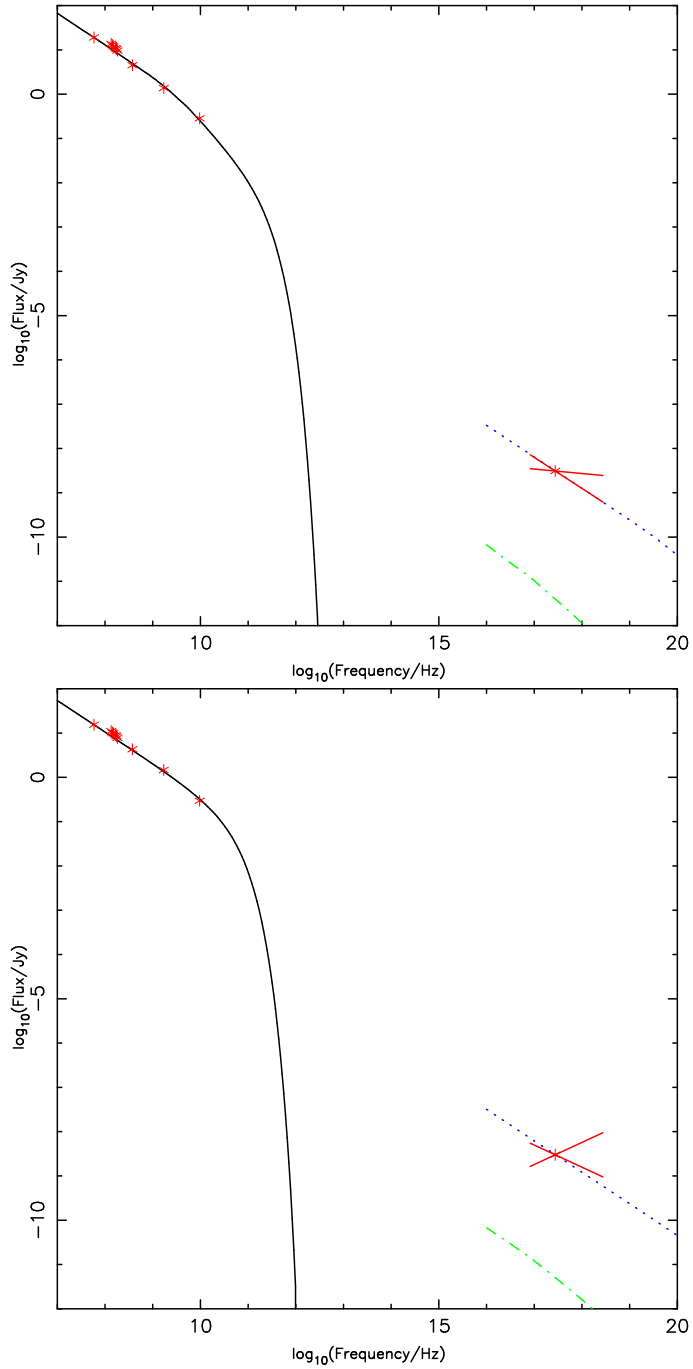

Figure 5.6: Synchrotron / inverse-Compton model fitting for the northern (top) and southern (bottom) lobes of 3C223. The red stars show the radio and X-ray integrated flux measurements taken from Croston et al. (2004) and this thesis. The red 'bow tie' shows the model constraints imposed by the X-ray observations. The solid black line shows the model synchrotron spectrum normalized to the 51.6 MHz flux and subject to JP losses, the dotted blue line the model iC/CMB emission, and the green dot-dashed line the model SSC emission. The magnetic field strength has been adjusted to ensure that the X-ray flux measurement is reproduced by the inverse-Compton model.

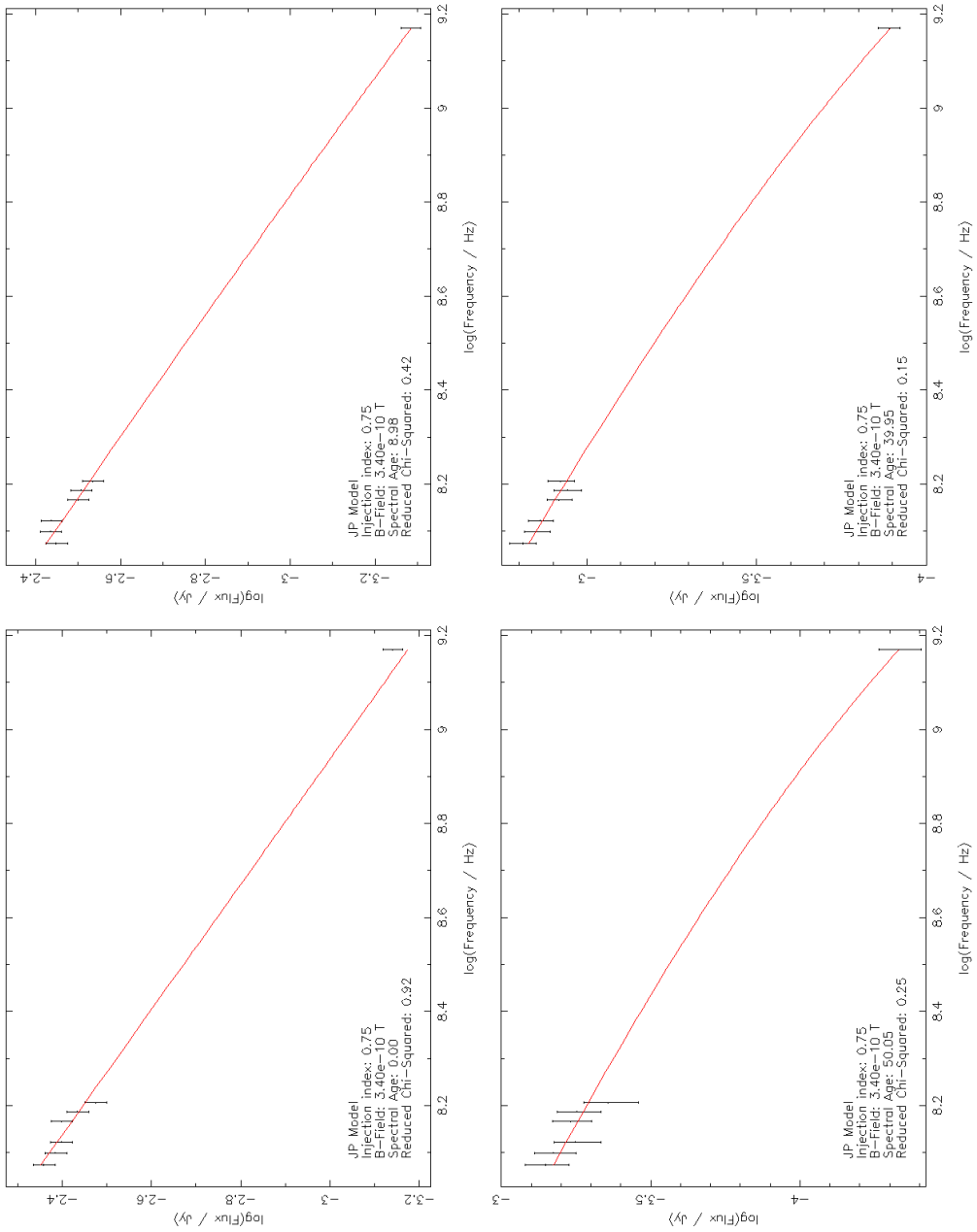

Figure 5.7: Plots of flux against frequency for four well fitted regions of 3C223 at various spectral ages. Ages increase in a clockwise direction starting at the top left. Red lines indicate the best-fitting JP model with parameters as noted on each plot.

In order to simultaneously provide good constraints on both the injection index and the spectral ages, observations over extremely wide frequency ranges (e.g. 100 MHz to 8 GHz) are required. The current capabilities of the JVLA (potentially combined with e-MERLIN observations) go a long way towards reaching this goal by allowing almost full frequency coverage between ∼230 MHz and 8 GHz. Once fully commissioned, the LOFAR international baselines will allow the lowest frequency data to be obtained at a resolution comparable to those at higher frequencies, allowing tight constraints to be placed on these key model parameters. Such studies will form part of my future work (Section 7.6).

5.4.2 Injection index

As discussed in Sections 5.3.3 and 5.1, at low frequencies spectral ageing models all converge to one common value; the injection index. The spectral index map of 3C223 (Figure 5.3) shows that large regions of the lobes located close to the core are well fitted by injection indices of $\alpha = 0.8$. Closer to the hot spot, the spectra of the diffuse emission becomes flatter reducing to values of ~ 0.7, with a similar values of 0.71 being found by the minimization of the spectral ageing model. Even at these low frequencies, the injection indices found are steeper than one would expect implying there is a physical reality behind these high values.

Further insight can be gained into the physical reality of the injection indices presented in this thesis from recent investigations of radio relics. Investigations into the radio source CIZA J2242.8+5301 (the 'Sausage') by van Weeren et al. (2012) and Stroe et al. (2013) derive an injection index of ~ 0.6. However, current work by myself and Stroe et al. (in prep) find using the methods presented in this thesis a higher value of 0.77 (Figures 5.8 and 5.9). Given that the Sausage is thought to have well ordered magnetic field and the dynamics of radio relics are much simpler than those of FR-II galaxies this is a somewhat surprising result, but suggests that higher injection index values may be common in a range of sources where spectral ageing is thought to occur.

As part of the study into the Sausage relic detailed above, additional tests of the injection index minimization process were also undertaken which can also be applied in resolving the uncertainty here. Simulated radio maps of a 'perfect' JP model between 0 and 40 Myrs and with injection index 0.77 were created and then convolved with Gaussian beams between 1 and 15 arc seconds to closer replicate real observations. Injection index minimization and spectral age fitting was then run to see if the original model parameters were recovered. We find that even when convolved to a 15 arc second resolution the recovered injection index only varies

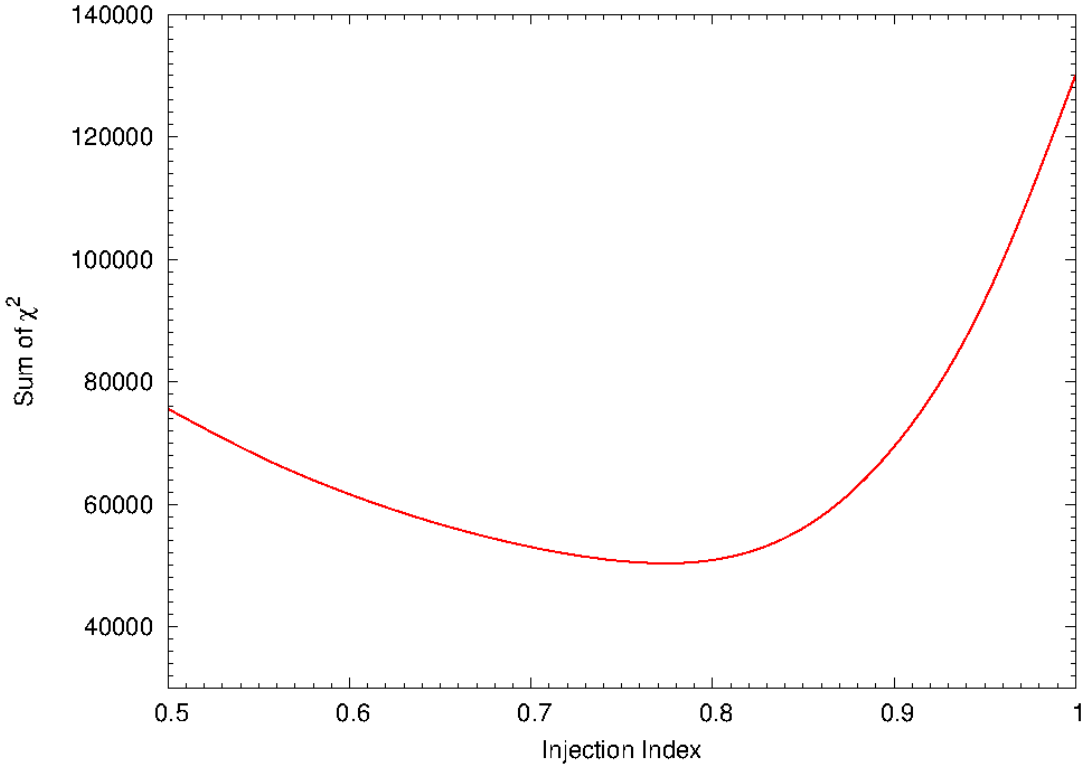

Figure 5.8: χ^2 values for the radio relic CIZA J2242.8+5301 (the Sausage) for varying injection index values fitted with a natural cubic spline (Stroe et al., in prep). The solid red line represents the JP model of spectral ageing fitted to observations at 153, 323, 608, 1221, 1382, 1714 and 2272 MHz and a magnetic field strength of 0.6 nT. Data points are taken at intervals of 0.1 between 0.5 and 1.0 inclusive and intervals of 0.01 between 0.65 and 0.75. As all data points lie on the fitted spline, they are excluded for clarity. Note that a minimum occurs at 0.77.

by ± 0.02, much less than is required to bring the injection indices in this thesis inline with the previously assumed values. It is also worth noting that the recovered spectral ages vary by a maximum of 10 per cent (less for smaller beam sizes), again within the errors of the results presented in this thesis.

Given that all four sources studied in this thesis have injection indices at or above the upper limit of the commonly assumed values, high injection index values are also found in radio relics, and the fitting of simulated data recover the initial model parameters, I conclude that the injection indices presented are a true representation of a source's intrinsic value.

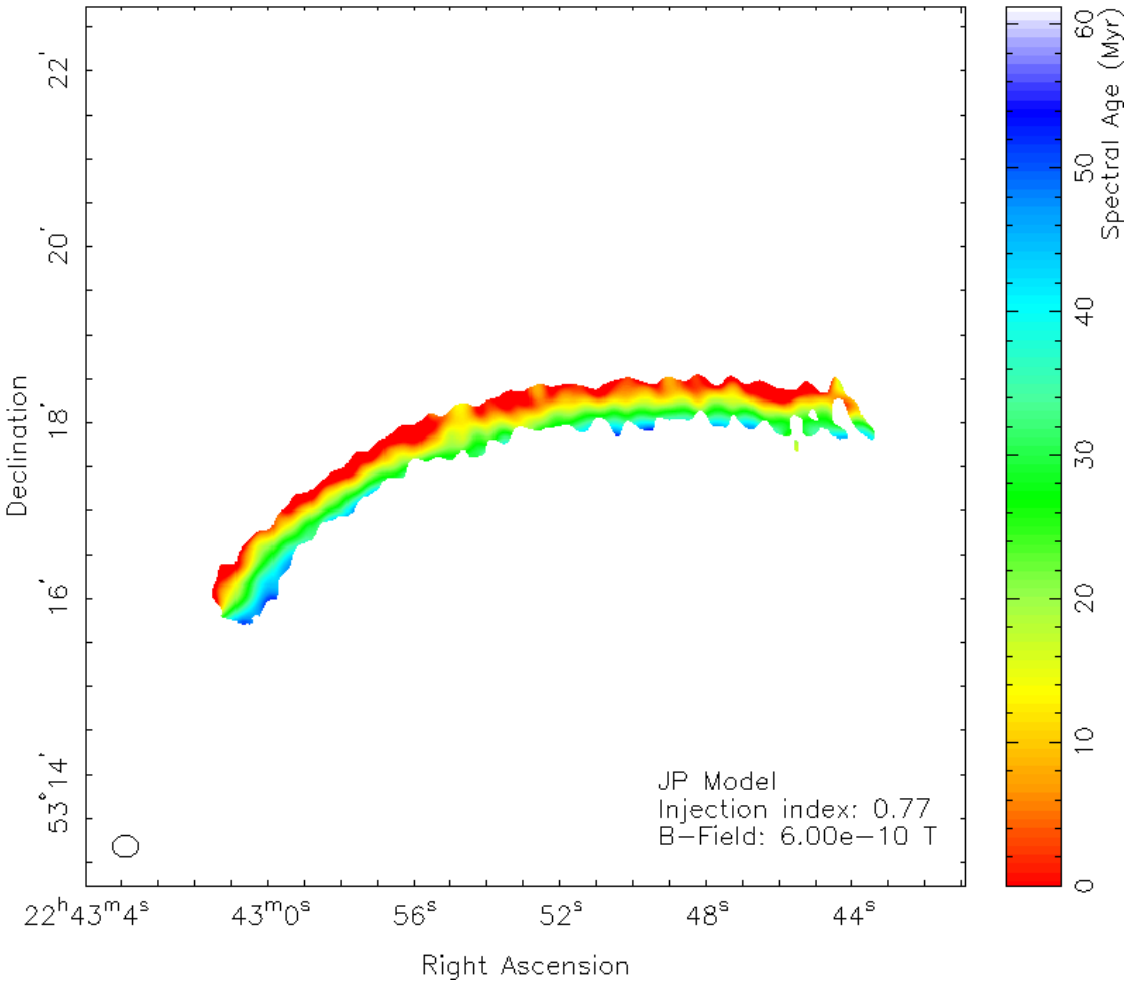

Figure 5.9: Spectral ageing map by Stroe et al. (in prep) of the radio relic CIZA J2242.8+5301 (the Sausage). The map shows the JP model fitted to observations at 153, 323, 608, 1221, 1382, 1714 and 2272 MHz using an injection index of 0.77 (Figure 5.8) and a magnetic field strength of 0.6 nT.

5.4.3 Synchrotron / inverse-Compton model fitting

The results of the synchrotron / inverse-Compton model fitting presented in Section 5.3.4 have implications for radio galaxy physics. The first which must be discussed is the determination of the magnetic field strength which is found to be lower than those used in Chapters 3 and 4. Whereas in previous chapters I have assumed that the lobes are in equipartition, the addition of X-ray observations allows the value of the magnetic field strength to be determined free from this constraint. For 3C223, the value of 0.34 nT is only ~ 75 per cent of the equipartition value of 0.45 nT. Deviation from equipartition is observed in similar FR-II sources by Croston et al. (2004, 2005), so such a difference comes as no surprise, but as was discussed in Section 3.4.3, these weaker field strengths may go at least some way to explaining the spectral / dynamical age discrepancy observed in some sources (e.g. Chapter 3). It is of course not feasible to use X-ray observations for all sources and, for most powerful radio galaxies, equipartition still provides a reasonable estimate of the magnetic field strength. However, the potential effects of such deviations from equipartition values should be carefully considered, particularly when considering model fits over very large frequency ranges where the spectral ages are well constrained.

The most significant results of the synchrotron / inverse-Compton model fitting relates to the energetics of 3C223. Comparing the total energy content of the lobes presented in Section 5.3.4 to the results of Croston et al. (2004), I find an increase by a factor of 2 in the northern lobe and 2.3 in the southern lobe of the source. The reason for this significant increase lies in the assumptions made about the radio spectrum at low frequencies where observational data were not available in the original investigations. The new integrated flux measurements made at LOFAR frequencies show that the spectrum is much steeper than previously assumed, due to a greater electron population being present at low energies. Using the standard equation for a relativistic plasma , $P_{lobe} = U/3$, where P_{lobe} is the lobe pressure and U is the total energy density, I derive pressures of 9.3×10^{-14} and 1.1×10^{-13} J m^{-3} for the northern and southern lobe respectively. Comparing these values to the external pressure at the end of the lobe derived by Croston et al. (2004) of $9.6 \times 10^{-14} \pm^{38.3}_{8.8}$ J m^{-3}, I find, contrary to the original findings, that the northern lobe is approximately in pressure balance with the external medium, with the southern lobe being overpressured. From this one can infer that the southern lobe is currently still expanding into the external medium. A summary of these pressures is given in Table 5.10.

While Croston et al. (2004) favour an underpressure interpretation in their original investigation, the large uncertainty of the external pressure at the end of the lobes means that both the

Table 5.10: Summary of lobe pressures for 3C223

Lobe	P_{lobe} (J m^{-3})	P_{ext} (J m^{-3})	$Ratio$
Northern	9.3×10^{-14}	9.6×10^{-14}	0.97
Southern	1.1×10^{-13}	9.6×10^{-14}	1.15

Table of derived lobe pressures for 3C223. 'P_{lobe}' refers to the pressure of the lobe listed in the 'Lobe' column. 'P_{ext}' is the external pressure taken from Croston et al. (2004) and 'Ratio' is the ratio of the lobe to external pressures.

overpressured and pressure balance cases fall within the error of the measurements. Conversely, the large upper error bars mean that the true external pressure may be much higher, causing the lobes to be underpressured even when the revised internal pressures presented within this chapter are considered. While the results presented here therefore suggest that the lobes are approximately in pressure balance, improved X-ray measurements are required if this question is to be answered with any reasonable degree of certainty.

Perhaps the biggest implication of the increased total lobe energy content is that the same assumptions about the low frequency spectrum were made in later work by Croston et al. (2005) for a much wider range of powerful radio sources. If this additional low energy electron population is found to be a common feature of FR-IIs, this will cause the total energy density (hence lobe pressure) of *all* FR-IIs to be increased, potentially solving the problem of underpressured, but seemingly static or expanding, radio lobes.

5.5 Conclusions

I have presented within this chapter the low-frequency study of the FR-II source 3C223. Using LOFAR observations to determine the spectrum of this powerful radio source on small spatial scales, I have investigated whether the high injection indices found in Chapters 3 and 4 are physically realistic or an artefact of the methods used. I have also investigated how these measurements impact on the calculations of the energetics of FR-II sources. The key points made within this chapter are as follows:

1. The injection index found from both the BRATS minimization method used in the previous two chapters, and through the analysis of spectral index maps are consistent with the higher values of Chapters 3 and 4. I discuss possible causes of bias but conclude that these values do have a basis in physical reality.

2. I show that whilst low-frequency observations provide excellent constraints on injection index values, GHz observations are vital if one wishes to simultaneously determine reliable spectral ages.

3. I find though synchrotron / inverse-Compton modelling that due to the steeper than previously assumed spectrum at low frequencies and subsequent underestimation of the low energy electron population, the total energy content of the lobe is increased by more than a factor of 2.

4. When the revised total energy content is accounted for, the northern lobe of 3C223 is in pressure balance with the external medium with the southern lobe being overpressured.

5. I suggest that if this additional low energy electron population is a common feature or powerful radio sources an revised estimates for the total energy content of the FR-II population as a whole will be required.

In the next chapter, I use X-ray observations of jets in low power radio galaxies to investigate what relations exist to their host galaxy properties, and if current models provide an adequate description of particle acceleration in X-ray jets.

6

What determines the properties of the X-ray jets in FR-I radio galaxies?

6.1 Introduction

In this chapter, I present the first large sample investigation of the properties of jets in Fanaroff and Riley type I radio galaxies (FR-I) based on data from the *Chandra* archive and explore relations between the properties of the jets and the properties of host galaxies in which they reside.

As was discussed in Section 1.4.3, X-ray emission from the jets of FR-I galaxies is well modelled by synchrotron emission. In many cases, a 'one-zone' model in which emission originates from a single electron population is used (e.g. Laing et al., 2008) which is supported by observations of smooth spectral transitions between the radio and optical components of jets to those observed at X-ray wavelengths (e.g. Hardcastle et al., 2001). In reality, although a one-zone model provides good agreement with many of the observed jet properties, it is unlikely that it provides a full description of the mechanism by which these jets radiate. For example, both Perlman & Wilson (2005) for M87 and Hardcastle et al. (2003) for Centaurus A require variations in the electron energy spectrum as a function of position. The short emitting lifetime of particles radiating at X-ray frequencies (Section 1.4.3) relative to the size of jets observed in FR-I galaxies also means that it is improbable that the electron energy spectrum will be the same at all points along the jet. There is therefore no *a priori* reason to assume a one-zone model. That said, this simplified model does seem to provide a good description of many observed jet properties and so is commonly used. However, while a synchrotron model appears to

describe the jets well, it leaves open the very important question of how the emitting electrons are accelerated to the high energies required to produce the X-rays.

The short radiative lifetimes of X-ray emitting electrons compared to their distance from the central core also means that this emission cannot be due to particles accelerated near the AGN; instead the emitting particles must be accelerated *in situ* in the jet (e.g. Biretta & Meisenheimer, 1993; Brunetti et al., 2003; Hardcastle, 2007; Goodger et al., 2010). Various theoretical models exist for the cause of this diffuse *in situ* acceleration, such as second order Fermi acceleration (Stawarz & Ostrowski, 2002; Rieger et al., 2007), magnetic reconnection (Birk & Lesch, 2000) and decaying beams of ultra high-energy neutrons (Atoyan & Dermer, 2004); however, determining which, if any, of these models if correct is fraught with difficulties.

Investigations into the mechanisms involved in the acceleration of jet particles to high energies have so far mainly focused around the details of individual galaxies (e.g. Kataoka et al., 2006 and Goodger et al., 2010 for Centaurus A; Birk & Lesch, 2000, Birk & Lesch, 2000 and Perlman & Wilson, 2005 for M87; see references in Tables 6.1, 6.2 and 6.3 for an extensive list of individual studies). However, with no large scale sample available for comparison, it has been hard to determine whether a feature of a particular galaxy is common across all FR-I galaxies, or whether it is unique to that target. This may, in part at least, be due to the limited number of objects which have been available for analysis; however, with a growing number of galaxies in which X-ray jets are known to be present, enough data now exist for investigations to be made into models requiring empirical data across a wider range of targets. When dealing with these bulk relations and treating the jets as a whole in this manner, one must be careful in the consideration of the underlying physics. For example, it is known that these jets must have at least two particle acceleration mechanisms; one for the small scale structure of features such as knots, and another for the large scale diffuse emission. All of these small scale and localized factors will introduce scatter in to any relations found. However, it is important to understand the large scale relations if one is to understand the underlying physics of these jets as a whole. Any general relations predicting the jets' photon indices [1], or relating jet properties to the intrinsic properties of the host galaxy in which the jets reside, have yet to be explored. It is critical that any acceleration model put forward should account for relations found in these populations. In this chapter I therefore aim to explore whether any relations exist, on large scales, between a range of jet properties and the properties of the host galaxy in which they reside, in an attempt to locate the

[1] I define the photon index to be $\Gamma \equiv \alpha + 1$ where the spectral index α relates the flux, S, and frequency, ν, by $S \propto \nu^{-\alpha}$

key variables upon which particle acceleration is dependent. In doing so I hope to give further insight into the acceleration process, and to provide a benchmark against which comparison of investigations of individual galaxies can be made.

The data I collect also allow us to test those relations which are currently assumed to exist. For example, as it is generally accepted that the emission mechanism of FR-I jets is synchrotron dominated at all wavelengths (see above), one would expect to see a smooth transition between spectra at varying wavelengths. There is therefore a general expectation that the luminosity of a galaxy's radio jets will be related to that in the X-ray; however, there is currently little empirical support at large scales for this prediction. As it is almost a requirement for this condition to be true to model X-ray jets in FR-I galaxies in a one-zone synchrotron framework, it is important to test its validity.

I make use of data collected from the *Chandra* archive to determine the luminosities and photon indices for a large sample of known X-ray jets in FR-I galaxies. These properties, along with the derived ratio of X-ray to 8.46 GHz radio flux and jet emissivity, are then compared to the luminosity of the host galaxy across the ultraviolet, visual and infrared pass bands as well as the high frequency radio luminosity in the region containing the X-ray component, the low frequency luminosity of the radio galaxy as a whole and the luminosity of the AGN core.

6.2 Target Galaxies and Analysis

I made use of the XJET website[1] (X-ray emission from extragalactic radio jets; compiled by Massaro, Harris & Cheung), which acts as a clearing house for radio galaxies and quasars in which X-ray emission has been detected and which are associated with the radio jet component, to compile a list of possible targets. As discussed in Section 6.1, the mechanism by which FR-I and intermediate FR-I/IIs emit is generally agreed to be synchrotron. This is in contrast to the on-going discussions as to the emission mechanism of FR-II galaxies in which no consensus has yet been reached. To maximize the number of data points available, all FR-I, intermediate FR-I/FR-II and BL Lac type galaxies were selected from the XJET list as of August 2010 for further investigation. The well known source 3C 78 was also included as a known good example of its class (e.g. Trussoni et al., 1999). For a galaxy within this list to be considered a suitable target, it must also have satisfied the following criteria;

[1] http://hea-www.harvard.edu/XJET

1. It should be a radio galaxy of type FR-I or be classed as intermediate between FR-I and FR-II.

2. Data should be available in the *Chandra* archive, and the count rate in the jet should have a fractional error ≤ 0.3 (equivalent to > 11 counts within the jet region).

3. Radio images of the target comparable in resolution to the *Chandra* images should be available.

Those galaxies which fulfilled these criteria were then divided into two subsamples; one complete sample including all BL Lacs and intermediate FR-I / FR-II cases and one containing only galaxies which can be considered *bona fide* FR-Is. The *Chandra* search and retrieval tool[1] (ChaSeR) was then used to resolve the target coordinates via the Simbad astronomical database[2] and retrieve a list of available data from the *Chandra* archive. In most cases only a limited number of observations were available, but for the best studied objects exposures on the AXAF (Advanced X-ray Astronomy Facility) CCD Imaging Spectrometer (ACIS) with no gratings were used for consistency with the most common setup for the fainter, less studied objects.

I reprocessed all the data using CIAO version 4.2 and the resultant calibrated event files were then used for all subsequent analysis. A summary of all potential target galaxies is displayed in Tables 6.1, 6.2 and 6.3, along with features noted on the XJET website and any reason for which a galaxy was excluded from further consideration in this chapter.

6.2.1 Jet and background region selection

I used the calibrated images to determine the regions in which the X-ray jets reside and to choose suitable regions for background emission in each data set. For this purpose SAOImage DS9 was used.

Definition of a jet region for this type of sample can be problematic. Methods such as signal to noise ratio or the use of algorithms to locate the point at which a jet terminates are not suitable due to most jets having a small angular size and low count rate, especially at the jet's furthest extent. Fixed regions both in terms of angular and physical sizes are also not suitable due to the wide variation in both redshift and morphology of the jets, so that there is no 'one size fits all' model which can be used for the sample. I therefore followed common practice in that the limit

[1] http://cxc.harvard.edu/cda/chaser.html
[2] http://simbad.u-strasbg.fr/simbad/

Table 6.1: List of target galaxies, observation IDs and noted features

Name	Class	OBSID	Exposure (ks)	X-Ray Features	z	References	Sample
0313-192	FRI RG	4874	19.17	Inner jet	0.0670	1	Both
3C 129	FRI RG	2218 - 2219	41.61	Two inner knots	0.0208	2	Both
3C 15	FRI/II RG	2178	28.18	Knot and lobes	0.0730	3	Full only
3C 264	FRI	4916	38.33	Jet	0.0217	4	Both
3C 296	FRI RG	3968	50.08	Inner jet	0.0237	5	Both
3C 31	FRI RG	2147	44.98	Inner 8" jet	0.0167	6	Both
3C 346	FRI/II RG	3129	46.69	Knot	0.1610	7	Full only
3C 371	BL Lac (FRI/II)	841	10.25	Inner and outer knots	0.0510	8, 33	Full only
		2959	40.86				
3C 465	FRI RG	4816	50.16	Knots	0.0293	9	Both
3C 66B	FRI RG	828	45.17	Inner 8" jet	0.0215	10	Both
3C 78	FRI	3128	5.23		0.0287	11	Both
		4157	53.47				

'Name' lists the name of the galaxy as used within this chapter. Centaurus A and B refer to the common names of NGC 5128 and PKS 1343-60 respectively and 0313-192 to OL97 0313-192. 'Class' lists the classification of the galaxy, 'OBSID' the *Chandra* observation ID. Exposure denotes the total observation time in kiloseconds and 'z' lists the redshift as stated on the XJET website. 'Sample' list which of the samples the galaxies are included in. 'Full only' refers to sample containing all FR-Is, intermediate FR-I/IIs and BL Lacs, those stated as 'Both' are included in this sample and the sample containing only *bona fide* FR-Is. Note that Centaurus B is excluded from either sample on the basis of it's low Chandra X-ray count and no high resolution VLA maps being available due to its location. Values taken from the XJET website herein are adopted from those declared in previous papers as listed in the 'References' column. The references are as follows: 1, Keel et al. (2006); 2, Harris et al. (2002b); 3, Kataoka et al. (2003); 4, Perlman et al. (2010); 5, Hardcastle et al. (2005b); 6, Hardcastle et al. (2002b); 7, Worrall & Birkinshaw (2005); 8, Pesce et al. (2001); 9, Hardcastle et al. (2005a); 10, Hardcastle et al. (2001); 11, Trussoni et al. (1999); 33, Sambruna et al. (2007).

Table 6.2: List of target galaxies, observation IDs and noted features (continued)

Name	Class	OBSID	Exposure (ks)	X-Ray Features	z	References	Sample
3C 83.1	FRI RG	3237	95.14	E and W knots	0.0251	12	Both
4C 29.30	FRI/II RG	2135	8.48	Hotspots	0.0640	13	Full only
		11688 - 11689	201.64				
		12106	30.45				
		12119	56.18				
B2 0206+35	FRI RG	856	8.57	Inner jet	0.0369	14	Both
B2 0755+37	FRI RG	858	8.26	4” long jet	0.0428	14	Both
Centaurus A	FRI RG	962	36.97	Knotty jet	0.0018	15 - 19	Both
		1600 - 1601	99.61				
		2978	45.18				
		3965	50.17				
		7797 - 7800	286.25				
		8489 - 8490	190.86				
		10722 - 10726	70.55				
		11846 - 11847	9.8				
Centaurus B	FRI RG	3120	5.16	Inner jet	0.0130	20	None
M84	FRI RG	803	28.85	Two inner knots	0.0035	21	Both
		5908	46.68				
		6131	41.45				

References: 12, Sun et al. (2005); 13, Sambruna et al. (2004); 14, Worrall et al. (2001b); 15, Feigelson et al. (1981); 16, Kraft et al. (2000); 17, Kraft et al. (2002a); 18, Kraft et al. (2003); 19, Hardcastle et al. (2003); 20, Marshall et al. (2005); 21, Harris et al. (2002a).

Table 6.3: List of target galaxies, observation IDs and noted features (continued)

Name	Class	OBSID	Exposure (ks)	X-Ray Features	z	References	Sample
M87	FRI RG	241	38.53	Knotty jet	0.0043	22 - 28	Both
		352	38.16				
		1808	14.17				
		2707	99.93				
		3084 - 3088	26.28				
		3717	20.83				
		3975 - 3982	43.01				
		4917 - 4923	37.03				
		5737 - 5748	62.57				
		6299 - 6305	35.7				
		7348 - 7351	20.48				
NGC315	FRI RG	4156	56.17	Inner jet knots	0.0165	29	Both
	FRI RG	855	5.15				
NGC4261	FRI RG	9569	102.24	Inner jet	0.0074	30	Both
	FRI RG	834	35.18				
NGC6251	FRI RG	847	37.44	Knots	0.0249	31	Both
		4130	49.17				
PKS0851+202	BL Lac	9182	49.97	Knots	0.306	32	Full only
PKS2201+044	BL Lac	2960	40.4	Inner and outer jet	0.027	33	Full only
S5 2007+777	BL Lac (FRI/II)	5709	36.87	Jet	0.342	34	Full only

Reference: 22, Biretta et al. (1991); 23, Marshall et al. (2002); 24, Wilson & Yang (2002); 25, Harris et al. (2003); 26, Perlman et al. (2003); 27, Perlman & Wilson (2005); 28, Harris et al. (2006); 29, Worrall et al. (2003); 30, Chiaberge et al. (2003); 31, Mack et al. (1997); 32, Marscher & Jorstad (2011); 33, Sambruna et al. (2007); 34, Sambruna et al. (2008).

of the jet was defined to be the point at which the emission was no longer discernible by eye from the background emission. This leads to some additional uncertainty and makes the process subjective in nature, but it allows us to retain a sample that is not restricted to one specific size or morphology. To help in reducing the subjective effects of this selection technique the jets were defined without reference to other work and before any measurements had been taken, so as to keep my definition independent of external influences. Once these regions had been defined they were fixed for the duration of the investigation.

Once the jet regions were determined, it was necessary to select an area for which a representative average background count could be taken to allow for any emission from the galaxy, such as thermal emission, that was not representative of the X-ray jet. These were defined using two methods, dependent on the nature of the region in question. For targets in which the background was not uniformly distributed, the region was selected to be approximately parallel to, and comparable in length and shape with, the X-ray jet region so as to account for any changes in background properties along the length of the region (Figure 6.1, left panel). This was my standard method for targets in which background emission displays significant irregular variation as a function of position along the jet. A good example of this is Centaurus A, in which the obscuring dust lane causes the background emission to vary along the length of the jet.

The second method was used for galaxies in which background emission was on average evenly distributed at any angle from the galactic centre. In these cases, a circular region was taken around the central point to the furthest extent of the jet (Figure 6.1, right panel). The central AGN, X-ray jet region and any point sources were then excluded from the selection. Although this is a more complex process than the first method, by encompassing a large area in this manner a more accurate average value for the background level can be obtained.

6.2.2 Collection of spectral and comparative data

The spectrum of the jet for each retrieved observation was extracted by use of a Perl script, which again calls upon the CIAO data analysis system by use of the *specextract* command. This script creates a variety of additional files containing a PHA (pulse height amplitude) formatted header compatible with the spectral analysis software XSPEC[1] by referencing the jet and background region files previously created. The extracted spectra files were loaded into XSPEC and any channels marked as bad due to the binning process were set to be ignored. The column density

[1] http://heasarc.gsfc.nasa.gov/docs/xanadu/xspec/

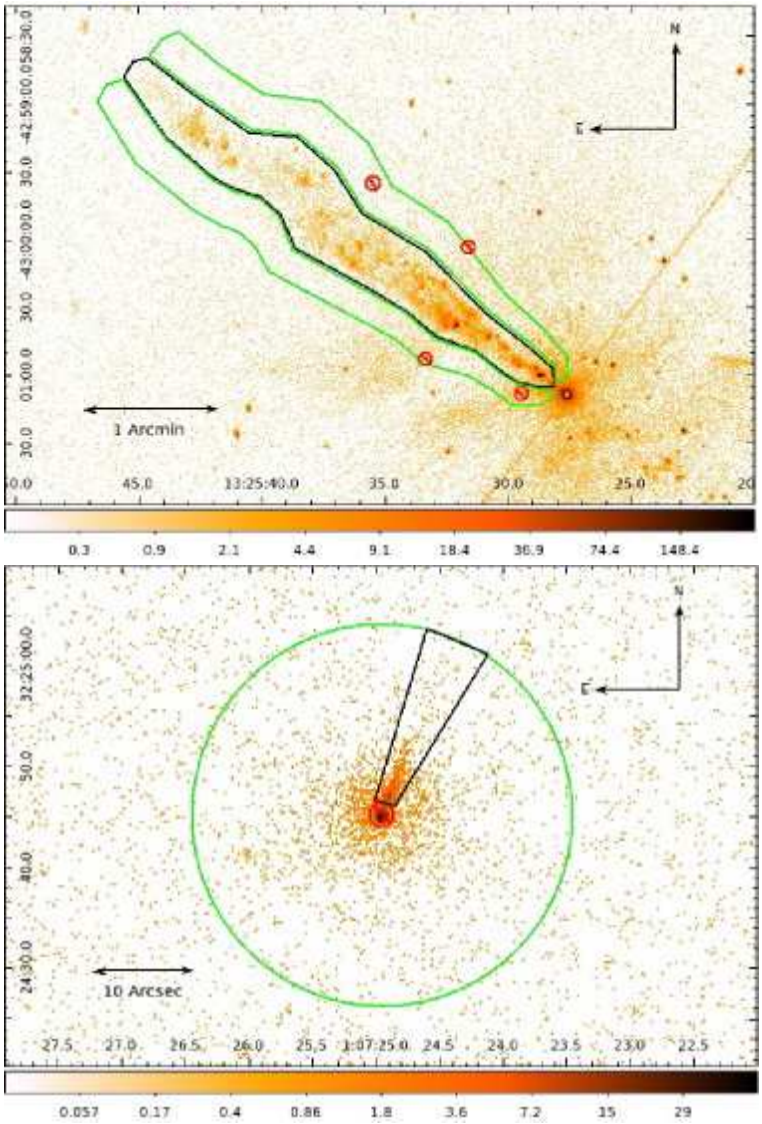

Figure 6.1: Examples of background region selection. Solid black regions denote the selected jet region; Solid green denotes are the boundary for inclusion in the background region; Red crossed areas denote regions excluded from consideration. Note: In the case of method 2 (bottom) black regions are included for the jet, but excluded for background measurements. The top image displays Cen A as an example of the method used for cases in which background emission varies irregularly as a function of position along the jet. The regions run alongside the jet to its furthest extent. Note the dust lane (see Section 6.2.3) which runs across the jet approximately $1/3$ of the way from the galactic centre and the exclusion of emission due to point sources which fall in the line of sight. The bottom image shows 3C 31 as a case in which background emission is symmetrical about the galactic centre. A large circular region encompasses the largest possible area for an improved uncertainty measurement. Note the exclusion of the jet and AGN regions.

Table 6.4: Tested host galaxy properties and their source

Tested Property	Region	Survey Name	References	Abbreviation / Comments
B band magnitude	Whole source	Updated Zwicky catalogue	1	UZC
H band magnitude	Whole source	The Two Micron All Sky Survey	2	2MASS
J band magnitude	Whole source	The Two Micron All Sky Survey	2	2MASS
K band magnitude	Whole source	The Two Micron All Sky Survey	2	2MASS
4.65 GHz emission	Whole source	New catalogue of 4.85 GHz sources	3	New cat of 4.85 GHz sources
8.46 GHz emission	X-Ray jet region	-	-	Measured from radio maps
Jet volume	X-Ray Jet Region	-	-	Measured from radio maps
Ratio of 4.65 GHz emission	X-ray flux / 4.65 GHz flux	-	-	Derived
Acceleration efficiency	X-ray flux / 8.46 GHz flux	-	-	Derived
Emissivity	Luminosity / Volume	-	-	Derived
Core luminosity	AGN core	-	4 - 5	5 GHz AGN core
Core prominence	Core flux / 4.65 GHz flux	-	-	Measure of beaming

'Tested Property' lists the host galaxy property against which the X-ray luminosity and photon index were compared. 'Region' lists the area over which this value was measured where 'Whole Source' refers to the integrated flux of the host galaxy taken directly from the survey referenced. 'Survey Name' lists the source from which the data was taken . The 'References' column refers to: 1, Falco et al. (1999); 2, Skrutskie et al. (2006); 3, Becker et al. (1991); 4, Hardcastle et al. (2005b); 5, Hardcastle et al. (2009a). 'Abbreviation / Comments' lists the short name used for the survey within this chapter where applicable, and any comments on the nature of the property. Derived refers to values which have been calculated from previously stated measurements.

for each target was obtained using the Colden neutral hydrogen density calculator[1]. The spectral energy distribution (SED) was then fitted in the 0.4 - 7.0 keV range with an absorbed power law model to determine the normalization, photon index and their associated errors. In cases where the target galaxy had multiple observations, spectra were extracted for each and the model was fitted to all the spectra simultaneously. A flux for the jet was then derived from the normalization values which was converted to a luminosity in the standard manner.

Due to the faint nature of the jets and the scarcity of target galaxies, every effort was made to include as much data as possible in the sample. In some cases, the number of counts within the jet region was too low for any usable data to be obtained. However, in some intermediate cases where the counts were too low to extract a reliable SED automatically via XSPEC, so that a photon index could not be measured, it was still possible to obtain a value for the flux by extrapolation of the available data points. In these cases, I used non-grouped versions of the spectra. These files were loaded into XSPEC and energies between 0.0 and 0.4 keV and above 7.0 keV were ignored. An average photon index of 2.1 was taken from the jets in which fits were possible (Tables 6.5 and 6.6) and, along with the column density, entered into the model fixing these values to leave the normalization as the only variable. Using the model in this way, it was possible to obtain the normalization of a power-law model that would produce the observed net count rate from which a flux can be derived in the same manner as previously stated.

[1] http://cxc.harvard.edu/toolkit/colden.jsp

Table 6.5: Observed jet properties

Name	nH (10^{22} cm^{-2})	Photon Index	$\pm$	X-ray Flux (Jy)	$\pm$	X-ray Lum (W Hz^{-1})	$\pm$	8.46 GHz Radio Flux (Jy)	8.46 GHz Radio Lum (W Hz^{-1})
0313-192	0.0318	-	-	4.29×10^{-10}	2.47×10^{-10}	4.55×10^{15}	2.62×10^{15}	0.0006	6.82×10^{21}
3C 15	0.0303	2.63	0.20	1.34×10^{-09}	5.64×10^{-10}	1.70×10^{16}	7.17×10^{15}	0.1321	1.68×10^{24}
3C 296	0.0186	1.96	0.24	1.52×10^{-09}	5.37×10^{-10}	1.89×10^{15}	6.68×10^{14}	0.0239	2.98×10^{22}
3C 31	0.0541	2.22	0.09	9.55×10^{-09}	9.34×10^{-10}	5.82×10^{15}	5.70×10^{14}	0.0997	6.08×10^{22}
3C 346	0.0561	2.06	0.26	9.58×10^{-10}	3.88×10^{-10}	6.67×10^{16}	2.70×10^{16}	0.1958	1.36×10^{25}
3C 371	0.0484	2.01	0.04	3.90×10^{-08}	1.89×10^{-09}	2.34×10^{17}	1.13×10^{16}	0.0984	5.91×10^{23}
3C 465	0.0506	1.85	0.44	1.65×10^{-09}	5.09×10^{-10}	3.16×10^{15}	9.76×10^{14}	0.0841	1.98×10^{22}
3C 66B	0.0891	2.38	0.08	1.76×10^{-08}	1.28×10^{-09}	1.78×10^{16}	1.30×10^{15}	0.0841	8.52×10^{22}
3C 78	0.0943	2.08	0.09	1.49×10^{-08}	1.39×10^{-09}	2.31×10^{16}	2.16×10^{15}	0.0981	1.52×10^{23}
3C 83.1	0.1445	-	-	4.04×10^{-10}	2.95×10^{-10}	5.63×10^{14}	4.12×10^{14}	0.0181	2.53×10^{22}
3C 264	0.0254	2.23	0.06	4.41×10^{-08}	2.71×10^{-09}	4.56×10^{16}	2.80×10^{15}	0.0889	9.20×10^{22}
4C 29.30	0.0398	-	-	3.15×10^{-09}	6.76×10^{-10}	3.04×10^{16}	6.52×10^{15}	0.0304	2.94×10^{23}

'Name' lists the designation of the target as per the conventions described in Table 6.1. 'nH' refers to the neutral hydrogen column density as given by the Colden calculator. Other columns are as described within the table, where $\pm$ indicates the uncertainty of the preceding column. Uncertainty in radio measurements are taken to be 3 per cent based on the uncertainty in absolute flux calibration of the VLA at the frequencies used.

Table 6.6: Observed jet properties (continued)

Name	nH (10^{22} cm^{-2})	Photon Index	$\pm$	X-ray Flux (Jy)	$\pm$	X-ray Lum (W Hz^{-1})	$\pm$	8.46 GHz Radio Flux (Jy)	8.46 GHz Radio Lum (W Hz^{-1})
B2 0206+35	0.0604	-	-	3.18×10^{-09}	8.45×10^{-10}	9.75×10^{15}	2.59×10^{15}	0.0427	1.31×10^{23}
B2 0755+37	0.0508	1.89	0.45	8.87×10^{-09}	2.62×10^{-09}	3.71×10^{16}	1.10×10^{16}	0.0316	1.32×10^{23}
Centaurus A	0.0841	1.78	0.01	2.67×10^{-07}	2.53×10^{-09}	3.92×10^{14}	3.71×10^{12}	7.1413	1.05×10^{22}
M84	0.0278	1.73	0.36	2.08×10^{-09}	5.33×10^{-10}	7.21×10^{13}	1.84×10^{13}	0.0328	1.13×10^{21}
M87	0.0254	2.36	0.00	3.39×10^{-07}	1.62×10^{-09}	1.04×10^{16}	4.96×10^{13}	5.0457	1.55×10^{23}
NGC315	0.0592	2.17	0.07	1.55×10^{-08}	1.20×10^{-09}	9.25×10^{15}	7.14×10^{14}	0.0841	5.02×10^{22}
NGC4261	0.0158	2.21	0.13	4.27×10^{-09}	4.78×10^{-10}	4.91×10^{14}	5.50×10^{13}	0.0360	4.13×10^{21}
NGC6251	0.0554	2.09	0.09	1.24×10^{-08}	1.16×10^{-09}	1.69×10^{16}	1.59×10^{15}	0.0347	4.75×10^{22}
PKS0851+202	0.0302	1.75	0.05	2.74×10^{-08}	1.69×10^{-09}	8.14×10^{18}	5.02×10^{17}	0.0042	1.25×10^{24}
PKS2201+044	0.0515	2.04	0.09	1.52×10^{-08}	1.32×10^{-09}	2.44×10^{16}	2.13×10^{15}	0.0408	6.57×10^{22}
S5 2007+777	0.0879	1.25	0.17	4.35×10^{-09}	8.84×10^{-10}	1.68×10^{18}	3.41×10^{17}	0.0040	1.53×10^{24}

'Name' lists the designation of the target as per the conventions described in Table 6.1. 'nH' refers to the neutral hydrogen column density as given by the Colden calculator. Other columns are as described within the table, where $\pm$ indicates the uncertainty of the preceding column. Uncertainty in radio measurements are taken to be 3 per cent based on the uncertainty in absolute flux calibration of the VLA at the frequencies used.

Table 6.7: Jet volume and derived properties

Name	Volume (m^3)	$\pm$	J(X) (W Hz^{-1} m^{-3})	$\pm$	J(8.46GHz) (W Hz^{-1} m^{-3})	$\pm$	X-ray to Radio Flux Ratio	$\pm$
0313-192	5.50×10^{59}	8.46×10^{59}	8.27×10^{-45}	1.36×10^{-44}	1.24×10^{-38}	1.90×10^{-38}	6.67×10^{-07}	3.85×10^{-07}
3C 15	2.89×10^{60}	1.91×10^{60}	5.90×10^{-45}	4.63×10^{-45}	5.82×10^{-37}	3.86×10^{-37}	1.01×10^{-08}	4.28×10^{-09}
3C 296	3.12×10^{59}	1.39×10^{59}	6.06×10^{-45}	3.45×10^{-45}	9.57×10^{-38}	4.28×10^{-38}	6.33×10^{-08}	2.25×10^{-08}
3C 31	3.43×10^{59}	1.80×10^{59}	1.70×10^{-44}	9.05×10^{-45}	1.77×10^{-37}	9.30×10^{-38}	9.58×10^{-08}	9.80×10^{-09}
3C 346	5.39×10^{60}	5.20×10^{60}	1.24×10^{-44}	1.30×10^{-44}	2.53×10^{-36}	2.44×10^{-36}	4.89×10^{-09}	1.99×10^{-09}
3C 371	1.48×10^{59}	1.06×10^{59}	1.58×10^{-42}	1.14×10^{-42}	3.99×10^{-36}	2.86×10^{-36}	3.97×10^{-07}	2.26×10^{-08}
3C 465	1.25×10^{60}	3.51×10^{59}	2.54×10^{-45}	1.06×10^{-45}	1.59×10^{-38}	4.50×10^{-39}	1.60×10^{-07}	4.96×10^{-08}
3C 66B	8.44×10^{58}	5.61×10^{58}	2.11×10^{-43}	1.41×10^{-43}	1.01×10^{-36}	6.71×10^{-37}	2.09×10^{-07}	1.65×10^{-08}
3C 78	1.62×10^{59}	6.70×10^{58}	1.42×10^{-43}	6.03×10^{-44}	9.39×10^{-37}	3.89×10^{-37}	1.52×10^{-07}	1.49×10^{-08}
3C 83.1	8.54×10^{59}	3.59×10^{59}	6.60×10^{-46}	5.57×10^{-46}	2.96×10^{-38}	1.25×10^{-38}	2.23×10^{-08}	1.63×10^{-08}
3C 264	3.21×10^{58}	2.13×10^{58}	1.42×10^{-42}	9.51×10^{-43}	2.87×10^{-36}	1.91×10^{-36}	4.96×10^{-07}	3.39×10^{-08}
4C 29.30	3.00×10^{61}	1.13×10^{61}	1.01×10^{-45}	4.40×10^{-46}	9.79×10^{-39}	3.71×10^{-39}	1.04×10^{-07}	2.24×10^{-08}

'Name' lists the designation of the target as per the conventions described in Table 6.1. 'Volume' refers to that of the jet as modelled by a truncated cone.'J(...)' refers to the derived emissivity at the stated wavelength and '$\pm$' to the uncertainty of the preceding column.

Table 6.8: Jet volume and derived properties (continued)

Name	Volume (m^3)	$\pm$	J(X) (W Hz^{-1} m^{-3})	$\pm$	J(8.46GHz) (W Hz^{-1} m^{-3})	$\pm$	X-ray to Radio Flux Ratio	$\pm$
B2 0206+35	4.27×10^{59}	2.13×10^{59}	2.28×10^{-44}	1.29×10^{-44}	3.07×10^{-37}	1.53×10^{-37}	7.44×10^{-08}	1.99×10^{-08}
B2 0755+37	1.09×10^{60}	5.92×10^{59}	3.40×10^{-44}	2.10×10^{-44}	1.21×10^{-37}	6.60×10^{-38}	2.80×10^{-07}	8.33×10^{-08}
Centaurus A	1.09×10^{58}	1.12×10^{57}	3.60×10^{-44}	3.72×10^{-45}	9.61×10^{-37}	1.03×10^{-37}	3.74×10^{-08}	1.18×10^{-09}
M84	2.95×10^{56}	1.98×10^{56}	2.45×10^{-43}	1.76×10^{-43}	3.85×10^{-36}	2.59×10^{-36}	6.36×10^{-08}	1.64×10^{-08}
M87	2.11×10^{57}	1.12×10^{57}	4.93×10^{-42}	2.62×10^{-42}	7.33×10^{-35}	3.91×10^{-35}	6.72×10^{-08}	2.04×10^{-09}
NGC315	3.67×10^{59}	1.96×10^{59}	2.52×10^{-44}	1.36×10^{-44}	1.36×10^{-37}	7.28×10^{-38}	1.84×10^{-07}	1.53×10^{-08}
NGC4261	8.49×10^{58}	1.93×10^{58}	5.79×10^{-45}	1.47×10^{-45}	4.87×10^{-38}	1.12×10^{-38}	1.19×10^{-07}	1.38×10^{-08}
NGC6251	2.49×10^{60}	8.81×10^{59}	6.81×10^{-45}	2.50×10^{-45}	1.91×10^{-38}	6.80×10^{-39}	3.56×10^{-07}	3.50×10^{-08}
PKS0851+202	1.23×10^{64}	3.37×10^{63}	6.61×10^{-46}	1.85×10^{-46}	1.02×10^{-40}	2.80×10^{-41}	6.49×10^{-06}	4.46×10^{-07}
PKS2201+044	2.44×10^{60}	8.96×10^{59}	1.00×10^{-44}	3.77×10^{-45}	2.69×10^{-38}	9.91×10^{-39}	3.72×10^{-07}	3.43×10^{-08}
S5 2007+777	1.22×10^{64}	3.25×10^{63}	1.38×10^{-46}	4.63×10^{-47}	1.26×10^{-40}	3.38×10^{-41}	1.10×10^{-06}	2.25×10^{-07}

'Name' lists the designation of the target as per the conventions described in Table 6.1. 'Volume' refers to that of the jet as modelled by a truncated cone.'J(...)' refers to the derived emissivity at the stated wavelength and '$\pm$' to the uncertainty of the preceding column.

6. WHAT DETERMINES THE PROPERTIES OF THE X-RAY JETS IN FR-I RADIO GALAXIES?

Once the luminosity of a jet had been determined, it was then possible to derive a value for its volume emissivity. I again used DS9 to measure the width of the jet at the top and bottom of the selected region along with the total jet length. Radio maps were used for this purpose as they provided greater resolution than those obtained at X-ray wavelengths. Modelling the jet as a truncated cone, I then calculated its volume in the standard manner. The jet's luminosity was then divided by this value to give a value for its mean volume emissivity in the radio and X-ray wavebands.

As no previous studies have been carried out of this nature, as many properties as were practicable, given the available data, were tested for a correlation with those properties intrinsic to the X-ray jet. The data to which the X-ray properties were compared can be broadly broken down into two types; those which represent the host galaxy as a whole and those which are contained within the bound region of the X-ray jet. The properties of the host galaxies as a whole were the most straightforward to obtain as, thanks to works such as the two micron all sky survey (2MASS), apparent magnitudes at a given passband are widely available for a large number of nearby galaxies. Although the data were collated from previous studies, it was important for consistency and reliability that a limited number of trusted sources were used. As no single survey covers the entire frequency range in question, the Updated Zwicky catalogue (Falco et al., 1999), the 2 mm all sky survey (Skrutskie et al., 2006) and the new catalogue of 4.85 GHz sources (Becker et al., 1991) were used to obtain the required values. A total of twelve properties were chosen for comparison against the X-ray jet luminosity and its photon index and values were retrieved from the NASA Extragalactic Database (NED)[1]. For the AGN core luminosities, a well studied relation exists between emission at radio and X-ray wavelength (e.g. Hardcastle et al., 2006b, 2009b). I therefore used 5 GHz radio data taken from Hardcastle & Worrall (1999), Canosa et al. (1999), Hardcastle & Worrall (2000a) and references therein as a measure of core luminosity. These values were also divided through by the total source 4.85 GHz luminosity to give its core prominence. This acts as a useful measure for comparison of properties and relations in which relativistic beaming may have a significant effect. A list of the chosen properties to be tested, and their origin, is shown in Table 6.4.

8.46 GHz radio measurements of the jet properties had to be obtained in a different way. Pre-existing radio maps were used which had been processed in the standard manner using AIPS and loaded into DS9. I then used the original region files created for determination of the X-ray flux to define the required radio jet area. I defined a representative background and used Funtools

[1] http://nedwww.ipac.caltech.edu/

Table 6.9: AGN core properties

Name	5 GHz Core Flux(Jy)	5 GHz Core Luminosity (W)	Core Prominence	References
0313-192	0.1030	1.09E+24	-	-
3C 15	0.0297	3.78E+23	0.0177	-
3C 296	0.0770	9.59E+22	0.0376	1
3C 31	0.0920	5.61E+22	0.0442	1
3C 346	0.2200	1.53E+25	0.1583	1
3C 371	1.9807	1.19E+25	-	-
3C 465	0.2700	5.18E+23	0.0912	1
3C 66B	0.1820	1.84E+23	0.0619	1
3C 78	0.5780	8.99E+23	0.1533	-
3C 83.1	0.0400	5.58E+22	-	1
3C 264	0.2000	2.07E+23	0.1163	1
4C 29.30	0.1060	3.25E+23	-	2
B2 0206+35	0.0082	7.91E+22	-	2
B2 0755+37	0.1900	7.95E+23	0.1845	2
Cen A	5.5100	8.08E+21	0.0877	-
M84	0.1800	6.22E+21	0.0503	3
M87	4.0000	1.23E+23	0.0670	3
NGC315	0.4500	2.68E+23	0.3782	2
NGC4261	0.3036	3.49E+22	0.0742	-
NGC6251	0.8500	1.16E+24	-	3
PKS0851+202	1.7404	5.17E+26	0.6643	-
PKS2201+044	0.3189	5.13E+23	0.4304	-
S5 2007+777	0.9689	3.74E+26	-	-

'Name' lists the designation of the target as per the conventions described in Table 6.1. '5 GHz Core Flux' values are taken from 'References'. Where no reference is given, values have been measured directly from radio maps. Where a 5 GHz measurement does not exist, values have been extrapolated from other frequencies using a spectral index of 0. The references are as follows: 1, Hardcastle et al. (1999); 2, Canosa et al. (1999); 3, Hardcastle & Worrall (2000a).

to calculate a background-subtracted measurement of the radio flux density. The luminosity of the radio jet was then derived from this value in the standard manner. For sources in which no 8.46 GHz data was available, measurements at alternative frequencies were made. These values were then converted using $S_{8.46GHz} = S_{\nu}(8.46 \text{ GHz}/\nu)^{-\alpha}$ where ν is the measured frequency; I assume a value of $\alpha = 0.6$ to give an equivalent radio flux density at the required frequency of 8.46 GHz. Where no 5 GHz AGN core data were available in the references, these maps were also used to measure the core flux where a value of $\alpha = 0$ was assumed.

6.2.3 Treatment of special cases

The amount of information relating to specific target galaxies within the sample varies widely, both in terms of the raw data and the literature available. For the nearest bright sources, small-scale features can be resolved which in the fainter and more distant galaxies cannot be seen. I therefore had to consider carefully what information from detailed studies should be taken into account, bearing in mind the need for consistency across the sample.

One target which required such special consideration was that of Centaurus A. This is one of the best-studied galaxies within the sample and, at its distance of only 3.7 Mpc, the jet can be very well resolved. Three issues had to be considered in this case. Firstly, it is known that a dust lane cuts across the jet, creating greater than average extinction within this region. Accounting for the differences in column density along the length of the jet would help to improve the accuracy of the derived values; however, in the vast majority of the other target galaxies the much lower quality of the X-ray data means that it is not possible to produce a spatially resolved absorption map. As there is nothing to suggest that Centaurus A is in any way a special case in this sense, the increased absorption in this region was not accounted for but simply noted for later discussion. Secondly, it is known (e.g. Hardcastle, 2007) that the photon index along the jet varies in magnitude. However, as I am only considering the average value across the extent of the jet, and as any variation of the photon index cannot be determined to a comparable accuracy in the case of most galaxies within the sample, this was again ignored for current purposes. Finally, an uneven distribution of the background emission can be seen much more clearly in Centaurus A than in most other galaxies in the sample. The uneven distribution of background emission is not limited to the best-resolved galaxies, so my knowledge of this distribution could be used in determining the most appropriate background region, leading to a reduction in uncertainty of the X-ray flux and photon index without compromising the consistency of the data as a whole.

Until recently it was thought that extended radio sources, such as those found in FR-I galaxies, and their related X-ray components were a feature limited to elliptical galaxies. It has subsequently been shown by Keel et al. (2006) however, that this is not always true; the so-called 'wrong galaxy' OL97 0313-192, has a spiral structure. Other examples of radio sources in disk type galaxies (e.g. Emonts et al., 2009) have also been found, showing that this is not an isolated case; however, OL97 0313-192 is the only such example for which both *Chandra* data and high resolution VLA maps are currently available. As this galaxy was already included on the XJET website and met all the selection criteria I saw no reason to reject this galaxy from consideration. This target also provided a good opportunity to test varying environments through which jets pass in relation to its elliptical counterparts.

6.3 Results

6.3.1 Statistical analysis

I searched for correlations between the measured values using a Spearman's rank test. If, and only if, a correlation was present between two quantities that both depended on redshift (e.g. two luminosities or magnitudes) then I used a partial correlation analysis based on the methodology presented by Akritas & Siebert (1996). These partial correlation results were then used to determine whether the relation was still statistically significant to a 5 per cent level. Statistically significant correlations for the full sample are listed in Table 6.10 and for the same restricted to *bona fide* FR-Is in Table 6.11. Correlations not found to be significant for the full sample are listed in in Table 6.12 and for the restricted sample in Table 6.13.

6.3.2 Photon index relations

One can see from Table 6.10 that when the full sample is considered, no properties are found to be related to the photon index of the jets; However, in my subsample of *bona fide* FR-Is I find relations with both the X-ray and 8.46 GHz radio luminosity.

One can see that in both of these relations photon index increases with increasing luminosity (Figure 6.2); relative intensity of high-energy emission is reduced in more luminous sources. It is evident from the plots that both these relations can be described in the form of a power law. Using the least squares fit method in the standard manner, I find that the relation to the X-ray luminosity is given by $\Gamma \propto L_X^{0.03\pm0.01}$ where Γ is the photon index. In the same manner I find that the relation to the 8.46 GHz radio luminosity is given by $\Gamma \propto L_{R8.46}^{0.04\pm0.02}$.

Table 6.10: Correlated test results (full sample)

Tested Property	Jet Property	Spearman's Rank Coefficient	τ/σ	Significance Level
8.46 GHz Radio Emissivity	X-Ray Emissivity	0.87923	7.52691	1%
8.46 GHz Radio Luminosity	X-Ray Luminosity	0.87538	4.40877	1%
4.85 GHz Radio Luminosity	X-Ray Luminosity	0.75965	2.46778	1%
Core 5 GHz	X-Ray Luminosity	0.74209	4.06009	1%
Jet Volume	X-Ray Emissivity	0.72769	5.20254	1%
Jet Volume	8.46 GHz Radio Emissivity	0.70923	4.20029	1%
Core 5 GHz	8.46 GHz Radio Luminosity	0.58597	2.01274	1%
Core 5 GHz	X-Ray Flux / 8.46 GHz Radio Flux	0.56917	2.85995	1%
Core Prominence	X-Ray Flux / 8.46 GHz Radio Flux	0.71311	-	2%
Absolute B Band Magnitude	X-Ray Luminosity	0.55038	2.28628	2%

Table of tested properties which show a statistically significant correlation. 'Tested Property' lists the measured value compared to that shown in the adjacent 'Jet Property' column. '8.46 GHz' refers to radio measurements confined to the same region as the X-ray jet as per Table 6.4. 'Spearman's Rank' refers to the value of the Spearman's rank coefficient of the two properties. 'τ/σ' lists the value obtained from the partial correlation analysis when compared to redshift, where a value >2 indicates that the null hypothesis can be rejected at a 95 per cent confidence level. Photon index and core prominence are not expected to have any dependence on redshift hence, under the criteria detailed in Section 6.3.1, was excluded from a partial correlation analysis. 'Significance Level' indicates to the significance level at which the relation is found.

Table 6.11: Correlated test results (*bona fide* FR-Is only)

Tested Property	Jet Property	Spearman's Rank Coefficient	τ/σ	Significance Level
8.46 GHz Radio Emissivity	X-ray Emissivity	0.89461	6.27738	1%
8.46 GHz Radio Luminosity	X-Ray Luminosity	0.87010	8.25512	1%
Jet Volume	8.46 GHz Radio Emissivity	0.75490	3.62678	1%
Core 5 GHz	X-Ray Flux / 8.46 GHz Radio Flux	0.74706	2.70024	1%
Core 5 GHz	X-Ray Luminosity	0.67353	2.68152	1%
Core Prominence	X-Ray Flux / 8.46 GHz Radio Flux	0.69780	-	2%
8.46 GHz Radio Luminosity	Photon Index	0.64835	-	2%
Jet Volume	X-Ray Emissivity	0.64216	3.67540	2%
X-Ray Luminosity	Photon Index	0.60440	-	5%
Core 5 GHz	8.46 GHz Radio Luminosity	0.60000	2.50615	5%

'Tested Property' lists the measured value compared to that shown in the adjacent 'Jet Property' column. '8.46 GHz' refers to radio measurements confined to the same region as the X-ray jet as per Table 6.4. 'Spearman's Rank' refers to the value of the Spearman's rank coefficient of the two properties. 'Significance Level' indicates the significance level at which the relation is found.

Given the result of Hardcastle (2007) on the variation of photon index with distance along the jet in Centaurus A, I searched for a correlation between photon index and jet length in my sample; however, it is immediately evident from the values in Table 6.13 that no correlation is present.

I also searched for correlations between the photon index and 9 other intrinsic properties of the host galaxy; however, no significant correlations were found in either the full sample, or the subsample (Tables 6.12 and 6.13).

6.3.3 Derived ratios

As discussed in the introduction, particles emitting at X-ray wavelengths must be accelerated *in situ*. The efficiency with which particles residing at low energies are accelerated is therefore well represented by the ratio $L_X/L_{R8.46}$, which is confined to the region of the X-ray jet. One can see from the results of the Spearman's rank test that the ratio of $L_X/L_{R8.46}$ is related to the 5 GHz radio core luminosity and core prominence. I discuss this relation further in the next section. Outside of these relations I observe no link between the derived ratios and the properties of the host galaxy.

This lack of correlation between $L_X/L_{R8.46}$ and luminosities at X-ray and radio wavelengths does, however, provide useful information about the processes involved. From the plot of $L_X/L_{R8.46}$ against 8.46 GHz radio luminosity, as shown in Figure 6.2, I find that the acceleration efficiency as measured by $L_X/L_{R8.46}$ shows little dependence on luminosity over a wide range of $L_{R8.36}$ if *bona fide* FR-Is are considered. This is again discussed further in Section 6.4.2.

6.3.4 Luminosity & emissivity relations

One would expect radio and X-ray luminosities to be correlated, and it can be seen from the results in Tables 6.10 and 6.11 that this is indeed the case for both the full and restricted sample; there is a strong correlation in the Spearman's rank test. This relationship is at the 1 per cent significance level in both cases and so one can be fairly confident that a true correlation exists; however, the emissivity's lack of correlation to the photon index is more unexpected and opens up an additional mystery which I discuss in Section 6.4. It is not surprising that this relation is found in both of the samples as the targets excluded from the restricted sample are primarily high luminosity galaxies at both X-rays and radio wavelengths (red points, Figure 6.2). This

therefore precludes any definite inferences being drawn from the full sample as even if a break or multiple relations are present, these additional galaxies are small enough in number and high enough in power at both wavelengths that they will still score well in a Spearman's rank test. Looking at Figure 6.2, one can see evidence of this with the much greater scatter exhibited by these high power objects compared to the *bona fide* FR-Is.

For the restricted sample, where the correlation is better constrained, the relations between X-ray luminosity and emissivity to those at 8.46 GHz wavelengths can again be described by a power law. This strong correlation, discussed further in Sections 6.3.3 and 6.4.2, lends the first good empirical support to the previously assumed relation between these quantities. It also provides reinforcement to the relationships found for *bona fide* FR-Is with the photon index, as a correlation between the two luminosities naturally leads to an expectation that either both, or neither, should be correlated with any third variable.

One can also see that volume emissivity reduces as a function of volume at both X-ray and radio wavelengths in both samples. The lack of correlation between volume emissivity and luminosity, however, implies that the effects of an increasing volume outweighs the effects of a reduced emissivity in terms of the total power output of the jet.

Relationships in both samples are also seen to exist between X-ray luminosity of the jet and the 5 GHz radio core luminosity (Figure 6.2). Both of these properties are known to depend on both jet power and orientation, but only the X-ray jet has a dependence on acceleration efficiency between X-ray and radio energies. The ratio of $L_X/L_{R8.46}$ which, as discussed in Section 6.4.2, can be taken as a measure of acceleration efficiency, also has a dependence on orientation. This is because as the jets are viewed from smaller angles to the line of sight one expects to observe an increase in the Doppler factor. Assuming a broken power law or similar concave spectrum, between emission at radio and X-ray wavelengths, the increase in emission at X-ray wavelengths will be greater due to the steeper spectral index at these energies compared to the relatively flat spectral index of the radio emission. This leads to an apparent increase in the ratio of $L_X/L_{R8.46}$. Knowing these dependencies, one can compare the 5 GHz core luminosity to $L_X/L_{R8.46}$. Out of these two properties, only the core luminosity is dependent on power, hence if a relation between X-ray luminosity and the 5 GHz radio core is either not present or much worse than that between X-ray luminosity and the 5 GHz radio core, it is likely that the jet power is the dominant property. However, if it is found that the relation is comparable or has improved, it is the common dependence on orientation and hence beaming that is the most

likely cause of the relation. From Tables 6.10 and 6.11 one can clearly see that in both samples relationships are found to comparable significance.

As mentioned in Section 6.2.2, core prominence can be used as a measure of beaming within these galaxies. I therefore decided to test this property against the ratio of $L_X/L_{R8.46}$ as additional confirmation of this conclusion. As expected a relation at the 2 per cent level is present. This drop in significance is not particularly surprising, as although core prominence is a commonly used measure of beaming, it does not allow for factors such as ageing and so additional scatter is introduced. I therefore believe that beaming rather than a relationship with the intrinsic power of the jet is the most likely explanation for this relationship in both cases.

There are two X-ray luminosity relations that exist in the full sample, which are absent from the restricted sample, being those with the absolute B band magnitude and 4.85 GHz radio luminosity. The relation to B band magnitude I believe is again a result of the effects of orientation. The B-band luminosities of BL Lac objects are, by definition, partly or wholly related to their nuclear jets. At the same time beaming causes an increase in X-ray luminosity, so for the full sample which contains several BL Lacs, the inclusion of these objects will lead to a natural correlation between B band and X-ray luminosities.

I believe that the correlation between the 4.85 GHz radio luminosity and the X-ray luminosity is also due to the nature of the full sample over that of the *bona fide* FR-Is. The jets and lobes of the intermediate FR-I / II and BL Lacs included in the full sample are observed to have a much higher power at radio wavelengths than their FR-I counter parts (Figure 6.2). The radio emission of these jets is included in the measurement of the galaxy's total 4.85 GHz luminosity and so, for these galaxies, the jets are likely to dominate the total galactic emission. I therefore believe that this relation is due to sample selection, rather than to any intrinsic property of the galaxies.

Although some correlations were initially seen to exist in other host galaxy properties when subjected to the Spearman's rank test, I find upon applying partial correlation analysis that these were merely a result of redshift (Tables 6.12 and 6.13). I therefore conclude that there are no statistically significant relations linking the properties of the host galaxy to that of the jet.

Table 6.12: Uncorrelated test results (full sample)

Tested Property	Jet Property	Spearman's Rank Coefficient	τ/σ
Absolute K Band Magnitude	X-Ray Luminosity	0.48271	1.63588
X-Ray Luminosity	X-Ray Flux / 8.46 GHz Flux	0.45923	1.77570
Absolute J Band Magnitude	X-Ray Luminosity	0.40902	1.21711
8.46 GHz Emissivity	Photon Index	0.43609	-
X-ray Emissivity	Photon Index	0.37744	-
Absolute H Band Magnitude	X-Ray Luminosity	0.31880	-
Core 5 GHz	Photon Index	0.25614	-
8.46 GHz Luminosity	Photon Index	0.22556	-
X-Ray Flux / 8.46 GHz Flux	Photon Index	0.20902	-
Absolute H Band Magnitude	X-Ray Flux / 8.46 GHz Flux	0.19549	-
Core 5 GHz	X-ray Emissivity	0.17095	-
Absolute B Band Magnitude	Photon Index	0.15196	-
4.85 GHz Luminosity	Photon Index	0.14551	-
Absolute J Band Magnitude	X-Ray Flux / 8.46 GHz Flux	0.09323	-
4.85 GHz Luminosity	X-Ray Flux / 8.46 GHz Flux	0.08596	-
Absolute B Band Magnitude	X-Ray Flux / 8.46 GHz Flux	0.06316	-
8.46 GHz Luminosity	X-Ray Flux / 8.46 GHz Flux	0.05692	-
Absolute K Band Magnitude	Photon Index	0.04231	-
Absolute J Band Magnitude	Photon Index	0.04025	-
X-Ray Luminosity	Photon Index	0.03158	-
Absolute K Band Magnitude	X-Ray Flux / 8.46 GHz Flux	0.01955	-
Absolute H Band Magnitude	Photon Index	0.00310	-

Table of tested properties which do not show a statistically significant correlation. 'Tested Property' lists the variable compared to that shown adjacent as 'Jet Property'. '8.46 GHz' refers to radio measurements confined to the region of the X-ray jet and '4.85 GHz' to total emission from the jet and host galaxy as per Table 6.4 'τ/σ' lists the value obtained from the partial correlation analysis when compared to redshift, where a value >2 indicates that the null hypothesis can be rejected at a 95 per cent confidence level. Note that luminosity is not tested against jet volume, as this is naturally biased towards a correlation due to the selection criteria. 'Spearman's Rank' refers to the value of the Spearman's rank coefficient of the two properties.

Table 6.13: Uncorrelated test results (*bona fide* FR-Is only)

Tested Property	Jet Property	Spearman's Rank Coefficient	τ/σ
4.85 GHz Luminosity	X-Ray Luminosity	0.68352	1.95037
X-Ray Luminosity	X-Ray Flux / 8.46 GHz Flux	0.57108	1.79649
Absolute K Band Magnitude	X-Ray Luminosity	0.55604	1.46254
Absolute J Band Magnitude	X-Ray Luminosity	0.55604	1.46254
Absolute H Band Magnitude	X-Ray Luminosity	0.55604	1.02397
Absolute B Band Magnitude	X-Ray Luminosity	0.42143	-
X-ray Emissivity	Photon Index	0.37143	-
8.46 GHz Emissivity	Photon Index	0.35824	-
X-Ray Flux / 8.46 GHz Flux	Photon Index	0.31868	-
4.85 GHz Luminosity	X-Ray Flux / 8.46 GHz Flux	0.30549	-
4.85 GHz Luminosity	Photon Index	0.29670	-
Absolute H Band Magnitude	Photon Index	0.18681	-
Absolute J Band Magnitude	Photon Index	0.18681	-
Absolute K Band Magnitude	Photon Index	0.18681	-
8.46 GHz Luminosity	X-Ray Flux / 8.46 GHz Flux	0.14951	-
Absolute H Band Magnitude	X-Ray Flux / 8.46 GHz Flux	0.11071	-
Absolute J Band Magnitude	X-Ray Flux / 8.46 GHz Flux	0.11071	-
Absolute K Band Magnitude	X-Ray Flux / 8.46 GHz Flux	0.11071	-
Core 5 GHz	Photon Index	0.10989	-
Core 5 GHz	X-ray Emissivity	0.07941	-
Absolute B Band Magnitude	X-Ray Flux / 8.46 GHz Flux	0.02647	-
Absolute B Band Magnitude	Photon Index	0.01648	-

Table of tested properties which do not show a statistically significant correlation. 'Tested Property' lists the variable compared to that shown adjacent as 'Jet Property'. '8.46 GHz' refers to radio measurements confined to the region of the X-ray jet and '4.85 GHz' to total emission from the jet and host galaxy as per Table 6.4. 'τ/σ' lists the value obtained from the partial correlation analysis when compared to redshift, where a value >2 indicates that the null hypothesis can be rejected at a 95 per cent confidence level. Note that luminosity is not tested against jet volume, as this is naturally biased towards a correlation due to the selection criteria. 'Spearman's Rank' refers to the value of the Spearman's rank coefficient of the two properties.

6.4 Discussion

6.4.1 Current models of particle acceleration

It is generally agreed (e.g. Hardcastle et al., 2003; Kataoka et al., 2006) that at least two forms of particle acceleration are present within the jets of radio galaxies. There is growing evidence, particularly in the case of Centaurus A (e.g. Goodger et al., 2010), that emission relating to small scale features such as knots is due to shock acceleration caused by interaction with a compact stationary or slow moving body. This acceleration is seen to dominate emissions from the innermost sections of the jet in galaxies such as Centaurus A (e.g. Hardcastle, 2007); however, the particles responsible for the more diffuse emission which dominates the outer jet regions cannot be explained in the same manner, so the particles radiating at these wavelengths must be accelerated by a second process (Hardcastle et al., 2004b; Kataoka et al., 2006). The inability to resolve all but the closest jets to this level of detail means it is uncertain whether this is the case for all FR-I galaxies; however, it is likely that diffuse emission will be present in the majority, if not all cases, based on those objects in which they can currently be resolved.

6.4.2 Key emission process variables

Determining which, if either, of the processes discussed in Section 6.4.1 causes the acceleration of particles to the very high energies required for X-ray emission to be produced has proved to be difficult, and a definitive answer has unsurprisingly not emerged in this thesis; however, the results of Section 6.3.2 do carry significant implications for key features of the acceleration process.

The photon index gives a measure of how emission intensity changes as a function of frequency; therefore it can be interpreted as giving an indication of how efficiently particles are being accelerated at the very highest energies, as it effectively tells us about the ratio between the number of low-energy and high-energy particles producing the X-ray emission. A lower photon index represents a harder X-ray distribution, with a greater proportion of particles having been accelerated to higher energies. I find that for *bona fide* FR-Is there is a reduction of the relative intensity of high-energy emission in more luminous sources. This suggests that acceleration to the highest energies is either less efficient, or that particles suffer greater radiative losses in conditions in which the jet luminosity is highest.

However, the photon index is not the only measure of acceleration efficiency. Whereas the photon index represents the efficiency of particle acceleration to energies required for the hardest

X-ray emission, the ratio of $L_X/L_{R8.46}$ provides a means of determining efficiency in terms of particles being accelerated from the energies required for radio emission, to those required for X-ray emission. It is interesting to note therefore that the BL Lac and intermediate FR-I / II objects occupy a range in this quantity almost double that in which the *bona fide* FR-Is reside. This increased scatter is a recurring feature of all common relationships between the full and restricted samples, suggesting that there are at a minimum two separate populations. For BL Lac objects, which are thought to be beamed FR-I galaxies, this is likely to be a result of beaming effects which increase greatly at small jet angles to the line of sight. However, the greatest scatter is exhibited in the intermediate objects which lie between the FR-I and FR-II classifications. I therefore suggest that this is a second population, operating under a separate set of conditions or mechanisms to that of the *bona fide* FR-I subsample.

Considering only the *bona fide* FR-Is in Figure 6.2, the ratio of L_X and $L_{R8.46}$ of the subsample falls within two orders of magnitude, and is reasonably constant across the range of photon indices. If the full sample does indeed contain two separate populations and so can be excluded from consideration, the relationship between X-ray and radio luminosities becomes near linear as $(L_X) \propto L_{R8.46}^{1.11\pm0.21}$. As the value of $L_X/L_{R8.46}$ also represents the relation between X-ray and radio luminosities with the power law removed, the plot of $L_X/L_{R8.46}$ against $L_{R8.46}$ therefore simply represents the scatter around this relationship. A linear scaling therefore provides the best description of the luminosity-luminosity correlation for bona fide FR-Is, providing a consistent interpretation across all observed data.

The lack of correlation between $L_X/L_{R8.46}$ and photon index also holds implications for particle acceleration models. As the two efficiencies are seen to be independent of each other, any models explaining the dependence of photon index on jet luminosity must also ensure they do not also affect the overall observed acceleration efficiency. In Section 6.4.3 I test one such model in which radiative losses dominate the relative number of particles emitting at the highest energies.

One can also see from Section 6.3.2 and 6.3.4 that the host galaxy luminosity in various optical and infrared bands, and hence the average host galaxy environment in which the jets reside, have little to no impact on either the luminosity or photon index of the X-ray jet in either of the samples. If the host galaxy environment did have a strong effect on the jet luminosities, one would most likely notice a peculiarity in the properties of the spiral galaxy OL97 0313-192 due to its morphology and composition in comparison to the ellipticals which comprise the majority of the sample. However, I find that this is far from the case; in fact the source exhibits

very average values both in terms of X-ray and radio jet luminosities, and is indistinguishable on my plots from the elliptical galaxies. The same reasoning can also be applied to the photon index, in that the ability to accelerate particles to the high-energy end of the X-ray range seems to be independent of the properties of the host galaxy through which the jet passes. Again, if the region of the host galaxy through which the jet passes were a dominant factor in determining the acceleration to the highest electron energies, the photon index in the environment of the spiral galaxy would be unlikely to take such an typical value. Therefore the mechanism causing the acceleration of these particles must on these large scales, be largely independent of the host galaxy's bulk properties. Although the case of OL97 0313-192 strengthens the case for this low dependence, I emphasize that the key observation underpinning this weak dependence on the host galaxy's bulk properties is the lack of correlation observed between jet properties and the host galaxy's luminosity in various optical and infrared bands.

6.4.3 Testing of viable acceleration models

As mentioned in Section 6.3.2, the photon index relations must either be a result of decreased acceleration efficiency, or increased radiative losses, at higher jet luminosities. Although it has been established that for at least some compact jet regions inverse-Compton losses dominate (e.g. Perlman et al., 2011), synchrotron losses will dominate on larger scales, and so the properties of a jet should depend on its magnetic field strength, in the sense that jets with a higher field strength will suffer stronger synchrotron losses and should therefore be less able to accelerate particles to the highest energies. In this section I investigate whether these losses alone can give rise to the photon index relation one observes in the sample of *bona fide* FR-Is in a similar manner to the process proposed for the emission from the hotspots of FR-II sources (e.g. Hardcastle et al., 2004a)

For synchrotron emission, intensity is peaked around a critical frequency which scales as

$$\nu_{crit} \propto \gamma^2 B \tag{6.1}$$

However, the effect of particle energy loss also counteracts this effect, scaling as

$$\frac{\mathrm{d}E}{\mathrm{d}t} \propto \gamma^2 B^2 \tag{6.2}$$

The loss timescale of an emitting particle is given by

$$\tau = \frac{E}{\mathrm{d}E/\mathrm{d}t} \tag{6.3}$$

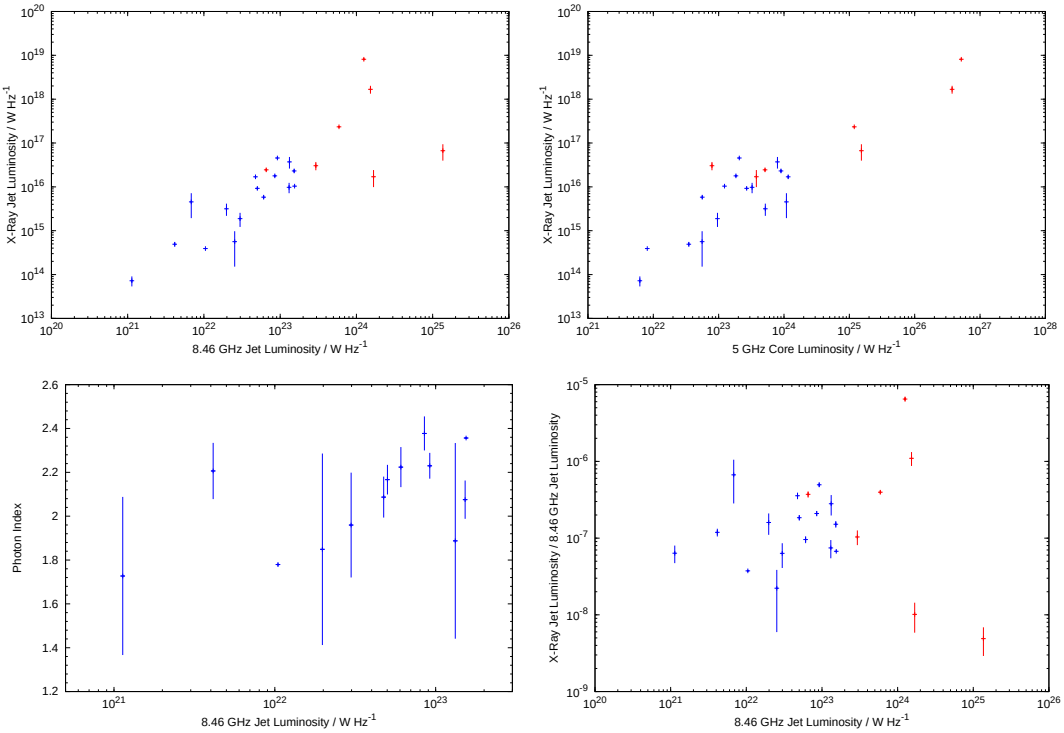

Figure 6.2: Top left: The strong correlation between jet luminosity at radio and X-ray wavelengths. Top right: The correlations between 5 GHz core luminosity and X-ray jet luminosity discussed in Section 6.3.4. Bottom left: The relation between 8.46 GHz radio luminosity and photon index in *bona fide* FR-Is discussed in Section 6.3.2. Bottom right: Plot of flux ratio against radio luminosity discussed in Section 6.4.2. Blue points are those classed as *bona fide* FR-Is. Red points represent the BL Lacs and intermediate cases included in the full sample.

where $E = \gamma mc^2$ is the particle energy. Applying the known scaling for synchrotron losses (6.2) to equation (6.3) one therefore finds that

$$\tau \propto \frac{\gamma mc^2}{\gamma^2 B^2} \tag{6.4}$$

Substituting for γ in terms of the critical frequency in equation (6.1) one finds that

$$\tau \propto \frac{mc^2}{\nu^{1/2} B^{3/2}} \tag{6.5}$$

As for my observations I can take the observing frequency ν to be fixed, I therefore find that the energy time loss scales as

$$\tau \propto \frac{1}{B^{3/2}} \tag{6.6}$$

Although values for the magnetic field within the jets cannot currently be measured directly, the field strength within the jets is often assumed to be around the equipartition value (e.g. Leahy 1991) in which the energy contribution of the field is equal to that of the emitting particles. Under this assumption, luminosity might be expected to increase with increasing field strength; therefore, if the magnetic field strength were the dominant factor in determining the jet properties, the short decay timescales required to describe the $\Gamma \propto L$ relations observed in the results could be explained due to a greater dependence of losses on the B-field. A model in which the B-field increases with luminosity, thus giving rise to shorter loss timescales, could explain the observed photon index softening seen in the results for an increasing luminosity.

However, there is a problem with this model. If one assumes equipartition, then the local magnetic field strength also depends on emissivity such that $J(\nu) \propto N_0 \nu^{-(p-1)/2} B^{(p+1)/2}$ (e.g. Longair 1994; Bordovitsyn 1999). One would therefore expect to see emissivity scale with photon index if the B-field is in equipartition. The results presented in Tables 6.12 and 6.13 show that this is not the case. There is also strong evidence from the observations of Centaurus A (Hardcastle, 2007) that losses in this manner do not dominate the emission process. They show that there is significant variation in the values of the photon index along the length of the jet which are hard to explain in the context of a B-field dominated model since presumably, if anything, the B-field is decreasing along the jet whilst Γ is increasing.

It is therefore unlikely that the model as it stands provides a good description of the true nature of the jets and we are therefore left with two viable options. The first is that the B dominated model is incorrect and losses due to the large scale magnetic fields do not play a significant role in the process that sets the observed Γ; the second is that the magnetic field

does not lie in equipartition throughout the jet, meaning that the mean volume emissivity is not representative of the field strength.

One thing that is clear is that the models of particle acceleration currently proposed do not account for the bulk relations that have been found within this chapter. If a true description of the acceleration process is to be made, any proposed model must account for these general relations, as well as those within small scale features and individual galaxies.

6.5 Conclusions

Although no definitive conclusions can yet be drawn about the cause of particle acceleration, I have found a number of key relations which are not currently considered in models of FR-I galaxies, along with empirical evidence for relationships which have been long assumed to exist. These can be summarized as follows;

1. I find that the luminosity of X-ray jets scales linearly with luminosity at radio wavelengths.
2. I find that the interstellar medium through which a jet passes is unlikely to have a direct effect on determining the intrinsic acceleration properties of jets.
3. I find that for *bona fide* FR-Is, the photon index is related to jet luminosity at both X-ray and radio wavelengths, but shows no correlation to any other tested property.

Although I have presented the first large sample investigation of the properties of X-ray jets in FR-Is, the uncertainties involved are limited by the number of FR-Is known to have X-ray jets and the amount of data available for those which do. An additional note of caution which should also be made is that the properties found to be correlated at the 5 per cent significance level may be a result of the large number of properties tested, rather than a true relationship. I therefore suggest that future attempts should be made to verify and constrain the relations found within this chapter. Increasing the sample size as more FR-I galaxies with suitably resolvable X-ray jets are discovered will help reduce the uncertainties involved. Even within the constraints imposed by the available data, it is apparent that many previously unknown correlations exist.

I have tested a simple model in which large-scale magnetic field variations are primarily responsible for determining jet properties; however, I found that this model is inconsistent with my best estimates of the relative magnetic field strength in my sample. If an accurate description of FR-I jets is to be achieved, it is vital that these relations should be accounted for within future models.

7

Conclusions and future work

In this thesis, I have performed a range of investigations into outstanding issues surrounding the dynamics and energetics of radio-loud AGN. In this chapter, I details how the main results of this thesis address the questions set out in Section 1.7. For ease of reference, these questions are:

- How can one best exploit the new generation radio interferometers for the determination of spectral age?
- Are the commonly assumed parameters of spectral ageing models valid when considered on small spatial scales?
- Is spectral ageing a physical reality in the lobes of powerful radio sources?
- Do models of spectral ageing currently provide reliable intrinsic ages for powerful radio sources?
- What is the spectral profile of powerful radio galaxy lobes at low frequencies?
- What impact do these findings have on calculations of the energetics of these sources?
- What relationships are present between the properties of X-ray jets and their host galaxies?
- Do any of the current models adequately describe particle acceleration in the X-ray jets of FR-I galaxies?

I go on to detail future work which will be undertaken based my results in this thesis.

7.1 New methods of analysis for broad bandwidth radio observations

In Chapter 2, I presented the BRATS software package for the spectral analysis of the new generation of broad bandwidth radio interferometer. Throughout this thesis I have used this software to apply new techniques to determine spectral ages for a range of powerful radio sources. I have found that it is now possible to consider these sources on a pixel by pixel basis. I find that not only does this allow for a detailed analysis of spectral structure but due to cross-lobe variations, which appear to be common in FR-II sources, this method of analysis reduces the effects of superposition which can cause unreliable spectral ages.

I suggest that in order to simultaneously provide tight constraints on both the injection index and the spectral age, a very broad frequency coverage (e.g. from 100 MHz to 8 GHz) is required. I find that these analysis methods are not only applicable to radio galaxies, but also to other sources which are well described by models of spectral ageing, such as radio relics.

7.2 Parameters in models of spectral ageing

In Chapters 3, 4 and 5, I have presented results from the study of four powerful radio sources where I find that previously assumed parameters of spectral ageing are less reliable than previously thought.

Throughout this thesis I consistently find a significant deviation of the injection index from commonly assumed values. Using the BRATS software to minimize of χ^2 values of spectral ageing models for varying of injection indices and spectral index maps at low frequencies, I find that these sources have values in the range of $\alpha_{inj} \sim 0.7$ to 0.9, much higher than the previously assumed range of 0.6 to 0.7. This finding implies that the low energy electron population is higher than previously assumed and should be accounted for in any future studies. It is interesting to note that similar studies of radio relics, in which I have been involved, also find these higher injection indices, suggesting a potentially more widespread underestimation of the low energy electron population in sources well described by models of spectral ageing.

A further assumption which I find must now be carefully considered is that of non-negligible age variation over large region of the lobe, such as have traditionally been used. My results have shown that even in archetypal FR-II sources, significant variations in age across the width of the lobe are observed which if not accounted for can lead to unreliable ages and poor model fits. I

therefore suggest that future studies use methods which consider these sources on small spatial scales, such as those presented in this thesis.

7.3 Spectral ageing: reliability and its physical reality

In this thesis I have tested three models of spectral ageing, the JP model, the KP model and the more complex Tribble model. I have found that, overall, there is a basis in physical reality for models of spectral ageing; however, I suggest that new or modified versions of these models may be required if one is to accurately describe radio galaxies.

I confirm that, at least for some sources, there is a large disparity between the spectral and dynamical ages. I find that although a departure from the equipartition magnetic field strength is likely to contribute towards this age difference, it cannot alone explain the large variations observed. I also suggest that a significant mixing of new and old regions of plasma is likely to be present in some FR-II sources, which can to lead to the underestimation of spectral ages. This assertion is given further support by similar work by Heesen et al. (2014) who find that this population mixing is likely to play a key role in FR-I sources.

Of the three models tested, I find that although the KP model provides an improved goodness-of-fit compared to the JP model of spectral ageing in all sources I have considered in this thesis, it requires a less physically plausible set of environmental conditions to be present. I therefore conclude that the Tribble model, which maintains the physical reality of the JP model whilst also providing an improved goodness-of-fit, provides the first step in determining a model which provides a highly accurate description of these complex sources. As using the BRATS software one can simulate a source at any given frequency for each of these models, future studies will be able to provide a definitive answer to whether models based on a KP or JP spectrum truly describe these sources. The flux of these models diverges sharply for any fixed age at frequencies of 10s of GHz, so there is a clear high-frequency prediction for each model when the ages are known, such as has been achieved by the studies undertaken in this thesis.

7.4 The spectral profile and energetics of powerful radio galaxy lobes at low frequencies

In Chapter 5, I have used low-frequency LOFAR observations to study the energetics of the powerful radio source 3C223 and to determine its spectrum at these wavelengths on small spatial

scales. Using BRATS to produce spectral index maps of the source, I find that the observed spectrum is much steeper than previously assumed. As I have already discussed the implication of this result in terms of spectral ageing model parameters in Section 7.2, I do not repeat myself here; however, I find that this increase in the low energy electron population also has a significant impact on the energetics of FR-II sources.

Fitting synchrotron / inverse-Compton models to the X-ray and radio data presented by Croston et al. (2004), further constrained by my low-frequency observations, I find that the total energy density in the both by northern and southern lobes of 3C223 increase by a factor of ~ 2. The cause of this increase is due to the underestimation of the low energy electron population in the original model fitting. The resultant increase in the derived internal pressure means that the northern lobe is approximately in pressure balance at the end of the lobe, with the southern lobe becoming overpressured. This result also has potentially large implications as the same assumption for the low-frequency spectrum has been made in later work over a wider range of radio galaxies (Croston et al., 2005). If this higher than expected low energy electron population is therefore common to all FR-II galaxies (as the high injection indices also found in Chapters 3 and 4 imply is plausibly the case), then the total energy content, hence pressure, of the FR-II population as a whole will significantly increase. I therefore suggest this may provide a solution to the issue of static or expanding radio lobes being apparently underpressured.

7.5 Relationships and models of X-ray jets in FR-I radio galaxies

In Chapter 6 I have performed the first large sample investigation of the properties of X-ray jets in FR-I radio galaxies and their relationships to the properties of the host galaxies in which they reside. I confirm the previously assumed relation between jet emission at X-ray and radio wavelengths and find it to be linear when only *bona fide* FR-I sources are considered. I also find that previously unknown relations exist between the jets photon index, volume and radio and X-ray luminosities. Due to the lack of correlation to the host galaxy properties, I conclude that the interstellar medium through which these jets pass have no direct effect on their overall intrinsic acceleration properties. This is given further support by the average jet properties found for OL97 0313-192 which is thought to reside in an spiral host, hence is likely to pass through a significantly different environment that its elliptical counterparts.

To explain the observed relationships, I have tested a simple model in which the large scale magnetic field variations are responsible for determining the jet properties, but, find it is in-

consistent with the magnetic field strength of my sample. I conclude that currently no particle acceleration models are able to fully explain the relationships found within this chapter and suggest that it is vital that they are accounted for in future models if an accurate description of X-ray jets is to be obtained.

7.6 Future work

The results presented in this thesis have addressed many issues surrounding the dynamics and energetics of radio galaxies, particularly in the area of spectral ageing, but have also raised new questions which must be answered if one is to understand the underlying physics of these important sources. Moving forward, I therefore intend to address three key questions. Why are the dynamical ages of some powerful radio sources up to an order of magnitude higher than those derived spectrally? Are high injection indices common in the FR-II population as a whole? Do models of spectral ageing provide a good description of radio galaxies over extremely wide frequency ranges?

To fully address these questions, observations over a wide frequency range are required for a variety of radio galaxies. Additional low-frequency observations are currently in hand (e.g. 3C452 discussed in Chapter 5) and further sources will be obtained through my role as lead scientist for the analysis of powerful radio sources in the LOFAR nearby AGN key science project. Complementary JVLA P-band observations have also been approved which, as well as providing almost continuous low-frequency coverage between 30 and 500 MHz, will also aid in the commissioning efforts of both the JVLA and LOFAR. As only a small frequency gap exists between these instruments, any absolute flux calibration errors will be immediately obvious as a jump in integrated flux. Differential calibration errors will also be identifiable due to real spectral curvature being position-dependent, whereas curvature due to differential calibration errors are not. As was noted in Chapters 4 and 5, the currently unknown relative error between the two instruments make it difficult to distinguish between spectral ageing models and to determine injection indices, hence this calibration check is vital to both the commissioning of these instruments and my science goals.

Once calibrated, these observations will allow me to test two key aspects of current spectral ageing models. In the standard KP and JP models magnetic fields are assumed to be uniform (Section 1.3.2); however, the complexity of FR-II sources mean that the validity of this assumption is far from clear. If high levels of low-frequency curvature are observed within these very

broad bandwidth observations, it is likely that a non-uniform field exists and modified JP models, such as the Tribble model, would be favoured. These observations will also further help to constrain injection indices over a wider variety of sources. If the discrepancy between commonly assumed values and those derived through direct model fitting is significantly reduced, new or modified models of spectral ageing will likely be required to accurately describe these sources over large frequency ranges. If the discrepancy remains, it is likely that the mixing of electron populations plays a key role in the observed spectra of these sources, forcing older regions of plasma to be best fitted by inflated injection index values. Future observations at low frequencies under the KSP umbrella will be made in later observing cycles which, if required, can be tailored to address any questions arising from these initial findings.

As injection index values play a key role in determining reliable spectral ages, the low-frequency investigations describe above will be supported by high resolution imaging of hotspots using e-MERLIN. As PI of the project "Spectral structure and particle acceleration in the hotspots of FR-II radio sources", for which 90 hours of e-MERLIN open time has been awarded, I will explore the spectral profile and underlying physics of these assumed sites of particle acceleration. These unique broad-bandwidth observations potentially hold the key to resolving the deviation of injection indices from assumed values. My involvement in the e-MERLIN legacy project, "Resolving key questions in extragalactic jet physics", will further reinforce our understanding of the underlying physics of these powerful radio sources and aid in the determination of accurate models of radio-loud active galaxies.

The unparalleled capabilities provided by ALMA also present an opportunity to investigate these hotspots at a level of detail never before possible. Spectral curvature is most prominent in the lobes of FR-II galaxies at a few GHz; however, if lobe expansion is adiabatic, emission from the electron population which will eventually radiate at these frequencies will be observed within acceleration regions as emission at ~ 100 GHz. The ability of ALMA to provide broad-bandwidth observations at high frequencies therefore allows us to investigate both the injection index and the spectral profile of these electron populations early in their ageing life cycle. A proposal will therefore be submitted to observe a small sample of hotspots using ALMA band 3 (84 – 119GHz), further increasing the understanding of these sources and providing greater constraints on model parameters.

At frequencies between 4 – 8 GHz, where spectral curvature is expected to be most prominent, further JVLA proposals will be made during 2014 to extend the frequency coverage of the sources studied in Chapters 3 and 4, along with the observation of additional 3C sources to

expand the generality of my results, to lower L- and S-band (1 – 4 GHz) and higher X-band (8 – 12 GHz) frequencies. These data will give continuous coverage over a very broad (11 GHz) frequency range and will provide a definitive answer to the debate over whether the KP or JP models of spectral ageing (or those derived from these models, such as the Tribble model) provide an accurate description of the spectrum of powerful radio galaxies.

7. CONCLUSIONS AND FUTURE WORK

References

Akritas M. G., Siebert J., 1996, MNRAS, 278, 919 191

Alexander P., 1987, MNRAS, 225, 27 4, 21, 76, 86, 107, 108

Alexander P., Leahy J. P., 1987, MNRAS, 225, 1 21, 31, 76, 86, 96, 110, 111, 133, 143

Andernach H., Feretti L., Giovannini G., Klein U., Rossetti E., Schnaubelt J., 1992, A&AS, 93, 331 19

Arshakian T. G., Longair M. S., 2004, MNRAS, 351, 727 30

Atoyan A., Dermer C. D., 2004, ApJ, 613, 151 25, 174

Avni Y., 1976, ApJ, 210, 642 68

Balogh M. L., Pearce F. R., Bower R. G., Kay S. T., 2001, MNRAS, 326, 1228 1

Barthel P. D., 1989, ApJ, 336, 606 6

Barthel P. D., 1994, in ASP Conference Series, Vol. 54, *'First Stromlo symposium: physics of active galactic nuclei'*, Bicknell G. V., Dopita M. A., Quinn P. J., eds. 6

Basson J. F., Alexander P., 2003, MNRAS, 339, 353 34

Becker R. H., White R. L., Edward A. L., 1991, ApJS, 75, 1 182, 188

Begelman M. C., Cioffi D. F., 1989, ApJ, 345, L21 31

Best P. N., 2004, MNRAS, 351, 70 32, 33

Bicknell G. V., 1984, ApJ, 286, 68 14, 16, 21, 28

REFERENCES

Bicknell G. V., 1992, in Proceedings of the 7th. I.A.P. meeting, Vol. 307, *'Extragalactic radio sources. From beams to jets'*, Roland J., Sol H., Pelletier G., eds. 21

Binney J., Tabor G., 1995, MNRAS, 276, 663 34

Biretta J. A., Meisenheimer K., 1993, in Lecture notes in physics, Vol. 421, *'Jets in extragalactic radio sources'*, Röser H. J., Meisenheimer K., eds. 25, 174

Biretta J. A., Stern C. P., Harris D. E., 1991, AJ, 101, 1632 179

Birk G. T., Lesch H., 2000, ApJ, 530, L77 25, 174

Birkinshaw M., Laing R., Peacock J. A., 1981, MNRAS, 197, 253 4, 19

Birzan L., Rafferty D. A., McNamara B. R., Wise M. W., Nulsen P. E. J., 2004, ApJ, 607, 800 34

Blandford R. D., Rees M. J., 1974, MNRAS, 169, 395 28

Blundell K. M., Rawlings S., 2000, ApJ, 119, 1111 110, 141

Blundell K. M., Rawlings S., 2001, in ASP Conference Series, Vol. 250, *'Particles and Field in Radio Galaxies'*, Laing R., Blundell K., eds. 99

Boehringer H., Voges W., Fabian A. C., Edge A. C., Neumann D. M., 1993, MNRAS, 264, L25 34

Bower R. G., Benson A. J., Malbon J. C., Helly J. C., Frenk C. S., Baugh C. M., Cole S., Lacey C. G., 2006, MNRAS, 370, 645 2, 33, 35

Bowman M., Leahy J. P., Komissarov S. S., 1996, MNRAS, 279, 899 16

Bridle A. H., Fomalont E. B., Cornwell T. J., 1981, AJ, 22, 319 viii, 24

Bridle A. H., Perley R. A., 1984, ARA&A, 22, 319 102

Brunetti G., Cappi M., Setti G., Feretti L., Harris D. E., 2001, A&A, 372, 755 27

Brunetti G., Mack K. H., Prieto M. A., Varano S., 2003, MNRAS, 345, L40 23, 25, 174

Burch S. F., 1979, MNRAS, 186, 519 108

Burns J. O., Feigelson E. D., Schreier E. J., 1983, ApJ, 273, 128 25

Canosa C. M., Worrall D. M., Hardcastle M. J., M. B., 1999, MNRAS, 310, 30 188, 189

Canvin J. R., Laing R. A., 2004, MNRAS, 350, 1342 28

Carilli C., Perley R., Dreher J., Leahy J., 1991, ApJ, 383, 554 12, 30, 76, 82, 86, 107, 110, 115

Celotti A., Fabian A. C., 1993, MNRAS, 264, 228 15

Celotti A., Ghisellini G., Chiaberge M., 2001, MNRAS, 321, 1 27, 30

Chartas G. et al., 2000, ApJ, 542, 655 27

Chiaberge M., Gilli R., Macchetto F. D., Sparks W. B., A. C., 2003, ApJ, 582, 645 179

Cisternas M. et al., 2011, ApJ, 726, 57 32

Clark B. G., 1980, A&A, 89, 377 56, 57

Cole S., 1991, ApJ, 367, 45 1

Cowie L. L., Binney J., 1977, ApJ, 215, 723 1, 33

Croston J. H., Birkinshaw M., Hardcastle M. J., Worrall D. M., 2004, MNRAS, 353, 879 xiii, 147, 154, 157, 159, 160, 164, 169, 170, 208

Croston J. H., Hardcastle M. J., 2014, MNRAS, 438, 3310 16

Croston J. H., Hardcastle M. J., Birkinshaw M., Worrall D. M., Laing R. A., 2008a, MNRAS, 386, 1709 17, 29

Croston J. H., Hardcastle M. J., Harris D. R., Belsole E., Birkinshaw M., Worrall D. M., 2005, ApJ, 626, 733 16, 17, 19, 31, 86, 113, 147, 154, 157, 169, 170, 208

Croston J. H., Hardcastle M. J., Mingo B., Evans D. A., Dicken D., Morganti R., Tadhunter C. N., 2011, ApJ, 734, L28 34

Croston J. H., Kraft R. P., Hardcastle M. J., 2007, ApJ, 660, 191 29

Croston J. H. et al., 2009, MNRAS, 395, 1999 34

Croston J. H. et al., 2008b, A&A, 487, 431 16, 113

REFERENCES

Croton D. J. et al., 2006, MNRAS, 365, 11 viii, 2, 33, 35, 37

de Gasperin F. et al., 2012, A&A, 547, A56 86

Dennett-Thorpe J., Scheuer P. A. G., Laing R. A., Bridle A. H., Pooley G. G., Reich W., 2002, MNRAS, 330, 609 23

Dreher J. W., Carilli C. L., Perley R. A., 1987, ApJ, 316, 611 viii, 24

Dunn R. J. H., Fabian A. C., Celotti A., 2006, MNRAS, 372, 1741 16

Eilek J. A., 1996, in ASP Conference Series, Vol. 100, *'Energy transport in radio galaxies and quasars'*, Hardee P. E., Bridle A. H., Zensus J. A., eds. 31, 37, 99, 110, 112, 116, 141

Eilek J. A., 2004, in *'The riddle of cooling flows in galaxies and clusters of galaxies'*, Reiprich T. H., Kempner J. C., , Soker N., eds. 33

Eilek J. A., Arendt P. N., 1996, ApJ, 457, 150 73, 99, 110

Eilek J. A., Melrose D. B., Walker M. A., 1997, ApJ, 483, 282 110

Emonts B. H. C., Tadhunter C. N., Morganti R., Oosterloo T. A., Holt J., Brogt E., van Moorsel G., 2009, MNRAS, 396, 1522 191

Fabian A. C., 1994, ARA&A, 32, 277 33

Fabian A. C., Nulsen P. E. J., 1977, MNRAS, 180, 479 1, 33

Fabian A. C. et al., 2000, MNRAS, 318, L65 21

Falco E. E. et al., 1999, PASP, 111, 438 182, 188

Falle S. A. E. G., 1991, MNRAS, 250, 581 36

Fanaroff B. L., Riley J. M., 1974, MNRAS, 167, 31P 4, 19, 21

Feigelson E. D., Laurent-Muehleisen S. A., Kollgaard R. I., Fomalont E. B., 1995, ApJ, 449, L149 27

Feigelson E. D., Schreier E. J., Delvaille J. P., Giacconi R., Grindlay J. E., Lightman A. P., 1981, ApJ, 251, 31 178

Feretti L., Perley R., Giovannini G., Andernach H., 1999, A&A, 341, 29 16

Ferrari A., 1998, ARA&A, 36, 539 31

Ghisellini G., Celotti A., George I. M., Fabian A. C., 1992, MNRAS, 258, 776 14

Giovannini G., Cotton W. D., Feretti L., Lara L., Venturi T., 2001, ApJ, 552, 508 21

Godfrey, L. E. H.; Shabala S. S., 2013, ApJ, 767, 9 36

Gonzalez-Serrano J. I., Carballo R., Perez-Fournon I., 1993, AJ, 105, 1710 32

Goodger J. L., Hardcastle M. J., Croston J. H., Kassim N., Perley R. A., 2008, MNRAS, 386, 337 110

Goodger J. L. et al., 2010, ApJ, 708, 675 21, 25, 174, 199

Govoni F., Falomo R., Fasano G., Scarpa R., 2000, A&A, 353, 507 32

Gull S. F., Northover K. J. E., 1973, Nature, 244, 80 21

Hardcastle M. J., 2005, RSPTA, 363, 2711 27

Hardcastle M. J., 2006, MNRAS, 366, 1465 30

Hardcastle M. J., 2007, ApJ, 670, L81 25, 174, 190, 194, 199, 203

Hardcastle M. J., 2013, MNRAS, 433, 3364 12, 14, 67, 116

Hardcastle M. J., Alexander P., Pooley G. G., Riley J. M., 1996, MNRAS, 278, 273 viii, 22

Hardcastle M. J., Alexander P., Pooley G. G., Riley J. M., 1997, MNRAS, 288, 859 xi, 76, 78, 87, 106

Hardcastle M. J., Alexander P., Pooley G. G., Riley J. M., 1999, MNRAS, 304, 135 30, 189

Hardcastle M. J., Birkinshaw M., Cameron, R. A. Harriss D. E., Looney L. W., Worrall D. M., 2002a, ApJ, 581, 948 27

Hardcastle M. J., Birkinshaw M., Worrall D. M., 1998, MNRAS, 294, 615 34, 82, 126, 154

Hardcastle M. J., Birkinshaw M., Worrall D. M., 2001, MNRAS, 326, 1499 23, 173, 177

Hardcastle M. J., Cheung C. C., Feain I. J., Stawarz L., 2009a, MNRAS, 393, 1041 182

Hardcastle M. J., Croston J. H., 2005, MNRAS, 363, 649 110

Hardcastle M. J., Croston J. H., 2010, MNRAS, 404, 2018 143

Hardcastle M. J., Croston J. H., Kraft R. P., 2006a, MNRAS, 366, 1465 6

Hardcastle M. J., Evans D. A., Croston J. H., 2006b, MNRAS, 370, 1893 188

Hardcastle M. J., Evans D. A., Croston J. H., 2009b, MNRAS, 396, 1929 188

Hardcastle M. J., Harris D. E., Worrall D. M., Birkinshaw M., Laing R. A., H. B. A., 2004a, ApJ, 612, 729 201

Hardcastle M. J., Krause M. G. H., 2013, MNRAS, 430, 174 31, 112

Hardcastle M. J., Looney L. W., 2001, MNRAS, 320, 355 65, 73, 76, 108, 144

Hardcastle M. J., Looney L. W., 2008, MNRAS, 388, 176 114

Hardcastle M. J., Massaro H., Harris D. E., 2010, MNRAS, 401, 2697 120

Hardcastle M. J., Sakelliou I., 2004, MNRAS, 349, 560 23, 30

Hardcastle M. J., Sakelliou I., Worrall D. M., 2005a, MNRAS, 358, 843 177

Hardcastle M. J., Worrall D. M., 1999, MNRAS, 309, 969 188

Hardcastle M. J., Worrall D. M., 2000a, MNRAS, 319, 562 17, 29, 31, 188, 189

Hardcastle M. J., Worrall D. M., 2000b, MNRAS, 314, 359 25

Hardcastle M. J., Worrall D. M., Birkinshaw M., Laing R. A., Bridle A. H., 2002b, MNRAS, 334, 182 23, 177

Hardcastle M. J., Worrall D. M., Birkinshaw M., Laing R. A., Bridle A. H., 2005b, MNRAS, 358, 843 177, 182

Hardcastle M. J., Worrall D. M., Kraft R. P., Forman C. J., Murray S. S., 2003, ApJ, 593, 169 21, 25, 173, 178, 199

Hardcastle M. J., Worrall D. M., Kraft R. P., Forman W. R., Jones C., S. M. S., 2004b, in Nuclear physics B - Proceedings supplements, Vol. 132, *'Proceedings of the 2nd BeppoSAX conference: The restless high-energy universe'*, van den Heuvel E. P. J., Wijers R. A. M. J., Zand J. J. M., eds. viii, 22, 25, 199

Harris D. E., Biretta J. A., Junor W., Perlman E. S., Sparks W. B., S. W. A., 2003, ApJ, 586, L41 179

Harris D. E., Cheung C. C., Biretta J. A., Sparks W. B., Junor W., Perlman E. S., Wilson A. S., 2006, ApJ, 640, 211 179

Harris D. E., Finoguenov A., Bridle A. H., Hardcastle M. J., Laing R. A., 2002a, ApJ, 580, 110 178

Harris D. E., Krawczynski H., 2006, ARA&A, 44, 463 23, 25

Harris D. E., Krawczynski H., Taylor G. B., 2002b, ApJ, 578, 740 177

Harwood J. J., Hardcastle M. J., 2012, MNRAS, 423, 1368 xviii, 39

Harwood J. J., Hardcastle M. J., Croston J. H., Goodger J. L., 2013, MNRAS, 435, 3353 xviii, 12, 39

Heckman T. M., Smith E. P., Baum S. A., van Breugel W. J. M., Miley G. K., Illingworth G. D., Bothun G. D., Balick B., 1986, ApJ, 311, 526 32

Heesen V., Croston J. H., Harwood J. J., Hardcastle M. J., Ananda H., 2014, MNRAS, 439, 1364 29, 207

Heinz S., Brüggen M., Young A., Levesque S., 2006, MNRAS, 373, L65 31

Hill G. J., Lilly S. J., 1991, ApJ, 367, 1 33

Högbom J., 1974, ApJS, 15, 417 56

Homan D. C., Wardle J. F. C., 1999, AJ, 118, 1942 16

Hughes P. A., 1991, Beams and Jets in Astrophysics. Cambridge University Press 113

Isobe N., Tashiro M., Makishima K., Iyomoto N., Suzuki M., Murakami M. M., Mori M., Abe K., 2002, ApJ, 580, L111 25, 27, 31

Jaffe W., Perola G., 1973, A&A, 26, 423 11, 12, 82, 86, 107

Jennison R. C., Das Gupta M. K., 1953, Nature, 172, 996 4

Jester S., Röser H. J., Meisenheimer K., Perley R., 2002, ApJ, 385, L27 27

Jetha N. N., Hardcastle M. J., Sakelliou I., 2006, MNRAS, 368, 609 21

Jones T. W., Odell S. L., 1977, A&A, 61, 291 15, 19

Jones T. W., Ryu D., Engel A., 1999, ApJ, 512, 105 23

Kaiser C. R., Alexander P., 1997, MNRAS, 286, 215 31, 36, 112, 113

Kaiser C. R., Alexander P., 1999, MNRAS, 305, 707 34

Kardashev N. S., 1962, AJ, 6, 317 11

Kataoka J., Leahy J. P., Edwards P. G., Kino M., Takahara F., Serino Y., Kawai N., Martel A. R., 2003, A&A, 410, 833 177

Kataoka J., Stawarz L., 2005, ApJ, 622, 797 27

Kataoka J., Stawarz L., Aharonian F., Takahara F., Ostrowski M., Edwards P. G., 2006, ApJ, 641, 158 25, 174, 199

Katz-Stone D. M., Rudnick L., Anderson M. C., 1993, ApJ, 407, 549 21, 65, 73, 82, 107, 108, 110

Keel W., White R., Owen F., Ledlow M., 2006, ApJ, 132, 2233 32, 177, 191

Kocevski D. et al., 2012, ApJ, 744, 148 32

Komissarov S. S., Gubanov A. G., 1994, A&A, 285, 27 ix, 66

Konar C., Hardcastle M. J., 2013, MNRAS, 436, 1595 16

Konar C., Saikai D. J., Jamrozy M., Machalski J., 2006, MNRAS, 372, 693 4, 21, 108

Kraft R. P., Forman C. J., Jones C., Murray S. S., Hardcastle M. J., Worrall D. M., 2002a, ApJ, 569, 54 21, 178

Kraft R. P. et al., 2000, ApJ, 531, L9 178

Kraft R. P., Forman W. R., Hardcastle M. J., Jones C., Nulsen P. E. J., 2007, ApJ, 664, 83 141, 143

Kraft R. P., Hardcastle M. J., Worrall D. M., Murray S., 2002b, ApJ, 622, 149 27

Kraft R. P., Vzquez S. E., Forman W. R., Jones C., Murray S. S., Hardcastle M. J., Worrall D. M., Churazov E., 2003, ApJ, 592, 129 29, 178

Krause M., Alexander P., Riley J., Hopton D., 2012, MNRAS, 427, 3196 19, 21, 31

Laing R. A., Bridle A. H., 2002a, MNRAS, 336, 328 vii, 3, 16, 21, 28

Laing R. A., Bridle A. H., 2002b, MNRAS, 336, 1161 21, 28

Laing R. A., Bridle A. H., 2013, MNRAS, 432, 1114 102

Laing R. A., Bridle A. H., Cotton W. D., Worrall D. M., Birkinshaw D. M., 2008, in ASP Conference Series, Vol. 386, *'Extragalactic jets: theory and observations from radio to gamma ray'*, Rector T. A., De Young D. S., eds. 23, 28, 102, 173

Laing R. A., Canvin J. R., Bridle A. H., Hardcastle M. J., 2006, MNRAS, 372, 510 102

Laing R. A., Parma P., de Reuiter H. R., Fanti R., 1999, MNRAS, 306, 513 21

Laing R. A., Peacock J. A., 1980, MNRAS, 190, 903 107, 152

Laing R. A., Riley J. M., Longair M. S., 1983, MNRAS, 204, 151 74, 76, 120, 148

Leahy J. P., 1991, Beams and jets in astrophysics: Interpretation of large scale extragalactic jets. Cambridge University Press 12, 14, 17, 23, 29

Leahy J. P., Black A. R. S., Dennett-Thorpe J., Hardcastle M. J., Komissarov S., Perley R. A., Riley J. M., Scheuer P. A. G., 1997, MNRAS, 291, 20 vii, 3, 76, 140

Leahy J. P., Perley R. A., 1991, AJ, 102, 537 150

Ledlow M. J., Owen F. N., Keel W. C., 1998, ApJ, 495, 227 32

Lilly S. J., Prestage R. M., 1987, MNRAS, 225, 531 32

Liu R., Pooley G., Riley J. M., 1992, MNRAS, 257, 545 21, 31, 96, 108, 111

Longair M. S., 2011, High Energy Astrophysics. Cambridge University Press 9, 11, 23, 65

Longair M. S., Ryle M., Scheuer P. A. G., 1973, MNRAS, 164, 243 28, 30

Machalski J., Jamrozy M., Saikia D. J., 2009, MNRAS, 395, 812 4, 21, 110

Mack K. H., Kerp J., U. K., 1997, A&A, 324, 870 179

Mackay C. D., 1973, A&AA, 162, 1 31

Marscher A. P., Jorstad S. G., 2011, ApJ, 729, 26 4, 19, 179

Marshall H. L., Miller B. P., Davis D. S., Perlman E. S., Wise M., Canizares C. R., Harris D. E., Biretta J. A., 2002, ApJ, 564, 683 179

Marshall H. L. et al., 2005, ApJS, 156, 13 178

Mathews W. G., Bregman J. N., 1978, ApJ, 224, 308 33

McNamara B. R., Nulsen P. E. J., 2007, ARA&A, 45, 117 33

McNamara B. R., Nulsen P. E. J., 2012, New J. Phys., 14, 055023 16

Meisenheimer K., Röser H. J., Hiltner P. R., Yates M. G., Longair M. S., Chini R., Perley R. A., 1989, A&A, 219, 63 30

Mendygral P. J., Jones T. W., Dolag K., 2012, ApJ, 750, 166 31

Merritt D., Ekers R. D., 2002, Science, 297, 1310 23

Mohr J. J., Mathiesen B., Evrard A. E., 1999, ApJ, 517, 627 113

Morganti R., Oosterloo T., Tsvetanov Z., 1988, AJ, 115, 915 17

Morsony B. J., Miller J. J., Heinz S., Freeland E., Wilcots E., Brüggen M., Ruszkowski M., 2013, MNRAS, 431, 781 31

Mullin L. M., Hardcastle M. J., 2009, MNRAS, 398, 1989 30

Mullin L. M., Hardcastle M. J., Riley J. M., 2006, MNRAS, 372, 113 4, 21

Myers S., Spangler S., 1985, ApJ, 291, 52 21, 30, 31, 96, 111, 143

Newman A. B., Tommaso T., Ellis R. S., Sand D. J., 2013, ApJ, 765, 25 113

Nulsen P. E. J., Hambrick D. C., McNamara B. R., Rafferty D., Birzan L., Wise M. W., David L. P., 2005, ApJ, 625, L9 34

O'Dea C. P., Owen F. N., 1986, ApJ, 301, 841 viii, 22

Offringa A. R., de Bruyn A. G., Biehl M., Zaroubi S., Bernardi G., Pandey V. N., 2010, MNRAS, 405, 155 55

Oosterloo T. A., Morganti R., Emonts B. H. C., Tadhunter C. N., 2004, in Proceedings of the IAU, Vol. 222, *'The interplay among black holes, stars and ISM in galactic nuclei'*, Storchi-Bergmann T., Ho L. C., Schmitt H. R., eds. 34

Orban de Xivry G., Davies R., Schartmann M., Komossa S., Marconi A., Hicks E., Engel H., Tacconi L., 2011, MNRAS, 417, 2721 32

Orru E., Murgia M., Feretti L., Govoni F., Giovannini G., Lane W., Kassim N., Paladino R., 2010, A&A, 515, A50 82, 107, 151

Owen F. N., Eilek J. A., Kassim N. E., 2000, ApJ, 543, 611 viii, 22

Owen F. N., Laing R. A., 1989, MNRAS, 238, 357 32

Owen F. N., Ledlow M. J., 1994, in ASP Conference Series, Vol. 54, *'The first Stromlo symposium: The physics of active galaxies'*, Bicknell G. V., Dopita M. A., Quinn P. J., eds. vii, 19, 20, 21

Pacholczyk A. G., 1970, Radio astrophysics. Nonthermal processes in galactic and extragalactic sources. San Francisco, Freeman ix, 11, 12, 66, 67, 113, 114

Peacock J. A. et al., 2001, Nat, 410, 169 1

Perley R. A., Butler B. J., 2013, ApJ, 204, 19 47

Perley R. A., Röser H. J., Meisenheimer K., 1997, A&A, 328, 12 76

Perlman E. S. et al., 2011, ApJ, 743, 119 201

Perlman E. S., Harris D. E., Biretta J. A., Sparks W. B., D. M. F., 2003, ApJ, 599, L65 179

Perlman E. S. et al., 2010, ApJ, 708, 171 177

Perlman E. S., Wilson A. S., 2005, ApJ, 627, 140 23, 173, 174, 179

Pesce J. E., Sambruna R. M., Tevecchio F., Maraschi L., Cheung C. C., Urry C. M., R. S., 2001, ApJ, 556, L79 177

Peterson J. R. et al., 2001, A&A, 365, L104 1

Ponman T. J., Cannon D. B., Navarro J. F., 1999, Nature, 397, 135 33

Press W. H., Teukolsky, S. A.and Vetterling W. T., Flannery B. P., 2007, Numerical Recipes 3rd Edition: The Art of Scientific Computing. Cambridge University Press 68, 71

Prestage R. M., Peacock J. A., 1988, MNRAS, 230, 131 33

Rafferty D. A., McNamara B. R., Nulsen P. E. J., Wise M. W., 2006, ApJ, 652, 216 34

Reynolds C. S., Fabian A. C., Celotti A., Rees M. J., 1996, MNRAS, 283, 873 15

Rieger F. M., Bosch-Ramon V., Duffy P., 2007, AP&SS, 309, 199 25, 174

Riess A. G. et al., 2000, ApJ, 536, 62 1

Rudnick L., Katz-Stone D. M., Anderson M. C., 1994, ApJS, 90, 955 110

Rybicki G. B., Lightman A. P., 1979, Radiative processes in astrophysics. Wiley, New York 9, 11, 65

Sambruna R. M., Donato D., Cheung C. C., Tavecchio F., L. M., 2008, ApJ, 684, 862 179

Sambruna R. M., Donato D., Tavecchio F., Maraschi L., Cheung C. C., M. U. C., 2007, ApJ, 670, 74 177, 179

Sambruna R. M., Gambill J. K., Maraschi L., Tavecchio F., Cerutti R., Cheung C. C., Urry C. M., Chartas G., 2004, ApJ, 608, 698 23, 30, 178

Sand D. J., Tommaso T., Smith G. P., Ellis R. S., 2004, ApJ, 604, 88 113

Sarazin C. L., 1986, Rev. Mod. Phys., 58, 1 33

Sarazin C. L., O'Connell R. W., McNamara B. R., 1992, ApJ, 389, L59 33

Scaife A. M. M., Heald G. H., 2012, MNRAS, 423, L30 49

Schawinski K., Treister E., Urry C. M., Cardamone C. N., Simmons B., Yi S. K., 2011, ApJ, 727, 31 32

Scheuer P. A. G., 1974, MNRAS, 166, 513 28, 30, 31

Scheuer P. A. G., 1995, MNRAS, 277, 331 31, 112

Schilizzi R. T. et al., 2001, A&A, 368, 398 21

Schwab F. R., 1984, AJ, 59, 1076 57

Sirothia S. K., Gopal-Krishna S., Wiita P. J., 2013, ApJ, 765, L11 149

Skrutskie M. F. et al., 2006, AJ, 131, 1163 182, 188

Smith D. A., Wilson A. S., Arnaud K. A., Terashima Y., Young A. J., 2002, ApJ, 565, 195 34

Spergel D. N. et al., 2007, ApJS, 170, 377 1

Stawarz L., Ostrowski M., 2002, ApJ, 578, 763 25, 174

Stroe A., van Weeren R. J., Intema H. T., Rttgering H. J. A., Brggen M., Hoeft M., 2013, A&A, 555, 19 ix, 65, 66, 166

Sun M., Jerius D., C. J., 2005, ApJ, 633, 165 178

Swain M. R., Bridle A. H., Baum S., 1998, ApJ, 507, 29 21

Tamura T. et al., 2001, A&A, 365, L87 1

Tashiro M. et al., 1998, ApJ, 499, 713 18, 25, 31

Tavecchio F., Maraschi L., Sambruna R. M., Urry C. M., 2000, ApJ, 544, 23 27, 30

Tregillis I. L., Jones T. W., Ryu D., 2001, ApJ, 557, 475 31

Treichel K., Rudnick L., Hardcastle M. J., Leahy J. P., 2001, ApJ, 561, 691 xii, 21, 23, 102, 122, 132, 136

Tribble P., 1993, MNRAS, 261, 57 12, 74, 116

Trussoni E., Vagnetti F., Massaglia S., Feretti L., Parma P., Morganti R., Fanti R., Padovani P., 1999, A&A, 348, 437 175, 177

Urry C. M., Padovani P., 1995, PASP, 107, 803 6, 8

van Weeren R. J., Röttgering H. J. A., Intema H. T., Rudnick L., Brüggen M., Hoeft M., Oonk J. B. R., 2012, A&A, 546, 124 166

Vermeulen R. C., Ogle P. M., Tran H. D., Browne I. W. A., Cohen M. H., Readhead A. C. S., Taylor G. B., Goodrich R. W., 1995, ApJ, 452, L5 8

Wardle J. F. C., 1977, Nature, 269, 563 15

Wardle J. F. C., Homan D. C., Ojha R., Roberts D. H., 1998, Nature, 395, 457 15, 16

White S. D. M., Frenk C. S., 1991, ApJ, 379, 52 1, 2, 35

White S. D. M., Rees M. J., 1978, MNRAS, 183, 341 1, 2, 35

Wilson A. S., Yang Y., 2002, ApJ, 568, 133 23, 179

Wilson A. S., Young A. J., Shopbell P. L., 2000, ApJ, 547, 740 25

Worrall D. M., Birkinshaw M., 2000, ApJ, 530, 719 17

Worrall D. M., Birkinshaw M., 2005, MNRAS, 360, 926 177

Worrall D. M., Birkinshaw M., Hardcastle M. J., 2001a, MNRAS, 194, 359 23

Worrall D. M., Birkinshaw M., J. H. M., 2001b, MNRAS, 194, 359 178

Worrall D. M., Birkinshaw M., J. H. M., 2003, MNRAS, 343, 73 179

Worrall D. M., Birkinshaw M., Young A. J., Momtahan K., Fosbury R. A. E., Morganti R., Tadhunter C. N., Verdoes Kleijn G., 2007, MNRAS, 424, 1346 29

Wu K. K. S., Fabian A. C., Nulsen P. E. J., 2000, MNRAS, 318, 889 33

Wykes S. et al., 2013, MNRAS, 558, 13 17

Zensus J. A., 1997, ARA&A, 35, 607 28